INVESTIGATION OF POROUS GLASSES BASED ON SODIUM-BOROSILICATE GLASS SYSTEM

MUHAMMAD HASANUZZAMAN
(B.Sc., M.Eng.)

A thesis submitted for the degree of
Doctor of Philosophy

School of Mechanical and Manufacturing Engineering
DUBLIN CITY UNIVERSITY

Supervisor:
Dr. Abdul-Ghani Olabi

March 2013

DECLARATION

I hereby certify that this material, which I now submit for assessment on the programme of study leading to the award of Ph.D. is entirely my own work, and that I have exercised reasonable care to ensure that the work is original, and does not to the best of my knowledge breach any law of copyright, and has not been taken from the work of others save and to the extent that such work has been cited and acknowledged within the text of my work.

Signed : _____

(Muhammad Hasanuzzaman)

ID No. : 53126505

Date : March 2013

ACKNOWLEDGEMENTS

It is with deep gratitude and appreciation that I would like to thank the many people who made this thesis possible.

I would like to express my sincere thanks and gratitude to my supervisor Dr. Abdul-Ghani Olabi. He provided knowledge, guidance, and advice that was invaluable throughout the course of this research. Without his continuous help and advice this work would not have been possible. I am very much grateful to Professor M. S. J. Hashmi for his continuous support while I carried out my study. I would also like to thank Dr. Joseph Stokes. As Head of School, he lent me his full and unreserved support.

I am indebted to my previous supervisor Dr. Aran Rafferty for giving me the opportunity, advice, and encouragement to undertake this PhD. He provided sound advice, good teaching, good company, and many good ideas throughout the study.

I would like to thank Chris Crouch, Michael May, Liam Domican, and all other staffs members of the school of Mechanical and Manufacturing Engineering.

Special thanks are also to Yoann Glocheux, Queens University Belfast, for the use of the nitrogen adsorption porosimetry facility.

I wish to thank my elder brother Dr. A.R.M. Harunur Rashid, my entire family, and all my friends, for helping me to get through challenging times, and for all the emotional support, comradeship, entertainment, and caring they generously provided.

I wish to thank my parents, Muhammad Isa and Syeda Raihana Begum. They bore me, raised me, supported me, taught me, and loved me.

Lastly and most importantly, very special thanks and appreciation go to my beloved wife and son, Samira Sharmin Mahbub and Nayl Hasan. Their love, patience, and

constant encouragement have made my PhD journey more meaningful. To embark on this PhD was a serious decision. I was then newly married and we both had jobs and a settle life in Bangladesh. My wife provided generous encouragement and made my decision easier to enable me to pursue my longstanding dream. During my PhD, I encountered some hurdles along with the good times. My son was born the year I started my PhD. There was a gap of almost two years, while I deferred my PhD work and spent time in Bangladesh. But, even though circumstances were going against continuing my PhD work, I did not give up. Without their continuous encouragement, patience, and tolerance, completing my PhD would simply not have been possible. My son spent almost two years without having me at his side. He was strong and always asked me when I would be finished. Nothing compared to the motivation that he gave me, and to the strength that he showed at his young age. To my wife Samira Sharmin Mahbub and my son Nayl Hasan, I dedicate this thesis.

TABLE OF CONTENTS

LIST OF FIGURES

LIST OF TABLES

ABBREVIATIONS

AFM	Atomic Force Microscopy
APS	Amorphous Phase Separation
ASTM	American Society for Testing and Materials
BET	Brunauer-Emmett-Teller
BJH	Barrett-Joyner-Halenda
CPG	Controlled Pore Glass
DSC	Differential Scanning Calorimetry
DTA	Differential Thermal Analysis
EDXS	Energy Dispersive X-ray Spectroscopy
eV	electron Volt
FTIR	Fourier Transform Infrared Spectroscopy
FWHM	Full Width at Half Maximum
HA	Hydroxyapatite
HT	Heat-treatment
ISO	International Organization for Standardization
IUPAC	International Union of Pure and Applied Chemistry
JCPDS	Joint Committee on Powder Diffraction Standards
MCM	Mobil Crystalline Materials
MIP	Mercury Intrusion Porosimetry
NMR	Nuclear Magnetic Resonance
PVG	Porous VYCOR Glass
SBA	Santa Barbara Amorphous
SEM	Scanning Electron Microscopy

SPG	Shirasu Porous Glass
TTT	Time-Temperature-Transformation
UV	Ultraviolet
XRD	X-ray Diffraction

ABSTRACT

This work investigated the development of porous glasses by making additions of zirconia (ZrO_2) and zircon ($ZrSiO_4$) to the sodium borosilicate glass system SiO_2-B_2O_3-Na_2O. Additions of Zr-based compounds were made in an attempt to yield more alkaline durable porous glasses compared to the silica-rich porous glass structures of the parent sodium borosilicate glass system. Glasses were fabricated using a high-temperature fusion process. X-ray diffraction (XRD) was used to confirm that the glasses were amorphous upon pouring from the melt. The glasses were characterised using differential thermal analysis (DTA) to identify important thermal events, including the glass transition temperature (T_g) and crystallisation temperature (T_x). The occurrence of amorphous phase separation was key to the formation of two-phase glasses and ultimately porous glasses. It was found that the quantity of sodium oxide (Na_2O) in the glass composition played an important role in determining whether phase separation occurred via nucleation and growth or spinodal decomposition. Based on the DTA data, a heat treatment temperature of 650 °C was selected for three different durations (14, 24 and 63 hours). The heat-treatment caused the glasses to phase separate into two phases; a silica-rich phase and a sodium borate phase. The sodium borate phase coarsened as a function of heat-treatment time. Fourier transform infrared (FTIR) spectroscopy, together with XRD, was found to be effective as a means of comparing the phase separation and crystallisation characteristics. Glasses heat-treated for longer times showed some evidence of crystal formation. Having formed two-phase glass, acid leaching was used to remove the borate phase and create a porous structure. The leaching process had to be carefully controlled in terms of acid type, acid concentration, leaching time and leaching temperature. For all glasses, a post-leach alkali wash step was needed to remove trapped silica gel. The porous glasses comprised a silica-rich porous skeleton. Scanning electron microscopy (SEM) revealed classic interconnected porous morphologies. The most consistent and best-defined morphologies were observed for the zircon-containing glass. Energy dispersive X-ray (EDX) analysis confirmed the presence of zirconium (Zr) in the porous silica-rich skeleton. Mercury intrusion porosimetry (MIP) was used to characterise the pore characteristics and measure pore volume, pore size, pore distribution, total pore surface area, and bulk and apparent density. In general, the porous glasses exhibited sharp, unimodal pore distributions, but there was also evidence of micropores, believed due to residual silica gel. Mean pore size ranged from 40 nm to 200 nm for the different porous glasses studied. It was observed that mean pore size linearly increased with square root of the heat-treatment time. Total pore surface area increased with decreasing size of pores and ranged from 5 to 35 m^2/g depending on glass composition and heat-treatment time. Alkaline resistance tests were carried out. Zircon- and zirconia-containing porous glasses are 3-4 times more alkali durable than the parent sodium borosilicate glass.

CHAPTER ONE

GENERAL INTRODUCTION

1.1 MOTIVATION AND BACKGROUND

Controlled pore glass (CPG) has long been associated with the sodium borosilicate glass system that was originally patented in 1938 by Hood and Nordberg of Corning Glass Works [1]. The key to CPG is its interconnected porosity; this makes it suitable for performing size exclusion and affinity chromatographic separations of proteins, lectins, antibodies, enzymes, and more. CPG has a rigid glass structure, and is durable, incompressible and is an inert medium with narrow pore size distribution for efficient purification, and a large internal surface area providing a high binding capacity [2, 3].

The sodium borosilicate glass system is widely known to undergo Amorphous Phase Separation (APS) by the spinodal decomposition mechanism [4]. Porous glass is derived from glass that is heat-treated (HT) to form two interconnecting phases: a silica-rich phase, and an alkali-rich borate phase. The heat-treated glass is then leached selectively to remove one of the phases. The heat-treatment step and leaching conditions can be adjusted to achieve the desired pore size, pore volume, and surface area. Therefore, porous glass based on the sodium borosilicate system can be tailor-made to required specifications with specific pore sizes over a wide range, thus offering flexibility in terms of end applications, e.g. enzyme immobilisation and side exclusion chromatography.

Sanitising by means of sodium hydroxide (NaOH) is almost always necessary for chromatographic media used in industrial applications in the biopharmaceutical industry [5]. Up to 1 N NaOH is desirable for cleaning and sanitisation of chromatography columns. Unfortunately, silica is attacked by alkali. This results in pore enlargement, leading to inaccurate separations and eventually to degradation of

the silica support. For this reason, an alkali-resistant material containing interconnected porosity that can survive NaOH sanitisation is highly desirable. This challenge has been the focus of many research studies and patented work over the course of the past two decades and will continue to be in the future.

Supports for size exclusion and affinity protein chromatography can be made using porous glass. This glass has an interconnected pore structure with a uniform pore distribution. Figure 1.1 shows a typical example of silica-rich interconnected pore structure after phase separation and leaching.

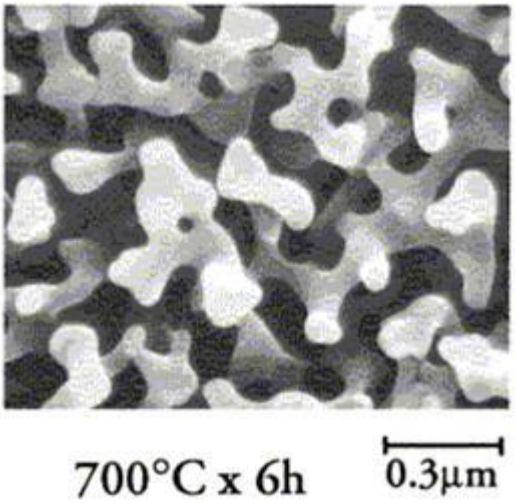

Figure 1.1: Example of a silica-rich interconnected pore structure following phase separation (heat-treated at 700 °C for 6 h) and leaching, from Nakashima [6].

Specification of what is needed:

Supports for size exclusion and affinity protein chromatography can be made using porous glass. Media for protein chromatography have a typical pore size of 30 nm, but can extend to much higher pore sizes than this [5]. What is needed is a porous material with interconnected porosity. The material is required to have a narrow pore size distribution coupled with a large internal surface area. The material must be capable of being sanitised with NaOH.

Advantages of the current CPG porous silica system:

- The APS phenomenon in the sodium borosilicate system is kinetically driven, which means that pore sizes can be controlled by using the appropriate heat-

treatment (See Figure 1.2). Without the APS phenomenon this is difficult to achieve.

- The APS in this system is via a spinodal decomposition mechanism, resulting in the required interconnected structure, high pore volume, and high surface area.
- The glass is made using traditional high-temperature glass processing. This allows large quantities of glass to be made.
- The resulting structure is a silica glass, which is relatively well understood in terms of affinity chromatography surface chemistry.

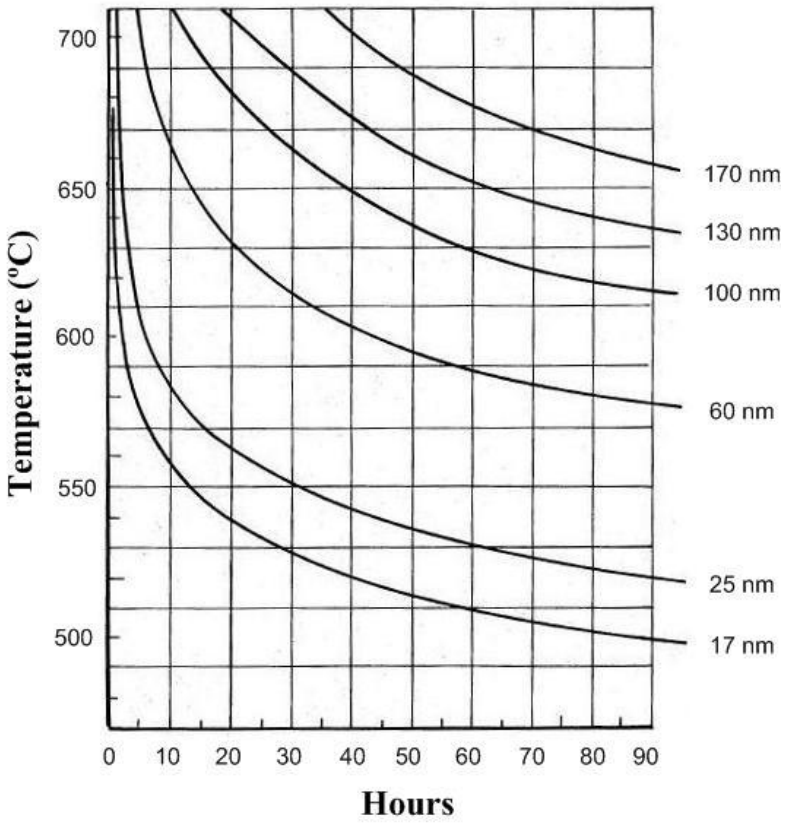

Figure 1.2: Graph showing the relationship of the heat-treatment operation versus the resultant pore diameter, from Haller [7].

Disadvantage:

The main disadvantage is the alkali solubility of silica in NaOH solution.

Some approaches used by researchers to solve the problem:

- Addition of ZrO_2, in an attempt to create an alkali-resistant SiO_2-ZrO_2 CPG, using traditional glass-making methods [6, 8-10].
- Coating porous silica with a ZrO_2-containing precursor (chemical method) [11, 12].
- Making of SiO_2-ZrO_2 porous glass using sol-gel [13].
- Making of SiO_2-TiO_2 or SiO_2-Al_2O_3 porous glass using traditional glass-making methods [14, 15].
- Use of ZrO_2-rich porous structures [16].

Research direction:

The approach of Eguchi et al. [8] uses traditional glass processing. It results in porous glass containing 15.1 wt% zirconia. 6-8 mol% of CaO is used to control ZrO_2 and retain it as part of the SiO_2 phase. But ZrO_2 is still being lost (approx 30 wt%). If an alternative way of retaining the ZrO_2 in the SiO_2 skeleton could be found then this 30 wt% would not be needlessly lost. If this could be achieved, then it is also possible that the 6-8 mol% CaO is unnecessary and could be replaced (or partially replaced) by ZrO_2. If the APS process is being hindered then glasses could be subjected to longer heat-treatment times to develop the interconnected structures, if this is necessary. A small quantity of TiO_2 may also need to be used as a flux, as per Kawamoto, to promote APS [17].

Therefore it was felt that the best approach is to devise methods whereby ZrO_2 with SiO_2 is structurally linked during firing of the glass. In doing so, it is anticipated that little or no ZrO_2 will be lost. Zircon ($ZrSiO_4$) could be a possible candidate to replace ZrO_2 as it is more likely to remain with silica. Clearly, compositions will have to be carefully 'tweaked.' Dramatic compositional changes may result in melts that will not pour, or will crystallise on pouring. It is believed that increasing Na_2O helps to keep ZrO_2 in the silica rich phase during heat treatment [18].

1.2 RESEARCH OBJECTIVES

The main objectives of the thesis are to investigate thermal behaviour of zirconia/zircon added sodium borosilicate glass, and to develop alkali resistant porous glass based on the sodium borosilicate glass system. To meet the main objectives, the thesis addresses four separate goals:

I. To investigate the effect of introducing ZrO_2/$ZrSiO_4$ into the sodium borosilicate glass system and to characterise their thermal properties in order to optimise heat-treatment conditions.

II. To optimise leaching conditions that will lead to a porous glass with interconnected structure.

III. To produce porous glass with interconnected structures containing at least ≥ 15 wt% Zr, but preferably ≥ 20 wt% Zr.

IV. To obtain improved alkali-resistance.

1.3 THESIS OUTLINE

Chapter One: General Introduction

Chapter one presents a brief introduction and background on the development of porous glass. The development of porous glass, and the major challenges it faces in applications, are discussed. The motivation and research objectives are then outlined.

Chapter Two: Literature Review

The second chapter of this thesis reviews the traditional sodium borosilicate system, including the phenomenon of amorphous phase separation that lies at the heart of this system. Efforts to improve this system in terms of alkali resistance and processing are then reviewed. The different approaches to improve the alkali resistance of the glass are also presented. Most popular pore characterisation techniques are discussed at the end of this section.

Chapter Three: Experimental Procedure

Chapter Three details the experimental procedures that were followed in this work.

Chapter Four: Results and Discussion

This chapter begins with the results obtained from laser diffraction based particle size analysis, and investigates the thermal behaviour of the glasses subjected to a traditional high temperature fusion process. Porous glasses resulting from optimised heat-treatments and appropriate leaching are characterised and the results are comprehensively discussed. The effect of ZrO_2/$ZrSiO_4$ additions on alkali resistance is further examined and discussed.

Chapter Five: Conclusions and future work

Conclusions are drawn from the research findings. Finally, suggestions are made for further research, as these could not be carried out due to limited availability of time.

Others: Appendices

Publication generated from this thesis is presented in Appendix 2. Parts of this thesis is already published in Thermochimica Acta. A second article is submitted for publication in the Ceramics International. A third article is accepted for publication in a peer reviewed conference proceedings of 37th International Conference and Expo on Advanced Ceramics and Composites (ICACC'13). Another article is already published in the proceedings of 15^{th} European Conference on Composite Materials (ECCM15).

CHAPTER TWO

LITERATURE REVIEW

2.1 DEFINITION OF GLASS

In everyday language the term glass designates a transparent substance, possessing the properties of hardness, rigidity, and brittleness. Glass also possesses a number of properties which are characteristic of the liquid state, and classification of glass as a liquid of very high viscosity rather than a solid would be in accordance with modern views [19]. Unlike crystals, glass does not have a sharp melting point, but like crystalline solids, glass show elasticity [20].

Due to the complexity of the structure of glass, it is not altogether surprising that an exact, all-encompassing definition for glass remains elusive, and instead a number of definitions have been suggested over the years. A more generally accepted definition is that offered by ASTM [21] which states "a glass is an inorganic product of fusion which has cooled to a rigid condition without crystallisation." However, the ASTM definition limits the definition of glass to inorganic constituents, which fails to explain organic and molecular glasses that now represent a rapidly growing area of study [22, 23]. X-ray and electronic diffraction studies showed that glass lacks long-range periodic atomic arrangement, and every type of glass exhibits time-dependent glass transformation behaviour [20, 24]. Pointing this out, Varshneya and Mauro [22] suggest a scientific definition of glass as "a solid having a non-crystalline structure, which continuously converts to a liquid upon heating." Zarzycki [25] avoids the debate about organic and inorganic trail, and suggests a more simplified definition: "a glass is a non-crystalline solid exhibiting the phenomenon of glass transition". Thereby this definition also conveniently separates non-crystalline materials into the categories of glass and amorphous materials.

2.2 THE GLASS TRANSITION

Glass is usually formed on solidification from the melting stage. The cooling is so rapid that crystallisation does not have the time to occur. With a further decrease in temperature, viscosity continues to increase, resulting in a progressive freezing of the liquid to its final solidification. The structure of glass can be easily distinguished from that of a liquid, as the glass structure becomes independent of temperature. The relationship between crystal, liquid, and glass can be explained by means of specific volume as a function of temperature (see Figure 2.1).

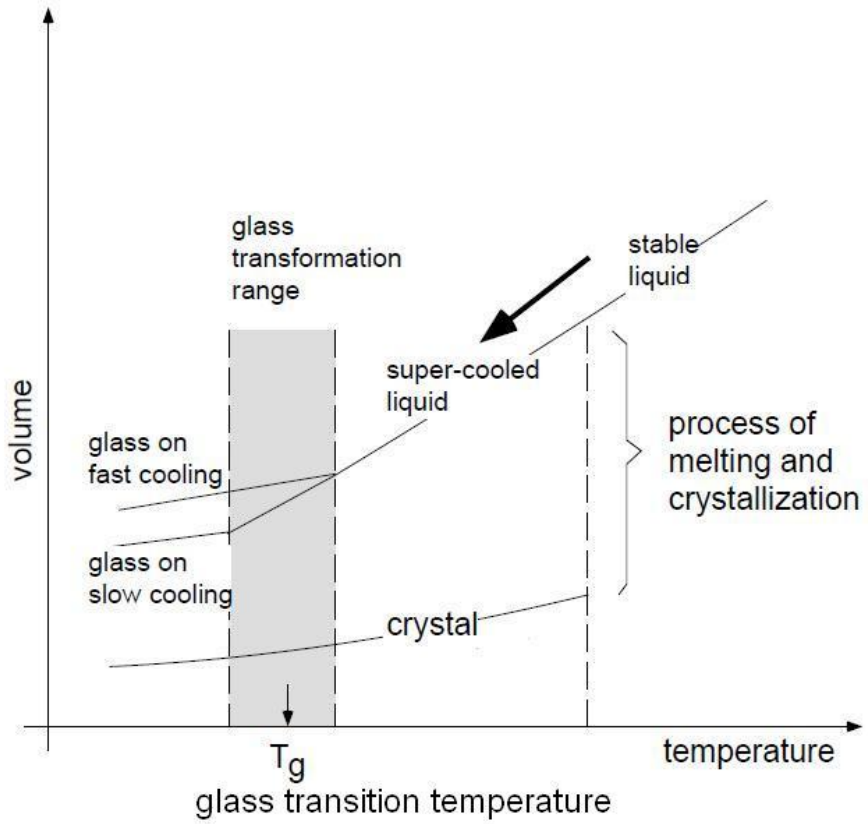

Figure 2.1: Schematic specific volume-temperature relationships for liquid, glass, and crystals [26].

On cooling from an elevated temperature, at the point of solidification (or freezing), two phenomena may occur. There is either a discontinuous change in volume at the melting point if the liquid crystallises, or crystallisation is avoided and liquid passes to a supercooled state. The volume of the liquid decreases steadily in this supercooled state until there is a decrease in the expansion coefficient at a range in temperature called the glass transformation range. Below this temperature range the

glass structure does not relax and the expansion coefficient is usually same as that for the crystalline solid. The intersection between the curve of the glassy state and that for the supercooled liquid is known as the glass transition temperature, T_g [27]. This T_g varies with cooling rate (see Figure 2.1) and thus it is more accurate to call it a transformation range rather than a fixed point [28]. The glass transition temperature increases with increasing cooling rate. The specific volume of the formed glass follows this same trend, increasing with increased cooling rate. With a slower cooling rate the time available for the structure to relax increased and the supercooled liquid persists to a lower temperature resulting a higher-density glass.

2.3 STRUCTURE OF GLASS

A number of models have been suggested to describe the structure of glass that include a crystallite model, a random network model, as well as other structural models. Here only a random network model will be discussed as it is widely accepted model. Readers are referred to the following literature for further details of other models [23, 25, 27, 29].

2.3.1 Random network model

Glass is viewed in the random network model as a three-dimensional network, lacking symmetry and periodicity, in which no unit of the structure is repeated at regular interval. For oxide glass, these networks are composed of oxygen polyhedra. Assuming that a glass should have an energy content similar to that of the corresponding crystal, Zachariasen [30] in 1932 suggested four rules for the formation of an oxide glass:

1. An oxygen atom should be linked to not more than two glass forming atoms.
2. The coordination number of glass-forming atoms is small, 4 or less.
3. Oxygen polyhedra share corners, not edges or faces.
4. For 3-D networks, at least three corners of each polydehron should be shared.

The bonding force responsible for the formation of the network structure in crystalline silica (SiO_2) forms similar networks in glass (see Figure 2.2 a) and is considered as network formers. Alkali silicates form glass easily and when alkali oxides such as Na_2O are added to silica glass, the sodium ions become part of the structure and occupy random positions distributed throughout the structure to provide charge neutrality (see Figure 2.2 b).

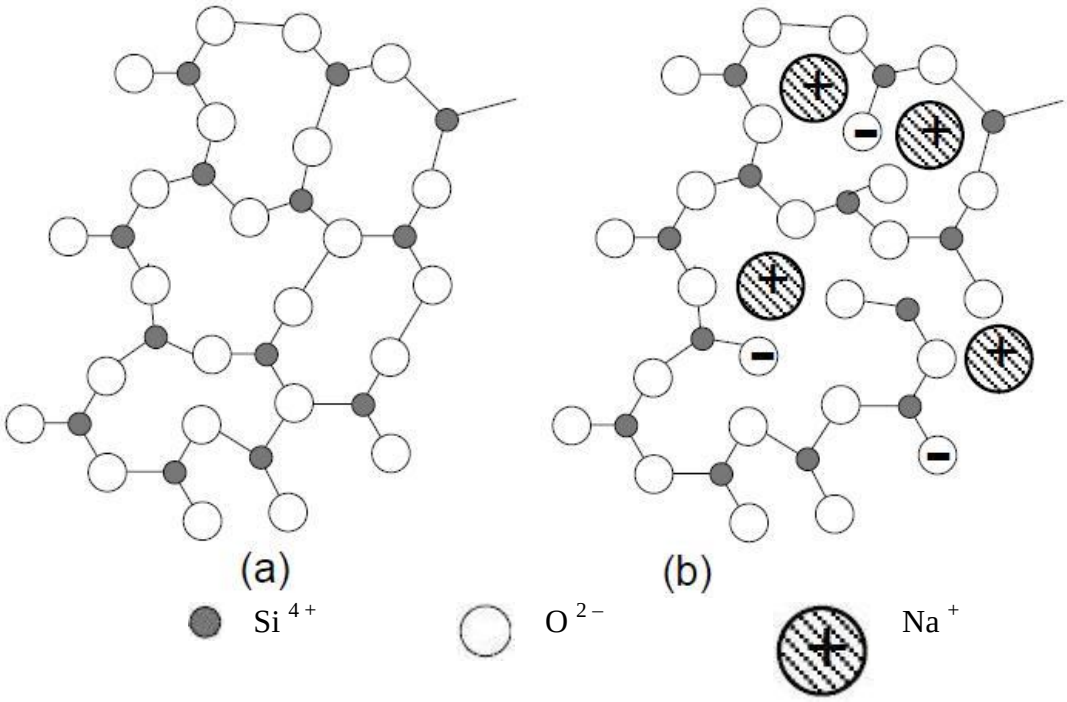

Figure 2.2: Schematic glass networks: (a) SiO_2 network; (b) SiO_2 network modified through addition of Na_2O [26].

Since the major function of these alkali oxides (e.g.: Na_2O, K_2O, Li_2O, CaO, MgO, and PbO) is believed to provide additional oxygen ions that modify the network structure, they are known as network modifiers. With an increase in the amount of modifiers, the ratio of oxygen to silicon also increases and breaks up the three-dimensional network with the formation of singly bonded oxygen that do not participate in the network, thus reducing the length of the chain. The principal effect of these modifiers is a reduction in melting temperature and working temperature by decreasing the viscosity. An excess of modifiers can make melting sufficiently simple and mobile that crystallisation occurs in preference during the formation of glass. Cations of higher valency and lower coordination number than the alkalis and

alkali earth metals may act as both network formers and modifiers and are referred to as intermediates; e.g. ZrO_2, TiO_2, Al_2O_3, ZnO.

2.4 AMORPHOUS PHASE SEPARATION

The phenomenon of amorphous phase separation (APS) in glasses has, for decades now, been an important topic in glass research [31]. It has been the subject of many investigations and there is an entire area of glass science devoted to this phenomenon in different glass-forming systems.

A homogeneous single phase separates into two or more phases of different compositions, if the free energy of the system with two or more distinct phases is lower than that of the system with one single homogeneous phase [20]. Phase separation that occurs above the liquidus is known as stable immiscibility, whereas phase separation at temperatures below the liquidus is known as metastable immiscibility. There are two routes to the formation of discrete phases by metastable phase separation; these are either by spinodal decomposition or by nucleation and growth process. The route taken is a function of the free energy of the mixing of the system.

2.4.1 Spinodal decomposition

Figure 2.3 illustrates the curve for free energy versus composition for a hypothetical mixture of two components X and Y at temperature T. The corresponding immiscibility dome shows the binodal region (Region I within which nucleation and growth will occur) and the spinodal region (Region II within which APS proceeds by spinodal decomposition). The line connecting phases *a* and *b* is known as a tie-line. The tie-line will connect the compositions of the phases in equilibrium at a specified temperature. A different tie-line exists for each temperature, with different compositions for the two phases.

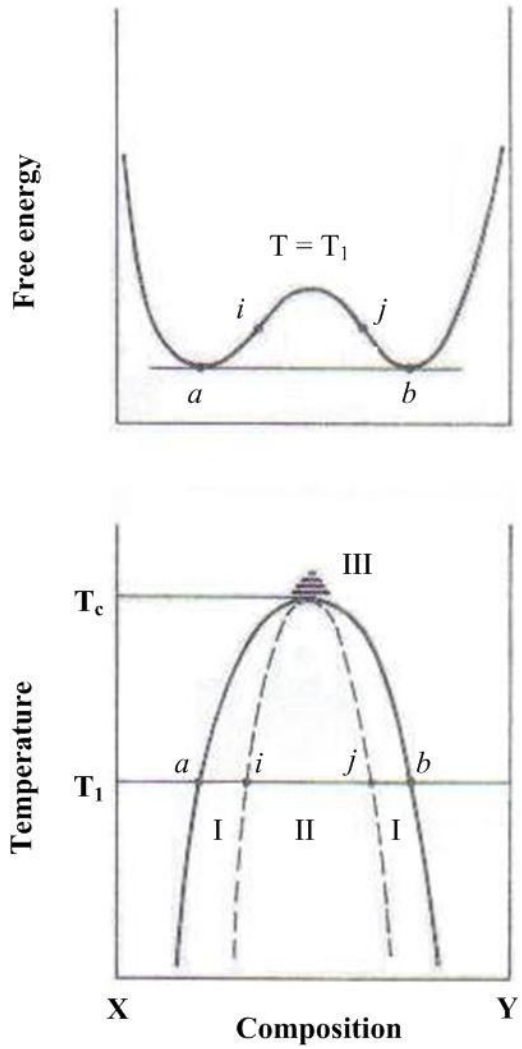

Figure 2.3: Free energy versus composition curve for a hypothetical mixture of two components X and Y at temperature T, and the corresponding immiscibility dome illustrating the binodal (Region I) and spinodal (Region II) [25].

Because phase separation into the binodal and spinodal regions are achieved by means of different processes, the morphology of the separated phases in each region are distinctly different. Phase separation in the spinodal region refers to a continuous type of phase transformation in which the change begins as small fluctuations in composition, and the compositional differences grow with time resulting in two continuous interpenetrating phases. Since these changes occur spontaneously and as apparently no energy barrier is present to hinder the separation, the region is considered unstable. The system will lower its free energy by continuously changing the composition of two phases until the equilibrium is reached. At this equilibrium, the free energy is in the lowest state and compositions remain constant. Afterwards the phase-separated regions will grow in size through diffusion. The boundary

between phases is initially diffuse but sharpens with time. The phases formed in the spinodal region show a high degree of connectivity [32].

2.4.2 Nucleation and growth

In the binodal region, large change in composition must occur to lower the free energy of the system, and thus formation of nuclei. This region is referred as the metastable region, as the system is unstable at small fluctuation in composition but becomes stable at larger changes in composition. Once nucleated, the new phase will grow in size through diffusion. During the growth stage, the composition of the nucleated phase is unchanged with time, for a constant temperature. The phase separation resulting from nucleation and growth is characterised by spherical droplets, with low connectivity, of random size and distribution with a sharp boundary existing between the two phases. Figure 2.4 shows etched surfaces of sodium borate glass where the structures are formed by (a) nucleation and growth and (b) spinodal decomposition.

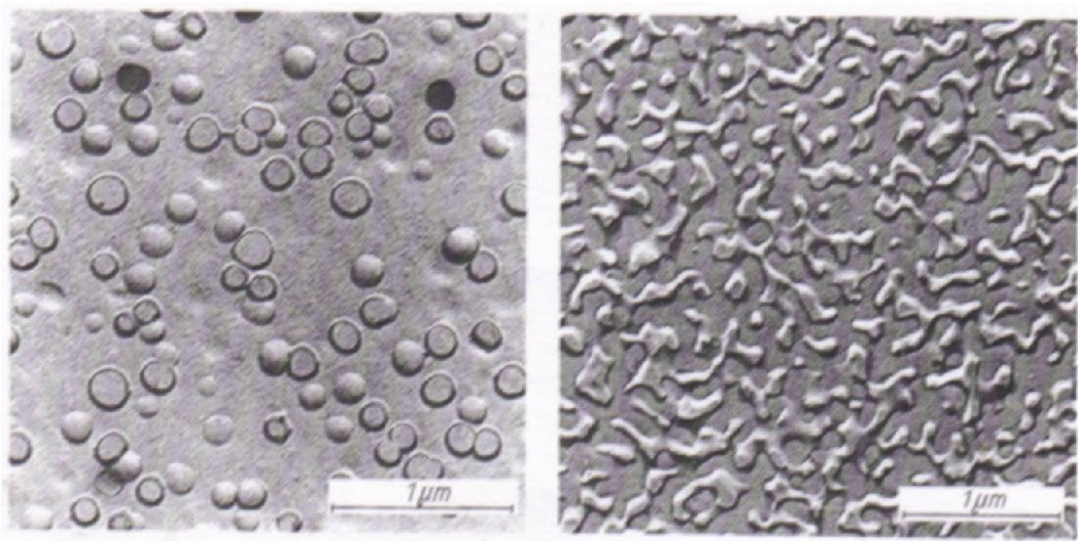

(a) (b)

Figure 2.4: Sodium borate glass showing (a) a droplet microstructure and (b) a connective structure [31].

It is untrue to say that spinodal decomposition is mandatory for forming interconnected microstructures. Droplet microstructures formed by nucleation and growth can merge and ultimately form a connected structure. Haller [33] proposed the intersecting growth theory, suggesting that spheres nucleate and grow but then

agglomerate to form a connected structure as a result of their high volume fraction. While many theories abound, what is known is that an interconnected structure is required for a successful controlled pore glass.

2.5 COMMON GLASS SYSTEMS

The primary glass formers in commercial oxide glasses are silica (SiO_2), boron oxide (B_2O_3), and phosphorus pentoxide (P_2O_5), all of which readily form single component glasses [24]. Of these, other than silica (SiO_2), only boron oxide has some commercial importance and only when mixed with silica. Silica (SiO_2) is the most important glass former and representing more than 95% of industrial glass production [25]. Silica based glass is technically important for its excellent chemical resistance (except HF and alkali) and small expansion coefficient which make it a very good candidate for thermal shock resistance [25]. Glass can be classified in different groups according to their intended usage or by their chemical composition. The following sections describe the most common types of glass according to their chemical composition and how silica (SiO_2) acts as a glass former.

2.5.1 Soda-lime glass or commercial glass

Soda-lime glass is the most common commercial glass and is less expensive. A typical composition of this glass is 70 – 75 wt% SiO_2, 12 – 16 wt% of Na_2O, and 10 – 15 wt% CaO [34]. A small percentage of other materials can be added for specific properties and application requirements. The principal addition in this type of glass, other than silica (SiO_2), is sodium oxide or soda (Na_2O). Even though sodium oxide contains oxygen atoms, it is held together by ionic rather than covalent bonds. The sodium atoms in the mixture donate electrons to the oxygen atom, producing a mixture of negatively charged oxygen ions and positively charged sodium ions. The oxygen atom with an extra electron binds to one silicon atom and does not form a bridge between pairs of silicon atoms (see Figure 2.5). Therefore, the melting temperature of the mixture is considerably reduced [35]. Since sodium ions are so soluble in aqueous solution, calcium oxide (CaO) is added to the mixture to make it more durable in aqueous solution.

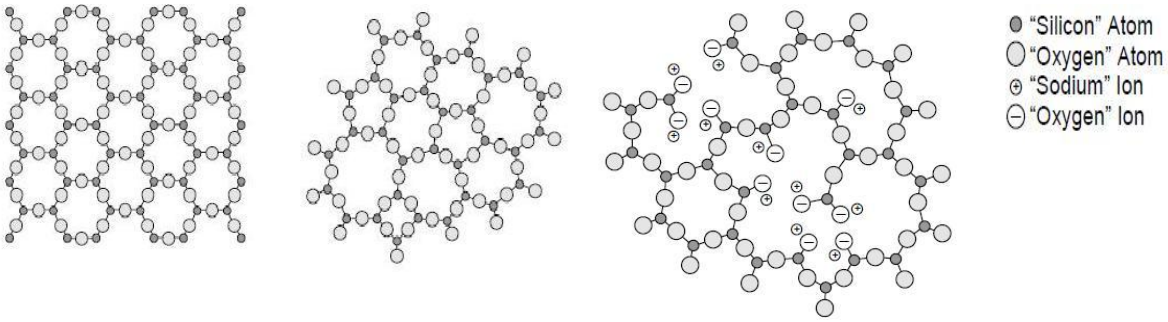

(a) (b) (c)

Figure 2.5: Illustration of two-dimensional structures of (a) crystalline silica, (b) glassy silica, and (c) glassy or vitreous silica containing sodium oxide [35].

Soda-lime glass is produced on a large scale and used for bottles, drinking glasses, and windows. Its light transmission properties, as well as low melting temperature, make it suitable for use as window glass. Its smooth and non-reactive surface makes it excellent as containers for food and drinks. Nowadays recycled glass, also known as cullet, is used to make green glass that contains 85 – 90 wt% of cullets and helps to save energy and reduce emissions.

2.5.2 Lead glass

Lead glass is similar to soda-lime glass where lime is replaced by a larger part of lead oxide (PbO). Lead glass typically contains 55 – 65 wt% SiO_2, 18 – 38 wt% of PbO, and 13 – 15 wt% Na_2O or K_2O [34]. Lead glass is usually used for decorative glassware [34]. It is also included in special optical glasses to increase their refractive index. The networks in lead glass are more complete than those in soda-lime glass and thus they are stronger and has less internal friction [35]. Lead oxide also makes the glass dense, hard, and X-ray absorbing, and therefore suitable for use in radiation shielding.

2.5.3 Aluminosilicate glass

Aluminosilicate glasses is usually prepared from a ternary system with a typical composition 52 – 58 wt% SiO_2, 15 – 25 wt% of Al_2O_3, and 4 – 18 wt% CaO [34]. With low thermal expansion and high softening temperature, this glass can tolerate high temperature better than soda-lime glass and is used in thermometers, combustion tubes, cookware, halogen lamps, furnaces, and fiberglass insulation.

2.5.4 Borosilicate glass

Borosilicate glass contains substantial amounts of silica (SiO_2) and boron oxide (B_2O_3> 8%) as glass network formers, and are typically composed of 70 – 80 wt% SiO_2, 7 – 13 wt% of B_2O_3, 4 – 8 wt% Na_2O or K_2O, and 2 – 8 wt% of Al_2O_3 [34]. This composition, which contains 7 – 13 wt% of B_2O_3, is known as low-borate borosilicate glass, and is mainly used to produce chemical apparatus, lamp, and tube envelops. Glasses containing 15 –25% B_2O_3, 65 –70% SiO_2, and smaller amounts of alkalis and Al_2O_3 as additional components is known as high-borate borosilicate glass. High-borate borosilicate glass is also known as leachable alkali-borosilicate glass with an optimum composition of 62.7 wt% SiO_2, 26.9 wt% of B_2O_3, 6.6 wt% Na_2O, and 3.5 wt% of Al_2O_3 [36]. This high-borate borosilicate glass is further processed to produce Controlled Pore Glass (CPG) which is widely used as a stationary media in chromatography and a clear impervious glass know as Vycor brand 96% silica glass. The increase of B_2O_3 content reduces the chemical resistance, and in this respect high-borate borosilicate glass differ widely from low-borate borosilicate glass. Since the porous glasses in this study are synthesised using the SiO_2– B_2O_3– Na_2O system, further details on this glass composition are discussed in the following sections.

2.6 POROUS GLASSES

A porous material is defined by IUPAC [37] as *"Any solid material which contains cavities, channels or interstices may be regarded as porous, though in a particular context a more restrictive definition may be appropriate."* The physical properties of a solid material, such as density, thermal conductivity, and strength depend largely on pore structure. Therefore controlling the porosity is of great importance in manipulating the properties of a solid material. It has drawn great interest in recent years, both in industry and research, due to the influence of pores on controlling chemical reactivity of solids and its physical interaction with gasses and liquids.

2.6.1 Pore size classification

Pores can be classified according to their availability to an external fluid. A few authors have also classified pores based on their accessibility to their surroundings in general [38].Using this approach, pores can be categorised in two types – one that is not accessible and totally isolated from its surroundings and termed as *closed pores*, and pores that have a continuous channel and are accessible from the surface into the body that are termed as *open pores*. It is important to mention that *closed pores*, while not associated with adsorption or permeability, do influences macroscopic properties such as bulk density, mechanical strength, and thermal conductivity. *Closed pores* are shown in Figure 2.6 as region (a) and *open pores* in regions (b), (c), (d), (e) and (f). Some *open pores* are described as *blind* pores which are open only at one end, like (b) and (f), whereas others may be opened at two ends (through) pores, like (e). Pores are also classified depending on their varied geometrical shape. The common shaped pores are: (i) C*ylindrical* which can be either open (c) or blind (f), (ii) *Ink-bottle* shaped (b), *funnel* shaped (d), and *slit shaped*. *Roughness*, represented by area (g), of the external surface looks similar to porosity but differs from porosity unless they are deeper compared to their width.

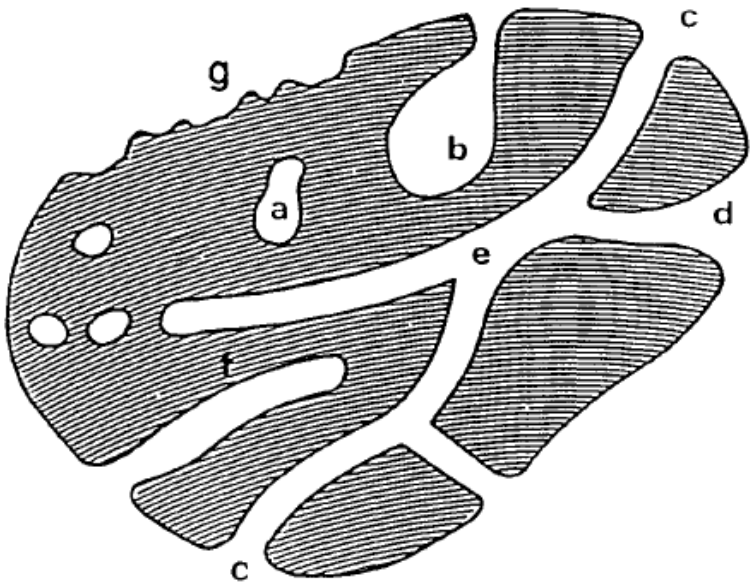

Figure 2.6: Schematic cross-section of porous solid [37].

Details on pore classification and characterisation of pores are described in a classic paper by Zdravkov et al. [38]. Despite the differences in pore size classifications, most recent papers adopted the International Union of Pure and Applied Chemistry (IUPAC) classification regarding the pore size, which is summarised in the Table 2.1.

Table 2.1: Classification of pore according to their pore-width[1] [37].

Pore type	Pore-width (nm)
Microporous	< 2
Mesoporous	2 – 50
Macroporous	> 50

2.6.2 Porous glasses in general

Porous glass has evoked new interest in recent years because of its importance in chemical, pharmaceutical, and biological science. Two special features of porous glass are its wide ranging geometric form, e.g.: beads, rods, fibers, hollow fibers, and membranes, and its broad pore size range which can vary from 0.3 to 1000 nm with a comparatively high surface area. Silica and polymers are used widely to prepare porous media. Porous glass prepared with silica exhibits high tolerance to chemicals and solvents, and combined with their mechanical and thermal stability, makes it superior to other organic/inorganic or inorganic/inorganic composites [39]. An increasing number of studies have been carried out in last decades using the alkali borosilicate glass system [40-50]. Porous glass can be produced by leaching phase-separated alkali borosilicate glass which results from proper sintering. Porous glass can also be prepared by the sol-gel process, but the present review primarily covers porous glass based on phase separation followed by leaching of the alkali borosilicate glass system which results in pore sizes ranging from meso to macro sizes.

[1] Diameter of a cylindrical shaped pore is referred here as *pore-width*.

2.6.2.1 Porous glass based on alkali borosilicate

Porous glass based on the alkali borosilicate system (R_2O–B_2O_3–SiO_2, where R = Na, K, or Li) was originally patented in 1938 by Hood and Nordberg of Corning Glass Works [1] which was later commercially available as Porous VYCOR Glass (PVG) and Controlled Pore Glass (CPG). The key to this type of porous glass is its interconnected porosity; this makes it suitable for performing size exclusion and affinity chromatographic separations of proteins, lectins, antibodies, enzymes, and more. In addition, this glass has a rigid glass structure and is durable, incompressible and is an inert medium. It also has a narrow pore size distribution for efficient purification, and a large internal surface area for high binding capacity [2, 3]. Porous glass based on the sodium-borosilicate system can be tailor-made with specific pore sizes over a wide range, thus offering flexibility in terms of end applications. The sodium-borosilicate glass system is discussed in further detail in Section 2.7.

2.6.2.2 Other porous materials synthesised by the sol-gel and other process

Of the other porous materials, the microporous zeolites, which are members of the aluminosilicate family, are most noteworthy. Many studies have been carried out in order to increase the pore size of zeolite materials from the micro to the meso pore range. Large pore sieves (> 1 nm), such as VPI-5 (1.2 – 1.3 nm) that were constructed using zeolite material, have been reported [51, 52]. In 1992, researchers at Mobil synthesised a new class of mesoporous silica nanoparticles which they named as Mobil Crystalline Materials (MCM), and which is popularly known as MCM-41 [53]. The pore size of this MCM-41 ranges from 1.5 to greater than 10 nm with a large surface area greater than 700 m^2/g. Six years later, similar nanoparticles with larger pores (4.6 – 30 nm) and surface area between 630 to 1040 m^2/g was fabricated by Zhao and co-workers at University of California, Santa Barbara, and the material was named as Santa Barbara Amorphous type material, or SBA-15. [54]. Both of these materials exhibit a hexagonal array of pores where large mesopores are accompanied by significantly smaller sized pores (< 3.4 nm) with broad pore distribution [53, 55]. A hybrid material based on silica was also formed using porous silica incorporated into aluminium oxide membrane, and which is mostly used as a membrane [56]. A successful synthesis of mesoporous

hydroxyapatite (HA) was reported by Yao et al. where nano-channels are formed within the rod-like structure with pore size mostly around 3 nm [57]. A special ceramic-based hydroxyapatite was also produced by Bio-Rad Laboratories, Inc. in which the pores are narrowly distributed with a size ranges from 60 to 100 nm [58].

2.7 PREPARATION OF POROUS GLASS USING THE SODIUM BOROSILICATE GLASS SYSTEM

Phase separation using the sodium borosilicate system (Na_2O-B_2O_3-SiO_2) has long been studied and considered as an important technical glass composition [29]. The sodium borosilicate system is also a source material for porous glass and is used for its superior usability in membrane technology, size exclusion, and affinity protein chromatography (separation science) [2, 24, 59]. Increasing chemical durability is one of the major challenges for borosilicate glass, in order to make it suitable and re-usable for many other applications [60]. Sodium borosilicate glass system is well known for its phase separation characteristics at higher temperature, which paved the way for preparing Controlled Pore Glass (CPG) of pore size ranges between meso and macro level depending primarily on the heating cycle [40]. The fabrication of sodium borosilicate glass is examined, with special attention being paid to the heat-treatment and leaching processes. The mechanism of phase separation in the Na_2O-B_2O_3-SiO_2 glass system is briefly discussed. Finally, a number of relevant patents in the field are reviewed.

2.7.1 Early development

In 1938, Hood and Nordberg's pioneering work discovered that glass compositions within a certain region of the ternary system R_2O-B_2O_3-SiO_2, could be heat-treated and leached in a controlled manner to yield a porous silica-rich structure [1]. Thirty five years later, Wolfgang Haller invented controlled pore glass from the same system, having a controllable pore size of narrow size distribution as described earlier [7]. Around the same time in work patented by Hammel and Allersma, phase separable borosilicate glass compositions produced microporous glass beads with high crush strength and high thermal stability [41, 61, 62]. Applications requiring dimensional stability at elevated temperatures and high crush strength include motor

vehicle catalytic mufflers. The glass beads can be heat-treated such that they undergo less than 25% volume shrinkage and lose less than 30% of its surface area, leading to beads with typical crush strengths of at least 138 kPa. In the meantime, chemical durability, especially resistance to alkali solution, of the porous glass became an urgent issue as it restricts its usage in a number of possible applications. In 1977, Paul [63] reviewed various hypotheses regarding the corrosion of glass surface by aqueous solutions. The introduction of another oxide into the existing glass system was proposed, such as CaO, ZnO, PbO, Al_2O_3, and ZrO_2, to increase the chemical durability. Use of ZrO_2 in the existing sodium borosilicate ternary system was examined in a number of studies, as even a small amount of ZrO_2 (about 2 wt%) significantly increases the acid and alkali durability of a glass. Later in 1988, Eguchi et al. [8] patented their findings on chemically durable porous glass with ZrO_2 content of 2 or more wt% in a sodium borosilicate system containing 40-75 wt% of SiO_2, 15-40 wt% of B_2O_3, 5-30 wt% of alkali metal oxide and alkali earth metal oxide. Attempts were made before this patent, where added ZrO_2 transferred into the soluble phase during phase separation, but was subsequently removed in the leaching treatment. However, presence of an alkali earth metal oxide was found to play a key role in retaining ZrO_2 in the final skeleton of the porous glass. After almost ten years, a more comprehensive insight towards the role of CaO on retaining ZrO_2 on porous skeleton was reported by Nakashima et al. [6]. During this time some studies were carried out to increase the alkali durability by adding ZrO_2 by the sol-gel process [13, 64]. Yazawa et al. [9] using the RO-B_2O_3-SiO_2 (R =Mg, Ca, Sr, Ba, and Zn) system containing Al_2O_3, Na_2O, and ZrO_2 noticed an increased alkali resistance if the porous skeleton contained 2-3 wt% of ZrO_2. However, the effect of RO on the ZrO_2 content in porous glass was not fully clarified but were mentioned as controlling components.

In the last decade most of the studies on the sodium borosilicate glass system emphasise understanding the role of ZrO_2 and other elements (Ti, Hf, Bi, Nd) on thermal and phase separation behaviour of the sodium borosilicate glass system. The effect of the addition of 1 mol% Nd_2O_3 on phase separation with both compositions (6.5 mol% of Na_2O-35.5 mol% of B_2O_3-58 mol% Si_2O) was investigated by Bartl et al. [65]. They found that doping levels larger than 0.1 mol% triggered submicroscopic phase separation during quenching. Du et al. [10] used a typical

composition of sodium borosilicate glass (9.4 mol% of Na_2O-25.4 mol% of B_2O_3-65.2 mol% Si_2O) and observed that ZrO_2 inhibited both initiation (at early stage) and the coarsening process (in later stage) of spinodal phase separation. Pore volume was found to be influenced by the amount of ZrO_2, with a slight decrease initially, but more dramatically when the addition of ZrO_2 content is more than 7 mol%. Pore size also decreased by increasing the amount of ZrO_2. In 2010, a number of investigations have been made on the sodium borosilicate glass system. Saiki et al. [66] studied the role of sulphur in phase separation of borosilicate glass. Spinodal decomposition was observed after heat-treatment of the borosilicate glass system containing 10 mol% of Na_2S-30 mol% of B_2O_3-60 mol% Si_2O. The sulphur was completely removed after acid treatment. The result of this phase separation can be utilised in the recycling process of sulphur containing glass, such as waste glass, radioactive waste, and furnace slug, from which high silica glass can be recovered. Kukizaki [48] made a detailed investigation on the influence of ZrO_2 addition on crystallisation and phase separation in Na_2O-CaO-Al_2O_3-B_2O_3-SiO_2 glass. They found that the addition of ZrO_2 suppressed the devitrification and reduced the growth rate of phase-separation due to an increase in viscosity or a decrease in ion mobility. The alkali resistance also increased by 3.5 times compared to that of ZrO_2-free porous glass. Thermal characteristics of sodium borosilicate glass has been investigated by various groups and are discussed below in the following sections [45, 49, 50, 67-70].

2.7.2 The ternary Na_2O–B_2O_3–SiO_2 system

The sodium borosilicate glass system has been well investigated and the existence of the immiscibility region for forming porous glass is shown in Figure 2.7. The region, known as Vycor™, is one of the most commercially successful industrial exploitation of amorphous phase separation. This region was first identified by Hood and Nordberg [1]. The composition in this Vycor™ region can be separated into phases when suitably heat treated. Pyrex glass (see Figure 2.7) is another commercially successful glass system which benefits from the phase separation of this system. Pyrex glass has a higher SiO_2 content than Vycor™ glass. At the high Na_2O corner, crystallisation interferes with glass formation, otherwise glasses could be made in all conditions.

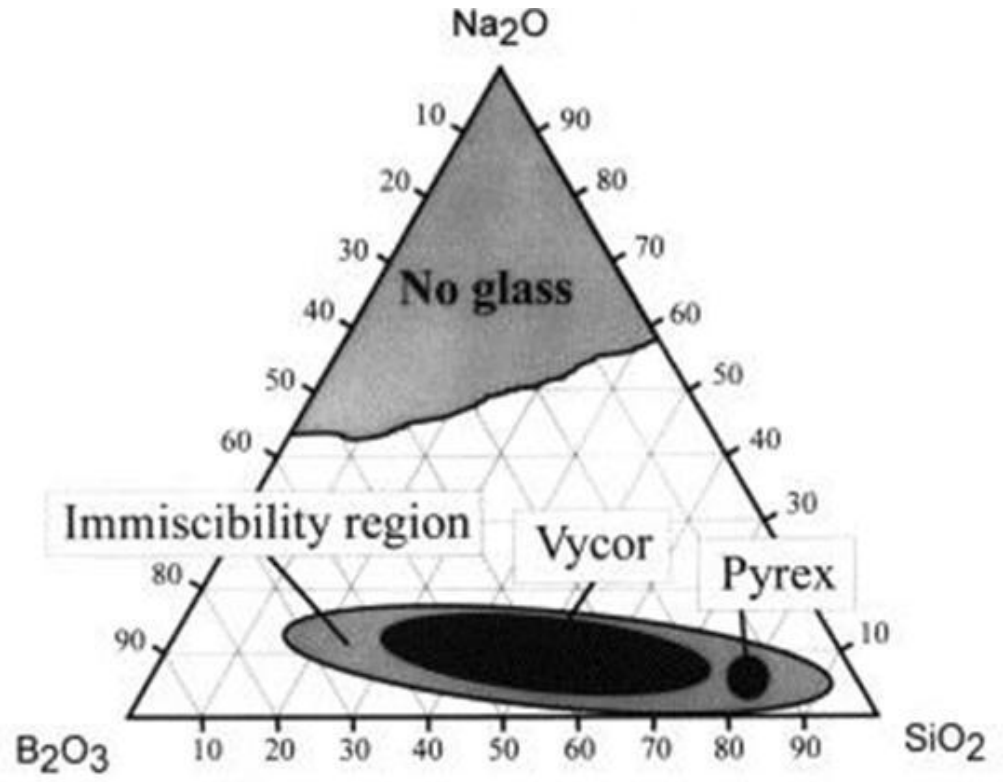

Figure 2.7: Simplified ternary phase diagram for the $Na_2O–B_2O_3–SiO_2$ system [65].

However, Hammel and Allersma [41] developed a low silica-high borate glass, with SiO_2 in the preferred range 38-46 wt%, B_2O_3 40-52 wt%, R_2O 8-12 wt%, and Al_2O_3 0-0.3 wt%. They suggested a trade-off in terms of alkali metal oxide content, since this component plays an important part in phase separation and leaching. By keeping the alkali metal oxide content down, the borate and silica phases are more soluble in one another during phase separation. Consequently, the coefficients of thermal expansion of these phases are better matched, and there is less shrinkage when the glass is cooled after phase separation heat-treatment. It is claimed that the beads made have excellent thermal stability and crush strength. This finding is of particular interest as it used to be believed that lower silica content compositions do not yield a sufficient amount of silica rich phase structure to have enough strength to hold together after leaching [71].

2.7.3 $ZrO_2–SiO_2$ binary phase diagram

The uncertain thermal stability of $ZrSiO_4$ is reflected in the published phase diagrams for the system ZrO_2-SiO_2. Curtis and Sowman [72] carried out one of the

most detailed and widely accepted studies for the ZrO_2-SiO_2 system in 1953 (see Figure 2.8). They showed zircon as decomposing in the solid state at 1540 °C, some 135 degrees below the zirconia-silica eutectic. The diagrams of Zhirnowa (1934) [73], Curtis and Sowman (1953) [72], and Toropov and Galakhov (1956) [74] featured solid solution extending from pure zirconia to the extent of 3 to 10 percent silica. This solid solution effect does not appear to have been founded very clear evidence by following research, and therefore may be ignored.

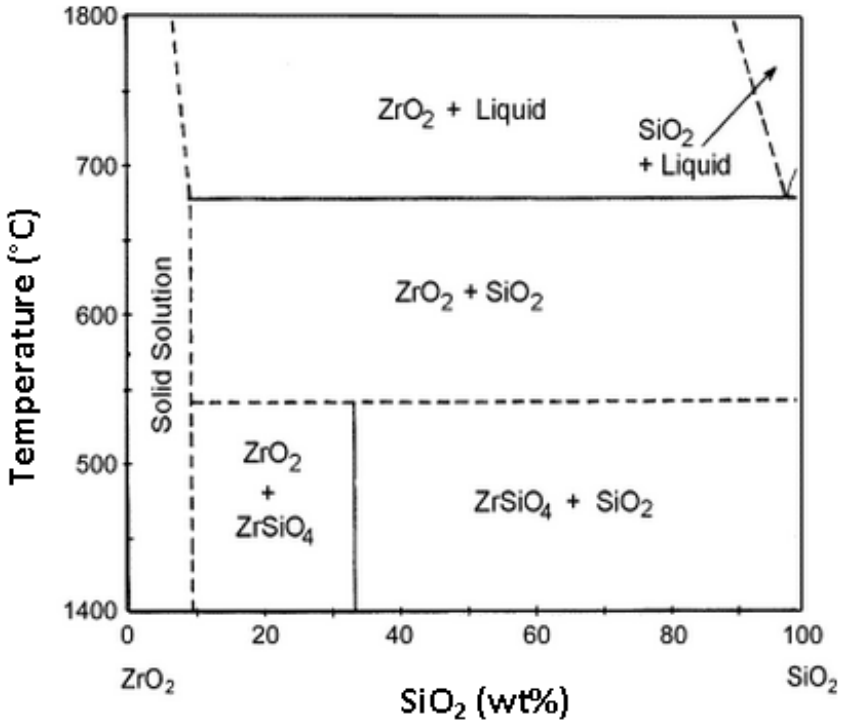

Figure 2.8: ZrO_2-SiO_2 phase diagram [72].

2.7.4 Effect of composition on glass properties

The major compounds in borosilicate glass are silicon dioxide and boron trioxide. Alkali metal oxides and alkali earth metal oxides are added to a certain level in order to optimise the properties. Some other oxides, e.g.: Al_2O_3, TiO_2, ZrO_2, are added to achieve certain properties depending on end use requirements. In some cases colouring and refining components are also added.

Silicon dioxide (SiO_2)

Silicon dioxide (SiO_2) is the glass former in borosilicate glass composition. Higher level of SiO_2 increases the melting temperature as well as the working point, and reduces the coefficient of thermal expansion. With lower levels of SiO_2 the resistance to acids deteriorates [75].

Boron trioxide (B_2O_3)

B_2O_3 reduces melting and working temperatures and improves hydrolytic stability when used below 13% by weight in the composition [69]. Higher content of B_2O_3 in borosilicate glass has an adverse effect on acid resistance and increases highly volatile alkali metal borates. On the other hand lower B_2O_3 content increases susceptibility to crystallisation because of a higher melting point of the glass. B_2O_3, like Al_2O_3, creates more secure bonds with alkali metal ions and effectively reduce the susceptibility to crystallisation [75]. B_2O_3 also plays a major role in reducing the dielectric constant of the glass [69].

Alkali metal oxides

Sodium dioxide (N_2O) is widely used as a flux in borosilicate glass composition, along with other alkali metal oxides like potassium dioxide (K_2O), lithium dioxide (Li_2O), and lead oxide (PbO). Alkali metal oxide reduces the working temperature but plays an important role in setting the thermal expansion. If the alkali metal oxides content is above a certain limit, glasses exhibit a high coefficient of thermal expansion [47]. A higher level of alkali oxide also causes an adverse effect on hydrolytic stability [75]. Peuchert et al. [75] in their work also discussed the role of alkali metal oxides in crystallisation. It was suggested to use at least two alkali metal oxides, even in small amounts, to have a positive effect on resisting devitrification. They also reported that beyond 1000 °C potassium borates evaporates more easily than sodium borates, while lithium borates is by comparison more stable in terms of evaporating from heated borosilicate glass [24]. Li^+ also forms strong bonds with glass network and increases the acid resistance of the borosilicate glass composition [47]. The use of PbO, which is an excellent flux, is becoming limited these days due to concerns regarding toxicity of heavy metals.

Alkali earth metal oxides

Calcium oxide (CaO) is most commonly used as a property modifier component in borosilicate glass composition. Small amounts of magnesium oxide (MgO), zinc oxide (ZnO), strontium oxide (SrO), and barium oxide (BaO) are also added separately based on application requirements. CaO helps profoundly to accelerate the phase separation [8, 9, 76]. CaO also has a stabilising action on acid resistance [77]. It has been found that limiting CaO to small amounts reduces the evaporation of highly volatile sodium and potassium borate compounds during hot forming [75]. If the amount of CaO exceeds certain limit, devitrification is likely to take place. Moreover, heat resistance and alkali resistance also deteriorates with high content of CaO [76]. The work done by Eguchi et al. has proposed to use alkaline earth metal oxide, or ZnO, to transfer ZrO_2 towards the SiO_2 rich phase at a time of phase separation, thereby confirming its presence in the leached and washed glass [8].

Other property modifying oxides

Zirconium dioxide (ZrO_2), aluminium trioxide (Al_2O_3), and titanium dioxide (TiO_2) are most commonly used property modifying oxides in borosilicate glass system. It has been shown in many studies that ZrO_2 greatly improves the alkali resistance of the borosilicate glass without suffering in terms of the hydrolytic stability and resistance to acids [20, 42, 47, 76]. However, higher content of ZrO_2 increases the working point as well as flaws in the glass. With excessively high ZrO_2 content, crystallisation is likely to occur [8]. Although small amounts of additional ZrO_2 suppress devitrification, they reduce the growth rate of phase separation due to an increase of glass viscosity [48]. There also remains the risk of passing the un-melted ZrO_2 into the product [75]. Kord et al. [78] claimed in their study that addition of ZrO_2 (6 mol%) increased the bending strength by almost double. Al_2O_3, most commonly used as a modifying oxide [8], has mixed effect on the property of the borosilicate glass. It increases the aqueous durability as well as the resistance to devitrification of the borosilicate glass, while inhibiting phase separation [23, 47, 70]. Fluidity of the glass decreases with the addition of Al_2O_3 in borosilicate glass composition [47]. Al_2O_3 also acts as a balancing component to tolerate relatively high levels of CaO in the borosilicate system. Al_2O_3 also acts as to prevent cracks during leaching and improve moldability by minimising the viscosity change relative

to the change in temperature [76]. TiO_2 is used in small quantities for special applications where UV absorption is required [43, 75]. It is also believed that the presence of TiO_2 suppresses crystallisation [79].

Refining component

Borosilicate glass can be refined with small amounts (≤ 1% by weight) of conventional refining agents, such as chlorides, e.g.: NaCl, and sulphates, e.g.: Na_2SO_4 or $BaSO_4$, fluorides and bromides. Amongst other refining agents CeO_2, As_2O_3, Sb_2O_3, and CaF are noteworthy [44, 75].

Colouring components

Fe_2O_3, Cr_2O_3, and CoO are the most commonly used colouring components in borosilicate glass. Usually their proportion in borosilicate glass system is kept below one percent by weight [24].

2.7.5 Porous glass preparation process using $Na_2O–B_2O_3–SiO_2$ system

Porous glass is the leaching product of phase separated sodium borosilicate glass. Proper heat-treatment, which is usually between glass transition and crystallisation temperature, initiates phase separation in sodium borosilicate glass of suitable composition [50, 66, 71]. Two distinct phases are obtained. One of which is an alkali-rich borate phase and is soluble in acids, while another one is almost pure silica and is insoluble in acids. After heat treatment, the glass is immersed in a hot dilute acid solution. These solutions are characterised by the presence of H^+ or H_3O^+ ions that react with the alkali-rich borate phase. The soluble phase is slowly leached out, leaving behind a porous high silica skeleton (96 %) [40]. Commercial porous Vycor^{TM} glass (PVG) is produced in this way, although another step is required in which the porous glass is slowly heated above 1200 °C whereby the porous structure is consolidated into a clear impervious glass. Due to very low solubility of silica in acidic media, finely dispersed colloidal silica precipitates, of which a greater portion remains in the pores of the macroporous glass [33, 80]. This colloidal silica strongly affects the pore structure and the properties of the resulting porous glass, by

increasing the specific surface area and reducing the pore volume [81]. These colloidal deposits can be removed with a dilute alkaline solution. This process is used for the preparation of commercial Controlled Pore Glass (CPG). Figure 2.9 shows a schematic diagram of the typical process for making porous borosilicate glass.

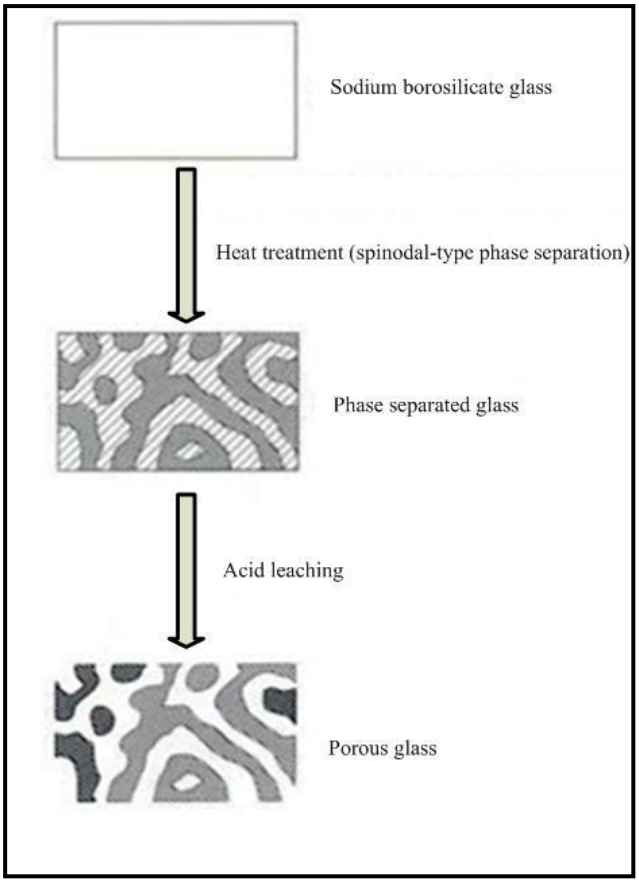

Figure 2.9: Schematic preparation procedure of porous glass (modified from [82]).

2.7.6 Amorphous phase separation mechanism

The Na_2O-B_2O_3-SiO_2 system is perhaps the most well known system in terms of Amorphous Phase Separation (APS) and the formation of interconnected microstructures. The initial glass separates into two intimately mixed phases, one of which is almost completely pure SiO_2 glass, the other one being sodium-borate glass [25, 40, 71]. The sodium-borate phase can be leached away by dissolving it in acid, leaving behind a porous silica matrix. The manufacture of Vycor relies on this system, whereby glass objects are first formed, then heat-treated and leached, then dried, and finally heated to approximately 1200 °C, yielding sintered, perfectly clear

glass objects, with about 30% volume contraction [20, 31]. This process thus circumvents the 2000 °C temperature range needed to form glass objects from a pure quartz melt. Depending on the composition of the original glass, and on the heat treatment temperature and its duration, the morphology of the phase separation can either take the form of two interconnected, interpenetrating, networks which is know as spinodal decomposition, or of droplets of one phase distributed within the other phase, which is known as separation by nucleation and growth [40]. Figure 2.10 exhibits the critical temperatures in the ternary Na_2O-B_2O_3-SiO_2 system below which phase separation occurs. Figure 2.10 also shows the tie-lines, essential to the determination of the compositions and concentrations of the phases, at selected temperatures which represent the chemical composition of the immiscible phases.

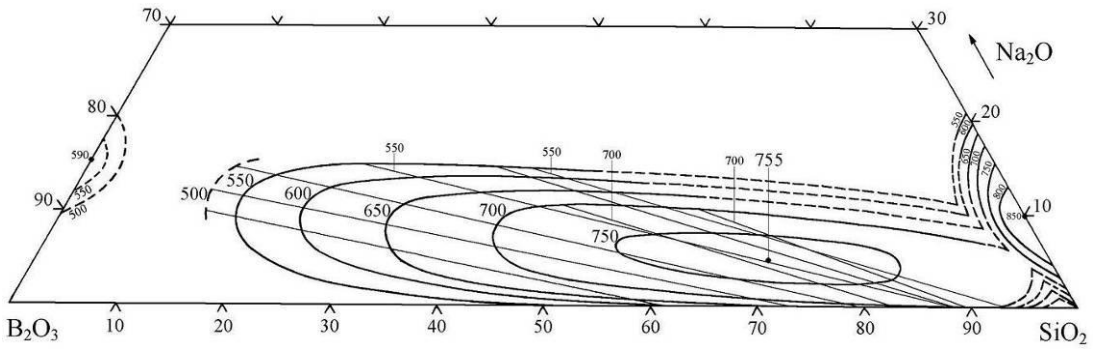

Figure 2.10: Phase separation in the sodium borosilicate glass system [83]. Dashed lines represent uncertain.

The two mechanisms, referred as spinodal decomposition and nucleation and growth, lead to very different microstructure and properties [32]. Identification of the immiscibility boundary and the spinodal boundary can indicate by which mechanism the phase separation will occur. The extent of the immiscibility region for the alkali borosilicate glass system depends on the presence of alkali content and decreases with an increasing number of alkali [23, 24]. Figure 2.11 shows the immiscibility diagram, for the binary sodium silicate system with microstructure when heat treated, for the different regions of the phase diagram. The dark phase in the figure represents a sodium rich composition and light phase denotes a silica rich composition. Phase separation in type A and type C (see Figure 2.11) are in a binodal region and undergo APS only by nucleation process, whereas type B is in the spinodal region and undergoes APS by spinodal decomposition.

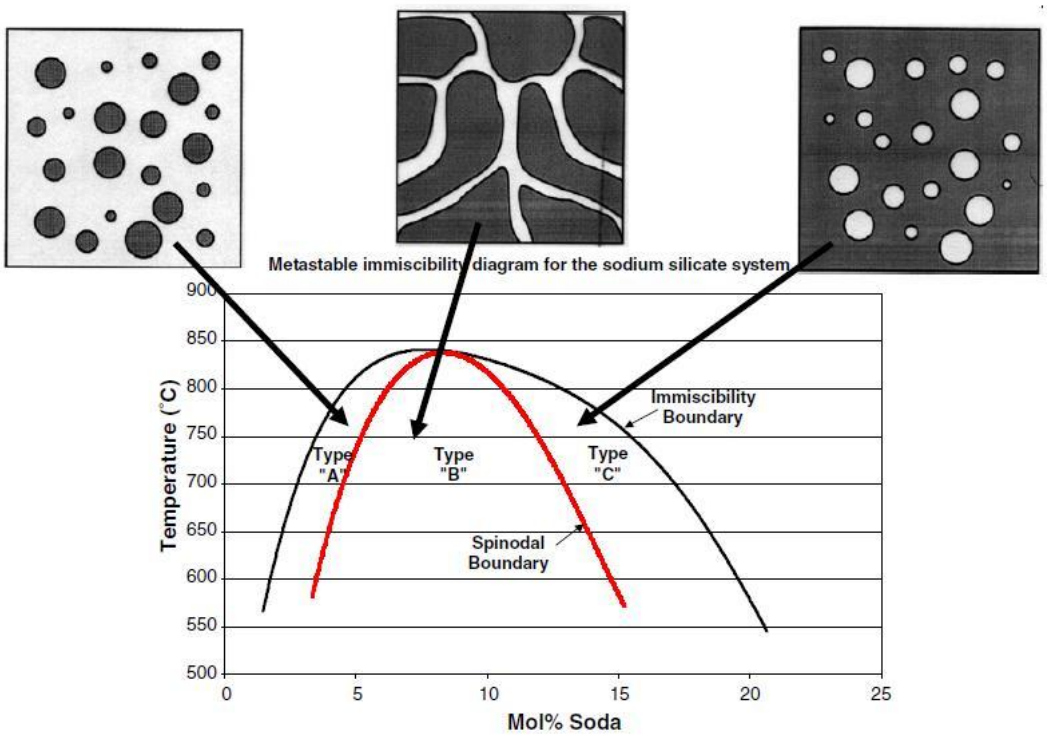

Figure 2.11: Metastable immiscibility diagram for the sodium silicate system showing typical microstructures [24, 32].

A more comprehensive study was carried out by Wheaton and Clare [32] on binary sodium silicate glass with a composition of 12.5 mol%Na_2O and 87.5 mol% of SiO_2. Atomic Force Microscopy (AFM) images were made after 15 min heat treatments at temperature within the spinodal decomposition and the nucleation and growth region of the immiscibility diagram (see Figure 2.12). The microstructure resulting from heat treatment at 637 °C is in the early stages of spinodal decomposition and shows two continuous phases. At 720 °C, which is just below the spinodal boundary, two distinct phases appear. Whereas, microstructures at 778 °C and 791 °C show bright droplets of the high silica phase and the separation is dominated by the nucleation and growth mechanism. A secondary phase separation is observed with a three phase microstructure at 778 °C. Secondary phase separation is likely to occur when heat treatment is carried out just above the spinodal curve, and the heat treated glass passes through the spinodal region during cooling.

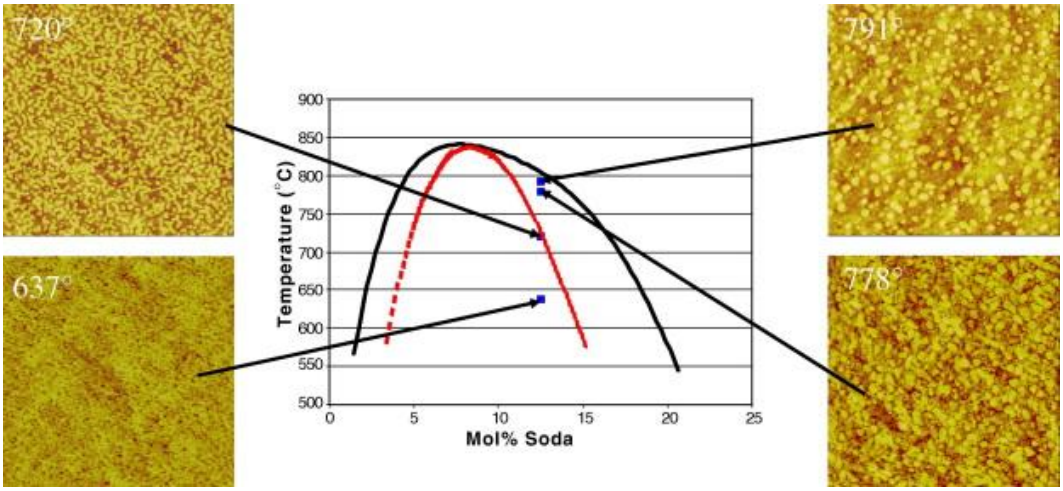

Figure 2.12: Immiscibility diagram for sodium silicate glass with corresponding AFM images [24, 32].

Hill et al. [84] explained the metastable APS for a glass composition below the liquidus in a classic way. They presented three scenarios that exist, which are shown schematically in Figure 2.13. Glass composition 1, which represents the critical composition stage where binodal and spinodal meet, enters directly into the spinodal region without passing through the metastable regions where nucleation occurs. Only spinodal decomposition occurs for this glass. Glass composition 2, will pass through the binonal before entering the spinodal region and exhibits two characteristics of phase separation. On the other hand, glass composition 3 will only enter the binodal region on cooling and never pass through the spinodal region. This glass will undergo APS by nucleation process. The effect of cooling rate also plays a key role in APS. In glass compositions that undergo both nucleation and spinodal decomposition, relatively slow cooling may result in phase separation by nucleation only, as it gets time for completion and thus inhibits a further spinodal decomposition process. Yazawa et al. [44] also investigated the effect of cooling rate on rapidly quenched sodium borosilicate glass that exhibits spinodal phase separation on heat treatment. They found that if the cooling rate is rapid enough it can entirely avoid spinodal phase separation. Thus the pore volume and surface area of the resulting porous glass decreased with increasing cooling rate.

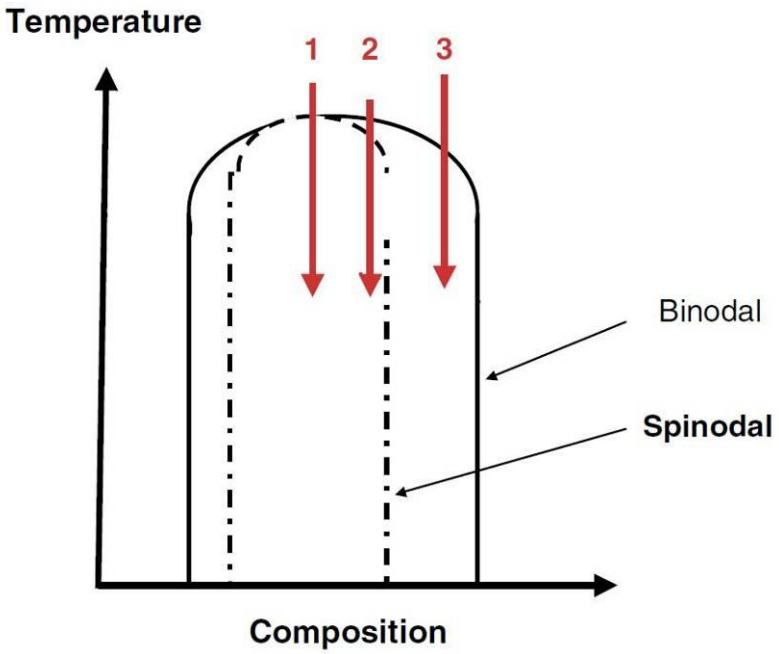

Figure 2.13: Schematic representation of possible cooling routes of glass undergoing amorphous phase separation [84].

2.7.7 Influence of heat-treatment time and temperature on phase separation

Porous glass is only useful if the size of the porosity can be closely controlled. The extent of the phase separation process and other properties such as pore interconnection, pore size distribution, and pore morphology is dependent on heat treatment [4]. In the SiO_2-B_2O_3-Na_2O system, size of pore is carefully controlled by the heat-treatment to form the separated phases, which is later leached and washed to form porous interconnected glass with narrowly distributed pores. Haller [3] devised a heat treatment which is in accordance with the formula:

$$r^n = kte^{-m/T} \qquad \text{Equation 2.1}$$

Where, r is desired pore radius (Å), t is time (h), T is temperature (K), and m, n, and k are experimentally determined constants. Figure 2.14 is a graph showing the relationship of heat treatment temperature operation versus controlled pore diameter.

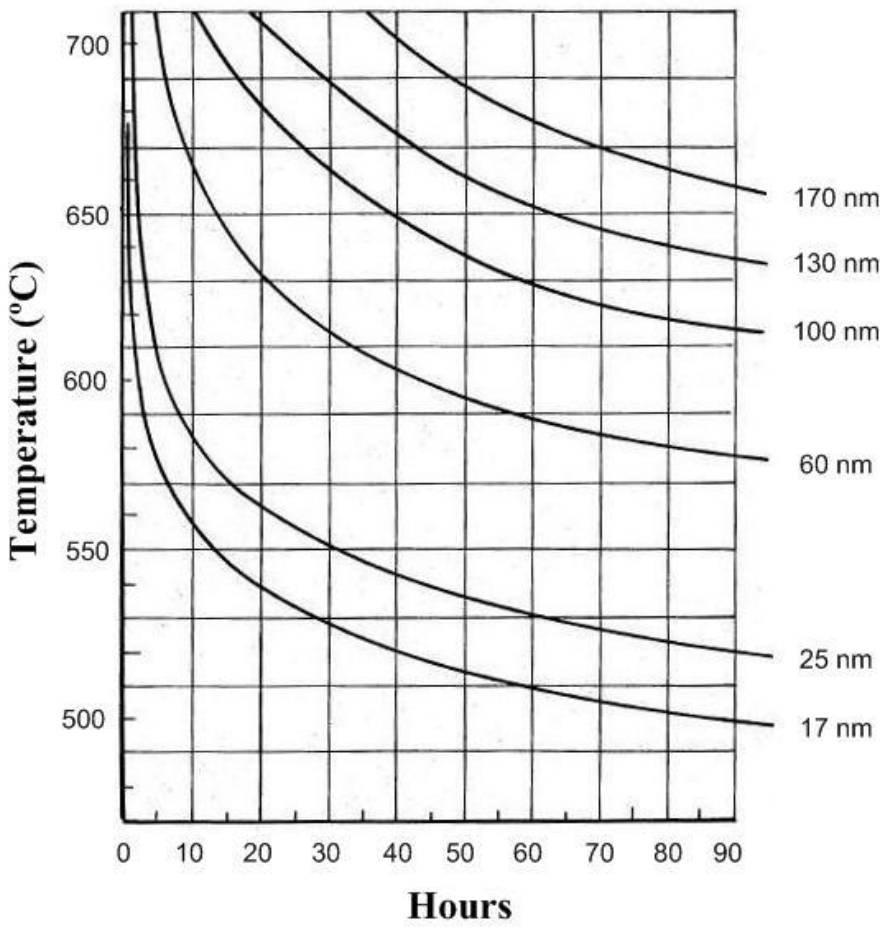

Figure 2.14: Graph showing the relationship of heat-treatment operation versus controlled pore diameter as a function of time, (modified from [7]).

Kukizaki [48] further deduced the following equation from the one which was first proposed by Haller [33]:

$$lnD_p = -\frac{E_p}{2RT} + ln(4K^{1/2}V_p t^{1/2}) \qquad \text{Equation 2.2}$$

Where, D_p is the pore diameter, E_p is the activation energy for diffusion in phase separation, R is the gas constant, K is a constant dependent on the composition of the parent glass, T is temperature, V_p is pore volume per unit mass, and t is the time used for the heat treatment. The Equation 2.2 shows that $ln\ D_p$ linearly decreases with increasing $1/T$. They found the relationship $ln\ D_p$ and $1/T$ valid for the glass they prepared, both in the case of the parent glass with 3.5 mol% ZrO_2 and without ZrO_2. The degree of phase separation usually increases with increasing duration of heat treatment [85]. A similar phenomenon was observed by Wheaton and Clare [9, 32] where they found a consistent increase in the area of the silica phase with cube root

of heat treatment time. Kukizaki [48] in his investigation of a sodium borosilicate glass system with the composition $6.7Na_2O$-$22.7B_2O_3$-$70.6SiO_2$-$3.5ZrO_2$ (mol%), found a relationship between mean pore diameter and time, where the mean diameter linearly increased with the square root of the heat treatment time. The same phenomenon was also found by Zhou [50] where pore size, pore volume, and porous skeleton enhanced with heat treatment time. However they suggested that it was necessary that an optimum duration of time at a fixed temperature be determined. Otherwise, mixing and partial dissolution occurs with the silica rich and sodium rich borate phase causing the pore size to decrease. Nakashima et al. [6] proposed the Time-Temperature-Transformation (TTT) diagram to determine the optimum heat-treatment temperature and the time. Figure 2.15 (after [6]) presents a TTT diagram for a sodium borosilicate composition of $10Na_2O$-$25B_2O_3$-$65SiO_2$ (mol%), where the C-shaped curves indicate the heat-treatment temperature and the time for the onset of both phase separation and crystallisation.

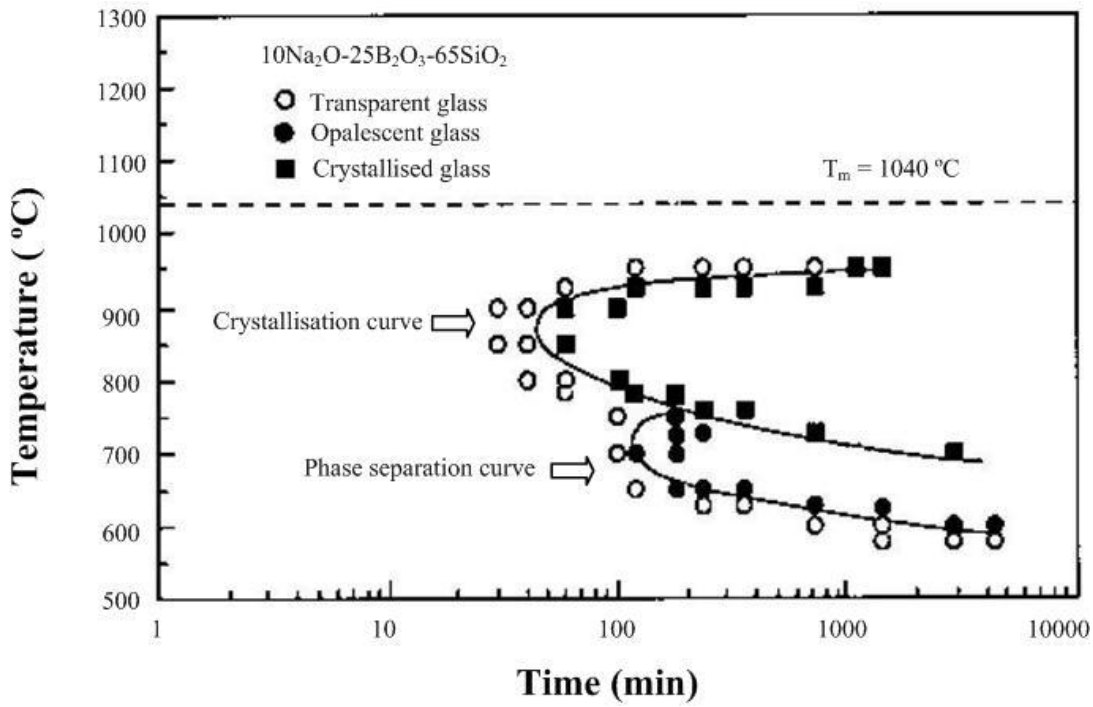

Figure 2.15: TTT diagram for sodium borosilicate glass composition $10Na_2O$-$25B_2O_3$-$65SiO_2$ [6].

2.7.8 Acid leaching and alkali washing

Following heat-treatment, a carefully controlled acid leaching process is required to remove the sodium-borate phase. Various concentrated inorganic acids, such as

hydrochloric acid (HCl), nitric acid (HNO_3), sulphuric acid (H_2SO_4), and phosphoric acid (H_3PO_4), are preferably used at elevated temperature to remove the acid soluble phase from the heat-treated glass. It is also possible to use organic acid such as oxalic acid, acetic acid, succinic acid, and citric acid [8]. The ratio of heat-treated glass to acid is maintained [3]. Most of the studies mention a ratio 1 gm : 8-10 mililitres [3, 9, 41]. The concentration of acid is the main focus of many research projects, as it plays a vital role in removing the soluble phase while keeping the structure intact. For the parent sodium borosilicate glass composition the acid that is usually used is HCl acid with a concentration varying from 0.5 N – 3 N in elevated temperatures between 50 – 100 °C [3]. According to Hood and Nordberg [86] the choice of leaching conditions should be governed by practical considerations. The temperature should be as high as possible to insure rapid leaching, and an increase in acid concentration within limits also increases the rate of leaching. Recently (2011), Torque et al. [87] extensively studied the effect of leaching conditions on the sodium borosilicate glass composition $5Na_2O$-$20B_2O_3$-$75SiO_2$ (mol%). Varied concentrations of HCl acid ranging from 0.1 to 3 N with treatment duration ranging from 2 to 48 hours were used, while the leaching temperature (90 °C), and the ratio between heat-treated glass powder and acid solution (1g : 10 ml), remained constant. They found a non-linear effect of acid concentration on the porous structure. The specific surface area and pore volume is low at lower acid concentrations. Increasing acid concentrations to around 0.7 N strongly increases the surface area and pore volume. However, further increases in acid concentration led to a decrease in both the surface area and the pore volume. This behaviour can be attributed to the variable content of colloidal silica which was produced and then remained in the pores of the silica skeleton when the acid concentration increased. They also found that an increase in leaching time with the same acid concentration does not affect pore volume but the surface area decreased due to an increase in silica particles being dissolved. A schematic view of the effect of different acid concentrations on pore morphology in porous glass is shown in Figure 2.16.

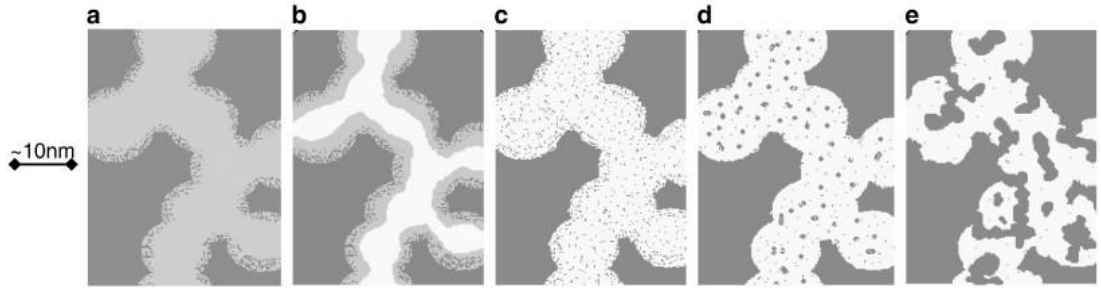

Figure 2.16: Schematic view of HCl acid concentration effects on the morphology of pores depicted as: (a) initial glass; (b) C_{HCl} = 0.1 N; (c) C_{HCl} between 0.3 and 0.7 N; (d) C_{HCl} = 1 N; and (e) C_{HCl} = 3 N [87].

When ZrO_2 is present in the Na_2O-B_2O_3-SiO_2 glass system, a different route of acid leaching steps is used. The ZrO_2 containing sodium borosilicate heat-treated glass is first immersed in 0.25 N – 3 N HNO_3 (nitric acid) at 50 – 100 °C for 4 – 100 hours [8]. In this initial step, where the sodium rich borate phase is removed, a gel forms that is rich in zirconia and silica and that then remains in the silica rich structure [8]. To remove this zirconia gel, a further acid treatment with 2 – 3 N H_2SO_4 acid is used [8, 9, 48]. Each step is followed by thorough washing with deionised water.

In the initial steps of the production process of porous glass, especially when producing precisely controlled pore glass (CPG), hot water (80 – 100 °C) is used to remove the soluble phase [41]. The solubility of the borate rich phase is very high at 90 – 100 °C with a duration of 6 – 8 hours [41]. The dissolved alkali-rich borate phase in water can be recycled and used in subsequent melt, which is economical from a commercial point of view [41]. A two-step water-acid treatment is proposed by Hammel et al. [41], where the acid leaching step is followed by a shorter period of hot water treatment, depending on the amount of alkali and borate remaining within the silica skeleton after the leaching step. They found the two-step water-acid leaching better than leaching with water only or acid only, and reported that this two-step leaching process significantly improved the thermal stability of the leached porous glass. However, most researchers avoid using hot water as a leaching medium as solubility of silica increases in aqueous solution of pH 6–8 with increasing temperature [88].

The rigid pores of the resultant silica-rich phase skeleton are substantially filled with colloidal silica which is a decomposition product of the previous microphase [7, 80].

To remove the colloidal silica, the skeleton is treated with a solvent, usually dilute sodium hydroxide solution, ranging in concentration from 0.1 N – 0.5 N, for 1 to 5 hours at 25–30 °C [3, 6, 8, 9, 76]. The sodium hydroxide solution should be within 0.5 N as the concentration beyond 0.5 N doubled the rate of attack in some instances [89]. Thereafter, the skeleton can be dried and the dried skeleton then is composed of a rigid matrix of interconnected porosity, free of contaminants. However, it is difficult to remove all the colloidal silica unless the washing with alkali solution is strong. The addition of zircon or zirconia in the parent sodium borosilicate glass increases the alkaline resistibility and thus makes the porous skeleton withstand strong alkali washing [8].

2.7.9 Applications

Sodium borosilicate porous glass poses some unique properties, such as interconnected pore structure, chemical inertness, high mechanical and thermal stability, and high surface area, making it suitable for applications where these special properties are required. In general sodium borosilicate porous glass can be used for the following applications:

- Enzyme immobilisation and size exclusion chromatography [2, 4, 24, 59].
- Optical chemosensors [90, 91].
- Material for the encapsulation of nuclear waste [4, 92, 93].
- Gas separation membranes [94, 95].
- Catalyst supports [96].
- Microelectronic packaging [97, 98].

Large surface area with controlled pore diameter make porous sodium borosilicate glass highly desirable as filtering material. The surface of glass has a high affinity for certain molecules, thus making it possible to separate not only on the basis of molecular size, but also on the basis of molecular type [41]. Controlled pore glass has a very sharp pore distribution and has a wide application for size exclusion and adsorptive chromatography of proteins, nucleic acids, viruses, and high polymers [36]. The primary application is in permeation chromatography, where the chemical resistance and mechanical stability of porous glass significantly exceeds that of

polymeric materials used for the same purpose. The internal surface of the porous glass can be modified due its organophilic nature. Surface treated controlled-pore glass is used for the preparation of specialised diagnostic products and for the immobilisation of enzymes[2] in fixed-bed reactors [4, 36, 99, 100].

Advantages of porous glass for filtration include rigidity, chemical inertness, high temperature capability, superior thermal shock resistance, and controlled porosity. These advantages allow higher processing temperature and pressure, back flushing or burnout cleansing, and processing of most corrosive products. Eaton [101] describes the use of porous glass as a chromatographic support medium, which involves packing porous glass particles or beads into a column through which a solvent is pumped. A mixture of compounds of different molecular weights is injected into the solvent stream to pass over and around the particles. In this process, the mixture tends to separate into different molecular size ranges due to the controlled geometry of the support material, which hinders the passage of molecules of varying molecular sizes. As the solution travels down the support column, smaller particles enter into the pores. Larger particles cannot enter into as many pores and are eluted. The larger the particles are, the faster the elution, thus providing a means of separating molecules by size exclusion. A schematic example of how the sizes are separated by size exclusion chromatography is shown in Figure 2.17.

[2] Enzymes are biological catalysts capable of initiating and governing chemical reactions without being used in the process or becoming a part of the product formed. Most enzymes are proteins and water soluble. As enzymes are expensive to produce, some form of immobilization is essential to reuse them and porous glass is found to retain proteins from solution due to strong protein-glass bonds [4, 99].

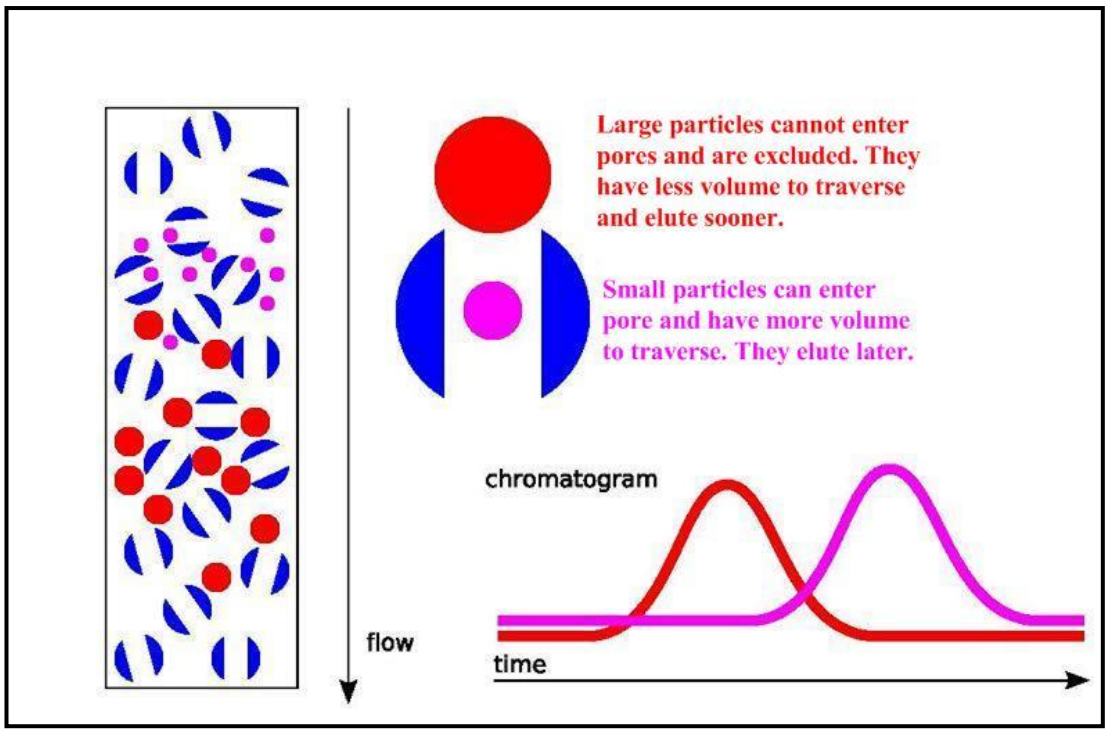

Figure 2.17: A schematic illustration of the theory behind size exclusion chromatography [102].

Porous sodium borosilicate glass systems can also be used for making optical fibre sensors [103]. The sensor is made by using a sodium borosilicate composition. At first the fibre is drawn and then heat-treated and leached. Thereafter, the porous structure is soaked with chemical indicator based on the properties of the chemical system to be detected. The interconnected pores allow the indicator and solvent to permeate through the pores. The porous glass is then dried so the indicator coats the pore surface and thus it can be used as sensor. The sensor is used in a vessel with a light source, a light detector, and a means for measuring the change in light caused by an agent (liquid or gas) to be tested within the porosity of the sensor [103].

2.8 ALKALI RESISTANCE

Porous silica glass with improved alkali-resistance has been the subject of many investigations. The ordinary Vycor-type porous glass has relatively poor water and alkali-resistance. The practical pore diameter is restricted from approx. 4–150 nm [9]. During the acid leaching step, colloidal silica is deposited in the pores. This colloidal silica is formed by the gelation of the SiO_2 component distributed during

the acid-soluble borate-rich phase (due to secondary unmixing). Removal of gelated SiO_2 is difficult because powerful washing can damage the porous glass itself as the solubility of silica increases with increasing pH and beyond a pH level 10 it becomes too drastic [104]. More strongly alkali-durable glass would be more capable of withstanding powerful washing, leading to more economical formation of a porous glass with a sharp pore-size distribution. Amorphous SiO_2 has a water solubility of about 100 p.p.m. at room temperature [88]. Contact with aqueous solutions is therefore restricted and this is a limitation when porous glass is to be used as a membrane. Simhan [105] highlights the importance of glass composition, duration and temperature of attack, the volume of the attacking solution, and glass surface area on chemical durability. Controlled pore glass typically has a surface area of several hundred meters squared per gram, making them especially vulnerable.

Sanitation by sodium hydroxide (NaOH) is almost mandatory for chromatographic media used in industrial applications in the biopharmaceutical industry [5]. Up to 1 N NaOH is desirable for cleaning and sanitisation of chromatography columns. Unfortunately, silica is attacked by alkali. This results in pore enlargement, leading to inaccurate separations and eventually to degradation of the silica support. For this reason, an alkali-resistant material containing interconnected porosity that can survive NaOH sanitisation is high desirable. This challenge has been the focus of many patented works over the course of the past two decades and beyond.

Alkali resistibility in sodium borosilicate glass is also desirable for high level nuclear waste immobilisation [106].

2.8.1 Approaches for improving alkali resistance

The 1980's saw a flurry of activity in the development of alkali-resistant porous glass, much of which originated in Japan. Up to now, the addition of ZrO_2 to the glass system has been the prime focus of all research to increase the alkali resistance of porous glass, as a ZrO_2 surface is stable at all conceivable pH ranges of solution and offers a high activation barrier for other ionic species to diffuse through it [63]. In 1986, Kokubu developed a porous titanate glass with a skeleton composed mainly of TiO_2 and SiO_2, in which the glass composition ratio (wt%) TiO_2/SiO_2 is 0.8 to 1.7

[14]. Starting materials also included Al_2O_3, B_2O_3 and CaO. This glass was prepared using traditional glass melting technology, followed by phase separation and leaching. Kokubu claimed to be able to produce pore structures with pore radius in the range 2 nm to 50 nm. However, the pore distributions shown were not uniform. Alkali resistance testing was carried out with 0.25 N NaOH at 40 °C. After 100 hours of leaching, the porous glasses lost 20-40% weight, compared to a commercially available silica glass that had completely dissolved. One year later Kokubu et al. filed a patent entitled: "Thermal and Chemical-Properties of TiO_2-SiO_2 Porous-Glass Ceramics" [107], where they added 0–10 wt% of ZrO_2 and TiO_2 in sodium borosilicate glass composition. They claimed that the leached porous glass has a high flexural strength and excellent alkali resistance; though no data about alkali resistance was provided, except that cracks and peeling appeared on the surface layer after washing with 1 N NaOH at 40 °C for 10 hours.

Richard W. Stout of E.I. Du Pont de Nemours and Company filed a patent at around the same time entitled: "Metal oxide stabilised chromatography packing" [11]. The porous materials of this invention are surface-stabilised porous silica bodies with uniform pore size, a particle diameter range of about 0.5 – 100 microns, and partial surface coverage of metal oxide in quantities insufficient to form a continuous layer over the silica, thereby providing a surface mosaic of metal oxide and silicon dioxide. The stabilised bodies are prepared by heating chromatographic packings (e.g. Zorbax® packings) with water soluble metal salts under reduced pressure and subsequently heating at 600 °C – 1000 °C to achieve a dried reaction product. The number of times samples may be successfully processed through a reusable column is commonly referred to as the number of throughput fluid column volumes that can be processed by a particular packing and still obtain separation of sample components. The zirconium stabilised packings invented by Stout are capable of processing a significantly larger number of throughput fluid column volumes and the stabilised packing functions well in a wide pH range. Zorbax® (Stout et al) employs this technology, thereby providing a surface mosaic of zirconia and silicon oxide. However, according to Jungbauer [5], Zorbax can only withstand short term use at pH 9.0.

D. R. De Villiers and R. O. Heckroodt [108] tried to substitute silica by a combination of Y_2O_3 and ZrO_2 and used composition $12Na_2O–64B_2O_3–12Y_2O_3–12ZrO_2$ (by wt%) for making porous glass. The resultant porous glass has average pore diameter of 8 nm with high surface area and found the alkali resistance 0.0041 mg/dm^2 based on ISO 695 [109]. However, they found the leached samples were mechanically very weak and crumbled easily during drying and handling.

In 1987, Murakami filed a patent entitled: "Method of strengthening the alkali resistance of a porous glass" [12]. With this method, porous glass is formed (by a traditional glass-making route) and then immersed in a solution of zirconium alcoholate to form a thin film of the zirconium salt on the surface of the porous glass. Hydrolyzing, drying, and calcining forms ZrO_2 polymer on the surface of the porous glass. Examples of zirconium alcoholate that can be used are zirconium n-propoxide, zirconium iso-propoxide, and zirconium n-butoxide. A vacuum impregnation method is used to permeate the solution through the pores. The dealcolation reaction between the silanol groups on the surface of the porous glass and the alkyl groups in the coating agent results in the zirconium alkoxide being covalently bonded to the glass surface. Coating with zirconia in this way results in a slight decrease in pore diameter/pore volume, as the inner pore walls are coated. The alkali resistance is quoted as the reduced % of the sample when treated with zirconium tetra (n-butoxide) (1% aq. at 50 °C for 1 hour), and for the material in this case, this value was 7.3 %, as compared to 28.4 % for the non-treated glass. This indicates only modest alkaline durability, compared to materials prepared by other investigators. It appears that coating techniques are only moderately successful in achieving alkaline durability.

Eguchi et al. in 1988 filed a patent entitled: "Chemically durable porous glass and process for the manufacture thereof" [8]. This patent continued the trend of using zirconia to improve the alkali durability of silica-based glass systems. However, rather than coating the glass surface, the approach of Eguchi et al. took involved adding zirconia powder to the starting material composition. A typical starting glass composition, as detailed in Example 2 of the aforementioned patent, is as follows: 49.2 wt% SiO_2, 24.6 wt% B_2O_3, 14.7 wt% ZrO_2, 6.9 wt% CaO, 4.6 wt% Na_2O. The purpose of the alkali earth metal oxide, in this case CaO, is to cause a substantial

quantity of ZrO_2 to enter the SiO_2 phase. It is believed that this is the key factor in increasing the ZrO_2 content in the resultant porous glass. Without the use of an alkali earth metal oxide, ZrO_2 enters the soluble phase and upon elution with an acid gets washed away. Use of the composition detailed above resulted in a porous glass (of average pore size 100 nm) comprising: 83.2 wt% SiO_2, 15.1 wt% ZrO_2, 1.1 wt% B_2O_3, 0.4 wt% Na_2O, and 0.2 wt% CaO. Alkali durability is quoted in terms of weight loss (in a 1 N NaOH solution maintained at 30 °C). In the patent by Eguchi, no actual figures are quoted, but data taken from the patent (Figure 2.18) could be interpreted as a weight loss of about 5 mg/cm^2 after about 50 hours.

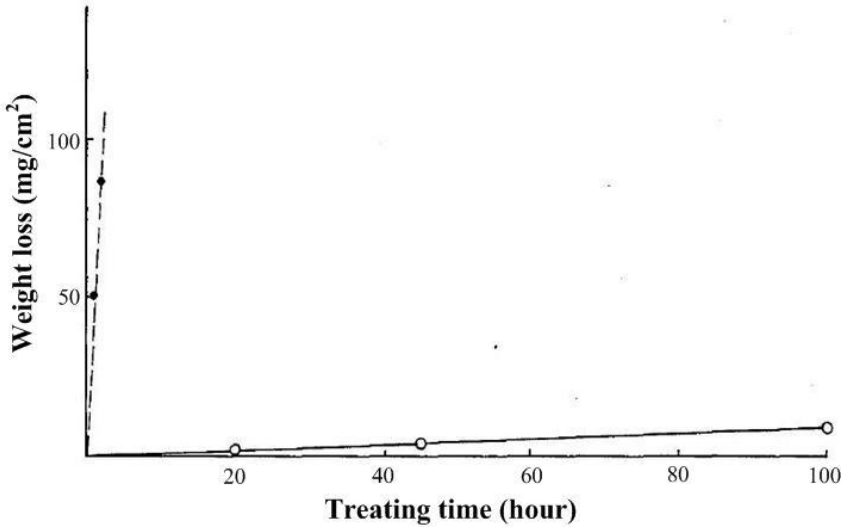

Figure 2.18: Alkali durability of Eguchi porous glass (open circle- o) compared with a Vycor-type porous glass (filled circle- •) [8].

Eguchi points out that ZrO_2 contents of < 2wt% are insufficient in terms of forming an alkali-resistant porous glass. While no upper limitation is placed on the ZrO_2 content, it should preferably be 40 wt% at the greatest. However, as the ZrO_2 content is increased, crystallisation is likely to occur during glass formation and pouring, and for this reason a practical limit of 20 wt% in the starting composition is preferred.

In 1990, Wada et al. of Mitsubishi Kasei Corporation, Japan filed a patent entitled: "Porous glass and process for its production" [13]. Again, the emphasis of this work centres around the addition of zirconia to silicate glass. However, in this case sol-gel-based approaches are used compared to the traditional high-temperature glass-forming route. Typical precursors include tetraethyl orthosilicate and zirconium n-butoxide. The reader is referred to the patent for specific details of gel formation.

After gel formation, calcination is required usually at temperatures less than 800 °C. The invention provides porous glass consisting essentially of silica, zirconia, and an alkali metal compound with a zirconia content of at least 5 wt%. However, based on the examples given in the patent, the content of zirconia in the porous glass is invariably ≥ 15 wt%. An exception is Example 11, where the porous glass contained 82.5 wt% SiO_2, 12.2 wt% ZrO_2, and 4.4 wt% Na_2O. Figure 2.19 (a) shows the pore distribution curve for this glass. Figure 2.19 (b) shows the TEM micrograph. Alkali durability of the glasses produced is measured in SiO_2 elution % per 100 mg of sample immersed in a 0.1 N NaOH aqueous solution and left to stand at room temperature for 24 hours. Elution rates measured were in the range 0 – 2.3% compared to up to 92.7% for silica only samples. These conditions are very mild relative to the conditions used by other researchers, yet 2.3% SiO_2 elution still occurs.

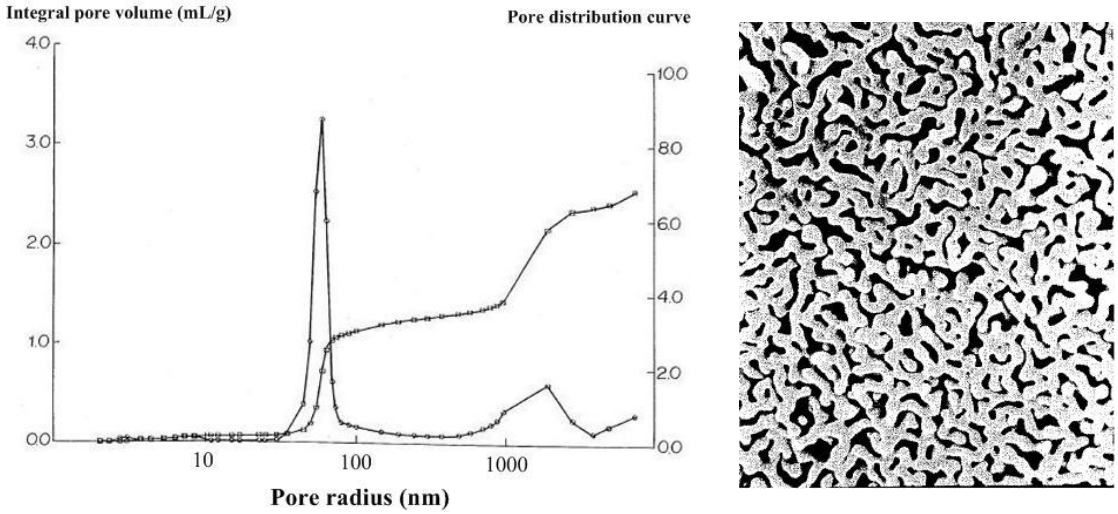

(a) (b)

Figure 2.19: (a) pore distribution curve for this glass and (b) pore structure [13].

Hosono reports in the literature on a similar system of Kokubu [14], but in his system B_2O_3 is replaced by Na_2O [15]. The system is: Na_2O-CaO-TiO_2-P_2O_5-SiO_2. This porous glass contained TiO_2 (67 mol%) and SiO_2 (33 mol%). Brooks et al. [110] at University of Sheffield have also investigated this composition. Hosono et al. reported pores of approximately 1 micron diameter and an impressive uniform distribution was observed from mercury porosimetry. However, when the porous ceramic was immersed in 0.5 N NaOH for 10 hours at 70 °C it broke into pieces. This contradicts the findings of Kokubu et al. [14], who reported modest alkali

resistance. However, it is important to note that the alkali test used by Kokubu was considerably milder than Hosono's. It is difficult to compare the different approaches as each investigator tends to use different alkaline test conditions.

Later in 1994, Yazawa along with Eguchi and Yokoyama [9] investigated an alkali resistant porous glass prepared from SiO_2–B_2O_3–RO (R = Ca, Mg, Sr, Ba, and Zn) system containing 3.2 mol% ZrO_2. They found the alkali resistance of the composition with ZrO_2 to be far greater than ordinary Vycor type porous glass (see Figure 2.20). Thirteen years later Arbab et al. [111] investigated the effect of RO oxides (R = Ca, Mg, Ba, and Zn) on borosilicate glass without ZrO_2, and found that specimens containing ZnO showed least resistance to alkali attack.

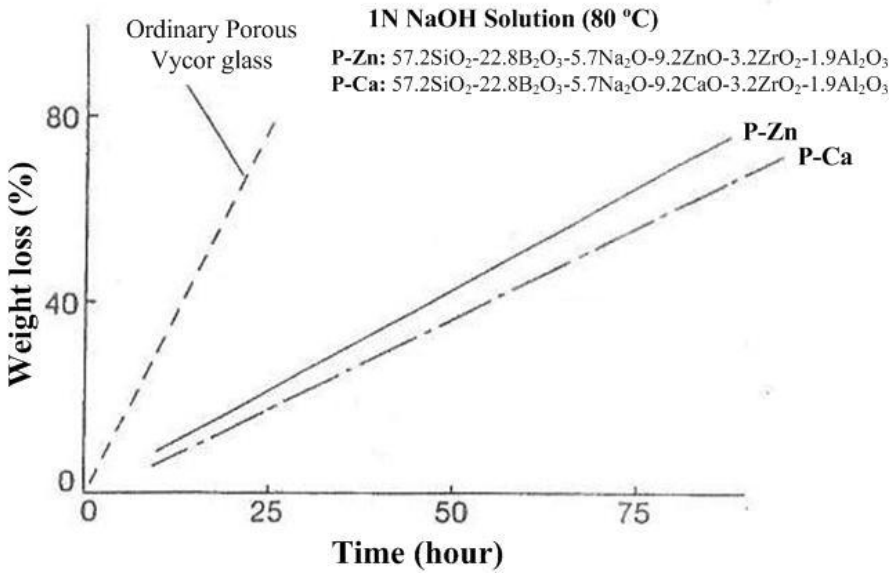

Figure 2.20: Relationship between weight loss and leaching time for various porous glass [9].

In 1997, Nakashima and his co-workers [6] studied a basic composition of 65 mol% SiO_2, 25 mol% B_2O_3, and 10 mol% Na_2O, where CaO and ZrO_2 were added in a varied range, i.e.: 2-10 mol% and 2-8 mol% respectively. It has been claimed that CaO represents "a convenient means of, and is the key factor in, increasing the ZrO_2 content in the porous glass." The alkali durability of Nakashima's SiO_2-ZrO_2 glass is shown in Figure 2.21. Clearly, glass composition H is 8-10 times superior to composition A (which contains no ZrO_2). Although the composition used by Nakashima differ from that of Euguchi et al. [8], but both of the study confirmed that CaO is the key factor in retaining ZrO_2 content in the resulting porous glass.

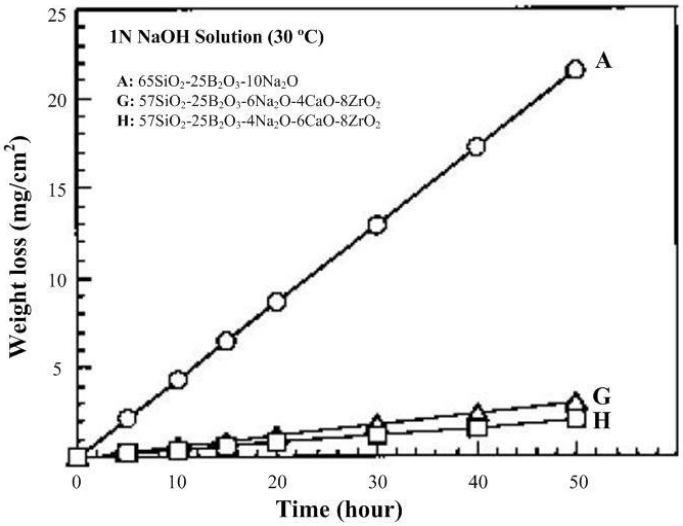

Figure 2.21: Relationship between weight loss and leaching time for various examples of porous glasses heat-treated at 700 ºC for 15 h [6].

More recently (2010), Kukizaki [48] investigated the influence of ZrO_2 addition in Na_2O-CaO-Al_2O_3-B_2O_3-SiO_2 glass for large scale production of alkali-resistant Shirasu porous glass (SPG). The composition used was 51.7SiO_2-17.3B_2O_3-6.6Na_2O-19.6CaO-4.8Al_2O_3 (mol%) where 1–5 mol% of ZrO_2 was added. The alkali resistance of the SPG membrane containing 3.5 mol% of ZrO_2 was found to be about 3.5 times higher than the ZrO_2-free membrane and much higher than the Vycor ™ (see Figure 2.22).

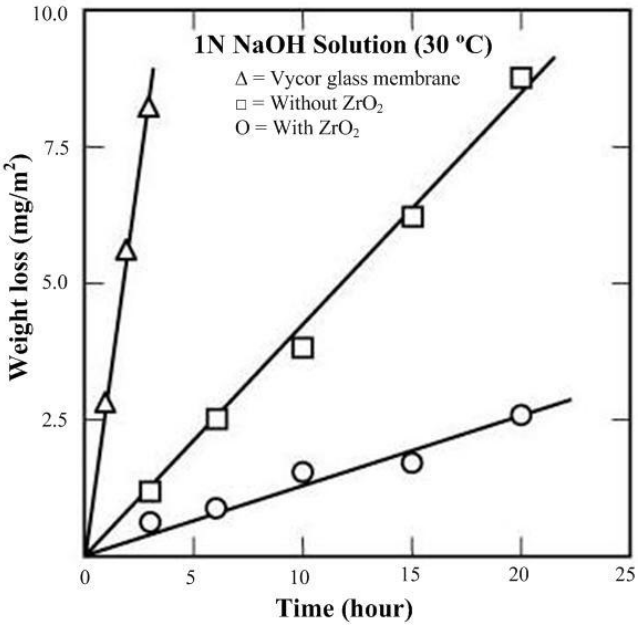

Figure 2.22: Alkali resistance of SPG membranes with leaching time [48].

2.8.2 Non-porous alkali-resistant glass

It is useful to consider non-porous glass systems that are designed specifically for alkali durability. One application area that requires such glass is the glass fibre industry. Glass fibres are used to reinforce cements, making them stronger. Different criteria apply to glasses used to make fibres [112]. Since they have to be drawn, parameters like viscosity and crystallisation suppression are critical. ZrO_2 is frequently added to silica-based glasses to impart alkali durability. This addition can be in large quantities since these glasses are not required to be porous and therefore do not need to undergo the APS process (which is hindered by large amounts of zirconia).

Kawamoto et al. [17] reported high-content ZrO_2 alkali-resistant glass. Typical wt% of ZrO_2 in the Kawamoto compositions range from 19.5 to 21.5 wt% and with the starting composition of 60.7 SiO_2, 20.5 ZrO_2, 1.5 Li_2O, 12.4 Na_2O, 2.4 K_2O, 0.5 MgO, and 2.0 wt% TiO_2 (wt%). In a very stringent alkali resistance test conditions (i.e.: 10% NaOH, 80 °C for 16 hours), the % weight loss recorded was 0.45 to 0.60. Clearly, this composition exhibits excellent alkali resistance.

In older glass fibre work by Mohri [113] a typical composition was 58% SiO_2, 21% ZrO_2, 16.5% Na_2O, and 3% ZnO (wt%). In an alkali resistance test: 1 N NaOH solution kept at 70ºC for 90 minutes, wt% loss was 0.04, so clearly this is also a very alkali-resistant glass composition. Kawamoto et al. [17] used TiO_2 in their composition to lower the viscosity and suppress crystallisation, which is a clear advantage over Mohri's older approach.

In 2010, a detailed investigation of the influence of IVB elements (Ti, Zr, and Hf) on chemical durability of soda lime borosilicate glasses was made by Bergeron et al. [114]. The glasses were obtained from $18Na_2O$-$17B_2O_3$-$61Si_2O$-4CaO (mol%) glass composition by replacing SiO_2 with ZrO_2, TiO_2, and HfO_2. A further replacement of Na_2O by CaO was also made and found to be effective in long term durability. They found that the initial dissolution rate decreases significantly with increasing ZrO_2 and HfO_2 bearing glasses, where TiO_2 has a lower effect on glass dissolution rate compared to glasses containing Zr and Hf.

2.9 PORE CHARACTERISATION TECHNIQUES

Of most interest as regards porous structure is their internal geometry, size, and connectivity. The performance of any porous glass highly dependents on their internal pore structure, rather than on the external surface. Different characterisation techniques have been described in detail in the literature [115-122]. The purpose of each characterisation is to characterise the pore size, their distribution, shape, accessibility, and surface area. The most popular pore characterisation techniques, such as using mercury porosimetry and nitrogen gas adsorption, are discussed in the following sections.

2.9.1 Mercury porosimetry

2.9.1.1 Theory

The pore characteristics of a porous solid material can be determined by using mercury intrusion porosimetry (MIP). The popularity of mercury porosimetry over other measurement methods is due to the short time it takes. In a single measurement it can quantify the pore opening size, size range, pore volume, surface area, bulk and apparent density as well as other porosity-related characteristics of a material.

Mercury (Hg) is widely used in pore characteristics due to its non-wetting behaviour combined with its high surface tension. Mercury does not penetrate pores by capillary action. It requires force to enter the pore spaces. Mercury also exhibits a high contact angle against most solids (see Figure 2.23) with ranges from 112° to 142° [115, 123, 124]. For mercury on glass material, contact angles of 128° to 148° have been identified [125]. The pressure that is required to make mercury entering the space is inversely proportional to the pore opening size, and this can be used in determining the pore diameter. When the force that is applied is resisted from entering the pore, then it is equal to $-\pi D\gamma \cos\theta$, where D is the pore diameter, γ the surface tension and θ the contact angle. The negative sign is due to the fact that $\theta > 90$ which makes the term intrinsically negative. The applied pressure acting over the circle of contact can be expressed mathematically by $\pi D^2 P/4$, where P is the

applied pressure. At equilibrium where the opposite forces equal can be expressed as:

$$-\pi D\gamma \cos\theta = \frac{\pi D^2 P}{4}$$

After rearranging,

$$D = \frac{-4\gamma\cos\theta}{P} \qquad \text{Equation 2.3}$$

The above equation is known as the Washburn equation and is used for calculating pore diameter, with the equation being based on the behaviour of a non-wetting liquid.

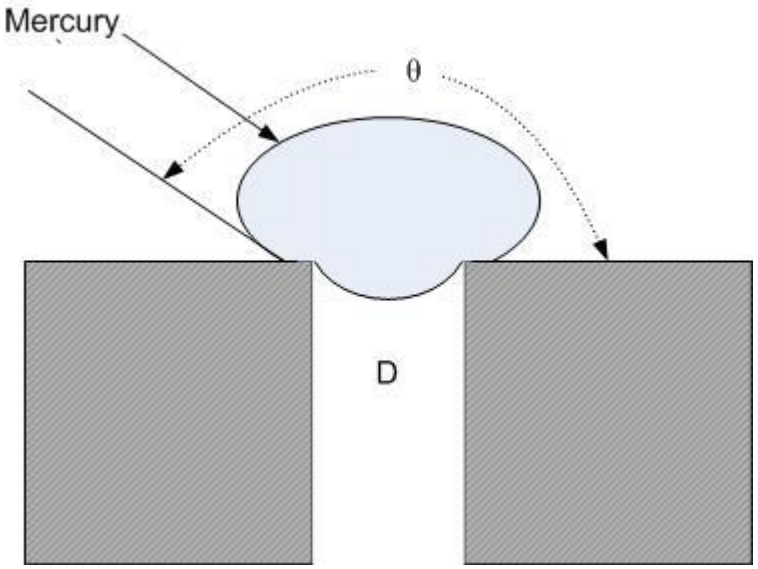

Figure 2.23: Mercury in contact with a porous solid (modified from [115]).

2.9.1.2 Pore size and total pore volume

Intrusion pressure values are directly converted into pore size by using the Washburn equation. The scanning speed that can be achieved during measurements using high-pressure porosimetry depends on the pore size of the sample, as small pore sizes can not be determined using fast scanning [115, 120]. Total pore volume, on the other hand, is the total volume of mercury intruded at the maximum pressure applied and

therefore does not require the Washburn equation. Dividing the total pore volume by mass of the sample gives total specific pore volume. Median pore diameter is at the 50 percentile point on any volume, area, or length distribution curve, whereas mean pore diameter depends on the model and is equal to 4V/A, where V represents pore volume and A the surface area. It is assumed that the model is cylindrical in shape and the pores are open at both ends [120, 126].

2.9.1.3 Density and porosity measurement

The bulk density, also known as envelope density, and the apparent density of a sample can also be measured by using mercury porosimetry. The bulk density can be determined by using a simple pycnometry-type calculation. The object's volume is determined by subtracting the volume of mercury in the sample from the total volume and weight of the sample, which can be measured with a laboratory balance. Being a non-wetting liquid, mercury does not enter small indentation, cracks and voids on the surface or into the pores. Whereas, the skeletal density that includes closed and inaccessible pores can be determined after maximum pressure is applied. The volume of mercury intruded into the open pores at high pressure, subtracted from the bulk volume of the sample gives the skeletal volume. Dividing the weight of the sample by this skeletal volume gives the skeletal (absolute) density. The volume measured is considered as true volume provided that the sample contains no blind pores and all pore spaces are filled [127]. If the sample contains pores that are smaller than the accessible limit at maximum pressure, then skeletal and true volumes cannot be obtained accurately. Use of helium pycnometer is recommended if the proportion of pores below the range of high pressure mercury porosimeter is significant.

The percentage porosity of a sample can be determined by using the following equation [115]:

$$\text{Percentage porosity, } \varepsilon = \left(1 - \frac{\rho_b}{\rho_s}\right) \times 100 \qquad \text{Equation 2.4}$$

Where, ρ_b is the bulk density and ρ_s is the skeletal density. In some studies true density measured by means of helium pycnometer is used instead of skeletal density [120, 123]. Paul A. Webb [127] proposed another simple equation to measure porosity which is:

$$\text{Mercury intrusion porosity, } \varepsilon = \left(\frac{V_T}{V_B}\right) \text{ x } 100\%. \qquad \text{Equation 2.5}$$

Where V_T is the total volume of mercury intruded up to the maximum pressure and V_B is the bulk volume. Kukizaki [48] in his study measured membrane porosity by using the following equation:

$$\text{Porosity, } \varepsilon = \frac{V_p}{V_p + (1/\rho_H)} \qquad \text{Equation 2.6}$$

Where V_P is the pore volume per unit sample mass that is determined by mercury porosimeter. And, ρ_H is the true density of the sample measured by helium pycnometer.

2.9.1.4 Pore size distribution

The accuracy of pore size and distribution measurements by means of mercury porosimetry depends largely on the actual pore size, shape, and their accessibility from the surface [128]. It is rare to encounter circular cross-sections of pores, or pores that have a regular geometric shape. Pores are typically variable in shape, e.g. slits, cracks, fissures, or highly irregular interstitial voids between particles. To make the pore characterisation calculation manageable, the convenient way is to consider complex pore shapes as a right cylinder and their opening as circular in cross-section [115]. The applied pressure continuously increased in magnitude, and the corresponding mercury volume intruded into the pores, provide the basic data for pore size distribution. A typical pore size distribution of silica is shown in Figure 2.24, where the intrusion contact angle (θ_I) and the extrusion contact angle (θ_E) are the same (140°). There is a hysteresis gap observed essentially in all mercury porosimetric measurements. Several explanations have been proposed in relation to

this hysteresis gap, among which three explanations are appeared to be favoured by different groups in the literature: (i) contact angle hysteresis, (ii) the ink bottle theory and (iii) network effect.

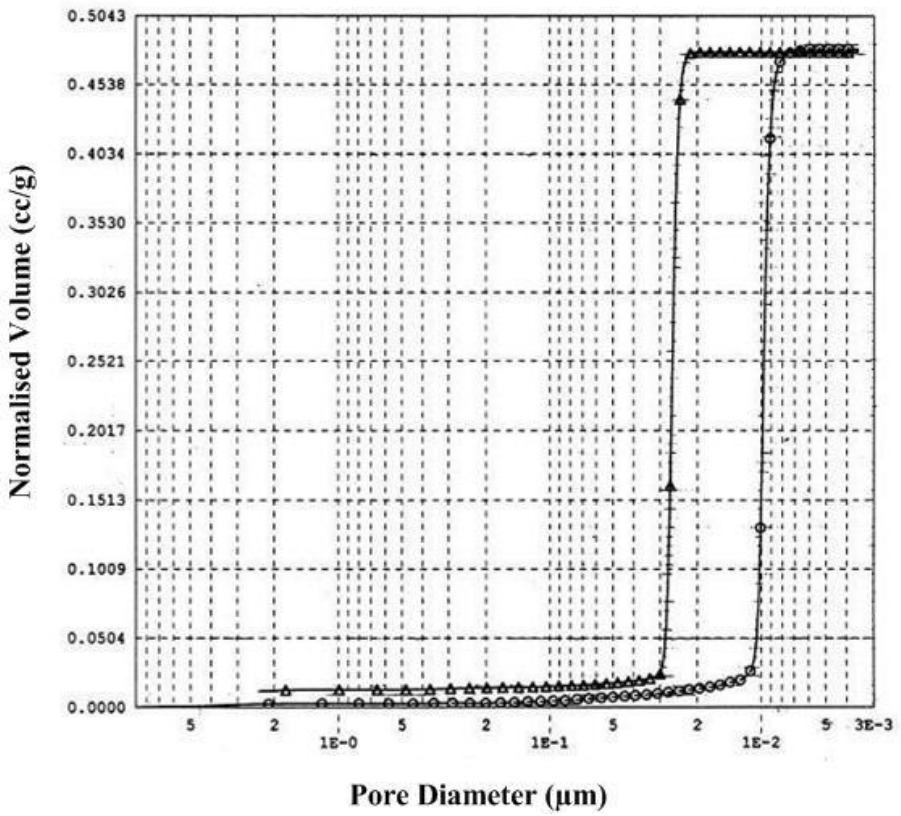

Figure 2.24: Standard mercury intrusion/extrusion volumes, as a function of pore sizes of silica calculated using a constant contact angle of ($\theta_I = \theta_E$) 140° [123].

(i) Contact angle hysteresis

Detailed studies have already been made on the contact angle effect on the mercury intrusion and extrusion gap, but no solid conclusion has as yet been reached [118, 122, 129]. During the extrusion stage, mercury is not fully expelled due to the difference in receding and advancing contact angle [115]. This argument was confirmed by a number of studies where the hysteresis gap is almost eliminated by modifying the extrusion contact angle [123]. Usually the retraction angles are 20 to 40° less than the advancing ones [115, 130]. Surface roughness and impurities on the sample or on the surface of the mercury can also be a reason for different values of contact angle during the intrusion and extrusion stage [118]. Porcheron et al. [122] investigated the relationship between entrapment and hysteresis. They performed an additional intrusion/extrusion cycle immediately after the first one so that the second

cycle begins with the mercury already entrapped in the pores. They found the hysteresis loop to be present in the second cycle without additional entrapment which indicates the different origin between hysteresis and entrapment. One possible explanation could be that the entrapped mercury represents only 10% of the total pore volume, which does not change the overall character of the pore network.

(ii) Ink bottle theory

The pores in a sample are not all the same shape. Those pores that have cylindrical symmetry, but with a neck narrower than inner cavity, are known as *ink-bottle*. During intrusion, the larger cavity inside cannot be filled until the higher pressure is reached which is required to fill the smaller entrance or neck. Therefore the filling pressure for these *ink-bottle* shaped pores is determined by their smaller sized neck and not by their actual size. At higher pressures when both the neck pore and the larger cavity are filled with mercury, the total volume is attributed to the diameter of the smaller neck of the pore. During extrusion when pressure is decreased, only the space ahead of the neck empties, leaving the mercury trapped in the larger cavity behind it (see Figure 2.25). However, surface tension allows mercury to be withdrawn by a connecting column of mercury, if the neck and cavity are near equal in size [115]. Thus, while the ink-bottle theory is clearly able to explain the reason behind the hysteresis gap as being due to the trapped mercury, but is unable to explain the size shift between intrusion and extrusion.

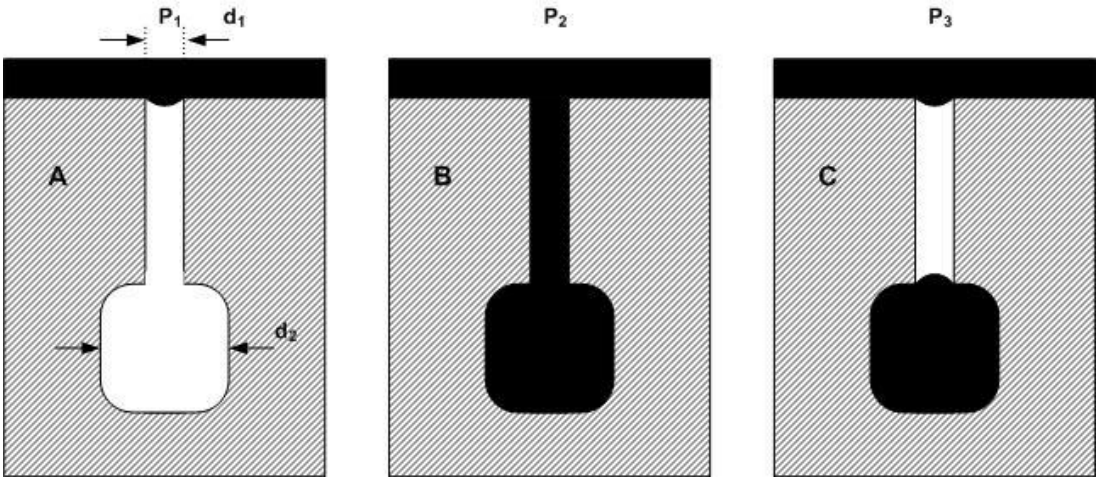

Figure 2.25: Mercury intrusion at pressure P_2 through a smaller opening (d_1) into larger diameter (d_2) cavity. Total intrusion volume is associated with pore diameter d_1.Extrusion at P_3 leaves mercury trapped in the cavity. Mercury remains trapped even when $P_3 < P_1$ [115].

(iii) Pore network effect

The connectivity model is used to explain the network effect of pores in relation to the hysteresis gap. As explained in the ink-bottle theory, a pore will fill with mercury when the applied pressure is equal or larger than the pore-size. It also requires a continuous path, so that mercury can follow the channel to the pore. Applied pressure is determined by the opening diameter, when the larger voids are surrounded by smaller openings. The reverse process occurs during the extrusion process and the mercury remains trapped once the connecting column to the surface breaks down. Therefore, intrusion of mercury into a cavity is controlled by pore opening diameter while the pore connectivity/network controls the extrusion of mercury from the cavity [127]. Salmas and Androutsopoulos [130] worked with different models and explained hysteresis based on the combined effect of the pore network and contact angle variation.

2.9.1.5 Advantages and limitations of mercury porosimetry

Mercury porosimetry is an extremely useful pore characterisation technique, in which the measurement covers a wide size range in pores, from 500 µm down to 3.5 nm, in a single analysis that usually takes between 30 to 45 minutes [115, 118]. The derived values for pore size and pore volume measured by means of mercury porosimetry are repeatable to better than 1% standard deviation, and the data are in significant agreement with the results obtained by other methods [131]. Varying contact angles of mercury and solid samples during the intrusion and extrusion stage, entrapped mercury due to *ink-bottle* pores, and the pore connectivity effect (already discussed in details in above sections), all need to be considered when interpreting MIP results. Due to the fact that mercury porosimetry measures the largest connection from the sample surface to the pore, it fails to measure the internal pore size. This is the reason why mercury porosimetry shows smaller pore sizes when compared with Scanning Electron Microscopy (SEM) [118]. However, total pore volume and pore surface area results are not dependent on pore shape [127]. Samples with a high surface area may require pre-treatment with heat and vacuum to drive of air/water vapour that occupy small pores and prevent the mercury from entering even at high pressure [115]. Diamond [128] in his study with a cement-based material

found the air voids, which constituted a minor but significant portion of the total pore volume, were mistakenly identified as small voids and were not intruded by mercury until a threshold pressure was reached. These voids were thus considered as pores in the size rage below the threshold diameter. A loosely packed powder might become further packed under pressure and the mercury intruded into the pore voids might be interpreted as porosity [118, 123]. The purity of already-used mercury also influences the results, as contamination causes change in the contact angle between the mercury and the sample [115].

2.9.2 Other methods for meso to macropore characterisation

Gas adsorption is another pore characterisation technique that can measure pores from 300 nm down to 0.3 nm [115]. Nitrogen is usually considered as a standard adsorptive for pore characterisation by means of the gas adsorption method. With nitrogen adsorption, pores with diameter ranging from 3–200 nm can be recorded [120]. For measuring microporosity, Nitrogen adsorption is not considered satisfactory for quantitative assessment. Alternative gas pore molecules, e.g.: argon and carbon dioxide, have been suggested for characterisation of microporous material [132]. However, for textural analysis of macroporous material (pore width > 50 nm), mercury porosimetry is considered as the most useful and reliable [133]. Due to concern about health issues while using mercury in recent years, other non-wetting metals that are liquids at room temperature are being considered in order to replace mercury in the useful intrusion porosimetry technique. A few possible replacements of liquid metals and alloys are Gallium, Indium, Galinstan, Wood's metal, and Fields metal. Unfortunately none of the alternative pure metal and alloys are as suitable as mercury in porosimetry [133]. Other methods are discussed in details by Rouquerol et al.; from which two popular methods are summarised below [133]:

(i) Water intrusion-extrusion for hydrophobic material

This type of intrusion-extrusion method is used primarily for hydrophobic materials in the mesopore range of 2–50 nm. This can also be extended to the macropore range. Sample preparation is the major challenge with this method, as it required

grafting of hydrophobic function in order to get a hydrophobic surface with a known contact angle with water.

(ii) Liquid porosimetry by wetting

Wetting-liquid porosimetry is the opposite of mercury porosimetry where the sample is completely wetted by overpressure of air. The assessment range is limited to 10–100 µm of pore sizes.

Methods other than liquid intrusion-extrusion are liquid permeametry, capillary condensation, freezing-melting detected by Differential Scanning Calorimetry (DSC), and Nuclear Magnetic Resonance (NMR). Imaging methods such as magnetic resonance imaging, computerised X-ray tomography, and electron microscopy are also used to visualise pore sizes.

2.9.3 Surface area determination

Specific surface area is defined by IUPAC [37] as "*The accessible (or detectable) area of solid surface per unit mass of a material.*" Measurement of surface area depends on the method and experimental conditions, and is influenced by particle size, particle geometry, and particle porosity. The importance of surface area is so pronounced that it is almost as important as the chemical composition of the material. Surface area is one of the key parameters in porous material characterisation and is especially important in applications where high specific surface area is a requirement. No single experimental technique provides an absolute measure of surface area due to the complex nature of mesoporous materials [132]. Surface area can be determined by both mercury porosimetry and gas adsorption methods. Nitrogen adsorption is mostly used to calculate specific surface area using Brunauer-Emmett-Teller (BET) equation. Both methods are briefly discussed in the following sub-sections.

2.9.3.1 Using mercury porosimetry

As discussed earlier in the mercury porosimetry section, the Washburn model is based on capillary forces acting on pores that are cylindrical in shape with a circular

opening. The total cumulative pore volume represents the total volume intruded into the pores against the maximum applied pressure. The surface area of all pores and voids filled up at pressure *P* can be calculated using the following equations [134]:

$$-2\pi rl\gamma\left|\cos\theta\right| = P\Delta V \qquad \text{Equation 2.7}$$

Where, *P* is the pressure, *V* is the intruded mercury volume, γ is the surface tension, θ is the contact angle of mercury.

Assuming cylindrical pores openings at each end, and recognising $2\pi rl$ as the pore surface area *S*, this gives

$$-S\gamma\left|\cos\theta\right| = P\Delta V \qquad \text{Equation 2.8}$$

Pores of radius *dr* that takes up volume *dV*, will exhibit a surface area, *dS*, which leads to

$$dS = \frac{PdV}{\gamma\left|\cos\theta\right|} \qquad \text{Equation 2.9}$$

Total pore surface area can be calculated by taking the cumulative area of pores that are filled by mercury and by integrating the above equation (assuming constant surface tension and contact angle) [120, 134]:

$$S = \frac{1}{\gamma\left|\cos\theta\right|}\int_0^V PdV \qquad \text{Equation 2.10}$$

Several publications [120, 121] have reported a good correlation between the surface area measured by mercury porosimetry and nitrogen adsorption in the overlapping pore size range. Large pores contribute relatively little to the measured surface area compared with the volume they represent, as opposed to porous material with small pores that have a greater surface area. On the other hand, surface area measured by nitrogen adsorption shows a greater surface area than the same porous material if it has significant numbers of pores below the range of mercury porosimetry. Thus it is

best to compare the two techniques within the overlapping portion of their range, e.g. 3 to 300 nm [115].

2.9.3.2 Using gas adsorption

Gas adsorption on solid surfaces and in pore walls is a complex phenomenon that involves mass and energy interaction and phase changes [115]. When a solid is exposed to a gas, the gas molecules impinge upon the solid and may adhere to the surface for a finite time. This phenomenon is termed adsorption, which is defined as a concentration of gas at an interface with a solid, without actual penetration of the gas into the solid [135]. The amount adsorbed depends on the nature of both the solid (adsorbent) and the gas (adsorbate), and on the pressure at which adsorption takes place [135]. Therefore one method that can be used (the volumetric method) involves calculating the amount of gas removed from the gas phase due to adsorption on the solid surface.

All adsorption processes can be divided into two categories of chemical and physical adsorption depending on the strength of the interaction. Chemical adsorption or chemisorption involves true chemical bonding of gas or vapour to the surface, and it needs to be restricted to, at most, a single layer of chemically bound adsorbate on the surface. With chemisorption, adsorbed molecules are localised on the surface, a property that often enables the number of active sites on catalysts to be determined by simply measuring the quantity of chemisorbed gas.

Reversible or physical adsorption exhibits characteristics that make it most suitable for surface area determination. This process is accompanied by low heats of adsorption with no violent or disruptive structural changes occurring to the surface during the adsorption measurement. The physical adsorption of gases on a solid surface increases with decreasing temperature and increasing pressure. Unlike chemisorption, physical adsorption may lead to surface coverage by more than one layer of adsorbate, meaning that pores can be filled by the adsorbate for pore volume measurement. As physical adsorption is fully reversible, both the adsorption and desorption processes can be studied. Physically adsorbed molecules are free to cover

the entire surface, enabling the surface areas rather than the number of sites to be calculated [136].

After Lowell [137], the amount adsorbed on a solid surface will depend on the absolute temperature *T*, the pressure *P*, and the interaction potential *E* between the vapour (adsorbate) and the surface (adsorbent). At a certain equilibrium pressure and temperature, the weight *W* of gas adsorbed on a unit of adsorbent is given by

$$W = F(P, T, E) \qquad \text{Equation 2.11}$$

If the quantity adsorbed is measured at a constant temperature, Equation 2.11 can be reduced to

$$W = F(P, E) \qquad \text{Equation 2.12}$$

If the temperature is below the critical temperature of the gas, the alternative form, i.e.: the equation below, is considered more useful.

$$W = F(P/P_0, E) \qquad \text{Equation 2.13}$$

Where P_0 is the saturated vapour pressure of the adsorbate. A plot of *W* (or volume adsorbed, *V*) versus P/P_0, at constant *T*, is referred to as the adsorption isotherm of a particular vapour-solid interface. The interaction potential *E* varies with the properties of the vapour and the solid and also changes with the extent of adsorption.

There are many theories [138] for surface area calculation but the one most commonly used is that of Brunauer, Emmet, and Teller [138], which is also known as BET method. The BET method is based on the calculation of monolayer capacity of a solid, W_m, which in turn can be used to calculate the specific surface of a solid. The monolayer capacity is defined as the amount of adsorbate that can be accommodated in a completely filled, single molecular layer (a monolayer) on the surface of unit mass of the solid.

The final form of the BET [137] equation is given below, where W is the weight adsorbed, W_m the monolayer weight, C a BET constant, P the adsorbate pressure, and P_0 the adsorbate saturated equilibrium vapour pressure.

$$\frac{1}{W[(P_0/P)-1]} = \frac{1}{W_m C} + \frac{C-1}{W_m C}\frac{P}{P_0} \qquad \text{Equation 2.14}$$

The determination of surface areas from the BET theory is a straightforward application of Equation 2.14. A plot of $1/W(P_0/P-1)$ versus P/P_0, will yield a straight line usually in the range $0.05 \leq P/P_0 \leq 0.35$ with slope s [137]:

$$s = \frac{C-1}{W_m C} \qquad \text{Equation 2.15}$$

And intercept, i

$$i = \frac{1}{W_m C} \qquad \text{Equation 2.16}$$

Solving the preceding equation for W_m gives

$$W_m = \frac{1}{s+i} \qquad \text{Equation 2.17}$$

Having established W_m, the sample's total surface area can be calculated from Equation 2.18.

$$S_t = \frac{W_m \overline{N} A}{\overline{M}} \qquad \text{Equation 2.18}$$

Where A is the cross-sectional area of a molecule of adsorbate, $\overline{M}$ is the molecular weight of an adsorbate molecule, and $\overline{N}$ is Avogadro's number. The specific surface area can be determined by dividing S_t by the sample weight.

CHAPTER THREE

EXPERIMENTAL PROCEDURE

3.1 GLASS SYNTHESIS

The basic sodium borosilicate glass used in this study contained three components: SiO_2, B_2O_3, and Na_2O. Zirconia (ZrO_2) or zircon ($ZrSiO_4$) was added to introduce ZrO_2/$ZrSiO_4$ into the glass. Calcium oxide (CaO) as $CaCO_3$ was also added in one glass composition to investigate the effect this would have on the properties of glass. The compositions of glasses that were produced in this study are listed in Table 3.1. Compositions of A and AA coincide with the metastable immiscibility dome of the SiO_2-B_2O_3-Na_2O system, and is the most well known system associated with Amorphous Phase Separation (APS) and the formation of an interconnected microstructure. When ZrO_2 was added to the SiO_2-B_2O_3-Na_2O system, the amount of alkali oxide (Na_2O) was varied between 6 wt% and 10 wt%. Compositions B to E involved substitution of SiO_2 with gradually increasing amounts of ZrO_2, while keeping the content of Na_2O at 10 wt%. Composition E-II, on the other hand, contained 6 wt% of Na_2O, and the ZrO_2 content was the same as in composition E. In compositions CC to EE, the addition of $ZrSiO_4$ was increased, while the amount of alkali oxide (Na_2O) was fixed at 6 wt%. Composition E-II was similar to composition EE, except the ZrO_2 was used instead of $ZrSiO_4$.

Special grades of SiO_2 (grade 18649), B_2O_3 (grade 11615), Na_2CO_3 (grade 223530), $CaCO_3$ (grade C6763), ZrO_2 (grade 230693), and $ZrSiO_4$ (grade 383287) were procured from Sigma-Aldrich, Ireland, for the preparation various types of glasses. For comparative purposes, two additional macro porous powder packings were procured. One was Controlled Pore Glass (CPG) of grade CPG 1000CL procured from Merck Millipore, Ireland, and the other was CHT ceramic hydroxyapatite type II which was procured from Bio-Rad Laboratories Ltd., UK.

All types of glasses were prepared by weighing out the appropriate quantities of glass reagents to make up batches of 500g. The glass components were mixed and rolled on a ball-mill for 14 hours. The mixed batches were melted in a zirconia crucible (Ref-TW78W, Almath Crucibles Ltd., UK) at 1450 °C for 2 h in a Carbolite RHF 1600 high temperature electric furnace (Carbolite Limited, UK) [78]. A one hour degassing plateau at 600 ºC and 1200 ºC was also carried out [33, 139]. Special care was taken during the melting of the alkaline earth metal oxide (CaO) containing glass F, where CaO was added as $CaCO_3$. It was found that eutectic mixtures of sodium and calcium carbonates, which melt at 775 °C, and sodium disilicate and silica, which melt at around 800 °C, become very fluid. In these temperature ranges the gasses develop rapidly which causes turbulence in the liquid and solid mixture. With increasing temperature the other refractory compounds started to melt and the release of the gasses decreased due to an increase of the viscosity of the mixture [24]. Therefore, to avoid spillage, a slow ramp (1 °C/min) was employed in the 800 °C–980 °C range, as in this temperature range the turbulence was severe. The melts were then water-quenched to produce frit. The glass frits were crushed and grounded in a ball mill for 12 hours. The resultant powder then screened through 212 µm and retained on a 45 µm sieve.

Table 3.1: Composition of Glasses in wt%.

	Composition (wt%)					
Glass	**SiO_2**	**B_2O_3**	**Na_2O**	**ZrO_2**	**$ZrSiO_4$**	**CaO**
A	65	25	10			
B	62	25	10	3		
C	58	25	10	7		
D	54	25	10	11		
E	50	25	10	15		
E-II	54	25	6	15		
AA	69	25	6			
CC	62	25	6		7	
DD	58	25	6		11	
EE	54	25	6		15	
F	50	25	4	15		6

3.2 PARTICLE SIZE ANALYSIS

A laser diffraction-based particle size analysis of the different compositions of the starting glasses were carried out using a Malvern Mastersizer S (Malvern Ltd., UK) covering a size range of 0.05 µm to 880 µm. Glass powders retained on a 45 µm sieve were used for the analysis. Each sample was prepared by adding glass powder to water, which was used as a dispersant medium, and the mixture was then put in an ultrasonic bath for five minutes. The mixture was then fed into the dispersant unit to measure the particle size. The integrated software (Mastersizer-S, Version 2.19) was used to convert the measurement results into a report containing the relevant data.

The distribution of the particles was characterised by the particle size dispersal coefficient, δ [140].

$$\delta = \frac{{}^{90}D_d - {}^{10}D_d}{{}^{50}D_d} \qquad \text{Equation 3.1}$$

where ${}^{90}D_d$, ${}^{10}D_d$ and ${}^{50}D_d$ are the diameters corresponding to 90, 10, and 50% (v/v) respectively on a relative cumulative size distribution curve. The particle size dispersal coefficient is also known as span.

3.3 THERMAL ANALYSIS

Differential Thermal Analysis (DTA) (Stanton Redcroft, UK) was used to measure the glass transition temperature (T_g) and to investigate the crystallisation behaviour of the glasses. Heating rates of 10, 15, and 20 °C/min were employed using 30 mg of sample and alumina as a reference.

Dilatometry (Model 402 E, Netzsch Ltd., Germany) was used to determine the dilatometric softening temperature (T_d), and the glass transition temperature (T_g), of a bulk glass specimen consisting of a nominal cylinder of approximate dimensions 11.5 mm (L) x 3 mm (D). The specimen was heated in air, increasing by 10 °C/min from room temperature to 1000 °C.

3.4 HEAT-TREATMENT OF GLASSES

Thermal treatment to induce phase separation was carried out on glass powder (>45 µm <212 µm particle size), using a horizontal tube furnace (Carbolite Ltd., Sheffield, UK) at a heating rate of 10 °C/min. The dwell temperature ranged from 630–700 °C and the dwell time was 14–63 h, depending on composition. The heat-treated glass samples were then ground to powders of certain sizes (45 – 355 µm range) by using a pestle and mortar for further characterisation and leaching purposes.

3.5 HEAT TREATED GLASS CHARACTERISATION

Figure 3.1 shows the characterisation techniques used for heat-treated glass samples. The heat-treated glasses were characterised by X-ray diffraction analysis (XRD) and Fourier Transform Infrared (FTIR) spectroscopy. XRD detects the phase change by comparing it with the phase identified after quenching. XRD analysis was also carried out to identify crystallisation if this occurred during heat-treatment. FTIR was used to get a more comprehensive insight into the intensity of the phase separation. Furthermore, FTIR also indicated if any crystallisation occurred during the heat-treatment cycle.

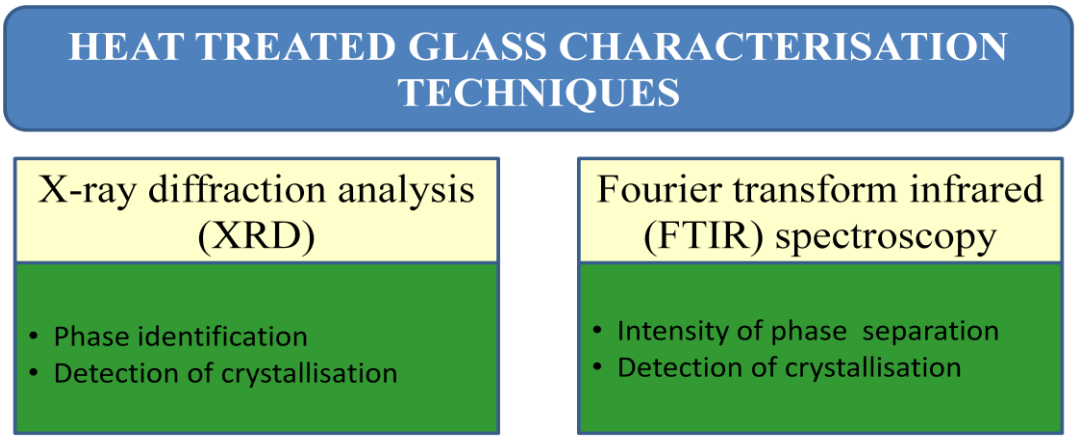

Figure 3.1: Outline of characterisation techniques for heat-treated glasses.

3.5.1 X-ray diffraction analysis (XRD)

Quenched and heat-treated glass powders of sizes < 45 µm were checked at room temperature by X-ray diffraction analysis to determine the crystallographic phases. A

Bruker advanced D8 X-ray diffractometer, using Ni-filtered Cu Kα radiation of wavelength 1.5406 Å, was used for this purpose.

The diffractometer has integrated XRD software (DIFFRAC plus XRD Commander, Version 2.6.0) that controls the power and scanning input parameters. The standard setting for the X-ray generator was 40 kV and 40 mA. The X-ray source is aligned to fall on the powder sample, which was positioned between the source and detector, through a slit of size 0.6 mm. A *Z*-scan was performed to position the sample at the correct height on the *Z* drive. A locked coupled scan was used to measure the XRD patterns with a step size of 0.1° in a range of 2θ values from 10 to 80° at a scanning speed of 10 sec/step. The X-ray diffraction pattern displays the intensity as a function of the detector angle, 2θ. A schematic diagram of the X-ray diffractometer is shown in Figure 3.2.

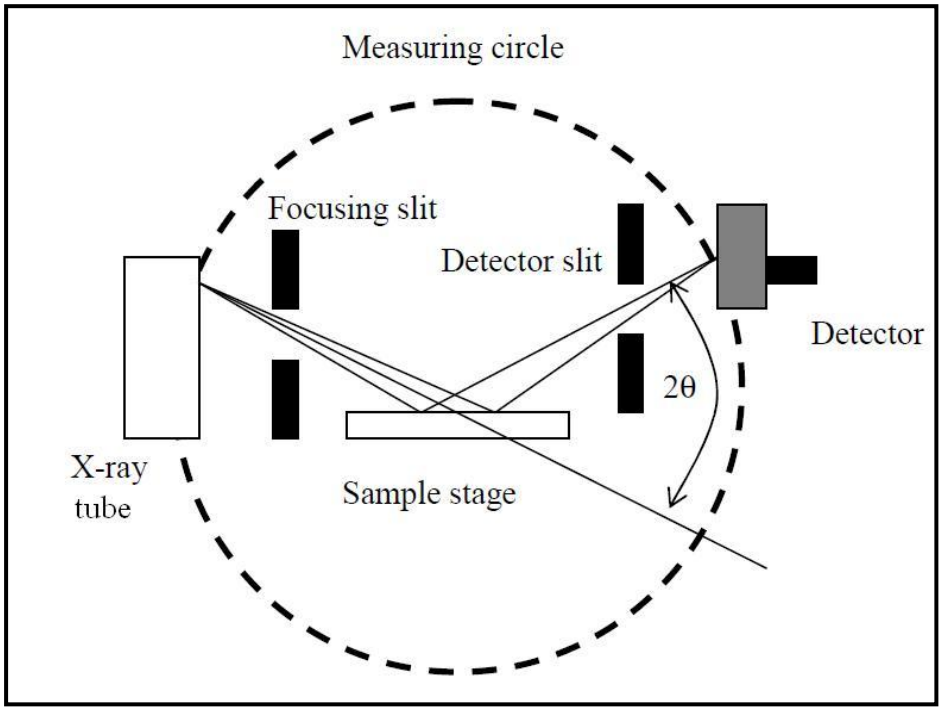

Figure 3.2: Schematic diagram of a powder X-ray diffractometer [141].

3.5.2 Fourier transform infrared (FTIR) spectroscopy

The infrared, IR, method was found to be a sensitive means to detect phase separation in glasses [142-144]. The basic components of the FTIR spectrometer are shown in Figure 3.3. The infrared source emits a broad band of radiation

wavelengths within the infrared zone that goes through an interferometer. The interferometer modulates the infrared radiation and allows it to pass through the sample where it is absorbed to various extents at different wavelengths. Finally, the intensity of the IR beam is detected by a detector and the detected signal is digitised and Fourier transformed by the software to get the IR spectrum of the sample.

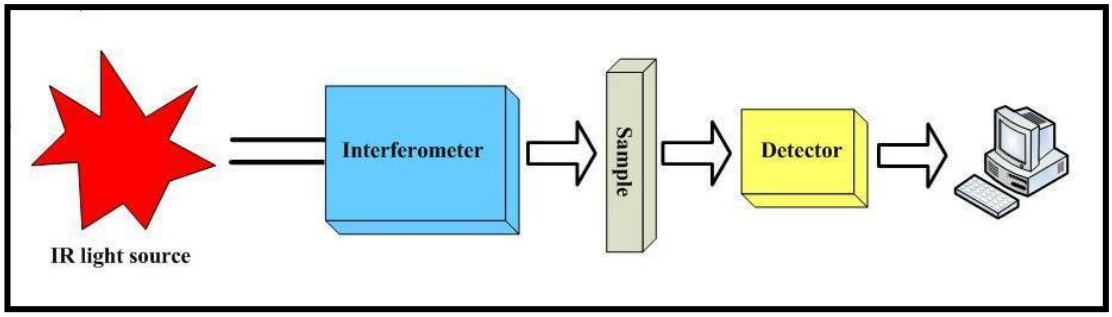

Figure 3.3: Block diagram of FTIR spectrometer.

FTIR spectra were obtained using a Perkin-Elmer GX instrument with a resolution of 16 cm^{-1} in the range 400 cm^{-1} to 4000 cm^{-1} at room temperature. Heat-treated glass samples of < 45 µm size were used for the FTIR investigation. The data points were averaged over 30 scans in absorbance mode and obtained at an interval of 1 cm^{-1}. A linear baseline was fitted to the corrected IR spectra and the peak positions were determined after a smoothening process using PE application spectrum software.

3.6 GLASS LEACHING

A heating bath, magnetic stirrer, and condenser were used to conduct the glass leaching experiments. The heat-treated glasses were crushed using a pestle and mortar, and sieved through 355 µm and retained on 75 µm sieve. The glass powder retained on 75 µm sieve was then immersed in 1 N HNO_3 for 24 h at 95-98 ºC to remove the boron phase, then in 3 N H_2SO_4 for 24 hour at 95-98 ºC to dissolve colloidal zirconia, and finally 0.5 N NaOH for 5 h at 25 ºC was used to wash out the gelated SiO_2. The H_2SO_4 leaching step was found to be unnecessary for $ZrO_2/ZrSiO_4$ free compositions. The leaching mentioned above was conducted in a flask equipped with a reflux condenser to prevent the acid solution from evaporating, and thus this allowed leaching to be carried out over a long time period. A magnetic stirrer was used to prevent the glass powder from settling on the bottom of the flask and to make

leaching more efficient. Deionised water was used to wash the glass powders several times after each acid leaching step. Following the leaching process, the resultant glass powders were washed with water several times and dried for 12 h at 120 °C.

3.7 LEACHED GLASS CHARACTERISATION TECHNIQUES

Figure 3.4 shows the characterisation techniques used for heat-treated glass samples. Mercury porosimetry was used to characterise the pore size, its distribution, total pore volume, surface area, and bulk and skeletal density. Nitrogen adsorption based pore characterisation was carried out with different selected leached glasses to compare the data with porosimetry. Scanning Electron Microscopy (SEM) is also widely considered to be a unique method to investigate the pore morphology. Energy Dispersive X-ray Spectroscopy (EDXS) was used for elemental analysis and made qualitative comparisons among the leached glasses.

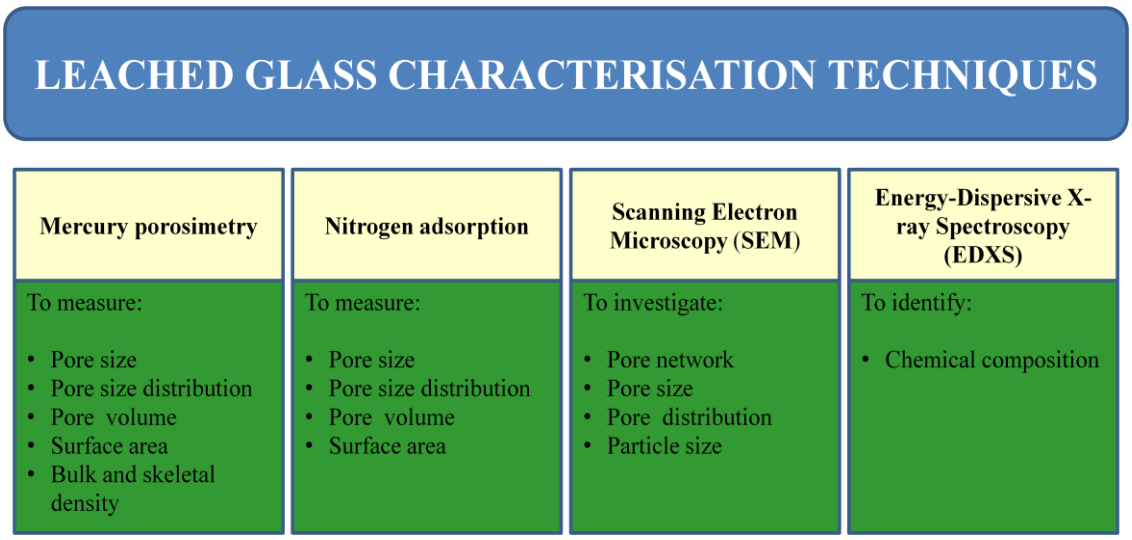

Figure 3.4: Outline of characterisation techniques for leached glasses.

3.7.1 Pore characterisation using mercury porosimetry

To characterise the pores of the leached glass compositions, experiments were performed, using mercury (Hg) based porosimetry (Autoscan-33 Porosimeter, Quantachrome, UK). Mercury intrusion and extrusion over a wide range of pressures (0-33000 PSIA) were performed. The porosimetry consists of two units – one is a

low pressure vessel for evacuation and preparing the sample, and the other is a high-pressure unit with maximum attainable pressure of 33,000 PSIA. Autoscan PORO2PC software, version 2.13, was used to analyse the recorded data.

Each leached glass sample was placed in the penetrometer (see Figure 3.5). After proper assembly, the penetrometer was placed in the low-pressure vessel for sample evacuation and mercury filling. The mercury was filled at around 100 kPa. The mercury used was procured from Sigma-Aldrich, Ireland (grade 261017).

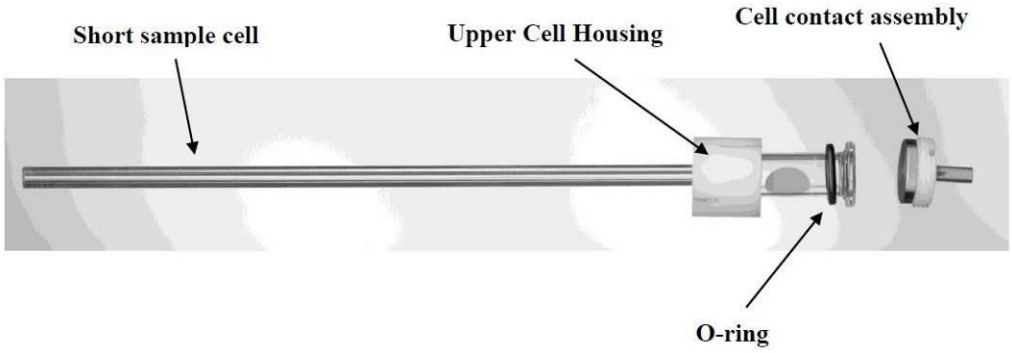

Figure 3.5: Penetrometer and closure components for short sample cell assembly [134].

The penetrometer with the filled mercury was then placed in the high-pressure vessel with the stem upward. The vertically installed penetrometer was surrounded by hydraulic fluid. The increasing pressure was transmitted by the fluid to the mercury in the penetrometer through its open capillary stem. When the pressure reached its maximum, reversing the hydraulic pressure then lowered the mercury pressure and generated the extrusion data. Both intrusion and extrusion data were recorded by the software and later converted for further analysis.

3.7.2 Pore characterisation by nitrogen adsorption

BET surface area, porosity, and average pore size of the selected leached glass samples were measured using a Nova 4200e surface area and pore size analyser using Nitrogen from Quantachrome Instruments (UK). The porous glass samples were prepared by drying under vacuum at 200 °C for 2 hours to remove adsorbed contaminants (especially water and carbon dioxide) which were acquired from

atmospheric exposure. The porous glass samples were then cooled to -196 °C under vacuum. Nitrogen was introduced to the samples in controlled increments and the quantities adsorbed were calculated. The quantity of gas required to form a monolayer on the external surface was identified from the adsorbed isotherm at a particular pressure and temperature. A further increase of gas pressure would form a multi layer coverage (see Figure 3.6). The specific surface area was calculated by using the BET equation (see Equation 3.2) at relative nitrogen pressure range 0.05–0.30 as the area covered by each adsorbed molecule is known.

$$S_{BET} = \frac{V_m \overline{N} A_m}{M_v} \qquad \text{Equation 3.2}$$

Where

V_m is the volume of the monolayer

A_m is the cross-sectional area occupied by each adsorbate molecule

$\overline{N}$ is Avogadro's number

M_v is the gram molecular volume

With increasing pressure, gas was first condensed on small pores (smallest diameter) and then continued until saturation pressure was reached, at which all pores are filled with liquid. The gas pressure was then reduced incrementally to allow evaporation of the condensed gas. The Kelvin equation (see Equation 3.3) was used to calculate the relative pressure of nitrogen in equilibrium with the porous glass. The pore size distribution was determined from the desorption data using the Barrett, Joyner, and Halenda (BJH) model [145]. A relative nitrogen pressure step, ranging from 0.98 to 0.37 was used.

$$ln\frac{P}{P_0} = -\frac{2\gamma V_L}{rRT}cos\theta \qquad \text{Equation 3.3}$$

Where

P is the equilibrium vapor pressure of a liquid in a pore of radius r

P_0 is the equilibrium pressure of the same liquid on a plain surface

γ is surface tension of the liquid

V_L is the molar volume of the liquid

θ is the contact angle with which the liquid meets the pore

R is the gas constant

T is the absolute temperature

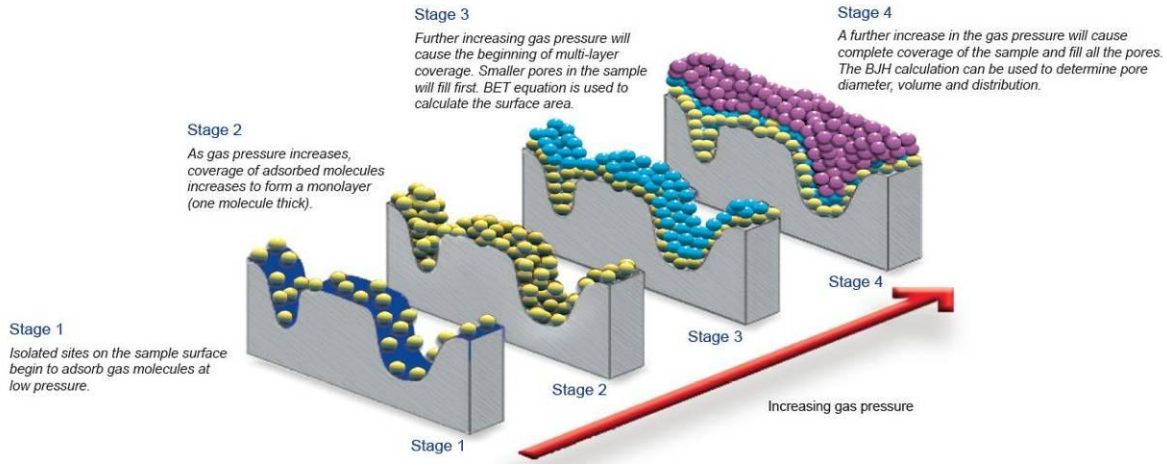

Figure 3.6: Gas adsorption data reduction methods [146].

3.7.3 Scanning Electron Microscopy (SEM)

The Scanning Electron Microscope (SEM) can generate various high magnification images by high-energy electron bombardment, which causes signals to be emitted from the surface of the sample. The intensities of the collected signals contain information about the sample's surface topography, and are used to produce images on the computer monitor.

The pore morphology of the leached glass samples was examined using an 'EVO LS 15' scanning electron microscope developed by Carl Zeiss, Germany. No prior coating was used.

3.7.4 Energy-Dispersive X-ray Spectroscopy (EDXS)

The SEM that was used was equipped with Energy-Dispersive X-ray Spectroscopy (EDXS), which can determine the elemental composition of the sample from X-ray spectra generated by high energy electron bombardment on the sample. EDXS is efficacious as a rapid method for identifying elements present in a sample with overall accuracy of about 1% and detection sensitivity down to 0.1% by weight [147].

The Oxford Instruments (Oxford INCA Energy 350) micro-analysis suit EDXS was used to detect the elements present on the leached glass samples, and analysed the data giving qualitative comparisons. The focusing distance was set at around 8.5 mm to allow the EDXS detector to collect the information from the sample surface. Rectangular acquisition with 180 sec live time in 0 – 10 KeV of spectrum range was used for the quantitative measurement. An acceleration voltage of 10 keV and beam current of around 100 pA was used for analysing of all leached glass samples. The integrated software (INCA suite, version 4.09) was used for quantification and identification of the spectrum, and it also processed the spectral data into MS word file format.

3.8 DENSITY MEASUREMENT BY PYCNOMETRY

A small volume helium pycnometer (Accupyc 1330, Micromeritics Ltd., UK) was used to measure the density of the leached glass samples at room temperature. Mean value and standard deviation was determined from five successive measurements.

3.9 ALKALI RESISTANCE TEST

The alkaline resistance of leached glass samples was determined from its resistance to aqueous solution of sodium hydroxide (NaOH) solution. The resistance was measured inversely from percentage loss in mass per unite surface area of the leached glass [109]. The alkali resistance was measured by incubating a 1 ml volume of leached glass sample in 10 ml of an aqueous sodium hydroxide solution (0.5 N) for 24 h. Following this, the leachant was neutralised with 1 N HCl acid and then washed in deionised water and dried at 100 °C for 18 h. After drying, each sample was weighed to an accuracy of 0.1 mg. The weight loss was then calculated in milligrams per square decimetre (mg/dm^2) by using the following equation [109]:

$$W_A = \frac{100 \times (m_1 - m_2)}{A} \qquad \text{Equation 3.4}$$

Where

m_1 is the initial mass, in milligrams, of the sample

m_2 is the final mass, in milligrams, of the sample

A is the total surface area, in square centimetres, of the sample

Two samples were tested for each composition of glass and the arithmetic mean of the values was used in measuring the weight loss. For each glass composition the experiment was repeated if the values differed by more than 10% from the arithmetic mean.

CHAPTER FOUR

RESULTS AND DISCUSSION

4.1 INTRODUCTION

An outline of the thermal behaviour study and characterisation of resultant porous glass after heat-treatment and leaching is presented in Figure 4.1. In this study, zircon and zirconia was added separately to the sodium borosilicate glass system. The thermal behaviour characteristics of a range of glass compositions were investigated thoroughly. The phase separation heat-treatment is the main determining factor that controls the formation of the desired pore size. Based on the thermal characteristics of different compositions, heat-treatment times and temperatures were optimised to achieve interconnecting porous morphologies. Another major challenge was to retain ZrO_2 in the porous glass as it plays a major role in increasing the alkali resistance of the porous glass. To achieve this objective, the primary consideration was to choose the most suitable sodium borosilicate glass composition which can phase separate readily and at the same time able to retain the ZrO_2 in the porous glass. ZrO_2 was added to the SiO_2-B_2O_3-Na_2O system, with the content of alkali oxide (Na_2O) varying between 6 wt% and 10 wt%. For addition of $ZrSiO_4$, the amount of alkali oxide (Na_2O) was fixed at 6 wt%. Higher alkali metal oxide (e.g. Na_2O) content in the glass composition is believed to increase the solubility of ZrO_2, and so does a higher CaO content [148]. On the other hand, considering the compositional effect, alkali metal oxide of 6 wt% is positioned in the optimum zone on the phase diagram of sodium borosilicate glass system for phase separation. Two commercial porous glass samples were also procured and characterised in order to carry out a comparison with the porous glasses prepared in this study.

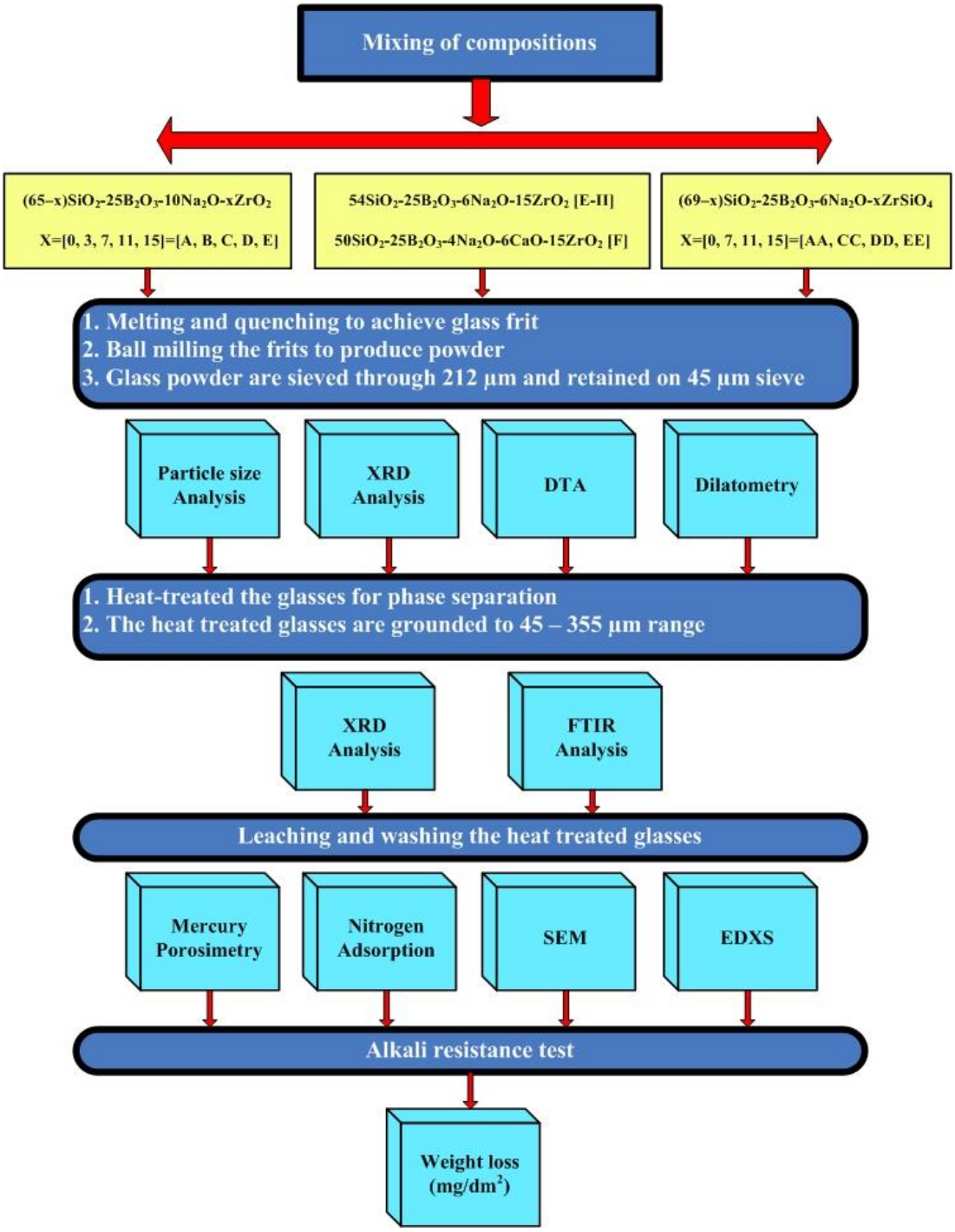

Figure 4.1: Outline of the order of results presented in this chapter.

4.2 PARTICLE SIZE ANALYSIS OF THE PARENTAL GLASS AND OF THE ZIRCON/ ZIRCONIA CONTAINING GLASS COMPOSITIONS

The glass frits produced after water quenching were ball milled for 12 h and screened through 212 µm and retained on a 45 µm sieve. The particle size of these glass powders were analysed by a light scattering particle size analyser to examine further details of particle size and its distribution. The results of the mean particle size (D[4,3]) and span analysis are summarised in Table 4.1. The span mentioned in Table 4.1 is a dimensionless number that illustrates whether the distribution spread is narrow or wide. The smaller the span, the narrower is the distribution. Even though the glass powders were retained on 45 µm sieve, the particle size analysis showed them to be smaller taking consideration of the mean size. From particle size distribution patterns, as shown in Figure 4.2 and Figure 4.3, it can also be noticed that particles were widely distributed, with a tendency towards particles with a larger diameter range. Glass F had the lowest mean particle size, with 41% below 14 µm in size. Glass DD and EE seemed to have a better particle size distribution compared to the other glass compositions.

Table 4.1: Mean particle size and size distribution measure of the glass powders after grinding and sieving.

Glass	Mean particle size µm	Span δ
A	19	5.36
B	57	10.1
C	121	5.77
D	41	9.89
E	61	8.58
E-II	27	3.52
AA	77	3.89
CC	23	5.40
DD	173	1.43
EE	102	2.06
F	11	3.31

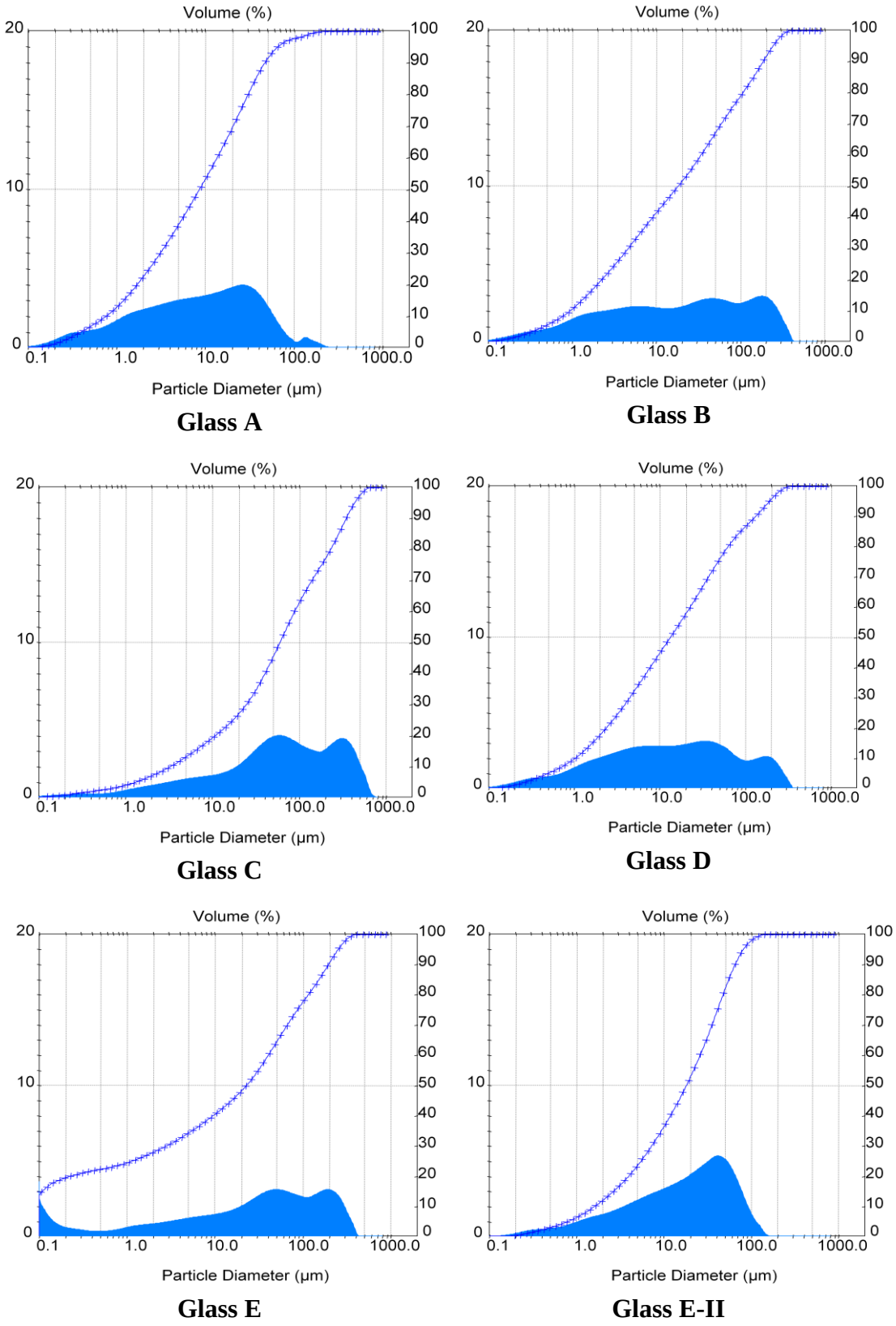

Figure 4.2: Particle size distribution pattern of glass A, B, C, D, E, and E-II.

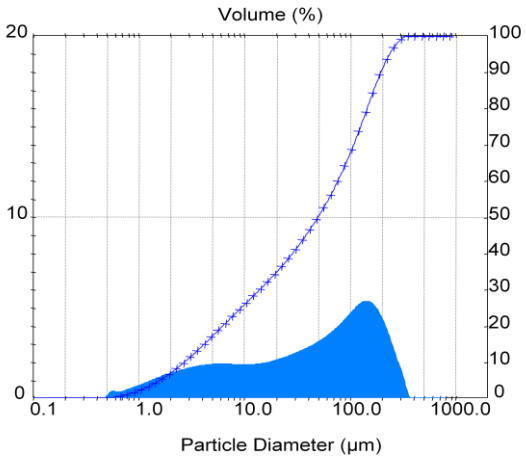

Glass AA

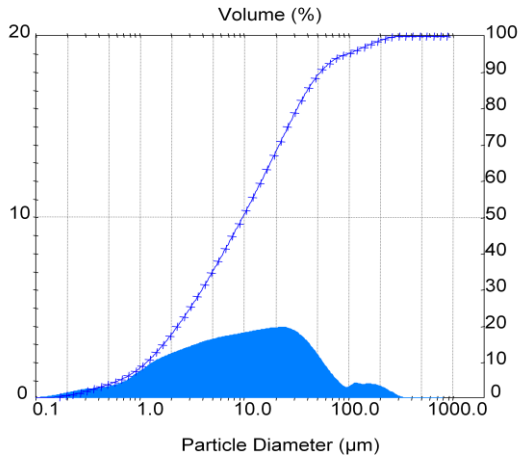

Glass CC

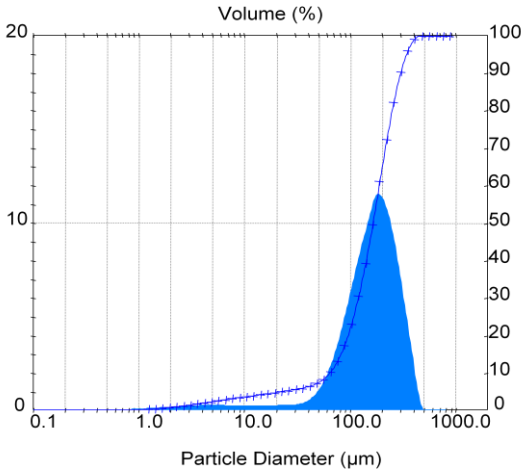

Glass DD

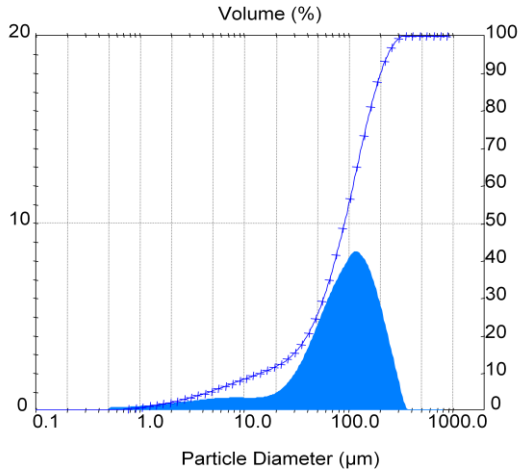

Glass EE

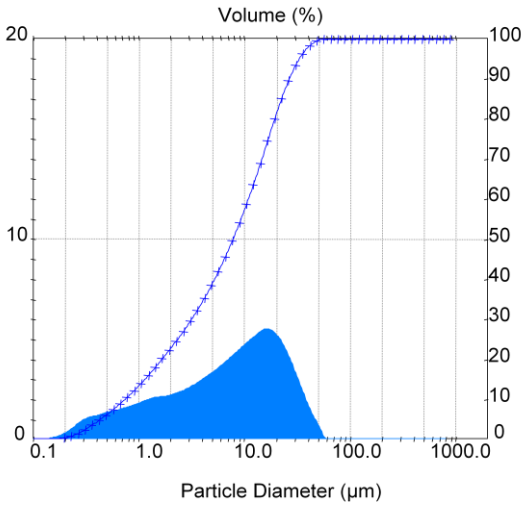

Glass F

Figure 4.3: Particle size distribution pattern of glass AA, CC, DD, EE, and F.

4.3 THERMAL PROPERTY OF THE GLASS COMPOSITIONS

4.3.1 XRD analysis

The glass frits of all compositions were found to be visually clear after water quenching. XRD analysis was performed on all glass compositions and the results are shown in Figure 4.4 and Figure 4.5. The peaks at 2θ = 21.8°, 28.5°, 31.3°, 36° [JCPDS 01-0438, 03-0267] were assigned for cristobalite; whereas peaks at 2θ =30°, 51°, 60° [JCPDS 02-0733] were assigned for tetragonal ZrO_2 [64]. In contrast to fully amorphous glass, a possible phase separation occurred during quenching which is revealed by the mesomorphic helical segments around 15.5° and 22.4° in Figure 4.4 and Figure 4.5. These broad peaks are more pronounced in the XRD analysis of glass series AA-EE (see Figure 4.5). The mesophase may act as a precursor to crystallization [149]. Yazawa et al. [44] in their study with similar sodium borosilicate system $9.4Na_2O$-$25.4B_2O_3$-$65.2SiO_2$ (mol%) found the glass phase separated by spinodal decomposition during quenching if the rate of cooling is between 10 to 10^6 K/sec.

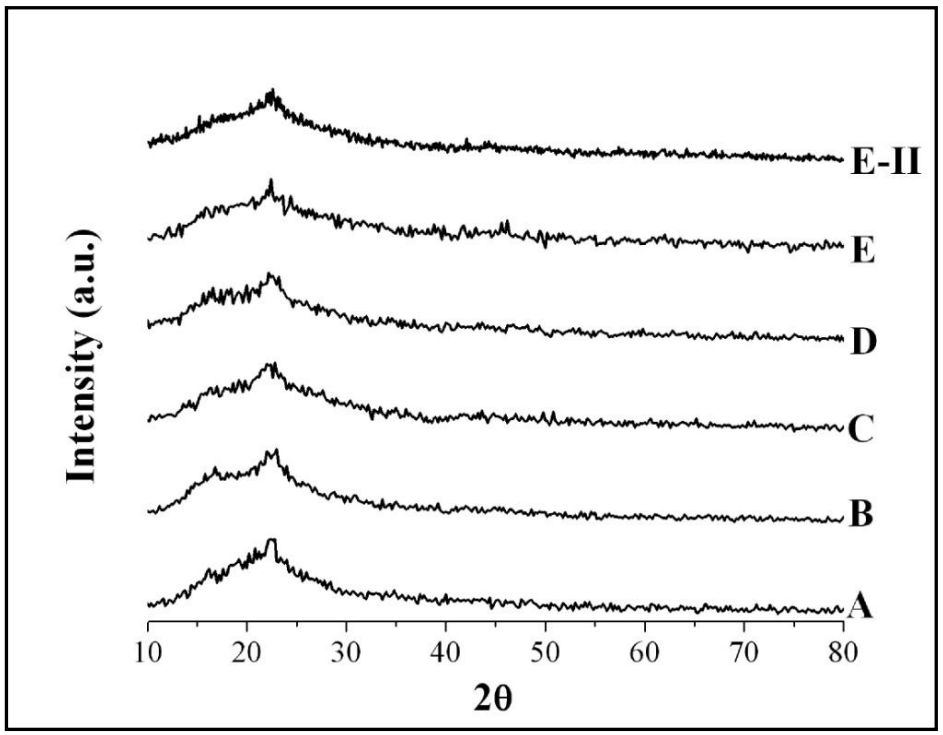

Figure 4.4: XRD patterns of glass composition A, B, C, D, E, and E-II before heat-treatment.

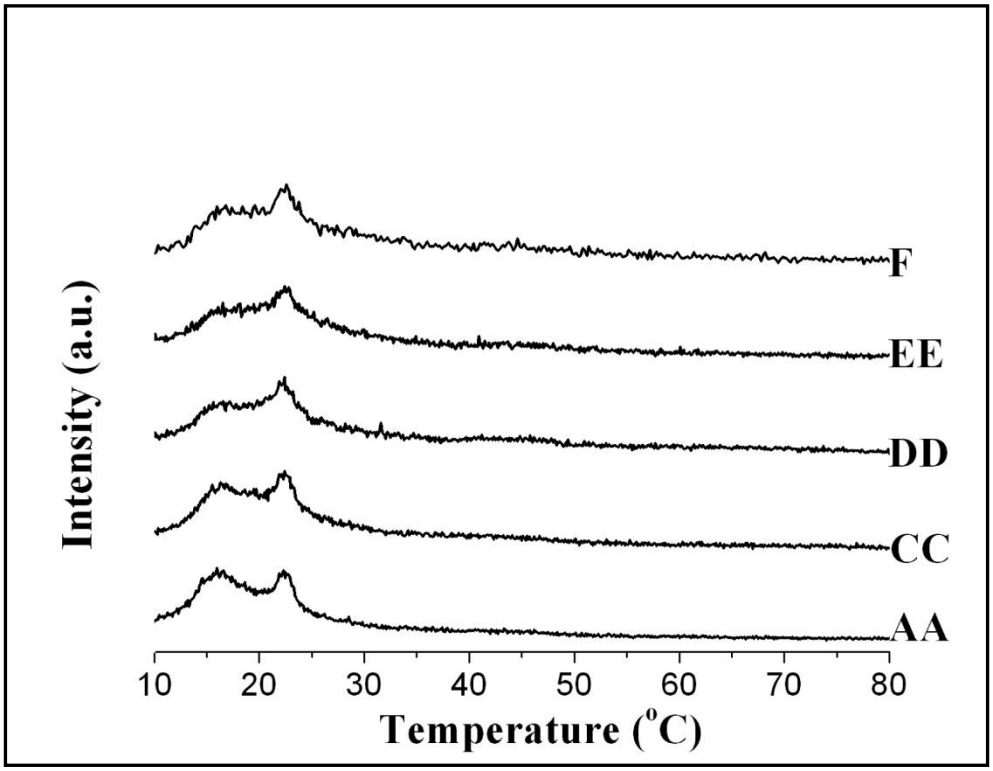

Figure 4.5: XRD patterns of glass of composition AA, CC, DD, EE, and F before heat-treatment.

4.3.2 DTA analysis

The results of the DTA analysis for all compositions are listed in Table 4.2 where T_f is denoted as the onset glass transition temperature (T_g), and T_m as the maximum of the endothermic inflection. T_f is generally accepted as T_g for most applications and in this study we considered T_f as T_g [69]. Some authors found that T_g depends on heating rate, and shifts towards a higher temperature with increased heating rate [24, 48, 150]. Dodd [151] argued that increasing heating rate decreases the resolution between the adjacent peaks, hence slower heating rates are preferable. In this study heating rates of 10, 15, and 20 °C/min were employed for all glass compositions to investigate the difference in thermal behaviour while keeping the sample size constant (30 mg). No significant changes were observed in T_g by increasing the heating rate for glass compositions as shown in Table 4.2. The DTA curves obtained from heating rates of 10, 15, and 20 °C/min of all glass compositions are shown in Appendix 1. It is evident that T_g increased incrementally with increasing ZrO_2 content from 515 °C to 522 °C for glass series A–E. A similar tendency was apparent for glass series AA–EE, where T_g increased from 478 °C to 509 °C with

increasing $ZrSiO_4$ content. Addition of ZrO_2 increased the number of bridging oxygens per silicon atom and the presence of Zr^{4+} ions imparted a higher packing density and higher T_g. This behaviour is consistent with the theory that ZrO_2 is believed to act both as an intermediate and a network glass former [152]. It can be seen from Table 4.2 that glass A, which contained more Na_2O (10 wt%) compared to AA (6 wt%), shows a higher T_g value. A similar trend is also observed when comparing glass E (10 wt% Na_2O, 15 wt% ZrO_2) and glass E-II (6 wt% Na_2O, 15 wt% ZrO_2), which differed in Na_2O content. In sodium silicate glasses, increasing the alkali content breaks up the three-dimensional network with the formation of singly-bonded oxygens that do not participates in the network, thus reducing the length of the chain. The principal effect of increased alkali content is to reduce the melting temperature by decreasing the viscosity, which would indicate a lower T_g. However, variations are observed for glass compositions containing B_2O_3, which is known as the boric oxide anomaly. Increasing alkali content in sodium borate glass compositions converts BO_3 triangles to BO_4 tetrahedra, thereby increasing the network connectivity. Therefore, the glass transition temperature increases. Non-bridging oxygen (NBO) sites do not become apparent until the alkali content is increased to approximately 30 mol% [31]. In other studies with borosilicate glass, it was mentioned that NBO is not produced in glasses with a Na_2O/B_2O_3 ratio <0.5 [66, 68]. The T_g of glass composition F was measured as 575 °C, which is significantly higher compared to other glass compositions. This huge shift in T_g can be attributed to the addition of 6 wt% of CaO, which replaced part of the alkali oxide (Na_2O) in glass E, and therefore the Na_2O content of glass F became 4 wt%. Replacement of alkali oxide (Na_2O) by alkaline earth oxide (CaO), while maintaining a constant silica concentration, strengthens the network by replacement of the low field strength sodium ion by the higher field strength divalent alkaline earth ions and thus increases the T_g [24]. Glass E-II (6 wt% Na_2O, 15 wt% ZrO_2) and EE (6 wt% Na_2O, 15 wt% $ZrSiO_4$) showed almost similar T_g values indicating that the presence of zircon or zirconia in the glass has a similar impact on T_g.

Table 4.2: DTA results in three different heating rates (10 °C/min, 15 °C/min, 20 °C/min).

Glass	10 °C/min		15 °C/min		20 °C/min	
	T_f	T_m	T_f	T_m	T_f	T_m
A	515	567	514	562	510	567
B	508	568	514	588	520	577
C	518	575	524	588	532	593
D	520	577	517	589	520	590
E	522	576	528	586	528	594
E-II	511	563	503	577	504	597
AA	478	520	472	522	468	522
CC	501	541	505	535	494	542
DD	504	548	513	556	518	570
EE	509	550	497	560	492	566
F	575	621	564	625	588	635

The DTA analysis for all glass compositions are discussed in the following sub-sections. The shape of the exothermic peak on DTA curve indicates whether bulk or surface crystallisation is predominant. Augis and Bennett [153] proposed an equation (see Equation 4.1) to calculate the Avrami parameter (*n*). This Avrami parameter is related to crystallisation behaviour and first described by Avrami [154-156]. A value of n close to 1 indicates surface crystallisation, and an *n* value greater than 3 indicates bulk crystallisation [157].

$$n = \left(\frac{2.5}{\Delta T}\right)\left(\frac{T_p^2}{E_c / R}\right) \qquad \text{Equation 4.1}$$

Where ΔT is the full width of the exothermic crystallisation peak taken at half of the maximum intensity; T_p is the peak crystallisation temperature; *Ec* is the activation energy for crystallisation; and *R* is the gas constant. Equation 4.1 indicates that a broad exothermic peak means a large ΔT value, which implies a small *n* value, resulting in surface crystallisation. On the other hand, a sharp peak corresponds to a small ΔT value, which implies a large *n* value, resulting in bulk crystallisation [24, 48].

4.3.2.1 Glass series A–E, $(65–x)SiO_2$-$25B_2O_3$-$10Na_2O$-$xZrO_2$

In this series of glass compositions, the content of ZrO_2 increased from 0 to 15 wt%. The objective of the thermal behaviour study of this group was to investigate the influence of ZrO_2 content while keeping the alkali oxide (10 wt%) and boron oxide (25 wt%) constant.

(i) Glass A ($65SiO_2$-$25B_2O_3$-$10Na_2O$)

The DTA curve of glass A at a heating rate of 10 °C/min is shown in Figure 4.6. The slope indicates an endothermic onset at around 515 °C. Two characteristic temperatures are used to define this endothermic gradient, which is attributed to the glass transformation range. T_f is denoted as the onset of the glass transformation temperature and T_m is the maximum of the endothermic inflection. An exothermic event is noticed at around 800 °C–900 °C which is possibly due to the crystallisation of cristobalite. No sharp exothermic peak was observed on the DTA curve of glass A at a heating rate of 10 °C/min, nor for heating rates of 15 and 20 °C/min (see Appendix 1a). Therefore, it is presumed that surface crystallisation is the dominant mechanism.

XRD analysis was carried out on glass A, as shown in Figure 4.7, to check for crystallisation when heat-treated for 14 h, 24 h, and 63 h at 650 °C. Peaks attributed to cristobalite at 2θ = 21.8°, 28.5°, 31.3°, 36° [JCPDS 01-0438, 03-0267] were identified for the sample heated at 650 °C for 14 h, 24 h, and 63 h. Cristobalite was just starting to precipitate when the sample was heat-treated for 14 h at 650 °C. The intensity of the cristobalite peak increased with increasing heat-treatment dwell time. However, no cristobalite peak was observed when heat-treatment was conducted at 600 °C for 48 h. For long heat-treatment, the crystallisation event, as shown in Figure 4.6, shifted and occurred at lower temperatures than 650 °C.

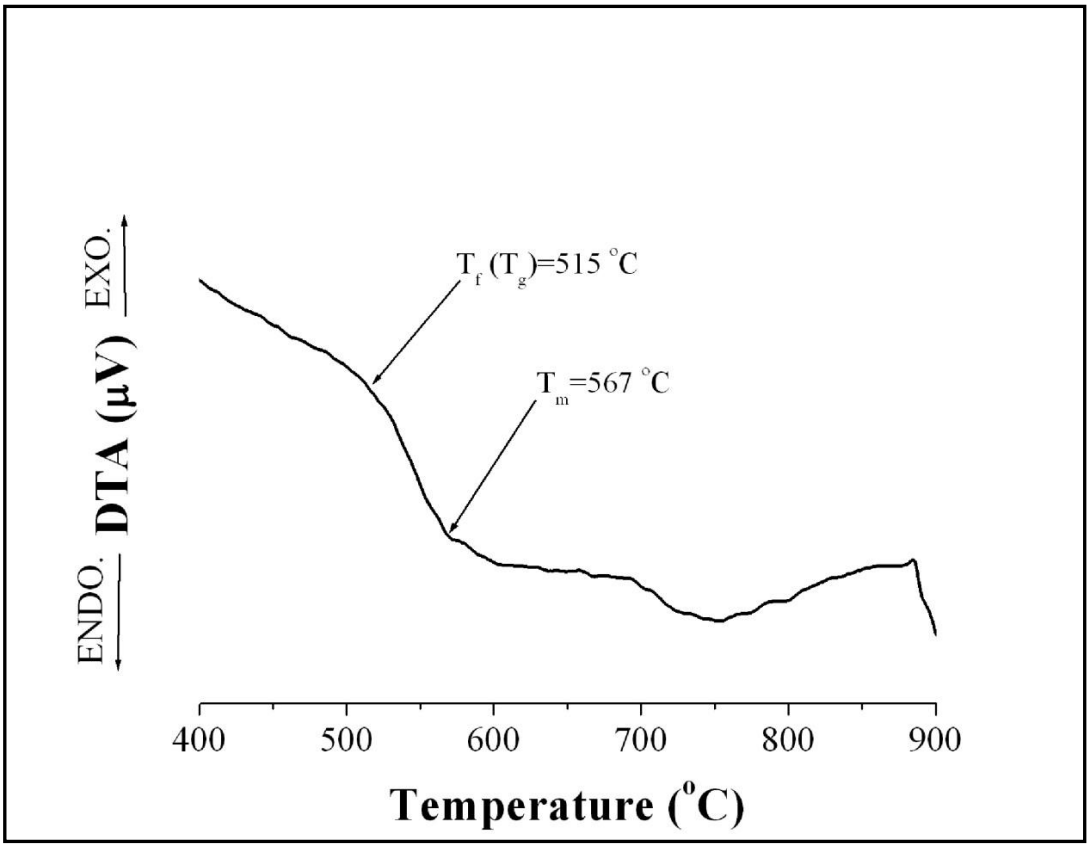

Figure 4.6: DTA curve of glass A at a heating rate of 10 °C/min.

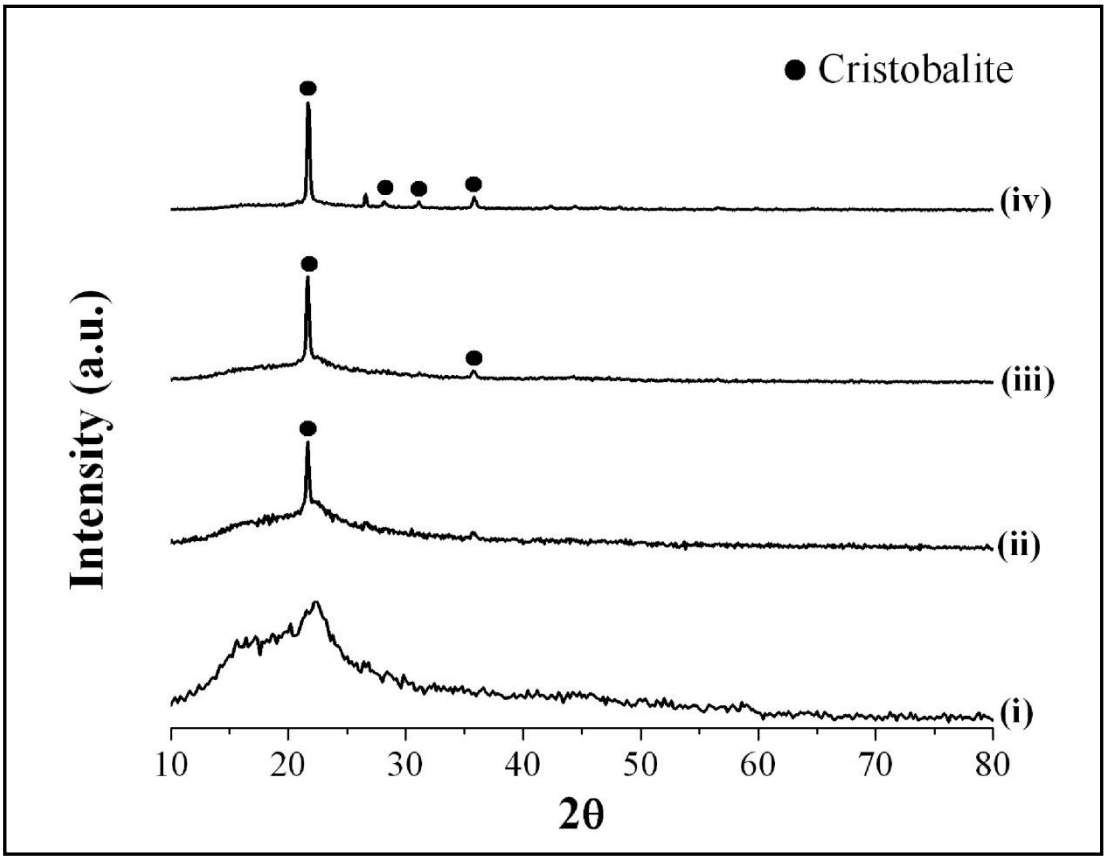

Figure 4.7: XRD patterns of glass A heat-treated for: (i) 48 h at 600 °C; (ii) 14 h at 650 °C; (iii) 24 h at 650 °C; (iv) 63 h at 650 °C.

(ii) Glass B, C, and D

The DTA curves of glass B ($62SiO_2$-$25B_2O_3$-$10Na_2O$-$3ZrO_2$), C ($58SiO_2$-$25B_2O_3$-$10Na_2O$-$7ZrO_2$), and D ($54SiO_2$-$25B_2O_3$-$10Na_2O$-$11ZrO_2$) are shown in Figure 4.8. As was expected, it was observed that the T_g temperature increased with increasing ZrO_2 content. No exothermic peak was observed in any of the B, C, and D glass samples. However, a small exothermic bulge was noticed centred around 850 °C for glass B. There are successive changes in slope observed in the DTA curve for glass D.

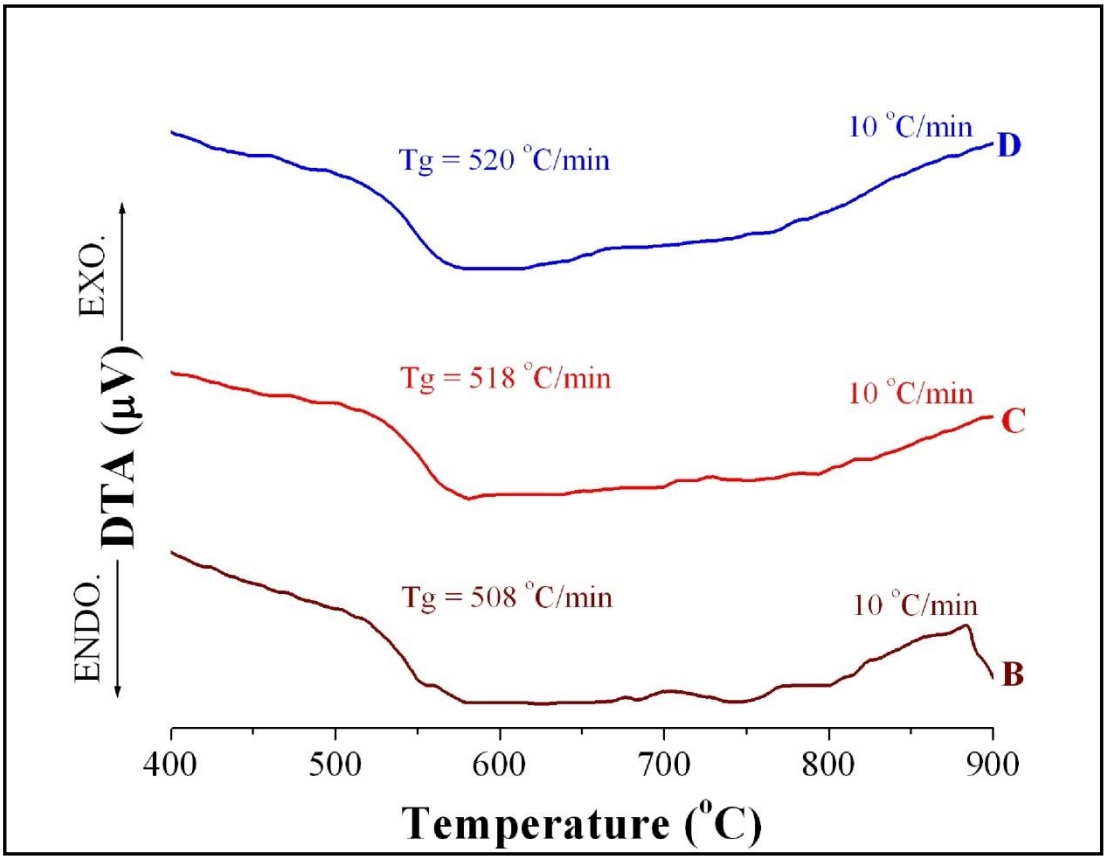

Figure 4.8: DTA curves of glass B, C, and D at a heating rate of 10 °C/min.

(iii) Glass E ($50SiO_2$-$25B_2O_3$-$10Na_2O$-$15ZrO_2$)

The DTA curve of glass E is shown in Figure 4.9 for a heating rate of 10 °C/min. No well-defined exothermic peak was exhibited by the curve. Onset of a broad exothermic bulge was observed at approximately 650 °C. Another broad exothermic

event can be seen in the range 800–900 °C. These broad exotherms indicate that surface crystallisation is the dominant mechanism for crystallisation.

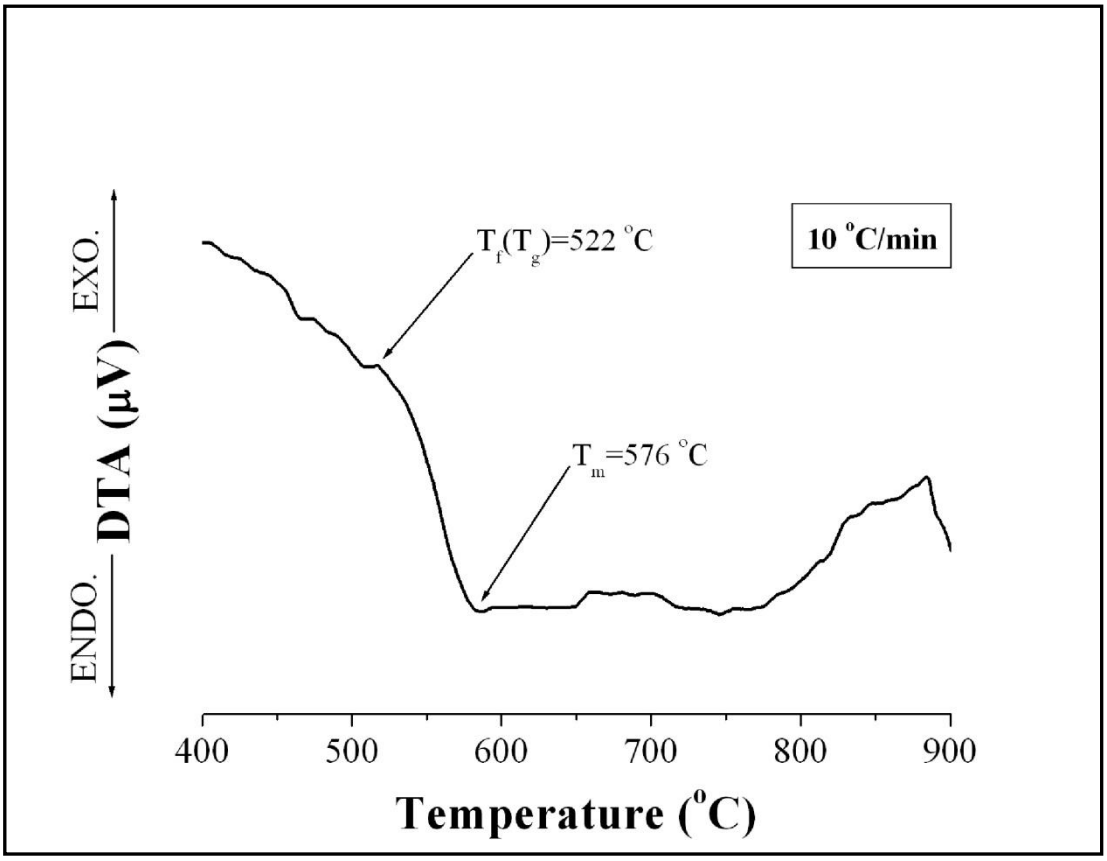

Figure 4.9: DTA curve of glass E at a heating rate of 10 °C/min.

4.3.2.2 Glass E-II ($54SiO_2$-$25B_2O_3$-$6Na_2O$-$15ZrO_2$)

Figure 4.10 shows the DTA analysis of the glass powder sample E-II for a heating rate of 10 °C/min. A change in slope is observed at about 511 °C (T_f) and continues until it reaches a plateau at 563 °C (T_m). Onset of a broad exothermic event occurs at approximately 650 °C, and is likely associated with surface crystallisation [45, 157-159].

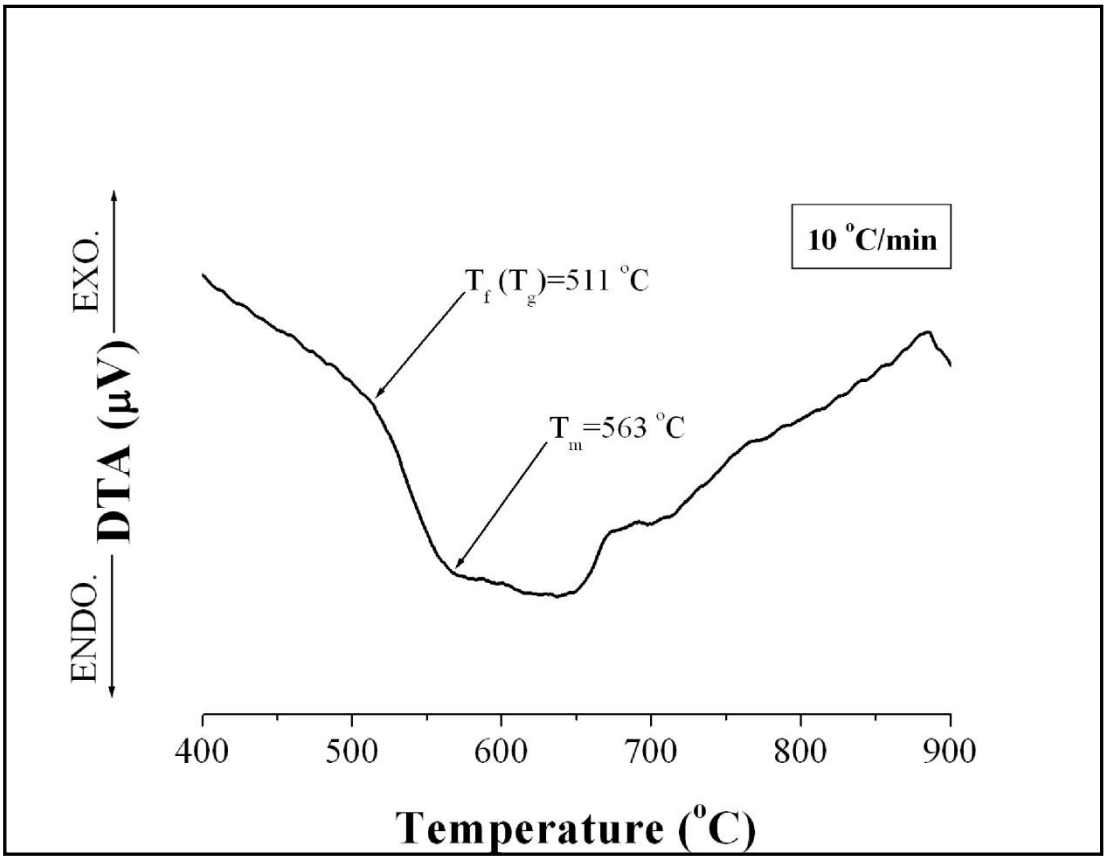

Figure 4.10: DTA curve of glass E-II at a heating rate of 10 °C/min.

4.3.2.3 Glass F ($50SiO_2$-$25B_2O_3$-$4Na_2O$-6CaO-$15ZrO_2$)

The DTA curves of glass F is shown in Figure 4.11 for heating rates of 10, 15, and 20 °C/min. The T_g for glass F was found to be significantly higher compared to other glass compositions due to the replacement of Na_2O by CaO, which contributes to strengthening the network and thus increasing the T_g. With increasing CaO content, the fraction of four-coordinate boron, denoted as BO_4, increased dramatically [160]. As BO_4 increases network connectivity, this in turn significantly increases the T_g. A broad exothermic peak is observed with an onset at approximately 740 °C, and centred at around 820 °C in the case of a heating rate of 10 °C/min. The broad peak indicates that surface crystallisation is the dominant mechanism for crystallisation in glass F. At a heating rate of 20 °C/min, a small exotherm at approximately 530 °C may represent the leading exotherm which is usually seen in highly quenched glasses just below the T_g [24].

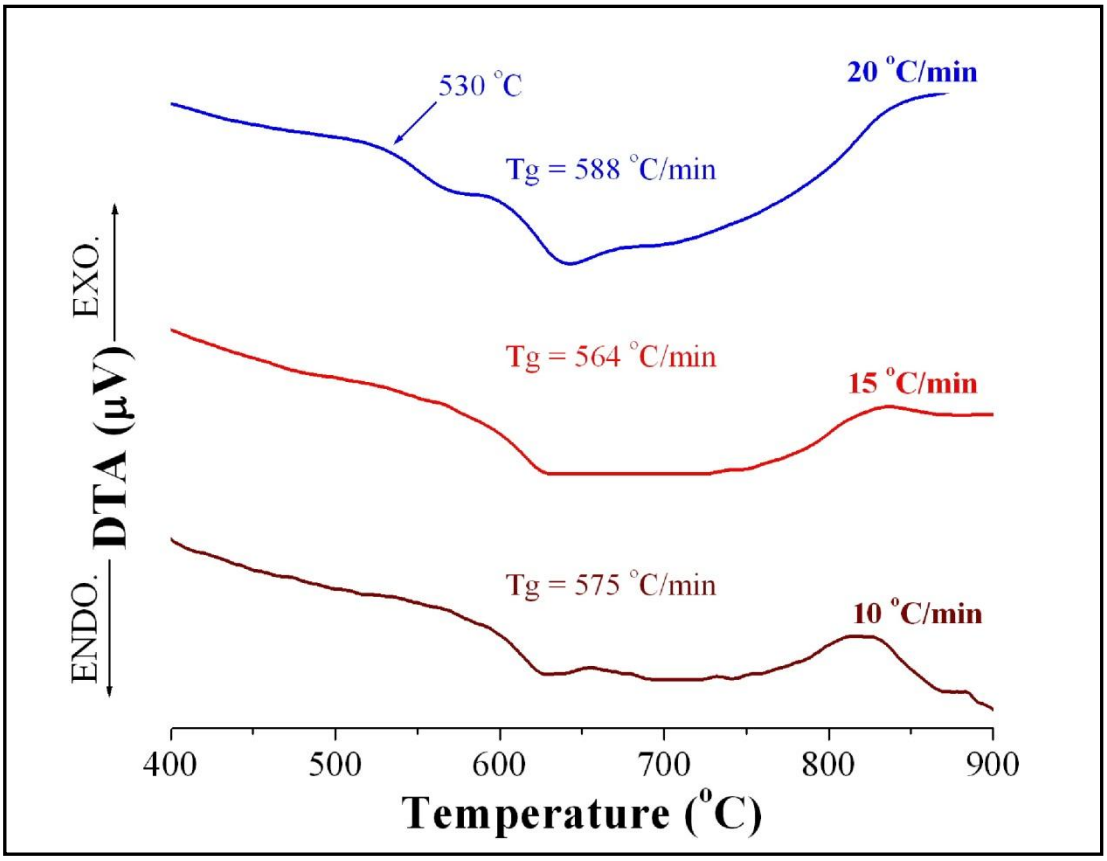

Figure 4.11: DTA curve of glass F at heating rates of 10 °C/min, 15 °C/min, and 20 °C/min.

4.3.2.4 Glass series AA–EE, $(69–x)SiO_2$-$25B_2O_3$-$6Na_2O$-$xZrSiO_4$

In this series of glass compositions the content of $ZrSiO_4$ was increased from 0 to 15 wt%. The objective of the thermal behaviour study of this group was to investigate the influence of $ZrSiO_4$ content while keeping the alkali oxide (6 wt%) and boron oxide (25 wt%) constant.

(i) Glass AA ($69SiO_2$-$25B_2O_3$-$6Na_2O$)

Figure 4.12 shows the DTA curve of glass AA at a heating rate of 10 °C/min. No specific information other than T_g was obtained. A broad exothermic event is observed in the range 740–900 °C. Surface crystallisation is considered the dominant mechanism, since no sharp exothermic peak was observed, even for DTA analysis of finer particle sizes, i.e. < 45µm.

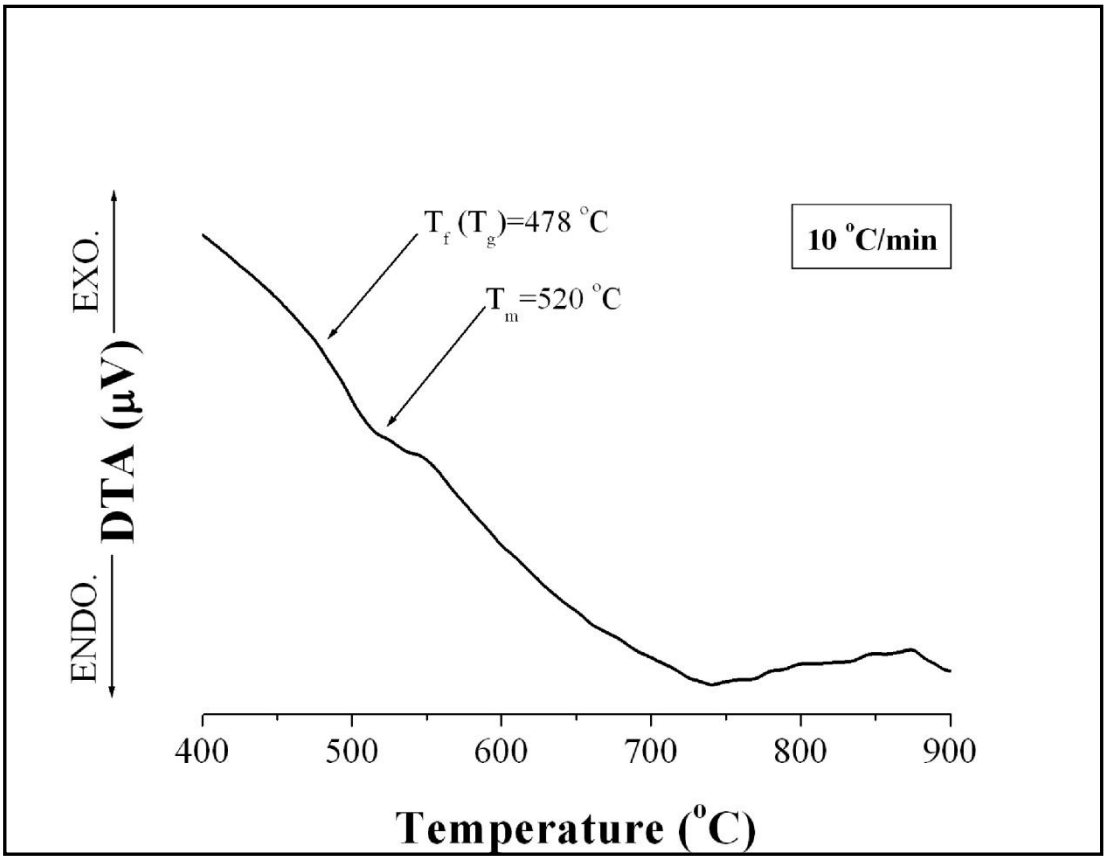

Figure 4.12: DTA curve of glass AA at a heating rate of 10 °C/min.

(ii) Glass CC ($62SiO_2$-$25B_2O_3$-$6Na_2O$-$7ZrSiO_4$)

No sharp exothermic peak was observed in any heating rate. However, an onset of small exothermic bulge was noticed at around 640 °C at a heating rate of 10 °C/min followed by subsequent successive slope changes as shown in Figure 4.13. This exothermic bulge was not prominent for the heating rates of 15 and 20 °C/min. Small details may be lost with rapid heating rates [161]. No crystallisation occurred with the base glass AA even when heat-treated ≤ 6 h at 650 °C (see Figure 4.21). Addition of ZrO_2/ $ZrSiO_4$ suppresses crystallisation [48]. Therefore the small exothermic event observed at around 640 °C may occur due to the formation of tetragonal zirconia.

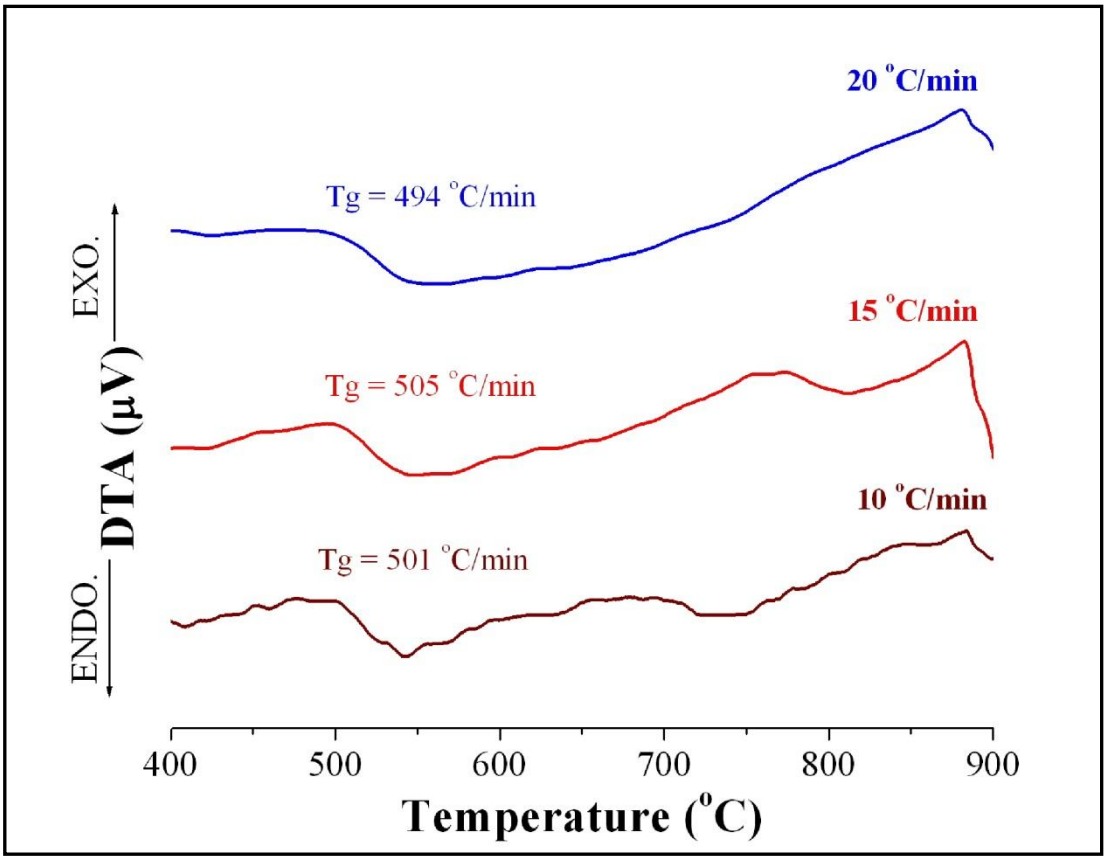

Figure 4.13: DTA curve of glass CC at heating rates of 10 °C/min, 15 °C/min, and 20 °C/min.

(iii) Glass DD ($58SiO_2$-$25B_2O_3$-$6Na_2O$-$11ZrSiO_4$)

A broad exothermic peak was observed on glass DD in the range 680–800 °C as shown in Figure 4.14. This small exothermic event may be due to the formation of tetragonal zirconia. When the heating rate was increased, this exothermic event broadened. This onset of a second exothermic event at about 840 °C is attributed to the precipitation of cristobalite. The broad exothermic events are indicative of surface crystallisation being the dominant mechanism.

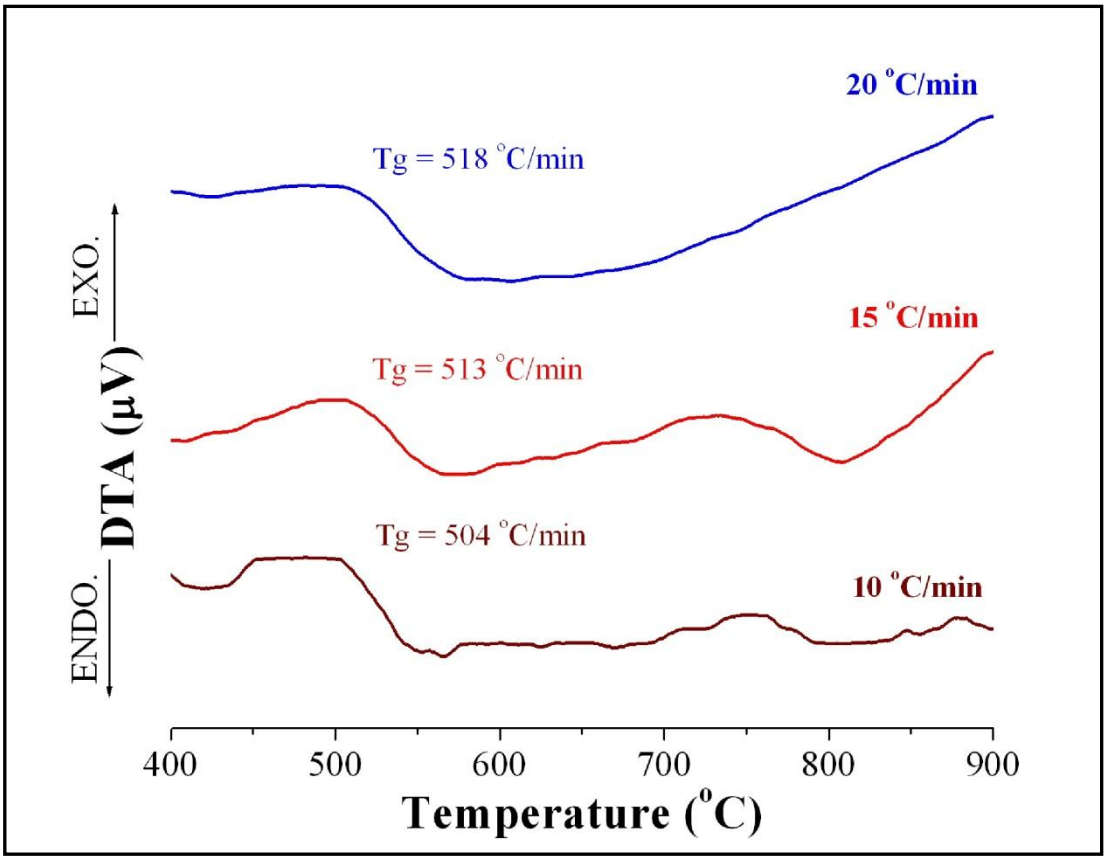

Figure 4.14: DTA curve of glass DD at heating rates of 10 °C/min, 15 °C/min, and 20 °C/min.

(iv) Glass EE ($54SiO_2$-$25B_2O_3$-$6Na_2O$-$15ZrSiO_4$)

Figure 4.15 presents the DTA analysis for glass EE at a heating rate of 10, 15, and 20 °C/min. DTA analysis for the same sample at a heating rate of 15 °C/min is shown in Figure 4.16. The changes in the curve are more conspicuous and increasing heating rate seems to broaden the changes in the curve. One cannot generalise from this trend as DTA curves vary with compositional changes. For the heating rate of 15 °C/min, a change in slope was observed at about 497 °C (T_f) and continued until it reached a plateau at approximately 600 °C. A sharp exothermic peak was observed at 667 °C and was attributed to crystallisation. The sharp nature of this peak, denoted as maximum crystallisation temperature (T_p), is indicative of bulk crystallisation [48, 157, 158]. In contrast, a broad peak was observed at around 650 °C on glass E-II (6 wt% Na_2O, 15 wt% ZrO_2). Therefore, it can be concluded that $ZrSiO_4$ promotes bulk crystallisation.

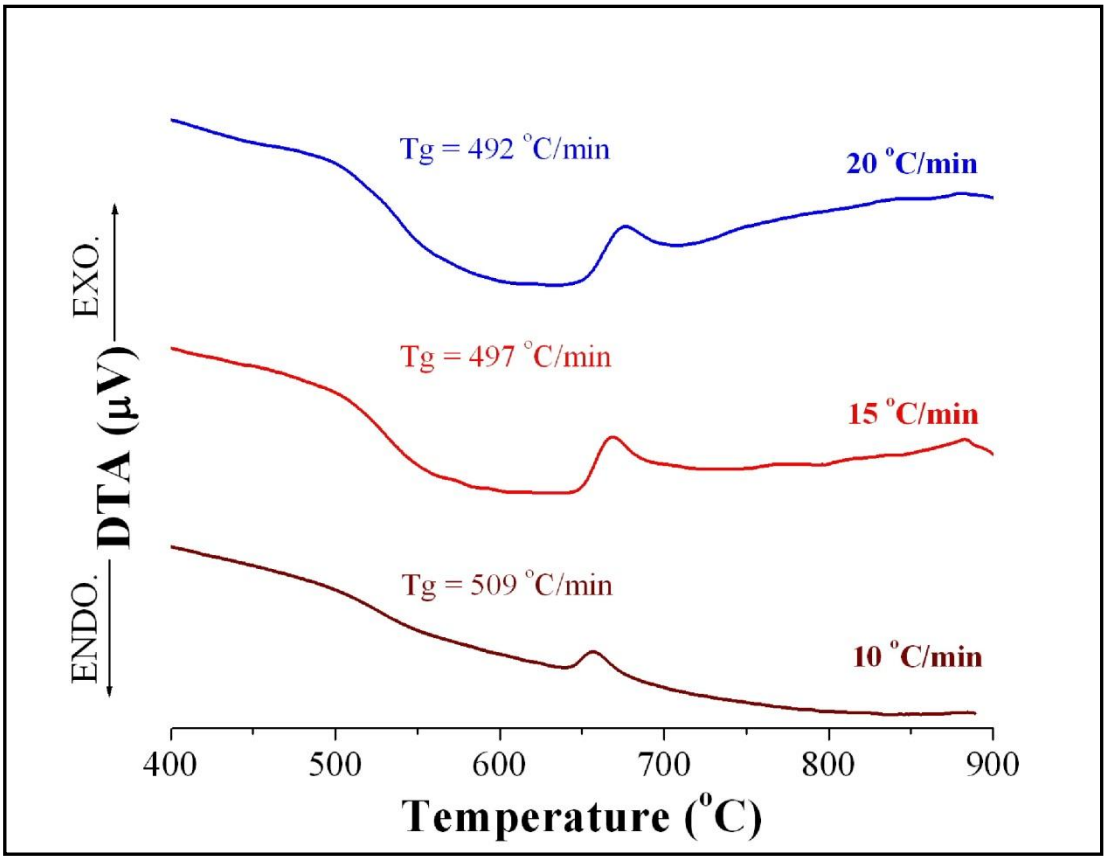

Figure 4.15: DTA curves of glass EE at heating rates of 10 °C/min, 15 °C/min, and 20 °C/min.

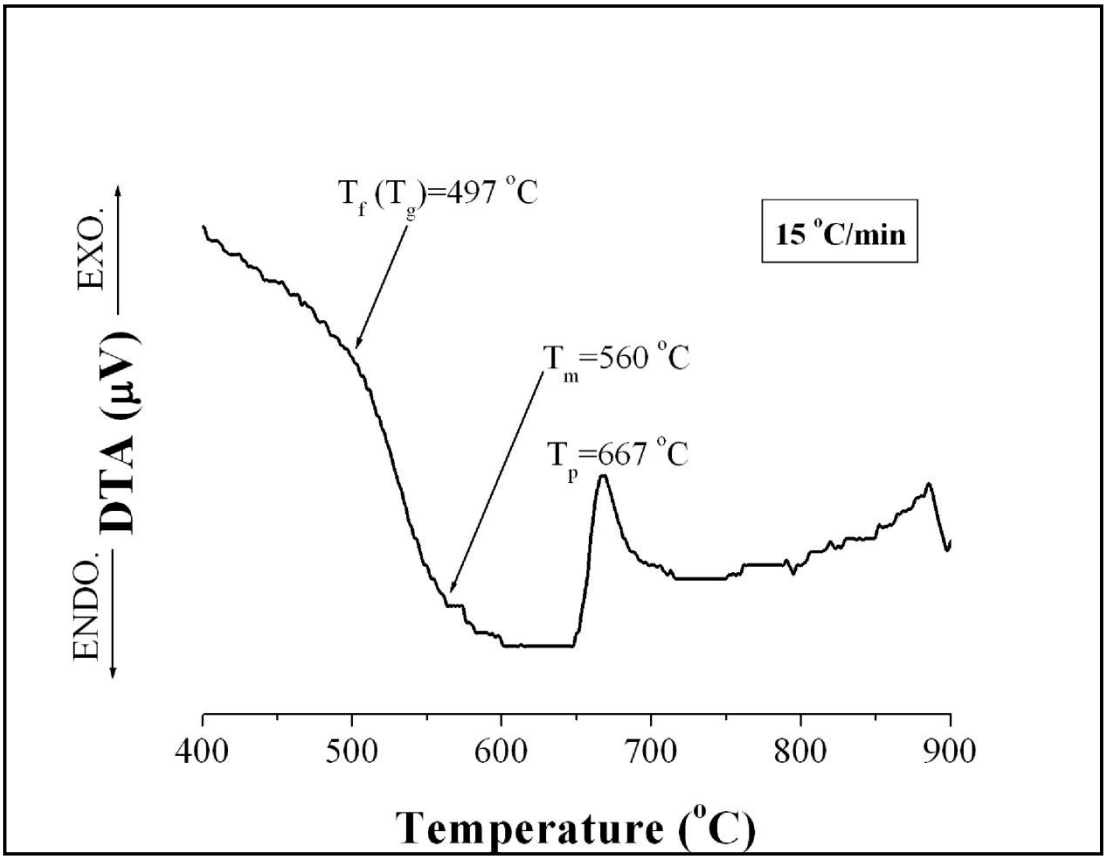

Figure 4.16: DTA curve of glass EE at a heating rate of 15 °C/min.

Using the sharp peaks that are apparent in the case of heating rates 10 °C/min, 15 °C/min, 20 °C/min, the Avrami number (n) can be calculated using Equation 4.1. This is the proven method used to indicate the occurrence of the crystallisation mechanism. In order to calculate the Avrami number, the activation energy for crystallisation was calculated by using the Kissinger equation [162] which is based on the crystallisation peak temperature at DTA heating rate, ϕ :

$$ln\frac{\phi}{T_p^2} = -\frac{E_c}{RT_p} + const. \qquad \text{Equation 4.2}$$

The activation energy can be obtained from the slope of $ln(\phi/T_p)$ versus $1/T_p$ as shown in Figure 4.17. The data in Table 4.3 are presented in graphic form in Figure 4.17. It can be seen from Figure 4.17 that a linear relationship exists between $ln(\phi/T_p)$ and $1/T_p$. The activation energy (E_c) is calculated as 253 kJ/mol. Kukizaki [48] reported the E_c value as 215 kJ/mol for the $70SiO_2$-$8.5B_2O_3$-$7.3Na_2O$-3CaO-$8Al_2O_3$ glass system.

Table 4.3: The results of DTA measurements for glass EE.

Heating rate, ϕ	**Crystallisation peak temperature, T_p**	**ΔT**
°C/min	**°C**	**°C**
10	657	15
15	667	17
20	676	19

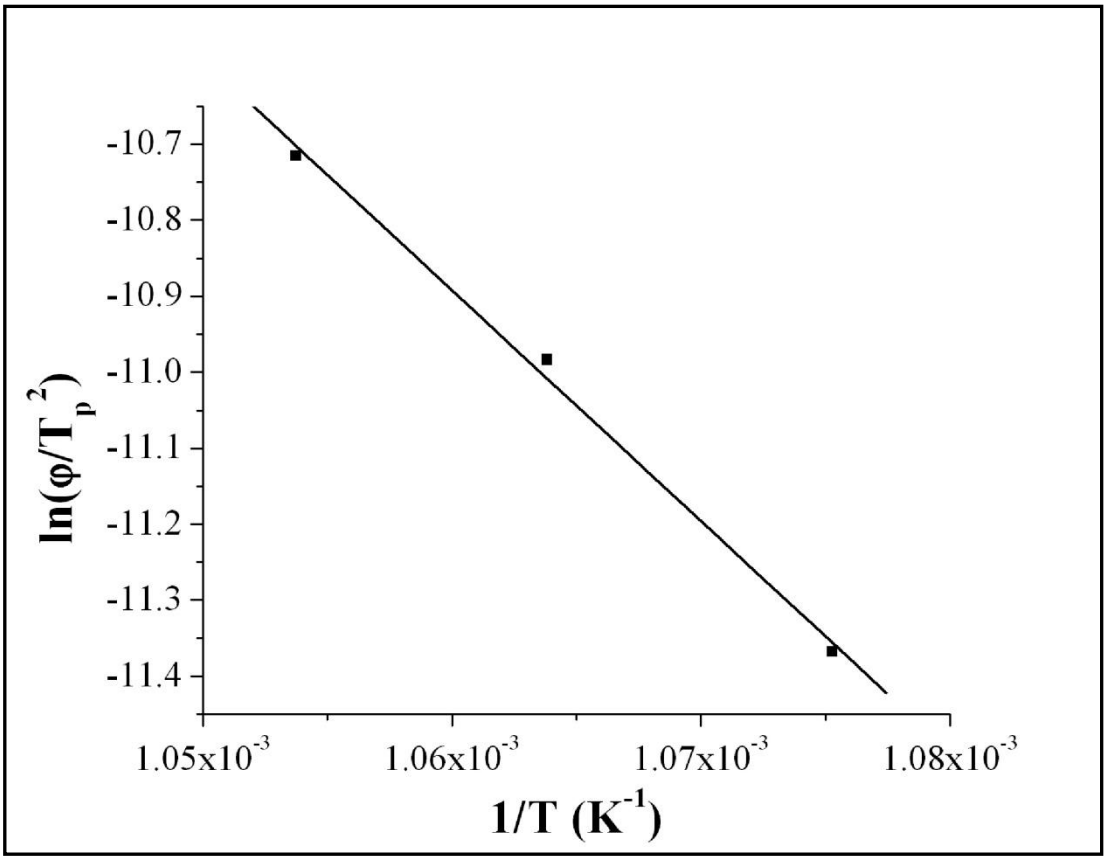

Figure 4.17: Determination of E_c/R for glass EE using the Kissinger method.

The Avrami number, *n*, calculated from Equation 4.1 are listed in Table 4.4. The *n* values of glass EE were found to be greater than 3 for all heating rates, which indicates that crystallisation was caused by bulk crystallisation. Kukizaki [48] obtained the n values of 4.2, 3.8, and 3.7 for heating rates of 10, 15, and 20 °C/min respectively using the $70SiO_2$-$8.5B_2O_3$-$7.3Na_2O$-$3CaO$-$8Al_2O_3$ glass system.

Table 4.4: The calculated values the Avrami parameter as a function of DTA heating rates.

Heating rate, ϕ °C/min	**Avrami parameter, n**
10	4.74
15	4.28
20	3.90

XRD analysis was performed on glass composition EE to identify the crystallisation phases associated with the exothermic peak observed in Figure 4.16. The samples were heat-treated at 650 °C, which is the onset of T_p, for various durations (1 h, 14 h,

24 h, and 63 h). Peaks attributed to tetragonal ZrO_2 (2θ = 30°, 51°, 60°) [JCPDS 02-0733] were identified for composition EE heated at 650 °C for 1 h, 14 h, 24 h, and 63 h (see Figure 4.18). The peaks at 2θ = 21.8°, 36° [JCPDS 01-0438, 03-0267] were attributed to cristobalite. For heat-treatment dwell time ≤ 24 h, the cristobalite peak exhibited low intensities compared with the tetragonal ZrO_2 peaks. For heat-treatment duration of > 24 h < 63 h, the intensity of the peaks relating to cristobalite increases. Crystallisation of cristobalite predominates over crystallisation of tetragonal ZrO_2 for heat-treatment times ≥ 24 h. The XRD finding suggested that the T_p observed in Figure 4.16 is due to crystallisation of tetragonal zirconia.

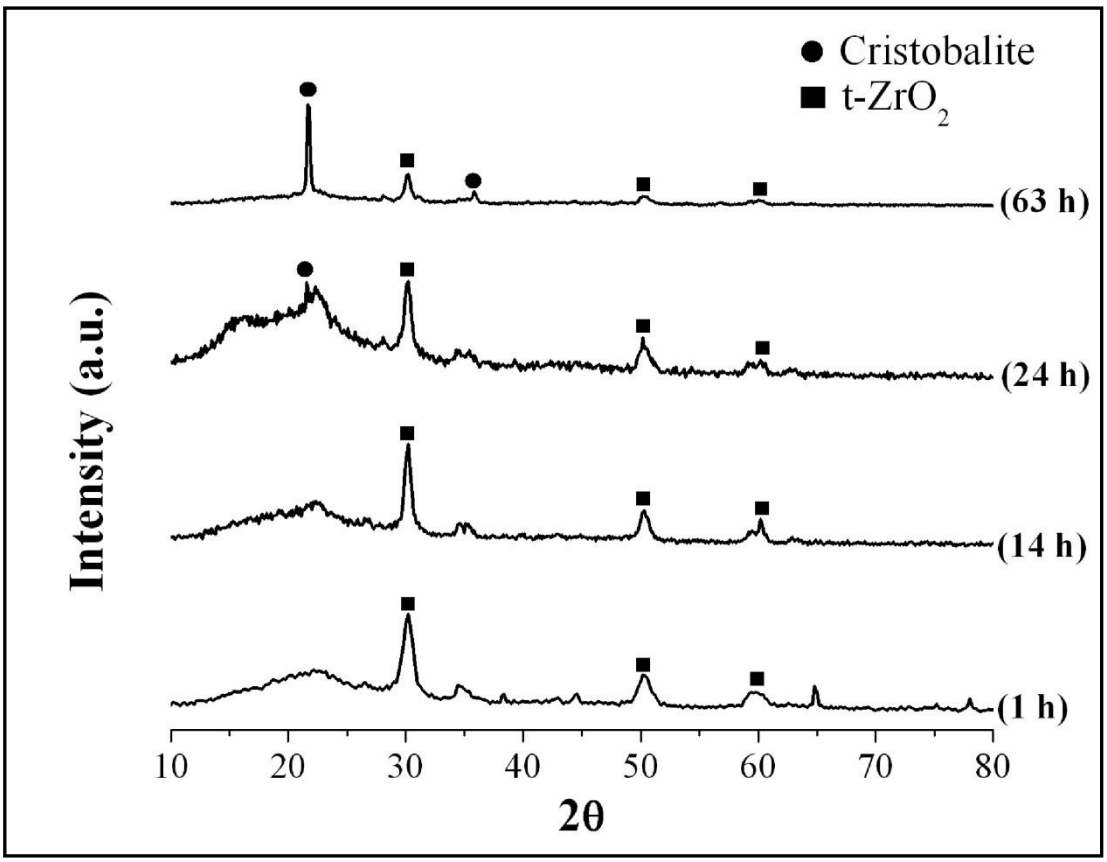

Figure 4.18: XRD patterns of glass sample EE heat-treated at 650 °C for different times (1 h, 14 h, 24 h, and 63 h).

4.3.3 Dilatometry analysis

(i) Glass AA ($69SiO_2$-$25B_2O_3$-$6Na_2O$)

Figure 4.19 shows the linear thermal expansion curve of a bulk sample of glass AA heated at 10 °C/min. The glass expands until 305 °C, above which the glass contracts

suddenly up to about 425 °C, before expanding again. This sudden expansion in the temperature range 430 °C to 520 °C is referred to as the transformation range and indicates the onset of viscoelastic behaviour, where bond breaking is predominant. The onset temperature of the transformation range at 430 °C is attributed to T_g. The DTA curve (see Figure 4.12) shows the glass transformation temperature of same sample (glass AA) at about 478 °C (T_g) with the same heating rate. The temperature of maximum expansion is identified at 550 °C and can be referred to as the dilatometric softening temperature (T_d). A sharp decrease in sample dimension is noticed at about 560 °C after the dilatometric softening temperature which corresponds to viscous flow of the sample under stresses imposed by the dilatometric push rod. Shelby [24] and Kingery [27] revealed a dramatic distinction in thermal expansion behaviour between quenched glasses and glasses which had been annealed prior to dilatometric characterisation. The quenched glasses showed very prominent contraction-expansion characteristics. For annealed glasses the expansion-contraction was minimal and to a large extent 'washed out' as a result of annealing the glass above T_g. The expansion behaviour of glass AA (quenched) is in good agreement with the findings of Shelby and Kingery. From the dilatometric data, the linear thermal expansion coefficient (α_l) of glass AA was measured as 4.77×10^{-6} $°C^{-1}$ in the temperature range between room temperature and 300 °C, which is in good agreement with the measured linear thermal expansion coefficient of similar borosilicate glass compositions reported in the literature [163].

Figure 4.20 illustrates the linear shrinkage behaviour of a bulk sample of glass AA heated at 10 °C/min. As can be seen in Figure 4.20, the bulk sample begins to shrink at about 560 °C and continues with a sharp fall upon reaching about 660 °C. Beyond 660 °C, there is no significant shrinkage observed. A total linear shrinkage of around 1.7% is observed. This shrinkage is attributed to viscous flow and continues until 660 °C.

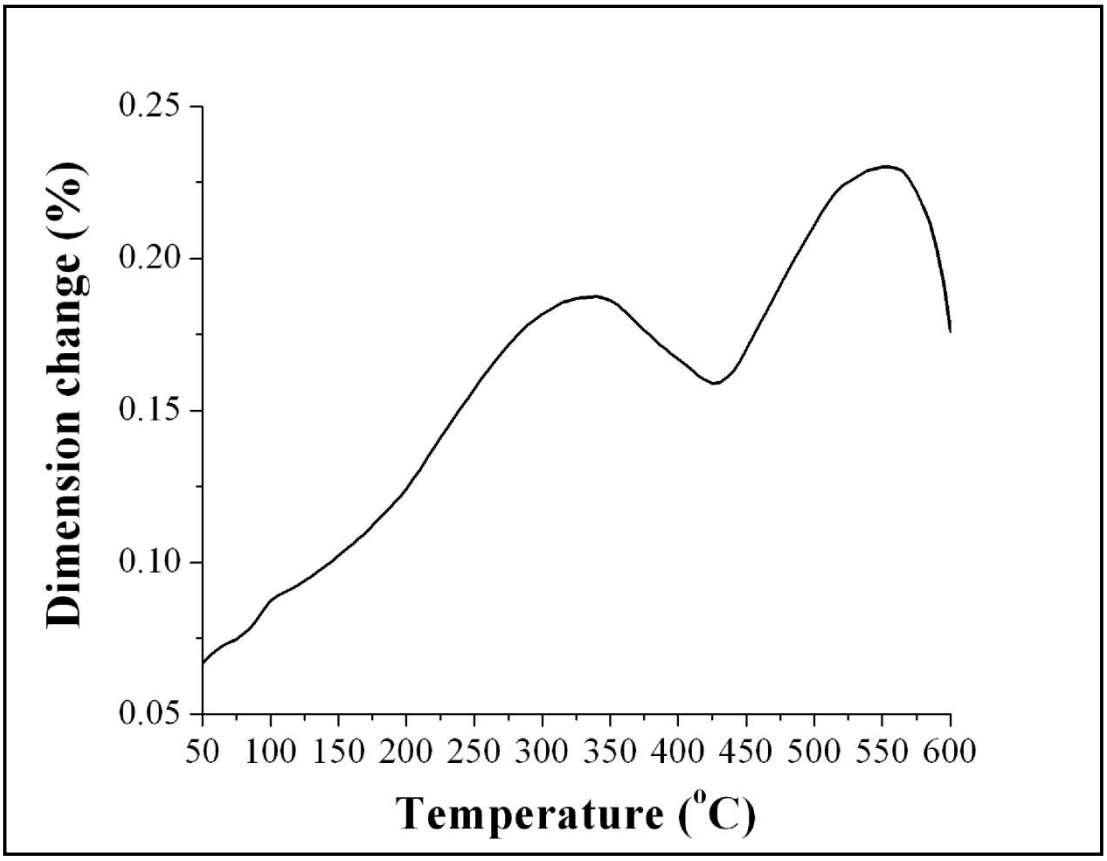

Figure 4.19: Linear thermal expansion curve of bulk glass AA obtained at 10 °C/min.

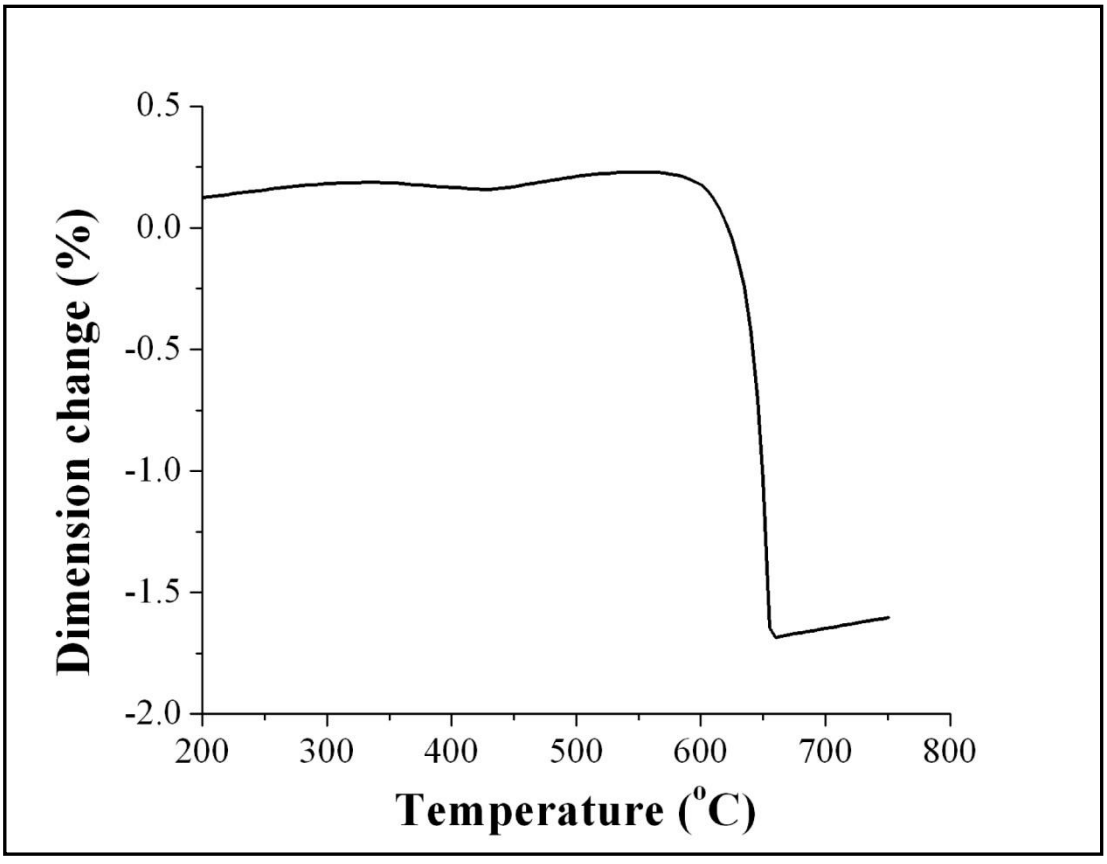

Figure 4.20: Linear shrinkage curve of bulk glass AA obtained at 10 °C/min.

Figure 4.21 presents XRD patterns for powdered samples of glass AA which was heat-treated at 650 °C for different time periods (1 h, 3 h, 6 h, and 14 h). Cristobalite peaks are observed in the sample heat-treated for 14 h. However, no crystallisation peaks appeared for the bulk sample of glass AA heat-treated under similar condition for 14 h. Other studies have shown that powder samples are more prone to surface crystallisation than bulk samples due to their higher surface area [45, 157, 158].

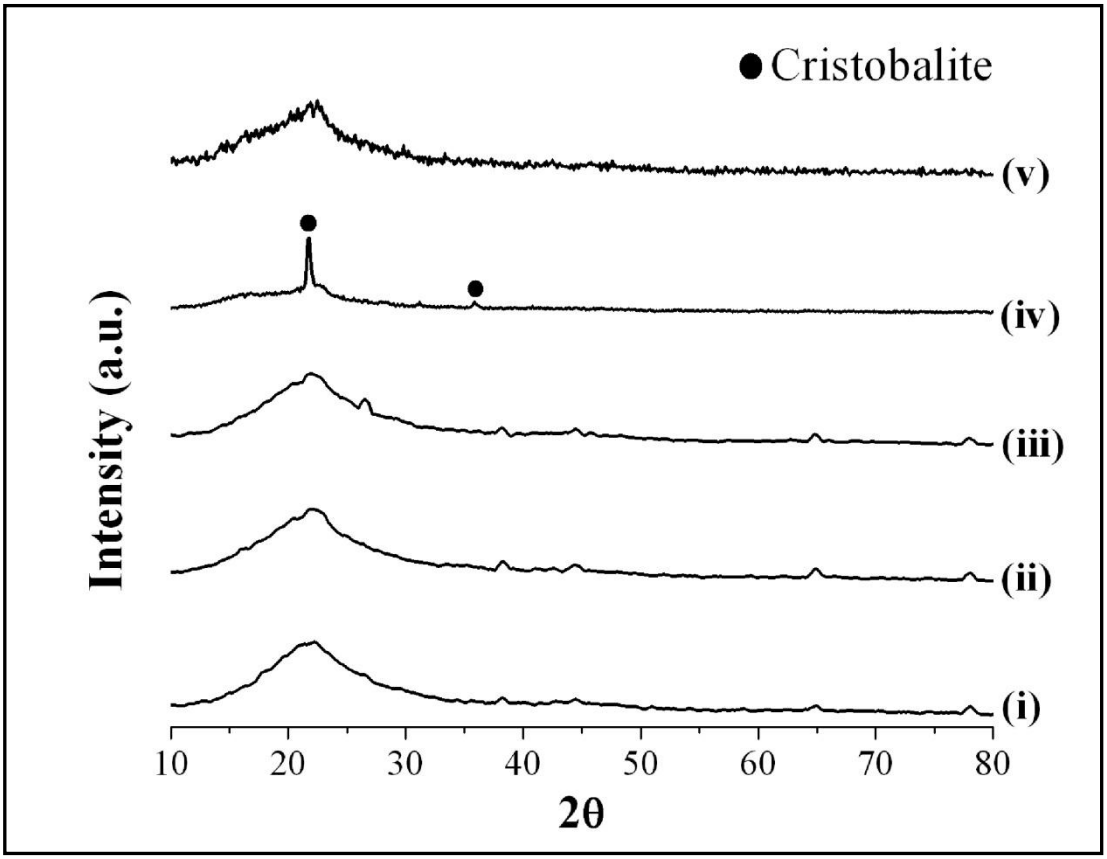

Figure 4.21: XRD patterns of glass AA heat-treated at 650 °C for: (i) powder sample, 1 h; (ii) powder sample, 3 h; (iii) powder sample, 6 h; (iv) powder sample, 14 h; (v) bulk sample, 14 h.

(ii) Glass EE ($54SiO_2$-$25B_2O_3$-$6Na_2O$-$15ZrSiO_4$)

Figure 4.22 shows the linear thermal expansion curve of a bulk sample of glass EE heated at 10 °C/min. A negative thermal expansion coefficient was noticed initially in the range 60 – 130 °C. This negative thermal expansion coefficient is believed to result from the ability of the fully linked network to absorb lattice expansion through bending of bonds [24]. This behaviour is in good agreement with the findings of

Shelby [24], where he showed that vitreous silica glass displays a negative thermal expansion coefficient over a temperature range of 50 – 180 °C. Addition of $ZrSiO_4$, which also acts as and intermediate and network glass former, decreased the number of non-bridging oxygens in glass EE compared to glass AA. The glass then expanded until 350 °C, above which the glass suddenly contracted up to about 470 °C, before expanding again. This sudden expansion in the temperature range 470 °C to 515 °C is referred as the transformation range and indicates the onset of viscoelastic behaviour, where bond breaking is predominant. The onset temperature of the transformation range at 470 °C is attributed as T_g. In contrast, the DTA curve (see Figure 4.15) shows the glass transformation temperature of the same sample (glass EE) at about 509 °C (T_g) with the same heating rate. The temperature of maximum expansion is identified at 515 °C and can be referred as the dilatometric softening temperature (T_d). A sharp decrease in sample dimension was noticed at about 520 °C after the dilatometric softening temperature which corresponded to viscous flow of the sample under stresses imposed by the dilatometer push rod. The expansion behaviour of glass EE was similar to glass AA, except for the initial negative thermal expansion coefficient. The linear thermal expansion coefficient (α_l) of glass EE was measured as 3.37 x 10^{-6} $°C^{-1}$ in the temperature range between room temperature and 300 °C. The decrease in the linear thermal expansion coefficient in glass EE, in contrast to glass AA, is due to the addition of intermediate oxides ($ZrSiO_4$) that reduces the concentration of non-bridging oxygen and thus reduces the asymmetry of the bonds.

Figure 4.23 illustrates the linear shrinkage behaviour of a bulk sample of glass EE heated at 10 °C/min. The bulk sample began to shrink at about 520 °C and continued with a sharp fall until reaching about 590 °C. Beyond 590 °C, no significant shrinkage was observed in the curve. A total linear shrinkage of around 3.7 % was observed. This shrinkage is attributed to the viscous flow and continued until 590 °C.

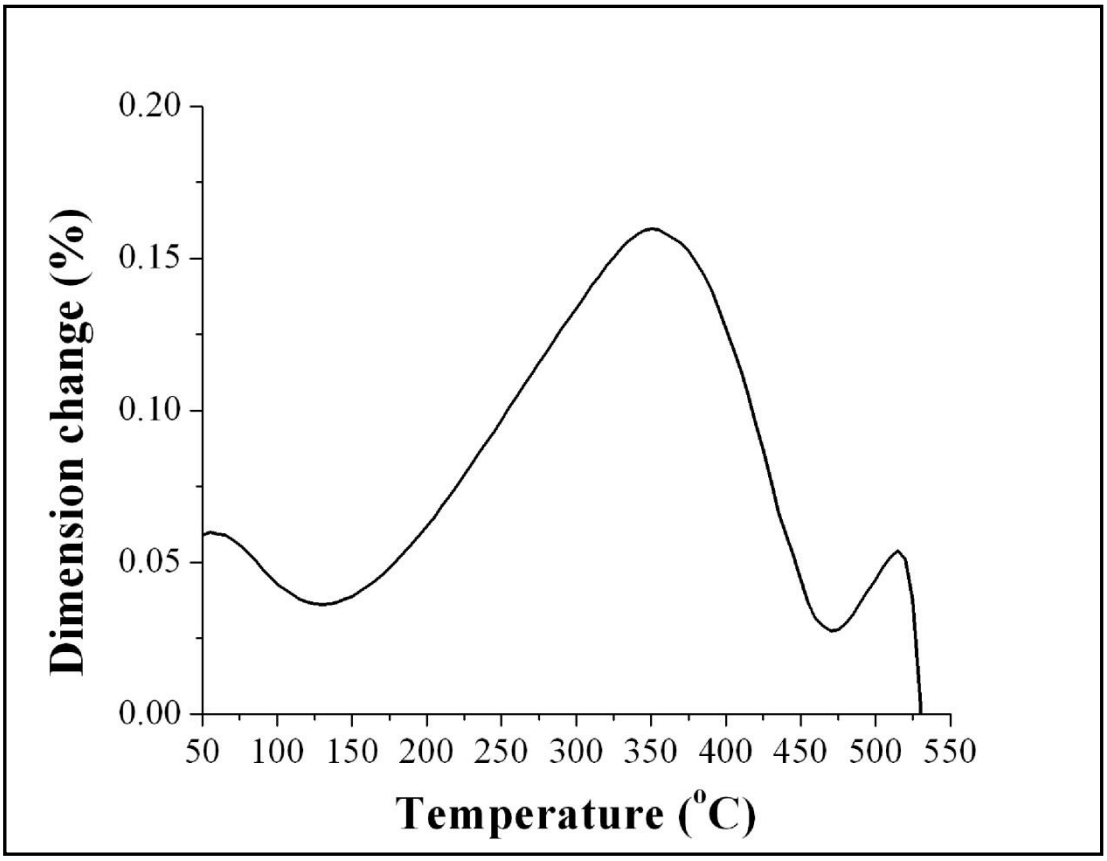

Figure 4.22: Linear thermal expansion curve of bulk glass EE obtained at 10 °C/min.

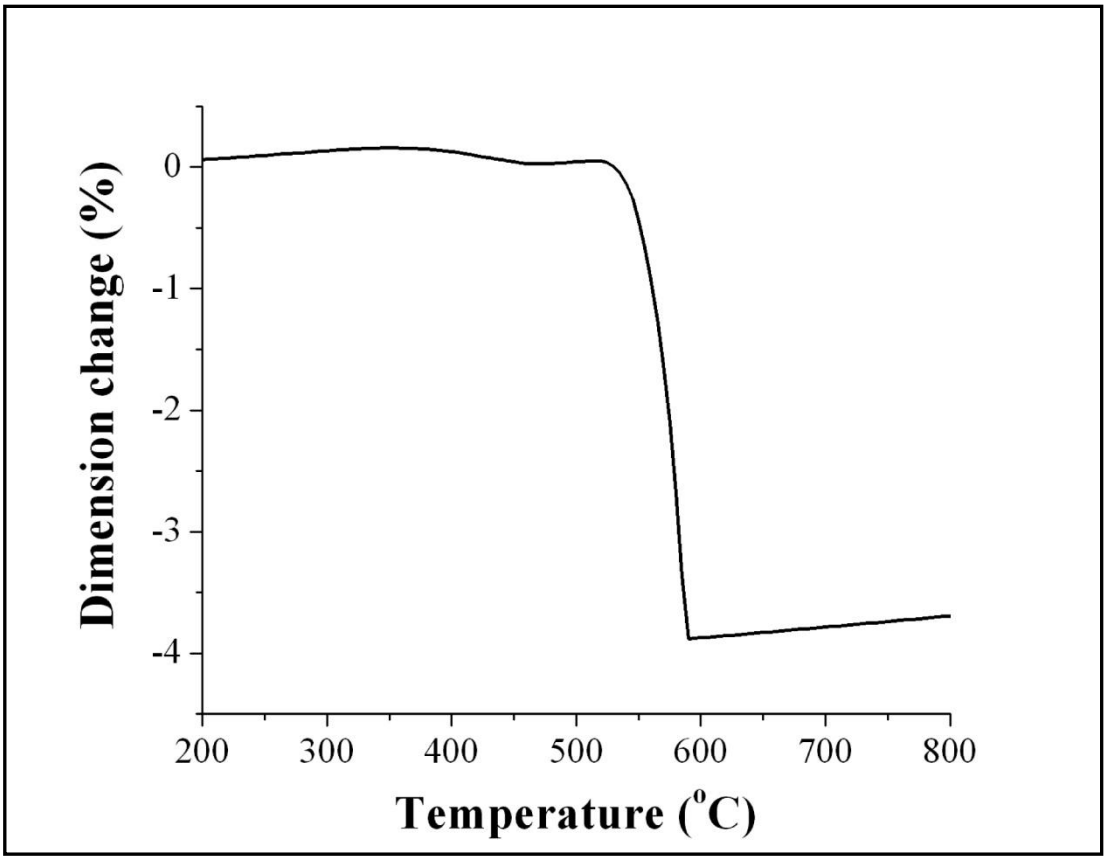

Figure 4.23: Linear shrinkage curve of bulk glass EE obtained at 10 °C/min.

4.3.4 TTT diagram

Visual examination was carried out to monitor phase separation in the samples subjected to different heat-treatment times and temperatures. Figure 4.24 shows the Time Temperature Transformation (TTT) diagram for composition AA. The glass frit was visually clear initially and remained clear within certain temperature ranges, which suggests no phase separation. Faint opalescence increased as a function of both time and temperature. This is in accordance with another study where phase separation was defined by the visual appearance of glass exhibiting opalescence [6]. As can be seen from Figure 4.24, the minimum time required for crystallisation onset is at about 800 °C. With decreasing temperature, the time required for crystallisation onset increased. The TTT curve located below the crystallisation curve indicated the initiation of phase separation. At higher temperature (> 650 °C) and time (>350 min), the glass will experience phase separation coupled with crystallisation, and the crystallisation increases with further extension of the heat treatment time. The TTT diagram also indicates that 630 °C would be an appropriate temperature for glass AA to initiate phase separation without crystallisation even for extended times.

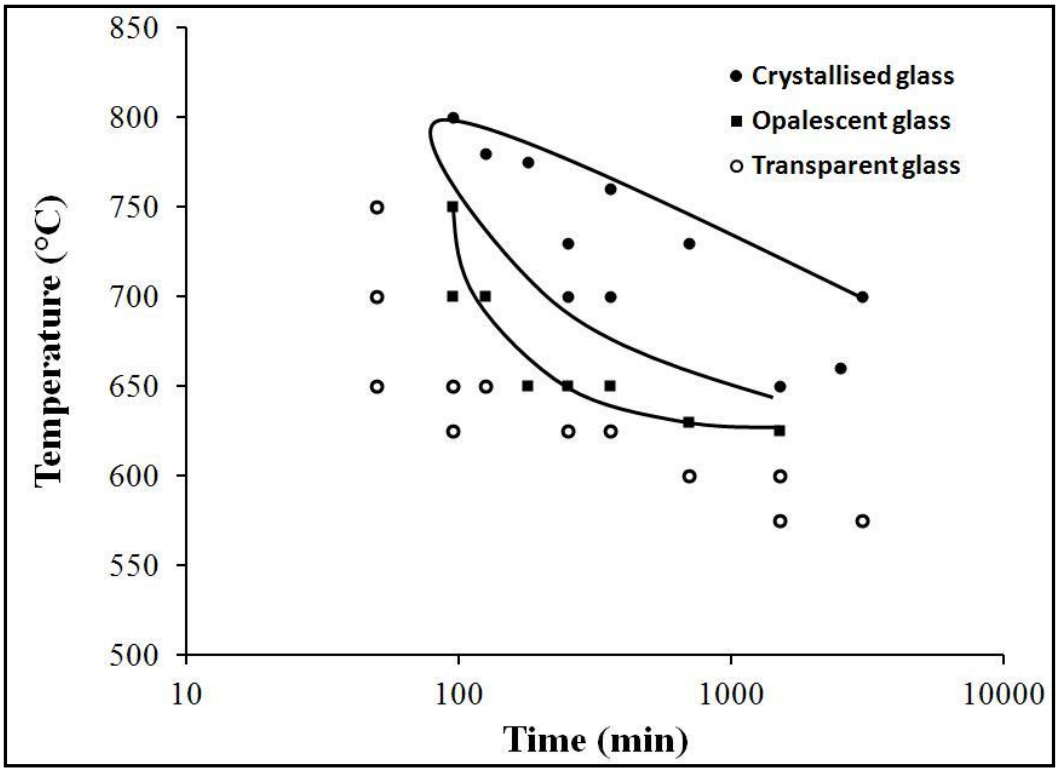

Figure 4.24: TTT diagram for Glass AA.

4.4 HEAT-TREATMENT FOR PHASE SEPARATION

The extent of phase separation depends on heat-treatment temperature and time as well as glass composition. The heat-treatment temperatures and times in this study were selected based on the thermal and crystallisation behaviour of the glass compositions. In general, the heat-treatment temperatures were selected between glass transition and crystallisation temperature. TTT diagram was also used as a guide in selecting heat-treatment temperature and time. For most of the glasses the heat-treatment temperature was selected near the crystallisation temperature. Near crystallisation temperature is possibly the optimum heat-treatment temperature, as phase separation often promotes the crystallisation process in glass [27]. Hijiya et al. [164] in their study also found that crystallisation occurred in phase separated glasses as the boundary of two glass phases acted as heterogeneous nucleation point. Heat-treatments were performed at dwell temperatures between 630 – 700 °C and dwell times between 14 – 63 h, depending on the composition. The effect of heat-treatment temperatures and times on phase separation and pore characteristics of the glass compositions is discussed in the following sections.

4.5 CHARACTERISATION OF HEAT-TREATED GLASSES

Heat-treated glass samples were characterised using XRD and FTIR to investigate the effect of the addition of ZrO_2/$ZrSiO_4$ on devitrification and phase separation. Attempts were also made to correlate the thermal behaviour characteristics of the glass samples after heat-treatment was carried out at various temperatures and times.

4.5.1 X-ray diffraction analysis (XRD)

The diffraction pattern and peak analysis of the powder glasses are shown in Figure 4.26, Figure 4.27, and Figure 4.28. The peaks at 2θ = 21.8°, 28.5°, 31.3°, 36° [JCPDS 01-0438, 03-0267] were attributed to cristobalite and peaks at 2θ = 30°, 51°, 60° [JCPDS 02-0733] were ascribed to tetragonal ZrO_2. Tsurita and Nogami [60] in their study on the preparation of porous support using the SiO_2-Na_2O-ZrO_2 system, identified a cristobalite peak around 2θ = 21° and tetragonal ZrO_2 peaks at 2θ = 30°,

35, 50° and 60°. Further findings by Arbab et al. [111] indentified cristobalite peaks at 2θ = 21.8°, 31.2°, and 36°.

4.5.1.1 Glass series A–E, (65–x)SiO_2-25B_2O_3-10Na_2O-xZrO_2

Figure 4.26 presents the XRD diffraction pattern obtained from glass A, B, C, and D, and Figure 4.27 shows the XRD pattern of glass E. All the glass samples were heat-treated at temperature 650 °C for three different dwell times of 14 h, 24 h, and 63 h. A cristobalite peak was identified (2θ = 21.8°) even at 14 h of heat-treatment on glass A. The intensity of the peak at 2θ = 21.8° increased with increasing dwell time, with other cristobalite peaks also being apparent at 2θ = 28.5°, 31.3°, and 36°. It is evident from the XRD analysis of glass A that cristobolite precipitates at 650 °C with long heat-treatment dwell time. With increasing zirconia content in glass B (3 wt% ZrO_2) the peak intensity at 2θ = 21.8° decreased compared to glass A. Eventually no peak at 2θ = 21.8° was observed for glass D (11 wt% ZrO_2) and glass E (15 wt% ZrO_2). It is therefore apparent that increasing ZrO_2 content suppresses crystallisation. This trend is consistent with the findings of Takahashi et al. [165] who found the thermal stability of silica improved by the addition of zirconia, as crystallisation temperature increases with incremental zirconia content. Tsurita and Nogami [60] also found that increasing zirconia content suppressed crystallisation. Figure 4.27 shows that it is possible to obtain a completely amorphous glassy system in glass E even after heat-treated for 24 h at 650 °C. It is interesting to note here that no tetragonal zirconia peak was detected in glass B and glass C even at longer periods of heat-treatment dwell time.

4.5.1.2 Glass E-II (54SiO_2-25B_2O_3-6Na_2O-15ZrO_2)

A clear difference in XRD diffraction patterns was evident between glass E-II (6 wt% Na_2O, 15 wt% ZrO_2) and glass E (10 wt% Na_2O, 15 wt% ZrO_2) as shown in Figure 4.27. Glass E-II was more prone to crystallisation compared to glass E. This result correlates with the DTA findings of glass E-II (see Figure 4.10) and glass E (see Figure 4.9), where the exothermic bulge of glass E-II is more pronounced at around 650 °C. Phase separation often promotes the crystallisation process in the glass [27]. With 6 wt% Na_2O content, the composition of glass E-II is more likely to

lie within the metastable immiscibility dome compare to glass E (10 wt% Na_2O). From the SEM images as shown in Figure 4.25, phase separation is more pronounced in glass E-II compared to glass E. Due to the superior degree of phase separation, glass E-II is more prone to crystallisation as the interface between the two separated phases acted as a nucleation site. This result is consistent with the findings of Hijiya et al. [164].

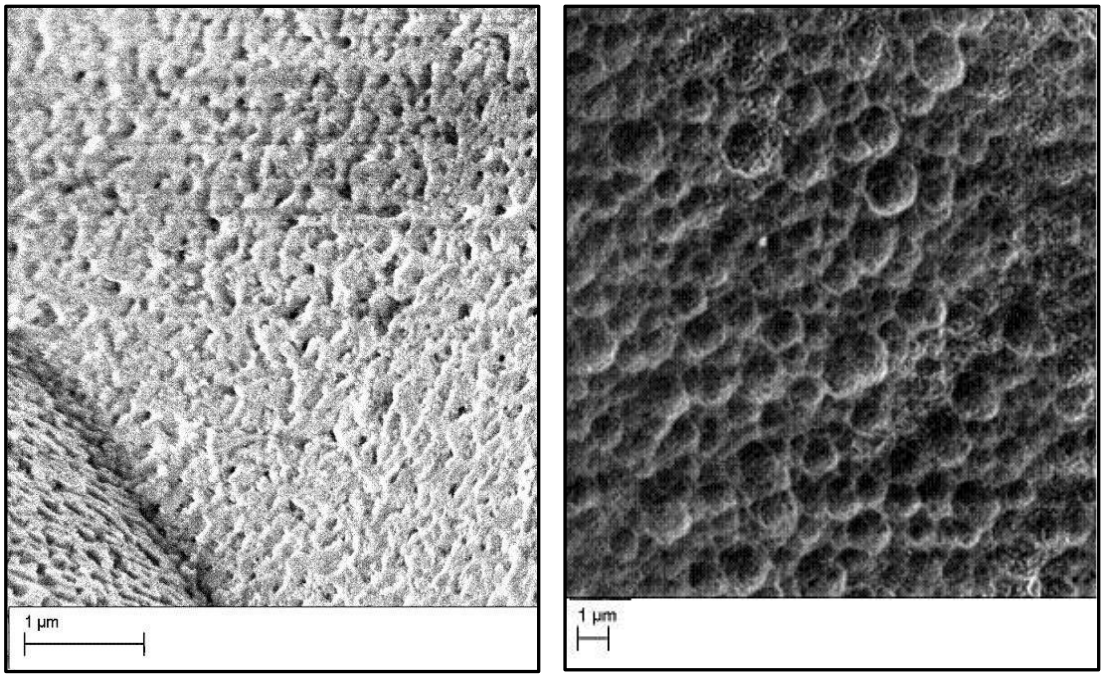

(a) (b)

Figure 4.25: SEM photograph of phase separated glasses of composition (a) E-II (650 °C x 14 h) and (b) E (650 °C x 14 h).

4.5.1.3 Glass F ($50SiO_2$-$25B_2O_3$-$4Na_2O$-6CaO-$15ZrO_2$)

Figure 4.27 shows the XRD diffraction patterns of glass F heat-treated at 700 °C for 14 h and 24 h. There was no peak observed even when heat-treated at 700 °C for 14 h. The small peak at $2\theta = 22.2°$ was attributed to the mesomorphic helical segments. This result is in accord with earlier DTA observation of glass F (see Figure 4.11), which showed that T_g increased significantly when 6wt% of CaO substituted part of Na_2O in glass E. It is interesting to see that increasing heat-treatment dwell time from 14 h to 24 h resulted in a substantial change in crystallisation behaviour of glass F.

4.5.1.4 Glass series AA–EE, $(69–x)SiO_2$-$25B_2O_3$-$6Na_2O$-$xZrSiO_4$

Figure 4.28 presents the XRD diffraction pattern obtained from glass AA, CC, DD, and EE. All the glasses were heat-treated at temperature 650 °C for three different dwell times of 14 h, 24 h, and 63 h. Cristobalite peaks were indentified (2θ = 21.8°, 31.3°, 36°) even at 14 h of heat-treatment on glass AA. The intensity of the peak at 2θ = 21.8° was increased with increasing dwell time and other cristobalite peaks were also apparent (2θ = 28.5°, 31.3°, 36°). It is evident from the XRD analysis of glass AA that cristobalite began to precipitate nearing 650 °C when a long heat-treatment dwell time was applied. With increasing zircon content in glass CC (7 wt% $ZrSiO_4$), the peak intensity at 2θ = 21.8° decreased and peaks at 2θ = 31.3° and 36° disappeared as was seen in the case of glass AA. A similar trend of decreasing crystallisation is observed on glass DD (11 wt% $ZrSiO_4$) compared with glass CC. It is therefore apparent that increasing $ZrSiO_4$ content suppresses crystallisation. This finding corroborates the previous results where increasing ZrO_2 content suppressed the crystallisation in glass series A–E. A significant difference is observed on the XRD pattern of glass EE (15 wt% $ZrSiO_4$). For heat-treatments $\leq$ 24 h, the cristobalite peaks exhibit low intensities compared with the tetragonal ZrO_2 peaks. For heat-treatment durations of > 24 h < 63 h, the intensity of the peaks relating to cristobalite increased. This finding is consistent with the DTA curve (see Figure 4.15), where the T_p observed was due to crystallisation of tetragonal zirconia.

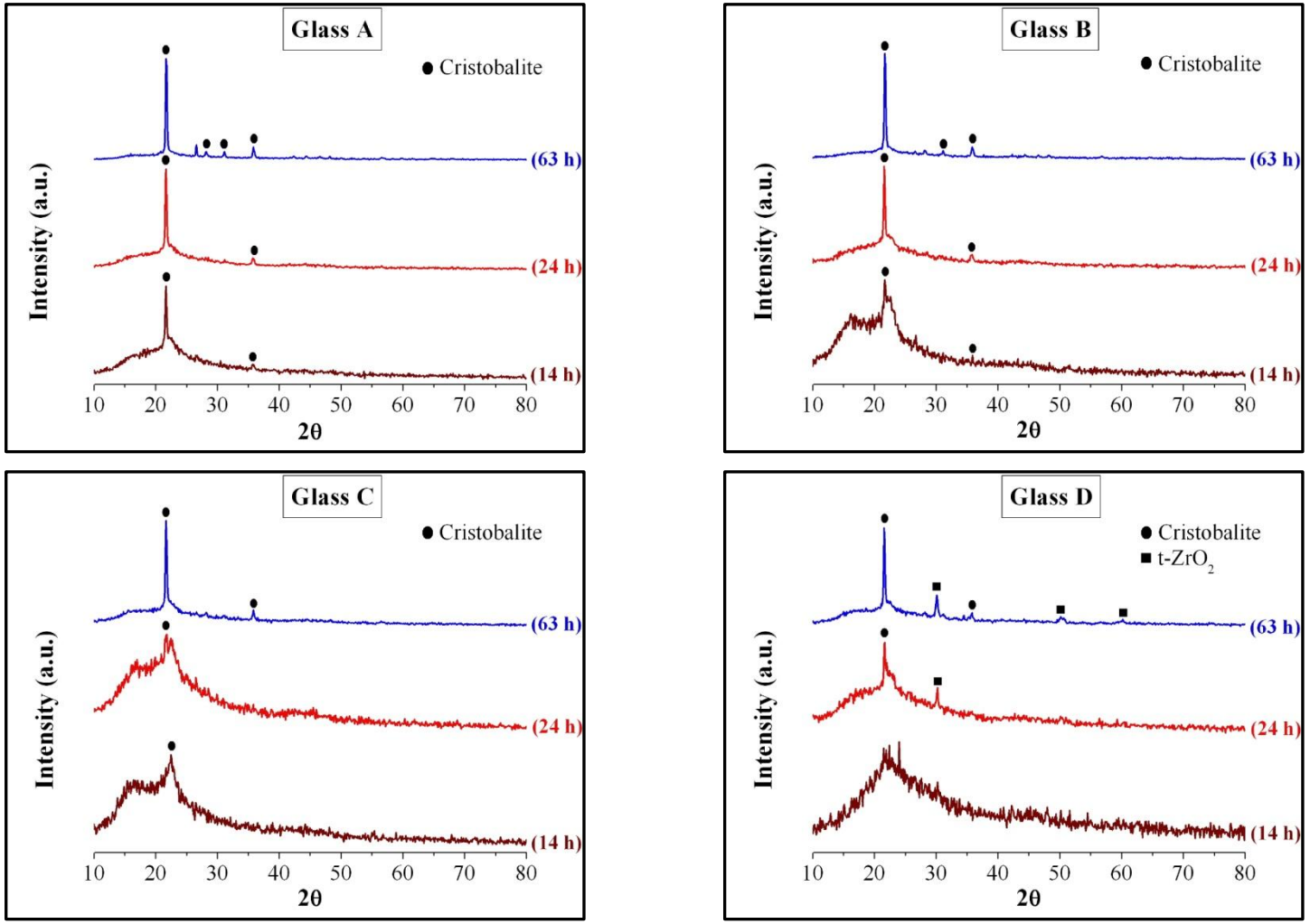

Figure 4.26: XRD patterns of glass A, B, C, and D heat-treated at 650 °C for 14 h, 24 h, and 63 h.

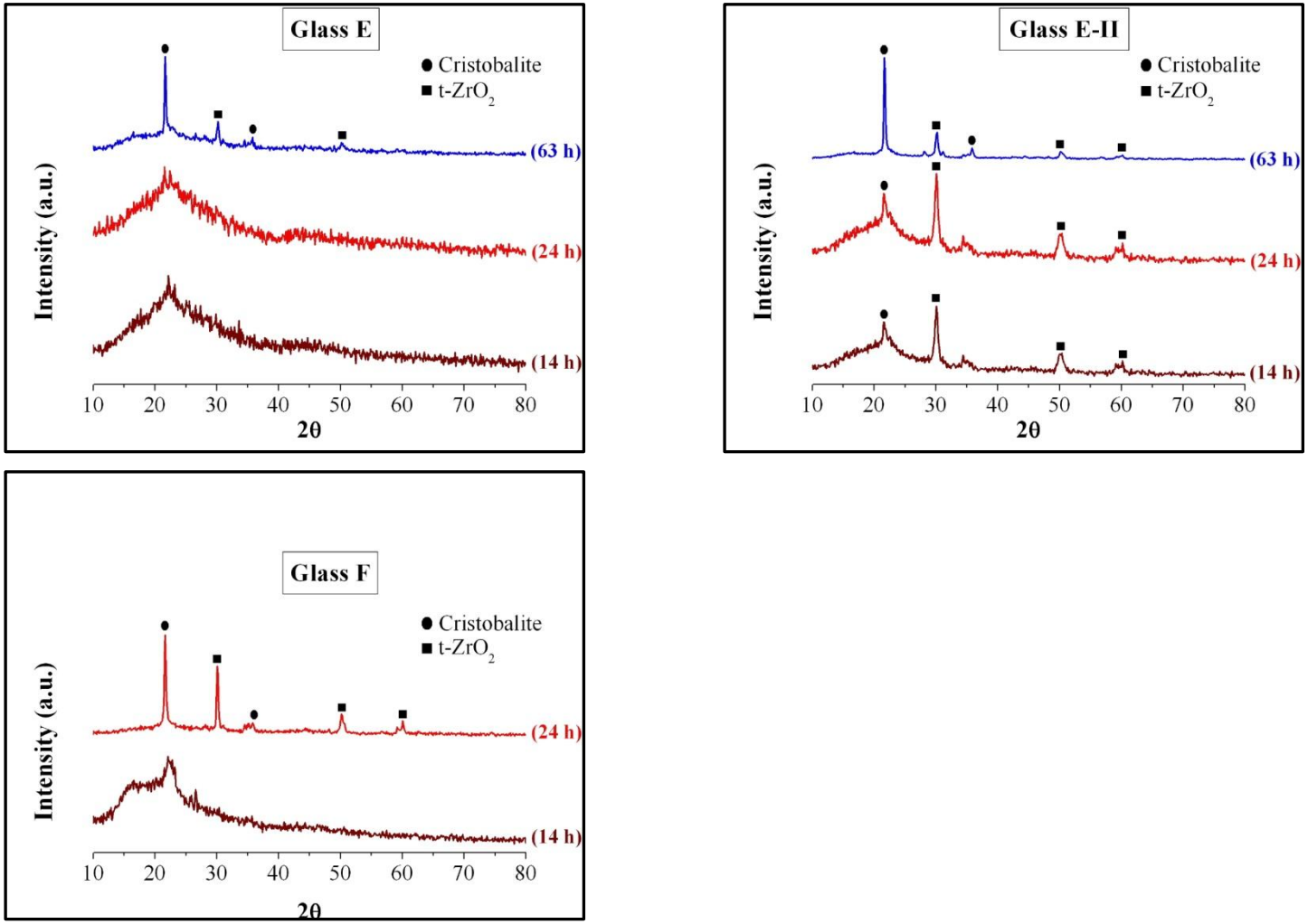

Figure 4.27: XRD patterns of glass E and E-II heat-treated at 650 °C for 14 h, 24 h, and 63 h. Glass F heat treated at 700 °C for 14 h and 24 h.

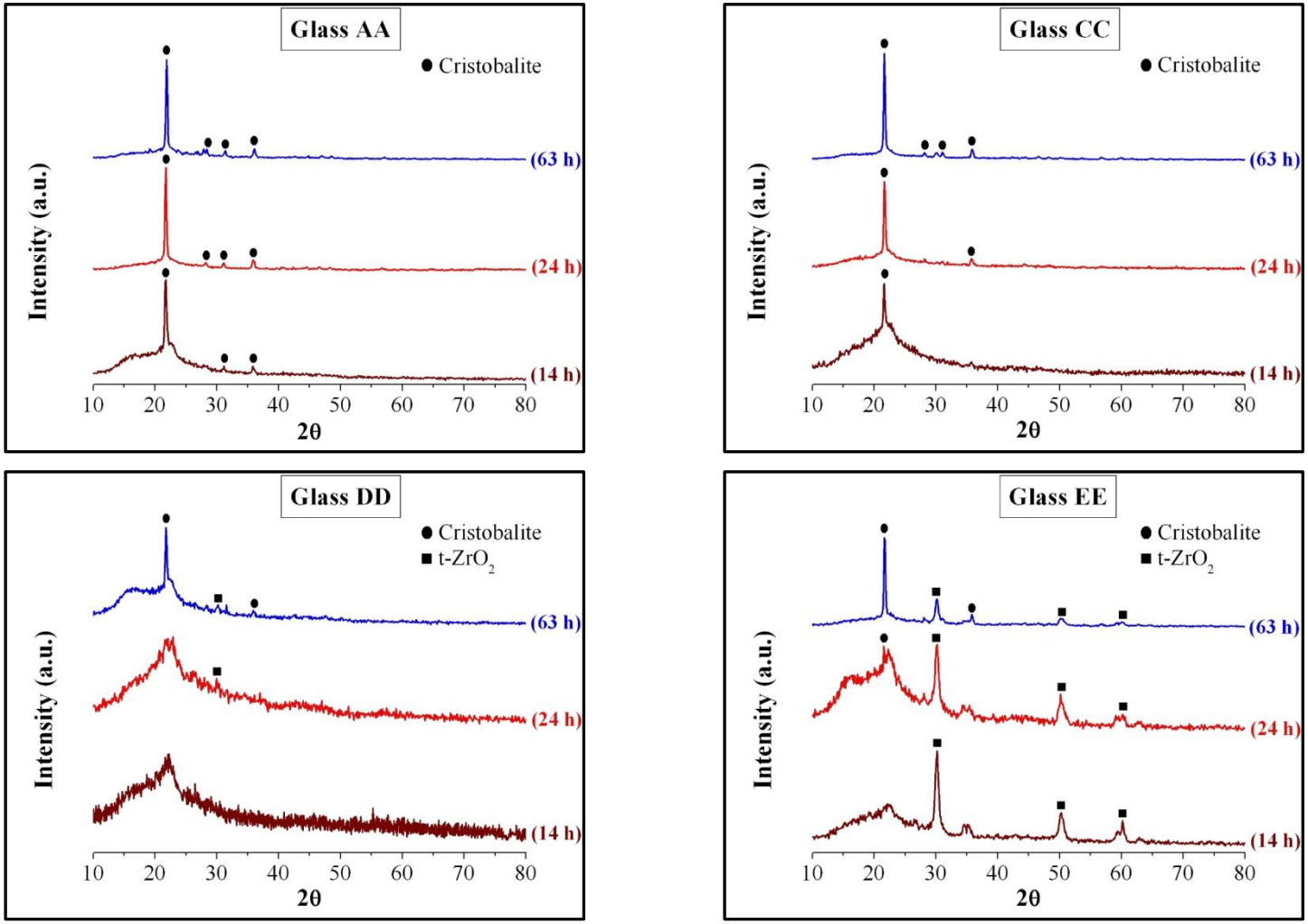

Figure 4.28: XRD patterns of glass AA, CC, DD, and EE heat-treated at 650 °C for 14 h, 24 h, and 63 h.

4.5.2 Fourier transform infrared (FTIR) spectroscopy

FTIR is widely used to interpret the structural modifications that occur during heat-treatment [142, 143, 166]. The FTIR spectrum of amorphous silica was reported on in other studies and the major peak corresponding to the asymmetric Si–O–Si stretching vibration has been recorded at approximately 1100 cm^{-1} [69, 142, 144]. The position of the Si–O–Si band changes depending on the type and amount of modifier cations introduced to the system [143, 167]. The increasing wavenumber with an increase of heat-treatment temperature or time in the structural band 1000–1100 cm^{-1} indicates a higher degree of phase separation and can be attributed to the increasing number of Si–O–Si bridging bonds [142, 143]. In the present study, it was found that the presence of a peak in the 610–627 cm^{-1} band indicates crystallisation.

4.5.2.1 Glass series A–E, $(65–x)SiO_2$-$25B_2O_3$-$10Na_2O$-$xZrO_2$

The FTIR absorbance spectra of glass series A–E are shown in Figure 4.31 and Figure 4.32. With higher alkali content (10 wt%) in glass series A–E, the spectra near 1100 cm^{-1} become broader. The major absorption peak at around 1035 cm^{-1} observed in the band 1000 – 1100 cm^{-1} may be attributed to asymmetric Si–O–Si stretching vibrations of the Si–O functional group present in glass A after heat-treated for 14 h at 650 °C. The broad peak shifts significantly towards the structural band near 1068 cm^{-1} as the heat-treatment dwell time was increased to 63 h. A peak at 610–627 cm^{-1} appears in the sample that was heat-treated for 63 h. The XRD study also identified the higher degree of crystallisation of cristobalite in this sample when heat-treated for 63 h (see Figure 4.26). Therefore, the presence of the peak at 610–627 cm^{-1} can be correlated with the crystallisation process. A decreasing trend was observed in the case of glass B where the broad peak shifted from 1057 cm^{-1} to 1050 cm^{-1} with increasing heat-treatment dwell time from 14 h to 63 h at 650 °C. An increasing trend in peak wavenumber, 1063 cm^{-1} to 1074 cm^{-1}, was observed in case of glass C when heat-treatment dwell time was increased from 14 h to 63 h at 650 °C. Figure 4.29 shows the FTIR spectra of as-quenched and heat-treated samples of Glass C, where heat-treatment was carried out for 24 h at varied temperatures between 630 and 700 °C. XRD analysis was also seen to correlate with these

findings (see Figure 4.30). It was noticed from the FTIR spectrum that the as-quenched non-heat-treated glass had a major peak at 1051 cm^{-1}. The peak started shifting towards a higher wave number as the heat-treatment temperature was increased to 680 °C. The peak shift then reversed towards a lower wavenumber at a heat-treatment temperature of 700 °C, while keeping heat-treatment duration (24 h) constant. The decrease in the IR peak wavenumber at 700 °C may be due to a decrease in the extent of phase separation. At a lower temperature, e.g. 630 °C, the immiscibility boundary was wide, but at a higher temperature it was near the edges and thus the extent of phase separation could decrease. The increasing wavenumber that corresponds to the incremental heat-treatment temperature rise in the range 630 – 680 °C, indicates a higher degree of phase separation and can be attributed to the increasing number of Si–O–Si bridging bonds [142, 143]. The broad band at about 680 cm^{-1} can be ascribed to BO_4 tetrahedrons [168]. A peak at 610–627 cm^{-1} appears in samples that were heat-treated at comparatively high temperatures (680 °C and 700 °C). The XRD study also identified the existence of cristobalite in these two samples.

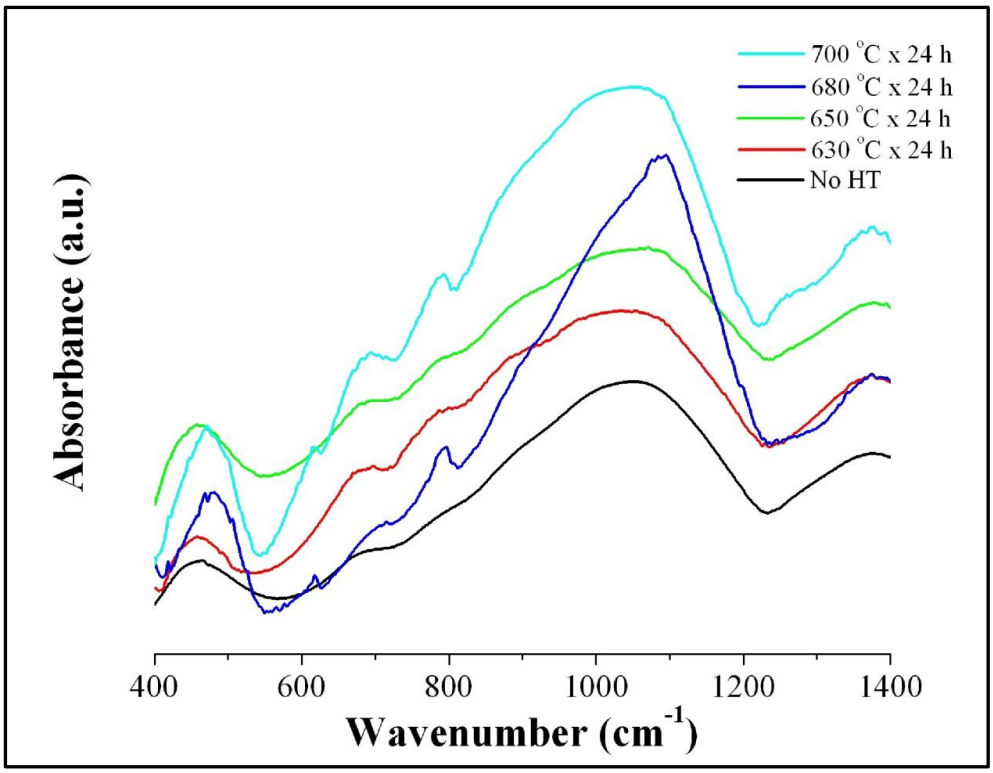

Figure 4.29: FTIR absorbance spectra for glass C as a function of heat-treatment: (i) before heat-treatment, (ii) 630 °C x 24 h, (iii) 650 °C x 24 h, (iv) 680 °C x 24 h, (v) 700 °C x 24 h.

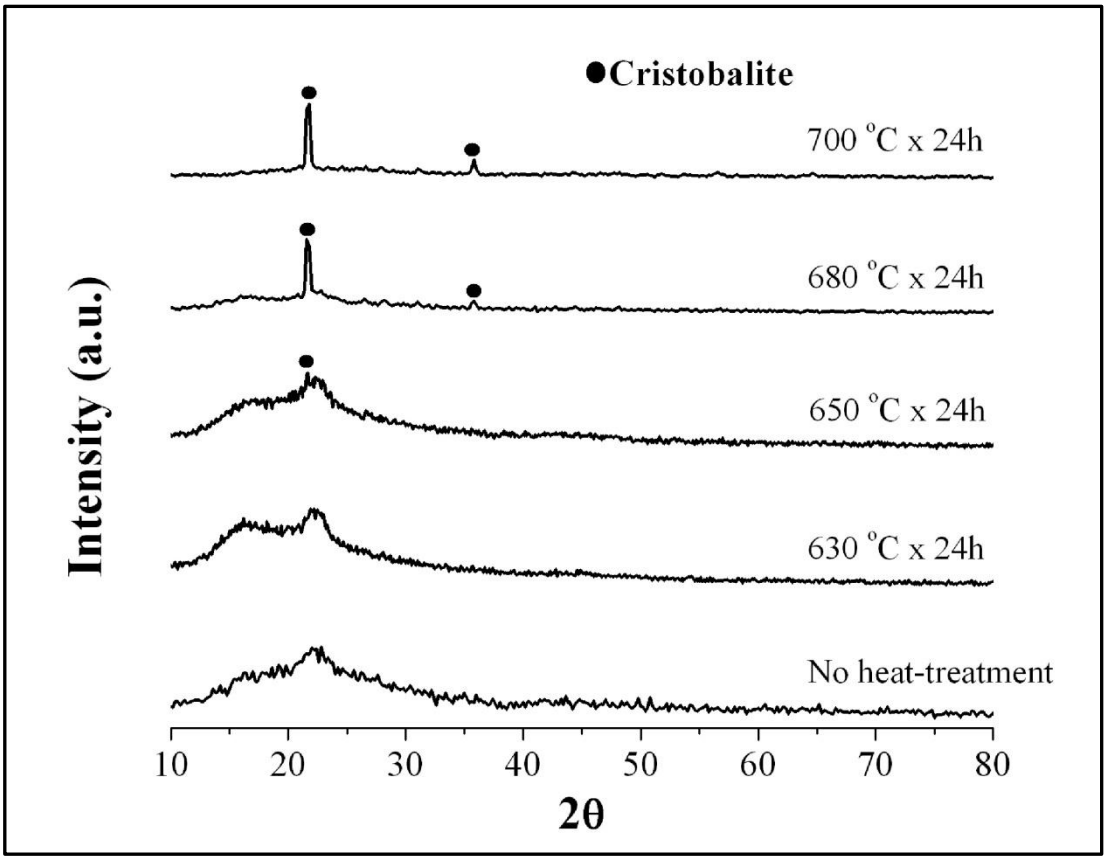

Figure 4.30: XRD patterns showing crystal formation before and after heat-treatment for 24 h at varied temperature (630–700 °C).

For glass D, a significant change in absorption peak shift from 1023 cm^{-1} to 1064 cm^{-1} was observed with increasing heat-treatment dwell time (14–64 h) at 650 °C. On the other hand, spectra for glass E show a peak at 991 cm^{-1} when heat-treated for 14 h at 650 °C, with the peak shifting to approximately 984 cm^{-1} with increasing heat-treatment dwell time (14–63 h). There was no peak observed in band 610–627 cm^{-1}. The XRD diffraction pattern indicated crystallisation of cristobalite when heat-treated for 63 h at 650 °C (see Figure 4.27).

4.5.2.2 Glass E-II ($54SiO_2$-$25B_2O_3$-$6Na_2O$-$15ZrO_2$)

An interesting absorbance peak spectrum was noticed in glass E-II as shown in Figure 4.32, where the strong peak at 1063 cm^{-1} shifted towards a lower wavenumber at around 1051 cm^{-1} with increasing heat-treatment dwell time (14–63 h) at 650 °C. The major peak observed in glass E-II was sharper compared to glass series A–E. A peak at 613 cm^{-1}, which is in 610–627 cm^{-1} band, was observed when

heat-treated for 63 h at 650 °C. This is consistent with the XRD pattern of glass E-II (see Figure 4.27) which shows crystallisation peaks.

4.5.2.3 Glass F ($50SiO_2$-$25B_2O_3$-$4Na_2O$-6CaO-$15ZrO_2$)

The shape of the absorbance peak in the 1000–1100 cm^{-1} band is broader in glass F as compared to glass series A–E as shown in Figure 4.32. With increasing heat-treatment dwell time from 14 h to 24 h at 700 °C, no shift was observed in the Si–O–Si stretching band. The peak appeared at 616 cm^{-1}, which is in the 610–627 cm^{-1} band, when heat-treated for 24 h. This is coherent with the XRD pattern of glass F (see Figure 4.27) where a strong cristobalite crystallisation peak was observed. There is a correlation between crystallisation and major peak wavenumber, with increasing crystallisation the major peak wavenumber also increased [144]. Therefore, it may be concluded that the extent of phase separation is higher when the heat-treatment dwell time is 14 h compare to 24 h at 700 °C even though the major peak observed was in the same wavenumber.

4.5.2.4 Glass series AA–EE, (69–x)SiO_2-$25B_2O_3$-$6Na_2O$-x$ZrSiO_4$

A common trend was observed in the shifting of the major peak towards lower wavenumber, indicating Si–O–Si stretching, in glass series AA–EE when heat-treated at 650 °C for varied dwell times (14–63 h), as shown in Figure 4.33. For glass AA, the spectra look broader in the 1000–1100 cm^{-1} band compared to the rest of the glass compositions (CC–EE) in this series. The broad peak shifted slightly from 1068 cm^{-1} to near 1073 cm^{-1} as the heat-treatment dwell time was increased from 14 h to 63 h. A small peak was observed in band 610–627 cm^{-1} for heat-treatment dwell times of 24 h and 63 h. With glass CC, the peak remains at 1078 cm^{-1} with increasing heat-treatment dwell time from 14–24 h at 650 °C. A significant decrease, from 1078 cm^{-1} to 1065 cm^{-1}, was observed with further increased heat-treatment dwell times (24–63 h). A small peak was observed in band 610–627 cm^{-1} when heat-treated for 63 h. The shifting trend of the major peak associated with a small peak in 610–627 cm^{-1} band when heat-treated for 63 h suggests that phase separation decreased with increasing dwell time for glass CC. No major peak shift was observed between 14 h to 24 h at 650 °C on glass DD. However, a significant move

from 1064 cm^{-1} to 1085 cm^{-1} was observed with further increments of heat-treatment dwell time (24–63 h). The presence of a small peak in band 610–627 cm^{-1} was observed when heat-treated for 63 h. Spectra for glass EE show that the peak shift from 1057 cm^{-1} to 1051 cm^{-1} when the heat-treatment dwell time was increased (14–24 h). With further increases in dwell time (24–63 h), the peak shifted towards the higher wavenumber of 1070 cm^{-1}, which is probably due to crystallisation as a small peak was present in band 610–627 cm^{-1} when heat-treated for 63 h. The presence of a small peak in the 610–627 cm^{-1} band indicating crystallisation is consistent with the XRD findings where crystallisation is detected in glass EE with the same heat-treatment as shown in Figure 4.28.

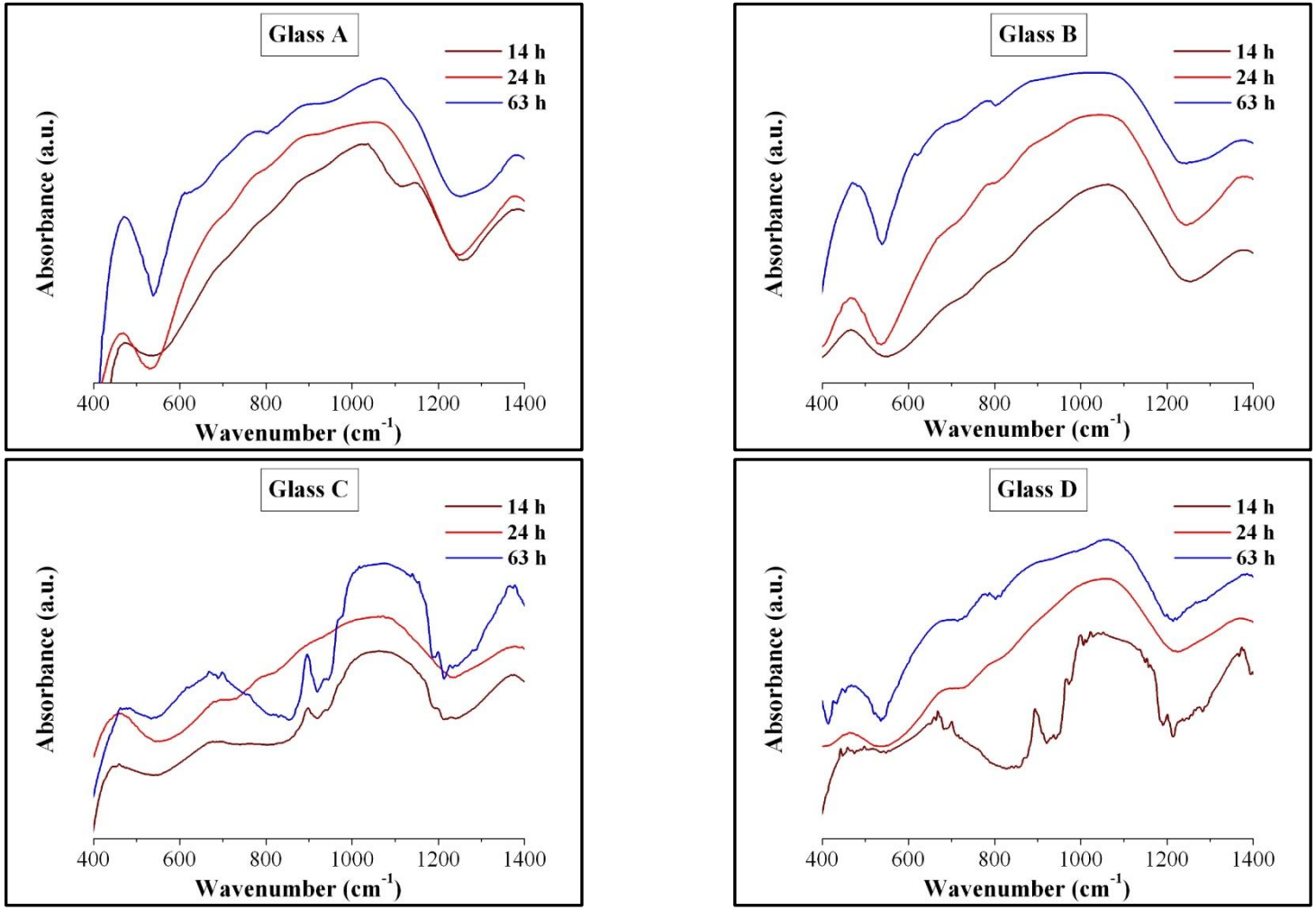

Figure 4.31: FTIR absorbance spectra for glass A, B, C, and D heat-treated at 650 °C for 14 h, 24 h, and 63 h.

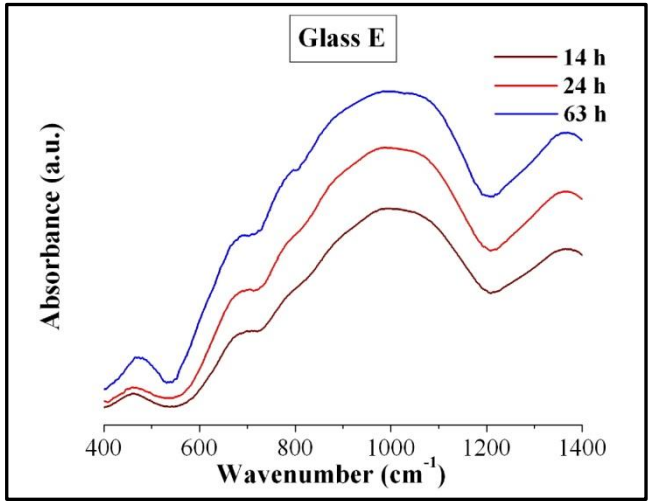

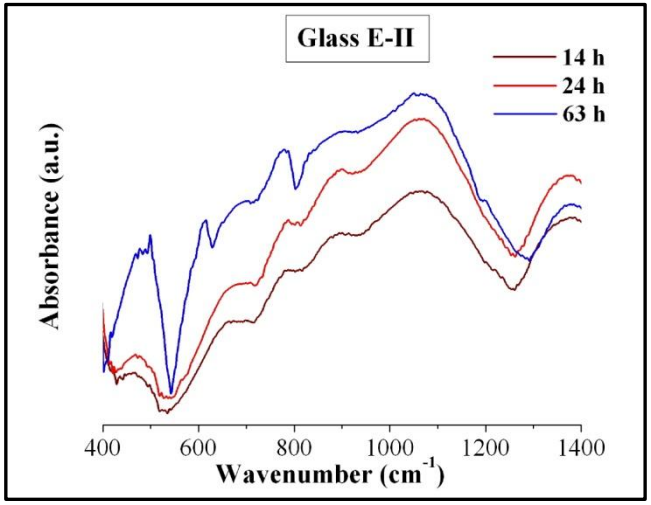

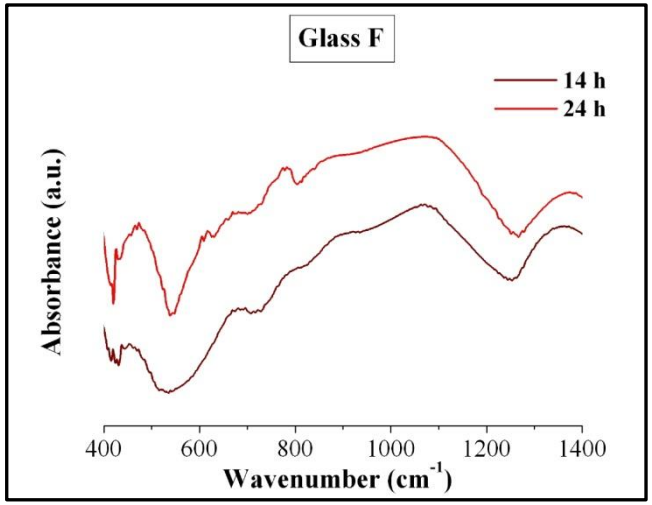

Figure 4.32: FTIR absorbance spectra for glass E and E-II heat-treated at 650 °C for 14 h, 24 h, and 63 h. Glass F heat-treated at 700 °C for 14 h and 24 h.

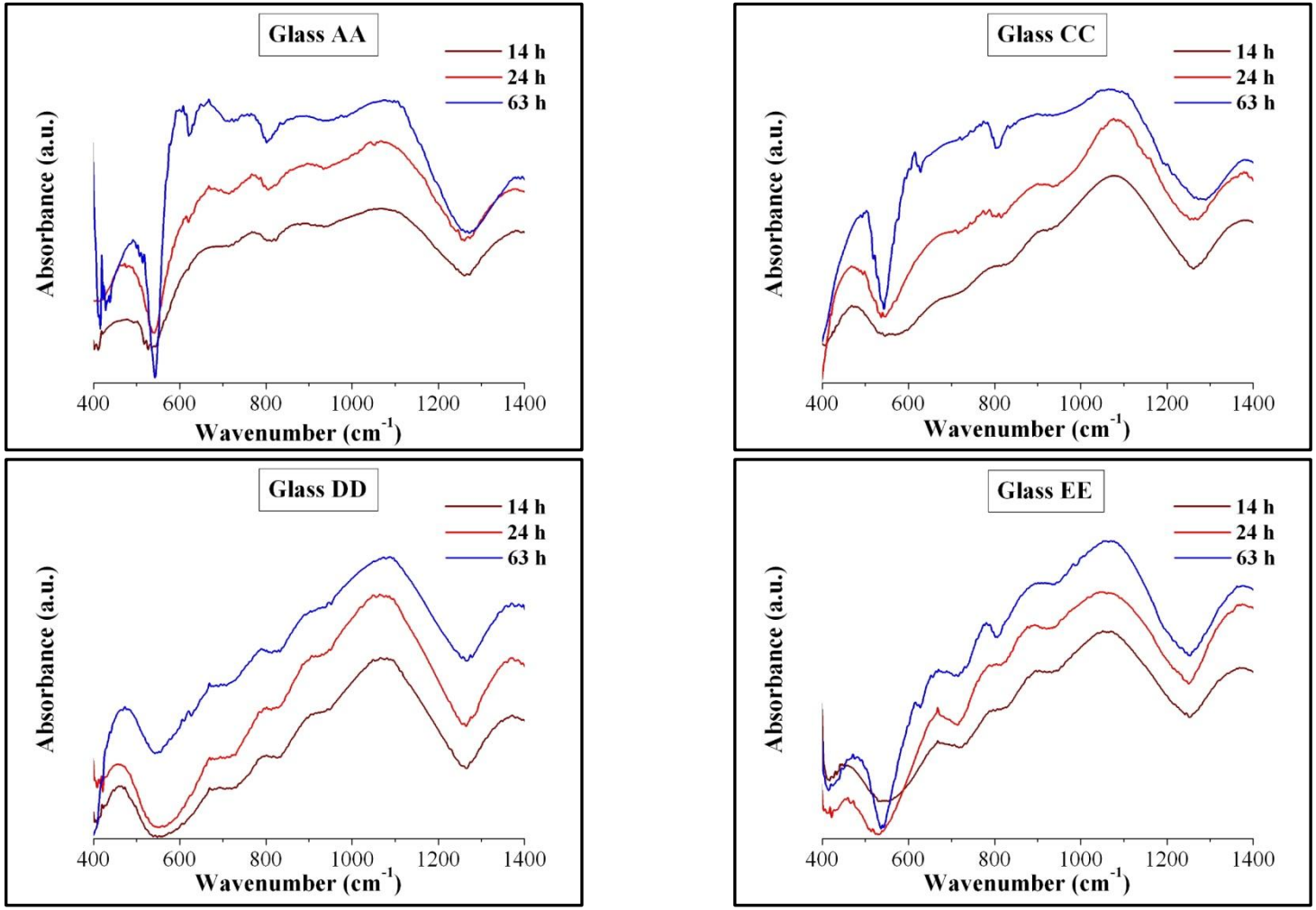

Figure 4.33: FTIR absorbance spectra for glass AA, CC, DD, and EE heat-treated at 650 °C for 14 h, 24 h, and 63 h.

4.6 ACID LEACHING FOLLOWED BY ALKALI WASHING

Porous glass can be derived from heat-treated glass that has been separated into two-phases by heat-treatment; i.e.: a silica-rich phase, and an alkali-rich borate phase. The heat-treated glass is then leached selectively to remove one of these phases. An extensive literature review was conducted to adopt the proper leaching procedure. When ZrO_2 is present in the sodium borosilicate glass system, a different sequence of acid leaching steps should be followed. Heat-treated glass of composition C and D were selected for determining the most suitable common leaching steps. Based on information from the literature, glass C (7 wt% ZrO_2), which had been heat-treated at 700 °C for 14 h, was first immersed in 0.25 N – 3 N HNO_3 at 95–98 °C for 24 h. In this initial step in which the sodium rich borate phase was removed, a gel rich in zirconia and silica formed and remained in the silica rich structure [8]. To remove the zirconia gel, a further acid treatment with 3 N H_2SO_4 acid was then carried out, as suggested in the literature [8, 9, 48]. The rigid pores of the resulting silica-rich phase skeleton were substantially filled with colloidal silica, which as suggested in the literature is a decomposition product of the removed microphase [7, 80]. To remove the colloidal silica, the silica skeleton was treated with a solvent of dilute NaOH solution of 0.5 N concentration, for 1 to 5 hours at 25 °C [3, 6, 8, 9, 76]. As suggested by Smith and Paul [89] the NaOH solution should be within the range of 0.5 N as concentrations beyond 0.5 N doubled the rate of attack in some instances. Table 4.5 compares the effect of varied leaching steps with pore characteristics data obtained from mercury porosimetry. It is interesting to see that the weak concentration of 0.25 N HNO_3 alone, without any gel removing steps, shows a higher surface area and pore volume compare to when it is followed by silica gel washing. Because of the use of acid with a lower concentration, there is less silica gel formation and the washing step of 0.5 N NaOH for 5 h may possibly destroy the silica skeleton. As a result pore volume is significantly reduced. Whilst keeping the leaching step constant (1 N HNO_3 for 24 h), the gel removing steps were varied to check their effect on pore characteristics. It is clear from the pore characterisation data that leaching did not work properly without the washing steps. Increasing the concentration of HNO_3, from 0.25 N to 1 N, increased the colloidal silica gel

formation, which then needed to be washed. With extending the duration of the gel removing steps, both surface area and pore volume increased.

Table 4.5: Different leaching steps and their impact on pore characteristics for glass C (700 °C x 14 h).

Leaching steps			Total surface area	Pore volume
Step 1	**Step 2**	**Step 3**	**(m^2/g)**	**(cm^3/g)**
0.25 N HNO_3 (24 h)	-	-	3.46	0.127
0.25 N HNO_3 (24 h)	-	0.5 N NaOH (5 h)	2.39	0.075
1 N HNO_3 (24 h)	3 N H_2SO_4 (6 h)	-	0.01	0.050
1 N HNO_3 (24 h)	3 N H_2SO_4 (6 h)	0.5 N NaOH (2 h)	5.53	0.166
1 N HNO_3 (24 h)	3 N H_2SO_4 (6 h)	0.5 N NaOH (5 h)	0.83	0.189
1 N HNO_3 (24 h)	3 N H_2SO_4 (24 h)	0.5 N NaOH (5 h)	3.44	0.355

The effect of different leaching steps on the pore characteristics of glass D heat-treated at 650 °C for 24 h is shown in Table 4.6. Increasing acid concentration, from 0.25 N HNO_3 to 1 N HNO_3, led to a decrease in both the surface area and the pore volume. Increasing the leaching duration with the same acid concentration increased the surface area and pore volume.

Table 4.6: Different leaching steps and their impact on pore characteristics for glass D (650 °C x 24 h).

Leaching steps			Total surface area	Pore volume
Step 1	**Step 2**	**Step 3**	**(m^2/g)**	**(cm^3/g)**
0.25 N HNO_3 (7 h)	-	-	3.04	0.078
1 N HNO_3 (5 h)	3 N H_2SO_4 (2 h)	0.5 N NaOH (1 h)	0.06	0.053
1 N HNO_3 (18 h)	3 N H_2SO_4 (6 h)	0.5 N NaOH (2 h)	2.69	0.033
1 N HNO_3 (24 h)	3 N H_2SO_4 (24 h)	0.5 N NaOH (5 h)	7.97	0.440

From the results outlined in Table 4.6 and Table 4.7, it is evident that the leaching steps of 1 N HNO_3 (24 h) followed by 3 N H_2SO_4 (24 h) and 0.5 N NaOH (5 h) led to high surface area with larger pore volume. Therefore, this sequence of leaching steps was carried out in this study for glasses containing ZrO_2/$ZrSiO_4$. An H_2SO_4 leaching step was found to be unnecessary for ZrO_2/$ZrSiO_4$ free compositions. This step (H_2SO_4 leaching) was not carried out for CaO containing glass (glass F), as the whole sample eluted when 3 N H_2SO_4 was used.

4.7 LEACHED GLASS CHARACTERISATION

Pore characterisation of leached glasses was conducted by using mercury-based porosimetry. Nitrogen based adsorption analysis was also carried out on selected leached glasses to measure specific surface area and compare the pore volume and average pore size with mercury based porosimetry. The Scanning Electron Microscopy (SEM) was used to identify the mechanism by which the phase separation occurred. Pore morphology was also studied with SEM. Energy Dispersive X-ray Spectroscopy (EDXS) was employed to identify the elemental composition of porous glasses.

4.7.1 Pore characterisation by mercury porosimetry

The pore characteristics of heat-treated and leached glasses were measured by using mercury intrusion porosimetry (MIP). In a single measurement it can quantify the pore size, size range, pore volume, surface area, bulk and apparent density, and other porosity-related information of porous glasses.

4.7.1.1 Glass series A–E, $(65–x)SiO_2$-$25B_2O_3$-$10Na_2O$-$xZrO_2$

The most basic graph representing mercury intrusion analysis data is a plot of pore diameter (nm) on a logarithmic scale *vs.* the corresponding cumulative intrusion volume (cc/g). The log differential intrusion superimposed on a plot of cumulative intrusion volume *vs.* diameter can identify the pore-size distribution as well as pore volume. Since larger pores are filled first at lower pressures in mercury porosimetry, the abscissa in the figures are plotted in reverse order. The effect of thermal treatment on the pore characteristics of glass series A–E are presented in Table 4.7. The pore-size distribution characteristics for each glass composition in this glass series are described in the following sections.

Table 4.7: Effect of thermal treatment on pore characteristics for the glass series A–E, $(65–x)SiO_2$-$25B_2O_3$-$10Na_2O$-$xZrO_2$, measured by porosimetry.

	Thermal treatment		Mean pore diameter	Total surface area	Pore volume	pore volume <1000 nm	Porosity	Porosity <1000 nm
Glass	Temperature (°C)	Period (h)	(nm)	(m^2/g)	(cm^3/g)	%	%	%
A	650	14	122	2.35	0.204	36	5.78	2.07
A	650	24	240	2.90	0.596	19	15.00	2.80
A	650	63	1495	1.26	1.030	18	19.49	3.59
B	650	14	67	6.37	0.267	47	7.62	3.60
B	650	24	58	8.32	0.296	59	7.53	4.42
B	650	63	642	1.53	0.650	35	13.77	4.77
C	650	14	74	2.42	0.109	25	2.68	0.68
C	650	24	61	1.56	0.066	32	2.17	0.68
C	650	63	232	2.13	0.336	46	9.35	4.26
C	700	14	186	3.44	0.355	46	9.39	4.35
D	650	14	466	1.53	0.531	9	11.60	0.99
D	650	24	85	7.97	0.440	27	11.85	3.16
D	650	63	642	3.05	1.148	27	23.59	6.47
D	700	14	222	9.65	1.246	32	21.65	6.84
E	650	14	92	2.36	0.200	11	5.93	0.65
E	650	24	41	6.10	0.192	21	7.37	1.55
E	650	63	283	1.83	0.419	17	11.76	1.99
E	700	14	805	1.45	0.827	16	19.64	3.18

(i) Glass A ($65SiO_2$-$25B_2O_3$-$10Na_2O$)

The pore size distribution for glass A, as obtained from mercury porosimetry, is presented in Figure 4.34. The glass was heat-treated for 14 h, 24 h, and 63 h at 650 °C. Distributions showing multiple peaks were observed below 500 nm. However, the major mercury intrusion occurred in the range 140 – 340 nm. The multiple peaks correspond to varied pore-size distributions that were developed during heat-treatment and leaching. Small peaks that appeared in the lower pore-size range may be attributed to the gels that formed during leaching and were trapped inside the pores. From Figure 4.34, it is apparent that the multiple peaks which appeared in lower pore-size range, disappeared with increasing heat-treatment dwell time. It was also observed that the pore volume increased, while surface area decreased, as a result of increasing heat-treatment dwell time. The increasing heat-treatment dwell time coarsens the phase separated structure and thus led to a reduction in surface area and an increase of the pore volume after leaching. It is interesting to note that the pore volume below 1000 nm dramatically reduced when dwell time was increased from 24 to 63 h. Mean pore diameter also increased from 240 to 1495 nm with this increment in dwell time.

(ii) Glass B, C, and D

Glass B shows a similar trend in pore distribution as glass A (see Figure 4.35). However, the distribution is narrower and average pore size is smaller compared to glass A. The pore volume increased with increasing heat-treatment dwell time, while surface area decreased. No mercury intrusion is noticed < 100 nm with dwell time increasing from 24 h to 63 h. The coarsening effect is more apparent here as the pore distribution peak shifted towards a broader distribution with a range of 200 – 1100 nm. The multiple pore distribution peaks in the lower pore-sizes changed to a broader pore distribution peak with increasing heat-treatment dwell time at 650 °C, as shown in Figure 4.36. A dramatic increase in pore volume is observed when dwell time was increased from 24 h to 63 h. Pore volume was found to be similar when glass C was heat-treated either at 650 °C for 63 h or at 700 °C for 14 h. However, the pore-size distribution curve is moved towards a larger size of pore when heat-treatment temperatures were increased from 650 °C to 700 °C, as shown in Figure 4.37.

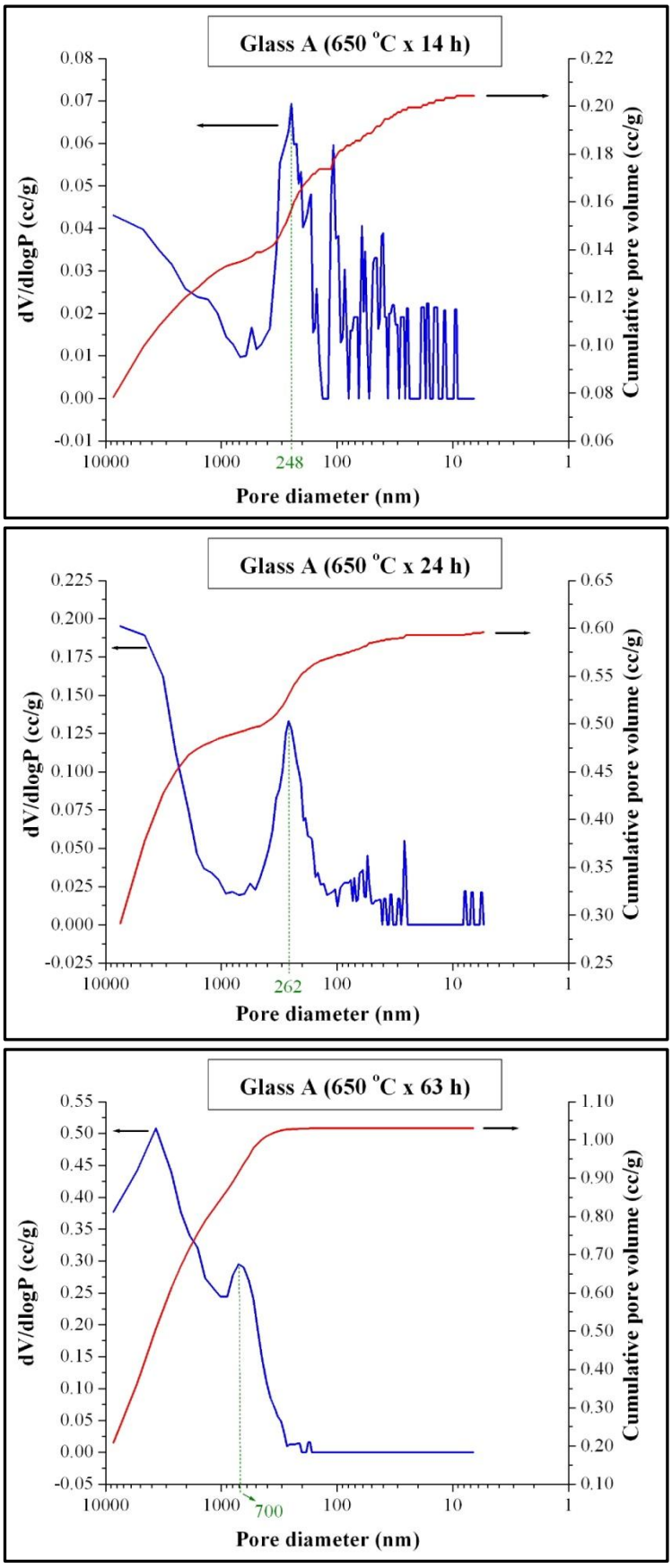

Figure 4.34: Pore-size distribution curves of porous Glass A determined by mercury intrusion.

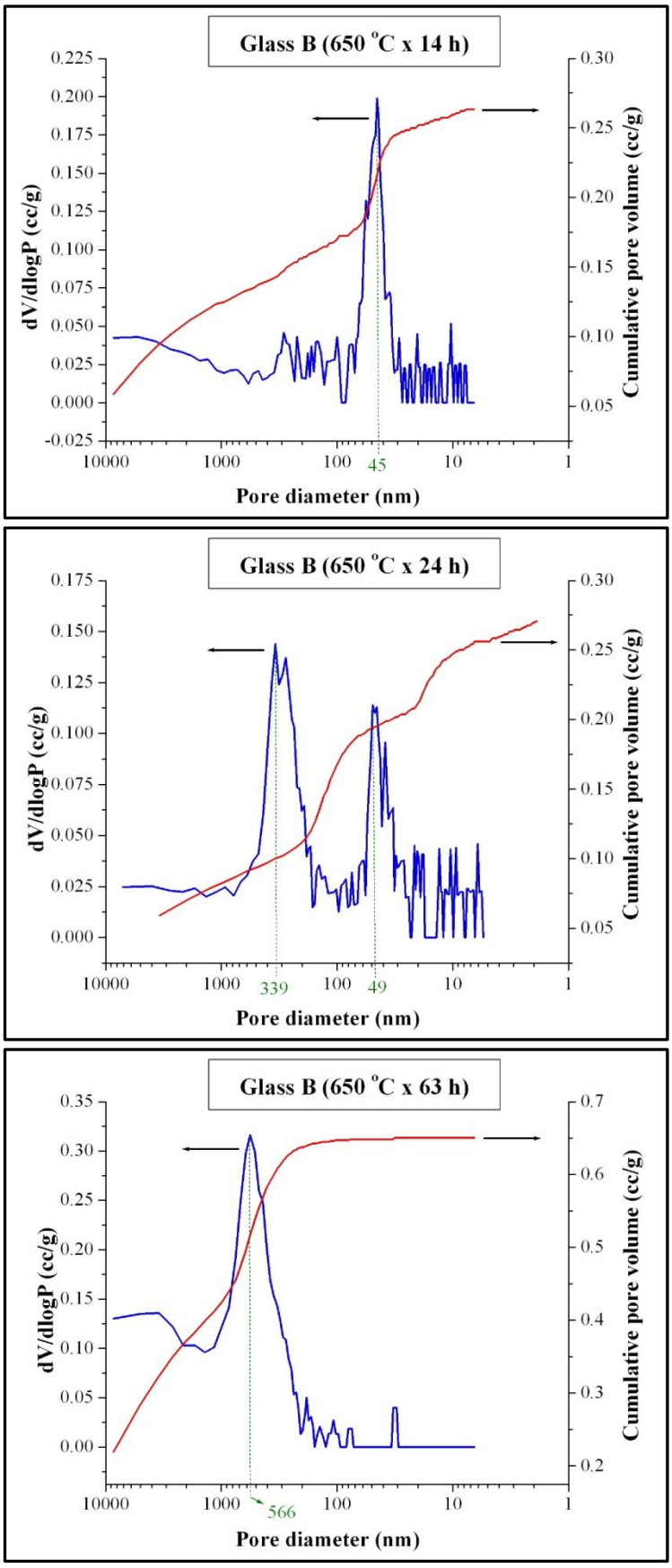

Figure 4.35: Pore-size distribution curves of porous Glass B determined by mercury intrusion.

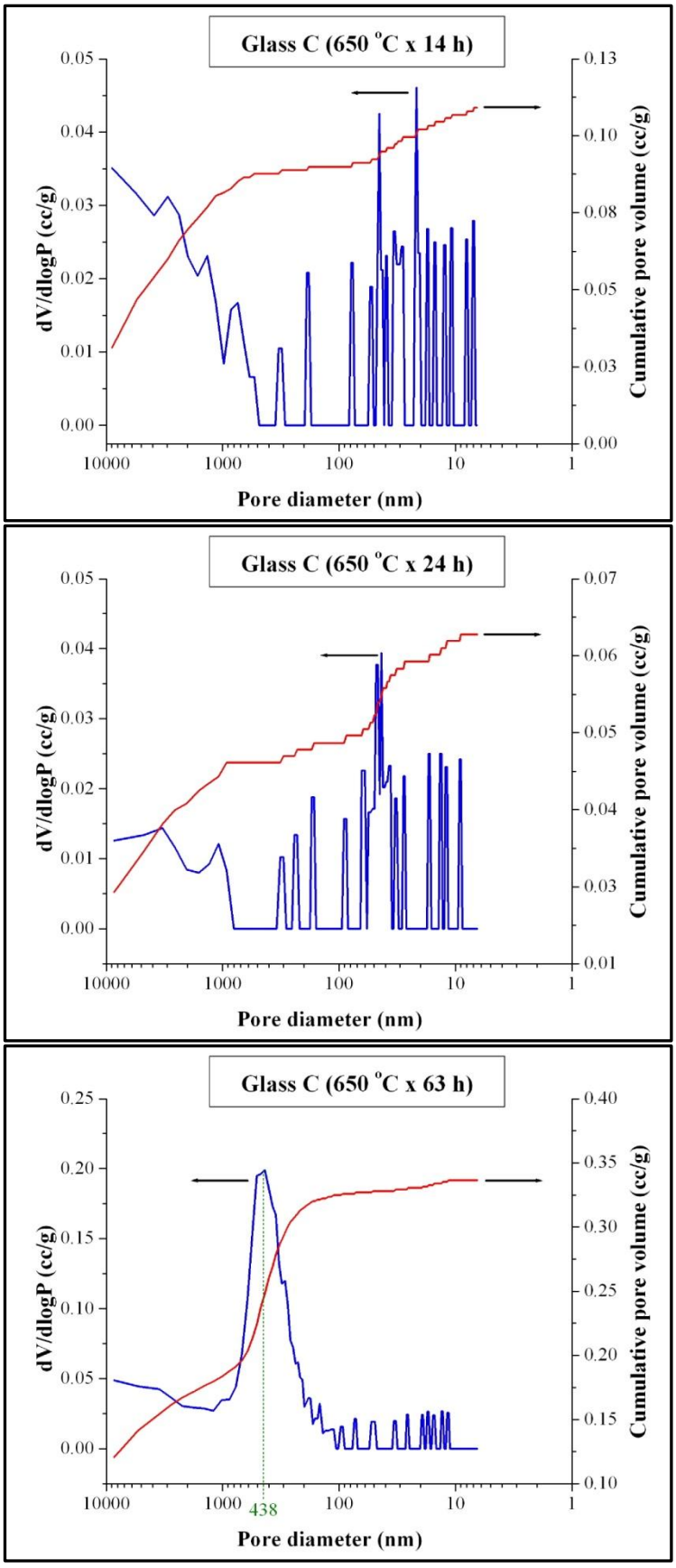

Figure 4.36: Pore-size distribution curves of porous Glass C determined by mercury intrusion.

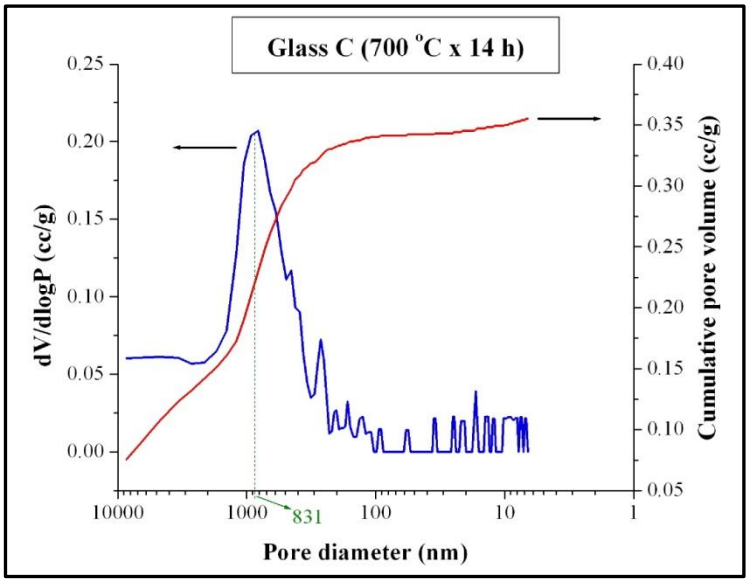

Figure 4.37: Pore-size distribution curves of porous Glass C determined by mercury intrusion after heat-treatment at 700 °C for 14 h.

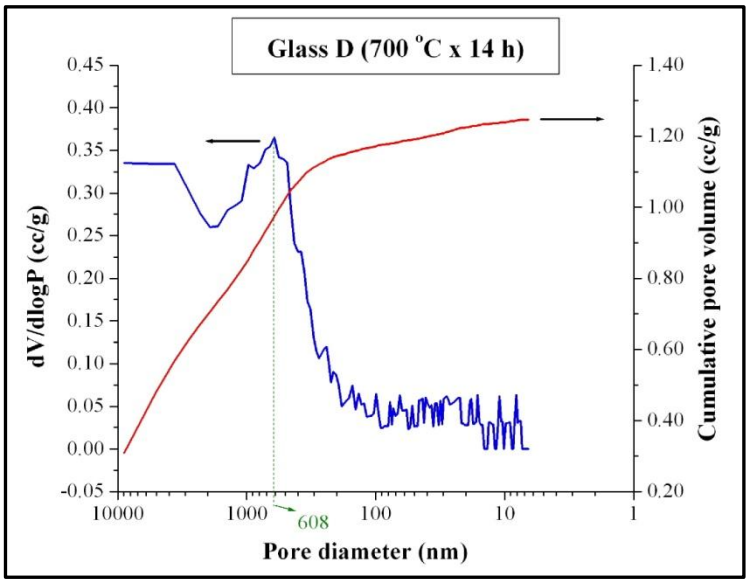

Figure 4.38: Pore-size distribution curves of porous Glass D determined by mercury intrusion after heat-treatment at 700 °C for 14 h.

No mercury intruded below 700 nm in glass D, which was heat-treated at 650 °C for 14 h, as shown in Figure 4.39. The pore-size distribution moved towards a smaller size with increased heat-treatment dwell time. Pore volume < 1000 nm also increased with increasing heat-treatment dwell time. Like glass C, pore volume in glass D was found to be similar when glass D was heat-treated either at 650 °C for 63 h or at 700 °C for 14 h (see Figure 4.38).

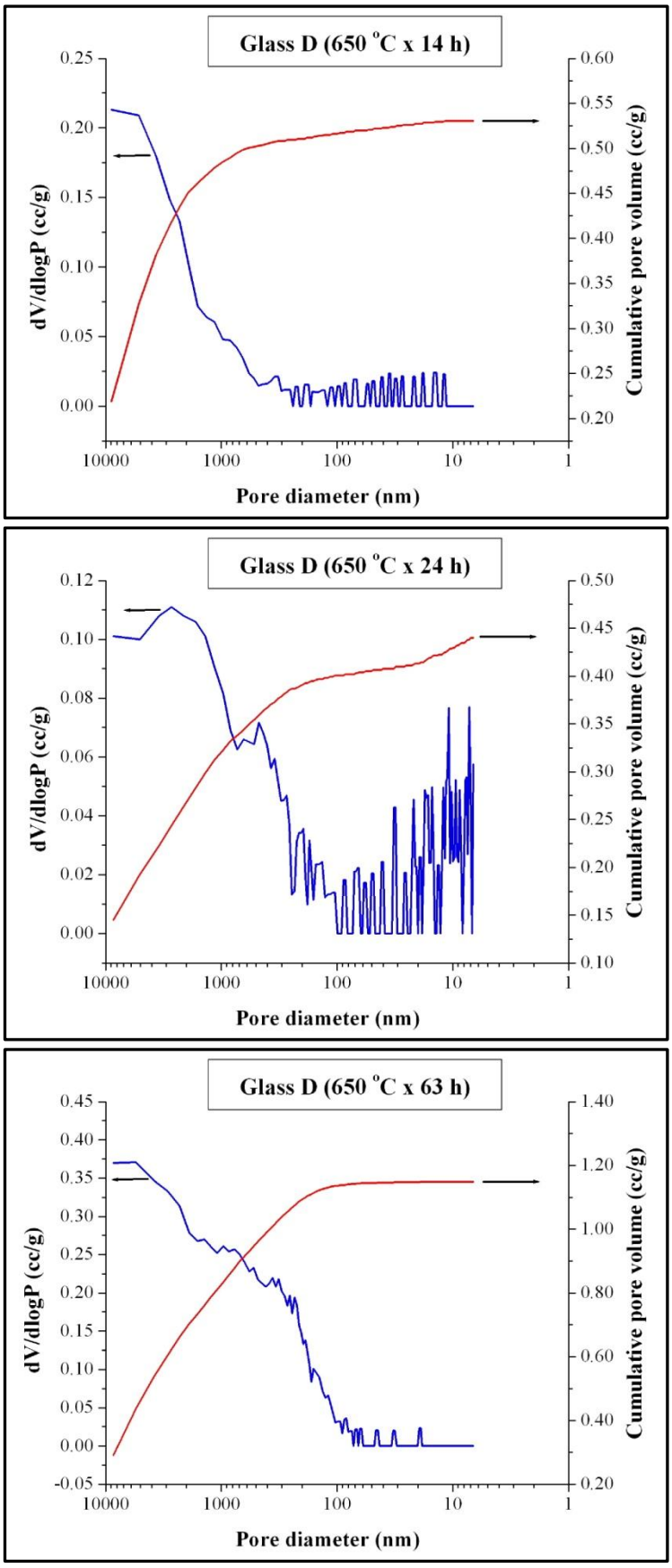

Figure 4.39: Pore-size distribution curves of porous Glass D determined by mercury intrusion.

(iii) Glass E ($50SiO_2$-$25B_2O_3$-$10Na_2O$-$15ZrO_2$)

Figure 4.40 and Figure 4.41 show the pore-size distribution of glass E, heat-treated at 700 °C and 650 °C respectively for various dwell times (14–63 h). The pore volume below 300 nm decreased with increasing heat-treatment dwell time. It is evident that increasing ZrO_2 content in glass series A–E impacted on pore-size below 300 nm. Introducing ZrO_2 <7 wt%, the pore volume decreased slightly but the mean pore-size decreased dramatically. This trend is consistent with the findings of Du et al. [10]. With a similar sodium borosilicate system containing > 12 wt% of ZrO_2, Du et al. found no peaks in the pore distribution pattern, and pore volume and surface area approached zero. In the present study pore volume below 1000 nm was increased with increasing heat-treatment dwell time at 650 °C when ZrO_2 content is ≤ 11 wt%. When ZrO_2 content increased to 15 wt% (glass E), the pore volume below 1000 nm dramatically decreased even at extended heat-treatment times. This result indicates that ZrO_2 has an inhibiting effect on phase separation. Initially the surface area increased significantly when ZrO_2 content in the sodium borosilicate glass being ≤ 3 wt%. Subsequently, the surface area was more likely to vary with varying heat-treatment conditions. However, Du et al. [10] reported a dramatic decrease in surface area when ZrO_2 content is > 7 wt%.

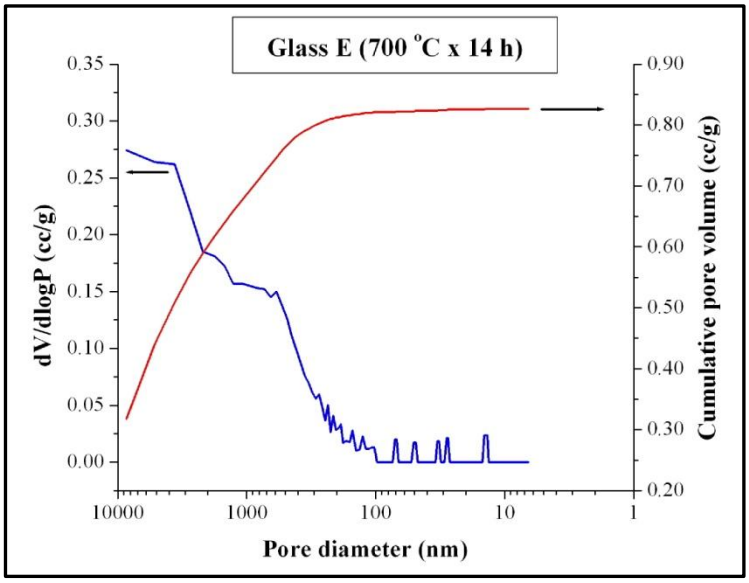

Figure 4.40: Pore-size distribution curves of porous Glass E determined by mercury intrusion after heat-treatment at 700 °C for 14 h.

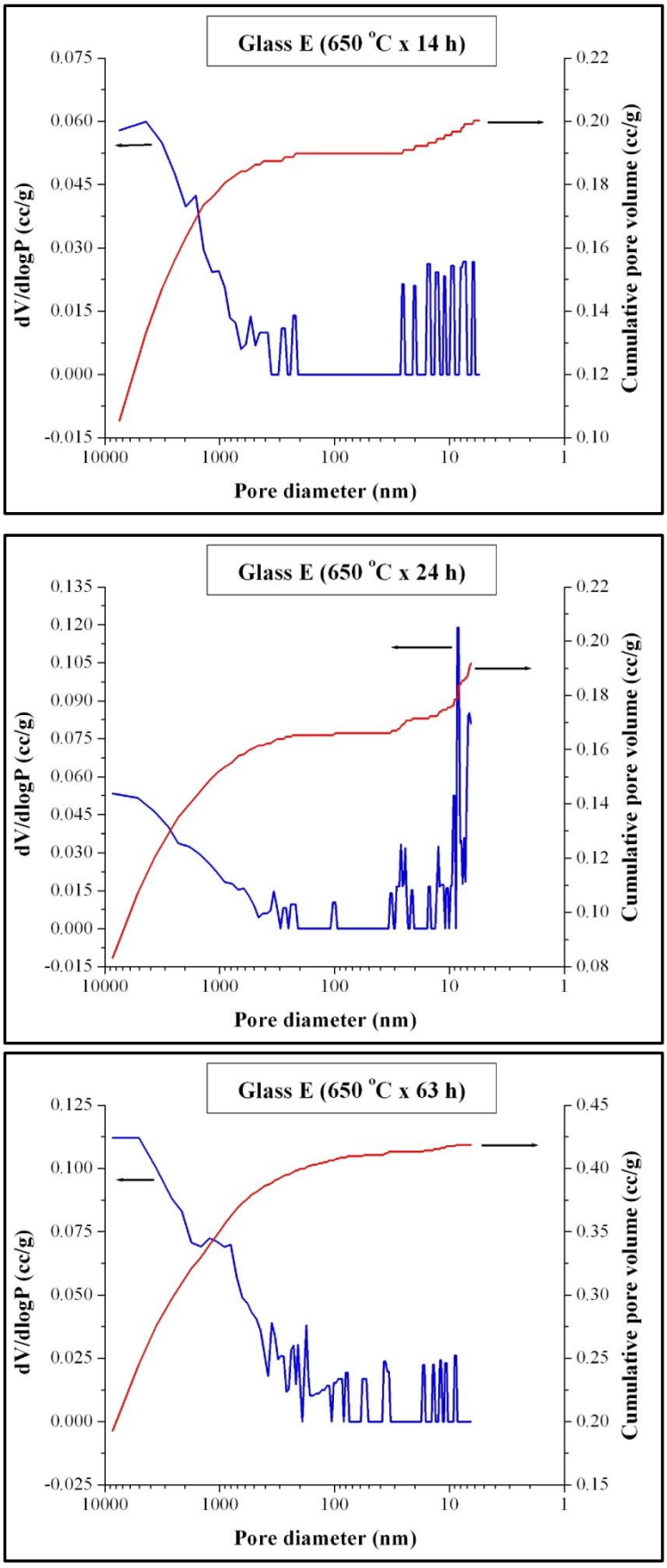

Figure 4.41: Pore-size distribution curves of porous Glass E determined by mercury intrusion.

The results presented in Table 4.7 show that ZrO_2 has an inhibiting effect on pore size growth. The mean pore size reduced dramatically when ZrO_2 was added. However, no further significant change in mean pore size was observed when ZrO_2 content was > 3 wt%. Figure 4.42 shows the relationship between the mean pore diameter and the square root of heat-treatment dwell time at 650 °C for glass series A–E. It is evident that mean pore diameter is linearly related to the square root of the heat-treatment dwell time. Kukizaki [48] and Yazawa et al. [9] also found a linear relationship between mean pore diameter and heat-treatment time.

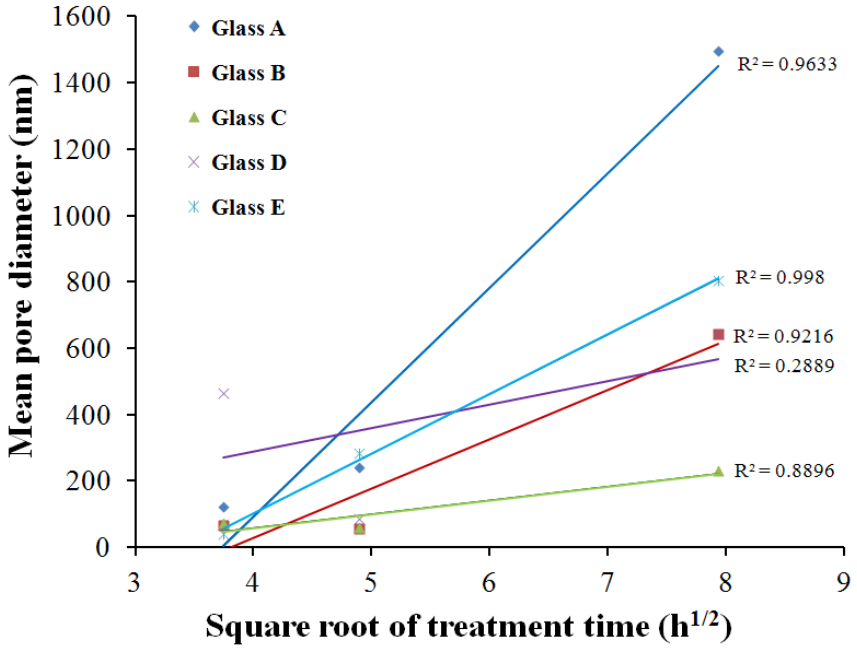

Figure 4.42: Relationship between heat-treatment dwell time and pore diameter for glass series A–E after heat-treatment at 650 °C.

4.7.1.2 Glass E-II ($54SiO_2$-$25B_2O_3$-$6Na_2O$-$15ZrO_2$)

A significant change is observed in the pore characteristics between glass E-II (6 wt% Na_2O, 15 wt% ZrO_2) and E (10 wt% Na_2O, 15 wt% ZrO_2). Figure 4.43 shows the pore-size distribution curve of glass E-II which shift towards larger pore size with increasing heat-treatment dwell time at 650 °C. The distribution peak also becomes broader with increasing dwell time. Considering the logarithmic scale in abscissa, the pore size distribution is narrower compare to any glass in glass series A–E.

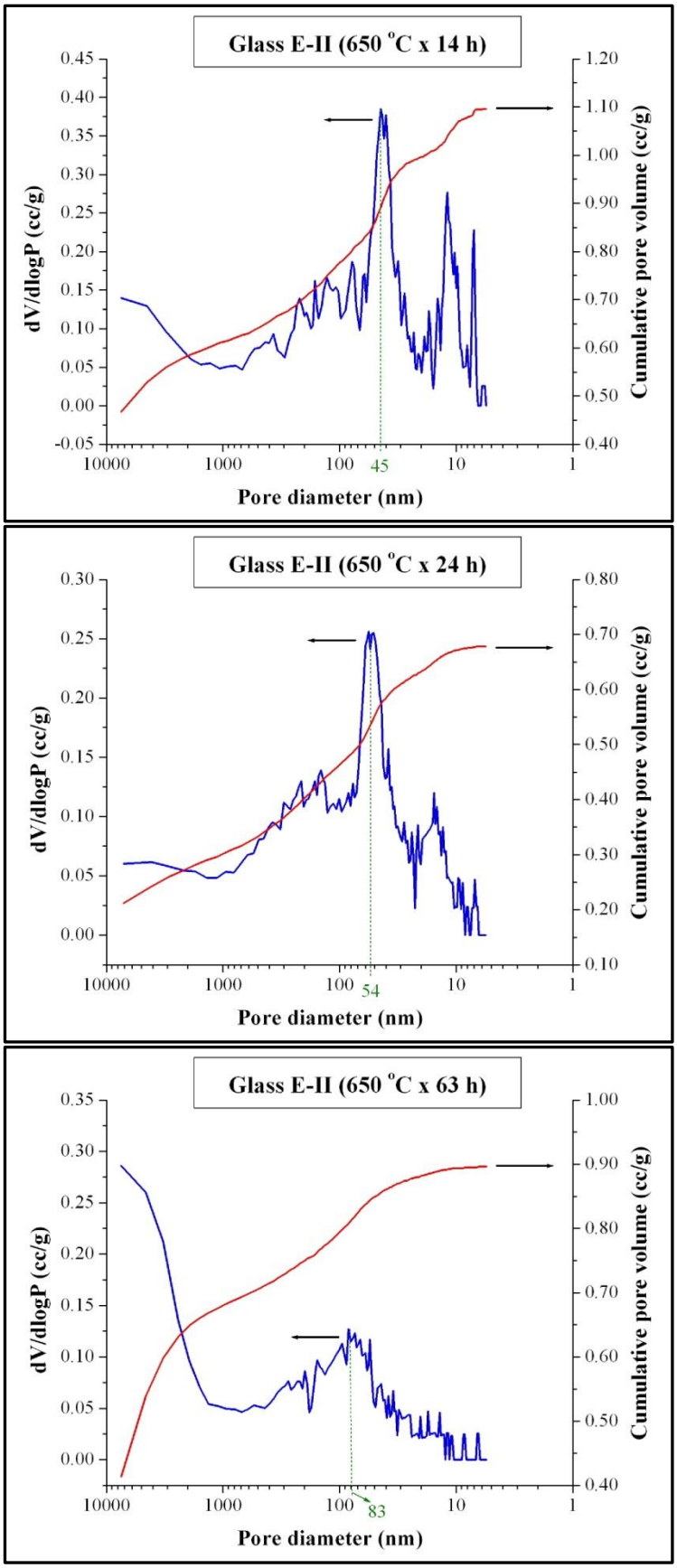

Figure 4.43: Pore-size distribution curves of porous Glass E-II determined by mercury intrusion.

Table 4.8 shows the effect of thermal treatment on pore characteristics of glass E-II. The pore volume decreased significantly when dwell time increased initially (14–24 h). However the percent of porosity < 1000 nm showed a decreasing trend with increasing heat-treatment dwell time. Surface area was measured ~ 35 m^2/g for the glass E-II when heat-treated for 14 h at 650 °C. The surface area is significantly higher compare to any of the glass compositions in glass series A–E. Figure 4.44 shows the relationship between the mean pore diameter and the square root of heat-treatment dwell time at 650 °C. It is evident that mean pore diameter is linearly related to square root of heat-treatment dwell time.

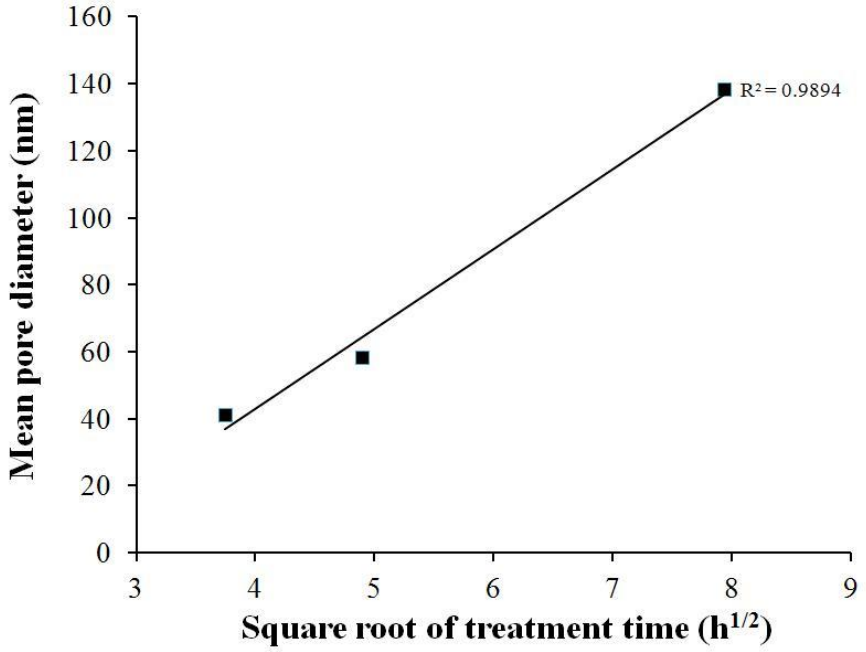

Figure 4.44: Relationship between heat-treatment dwell time and pore diameter for glass series E-II after heat-treatment at 650 °C.

4.7.1.3 Glass F ($50SiO_2$-$25B_2O_3$-$4Na_2O$-6CaO-$15ZrO_2$)

Figure 4.45 shows the pore-size distribution curve of glass F heat-treated at 700 °C for 14 h. The pore-size distribution is narrower compare to any glass composition in glass series A–E and encompasses pores of 22 – 60 nm. Due to narrow distribution of pore-size, the major contribution in total pore volume came from the pores size of 22 – 60 nm. As can be seen from the pore characterisation data in Table 4.8, the surface area of this glass is ~ 34 m^2/g. This surface area of glass F is almost the same as E-II when heat-treated for 14 h at 650 °C. However, the mean pore size of glass F

is 28 nm, which is smaller than mean pore size of glass E-II when heat-treated for 14 h at 650 °C. Formation of the Si–O^{-}Ca^{2+}O^{-}–B structure is one of the reason for reduced phase separation leading to smaller pores in glass F with added CaO [160]. A substantial increase in pore size and pore volume is noticed with increasing heat-treatment dwell time (14 h to 24 h), whilst the surface area decreased to ~ 6 m^2/g (see Figure 4.46). Although the total pore volume increased, the pore volume < 1000 nm decreased with increasing heat-treatment dwell time.

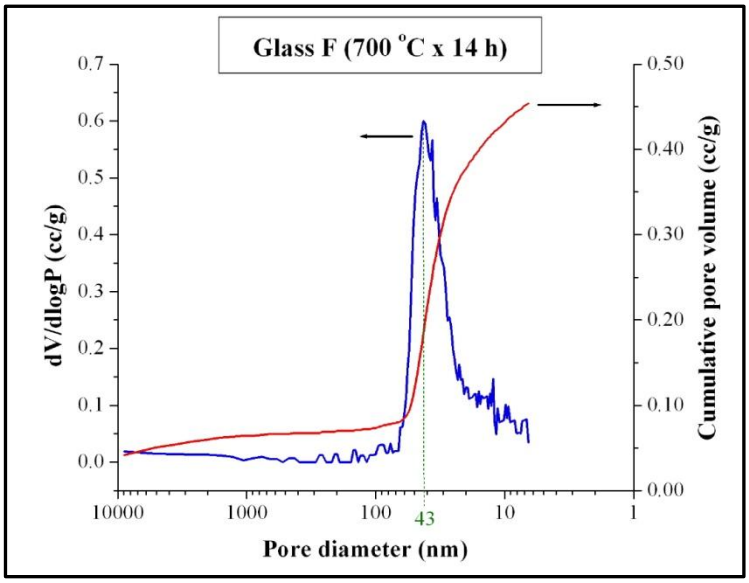

Figure 4.45: Pore-size distribution curves of porous Glass F determined by mercury intrusion after heat-treatment at 700 °C for 14 h.

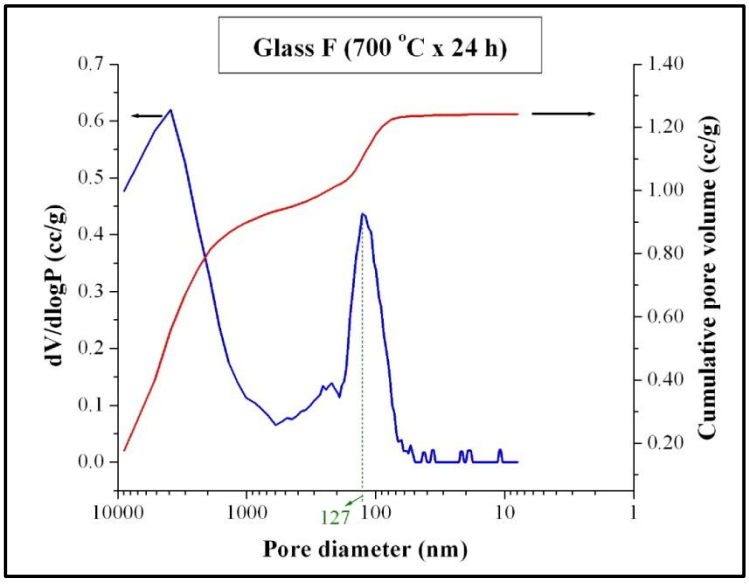

Figure 4.46: Pore-size distribution curves of porous Glass F determined by mercury intrusion after heat-treatment at 700 °C for 24 h.

Table 4.8: Effect of thermal treatment on pore characteristics of glass E-II ($54SiO_2$-$25B_2O_3$-$6Na_2O$-$15ZrO_2$) and glass F ($50SiO_2$-$25B_2O_3$-$4Na_2O$-$6CaO$-$15ZrO_2$) measured by mercury porosimetry.

	Thermal treatment		Mean pore diameter	Total surface area	Pore volume	pore volume <1000 nm	Porosity	Porosity <1000 nm
Glass	**Temperature (°C)**	**Period (h)**	**(nm)**	**(m^2/g)**	**(cm^3/g)**	**%**	**%**	**%**
E-II	650	14	41	34.88	1.096	44	21.10	9.27
E-II	650	24	58	18.23	0.678	55	16.02	8.84
E-II	650	63	139	7.96	0.896	24	17.58	4.18
F	700	14	28	33.98	0.454	86	10.32	8.86
F	700	24	188	6.27	1.241	28	25.67	7.09

4.7.1.4 Glass series AA–EE, $(69–x)SiO_2$-$25B_2O_3$-$6Na_2O$-$xZrSiO_4$

The effect of thermal treatment on pore characteristics of glass series AA–EE are presented in Table 4.9. The pore-size distribution characteristics of each glass of this glass series are described in the following sections.

(i) Glass AA ($69SiO_2$-$25B_2O_3$-$6Na_2O$)

As can be seen from Figure 4.47, the pore-size distribution is narrow and encompasses pores of 45 – 95 nm when heat-treatment dwell time is 14 h. With increasing heat-treatment dwell time the pore-size distribution became broader and shifted towards a larger pore size range. Although the total pore volume remained almost same, the pore volume < 1000 nm and the surface area decreased with increasing heat-treatment dwell time (14–63 h).

(ii) Glass CC ($62SiO_2$-$25B_2O_3$-$6Na_2O$-$7ZrSiO_4$)

Dual peaks are observed in pore-size distribution range ~ 40–140 nm when heat-treated at 650 °C for 14h as shown in Figure 4.48. A similar trend as glass AA was noticed, where the pore-size distribution became broader and shifted towards a larger pore size range with increased heat-treatment dwell time. The surface area as well as the percentage of porosity < 1000 nm decreased with increasing heat-treatment dwell time. However, the total pore volume increased initially (14–24 h). With further increases in heat-treatment dwell time (24–63 h) at 650 °C, the total pore volume then decreased significantly.

(iii) Glass DD ($58SiO_2$-$25B_2O_3$-$6Na_2O$-$11ZrSiO_4$)

Similar to glass CC, in glass DD dual peaks were observed in pore-size distribution range ~ 25–115 nm when heat-treated at 650 °C for 14 h, as shown in Figure 4.49. The pore-size distribution became broader and shifted towards a larger pore size range with increasing heat-treatment dwell time. Surface area decreased with increasing heat-treatment dwell time at 650 °C and 680 °C. The total pore volume decreased initially (14–24 h) and then increased again with a further extension of heat-treatment dwell time (24–63 h), whilst a significant increase in pore size was also noticed (from 56 to 100 nm).

Table 4.9: Effect of thermal treatment on pore characteristics of different glass series AA–EE, $(69–x)SiO_2$-$25B_2O_3$-$6Na_2O$-$xZrSiO_4$, measured by mercury porosimetry.

	Thermal treatment		Mean pore diameter	Total surface area	Pore volume	pore volume <1000 nm	Porosity	Porosity <1000 nm
Glass	Temperature (°C)	Period (h)	(nm)	(m^2/g)	(cm^3/g)	%	%	%
AA	650	14	80	12.37	0.553	66	12.35	8.11
AA	650	24	115	8.35	0.678	44	15.63	6.87
AA	650	63	139	5.17	0.566	39	13.44	5.24
CC	650	14	112	25.15	1.537	55	23.99	13.17
CC	650	24	151	16.87	1.605	41	26.59	10.92
CC	650	63	173	7.59	0.719	52	14.13	7.33
DD	650	14	57	28.32	0.814	77	15.00	11.48
DD	650	24	56	22.08	0.580	88	13.60	12.02
DD	650	63	100	15.13	0.823	69	17.73	12.17
DD	680	14	86	19.57	0.839	82	18.14	14.84
DD	680	24	85	15.15	0.641	84	14.77	12.47
EE	650	14	52	31.44	0.407	93	23.02	21.44
EE	650	24	65	28.65	0.964	69	21.49	14.78
EE	650	63	115	12.79	1.024	38	18.26	6.96

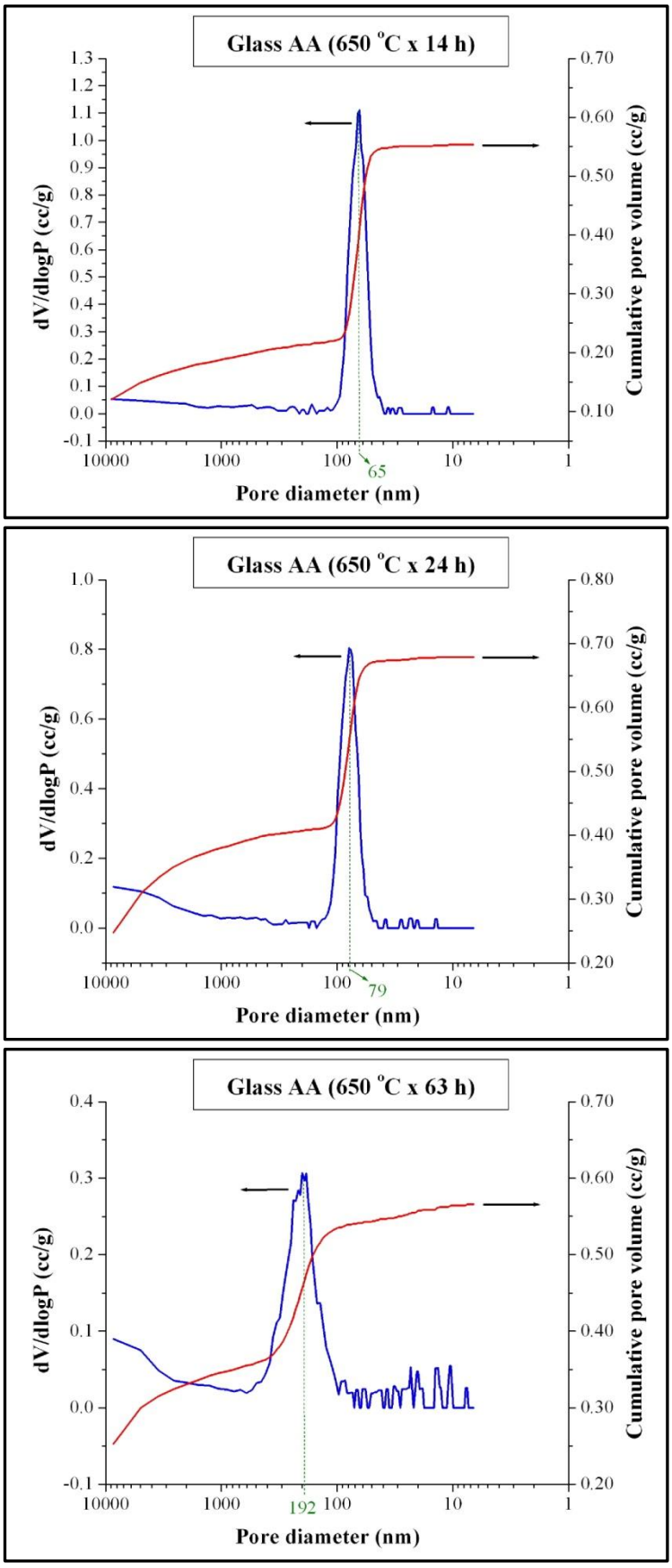

Figure 4.47: Pore-size distribution curves of porous Glass AA determined by mercury intrusion.

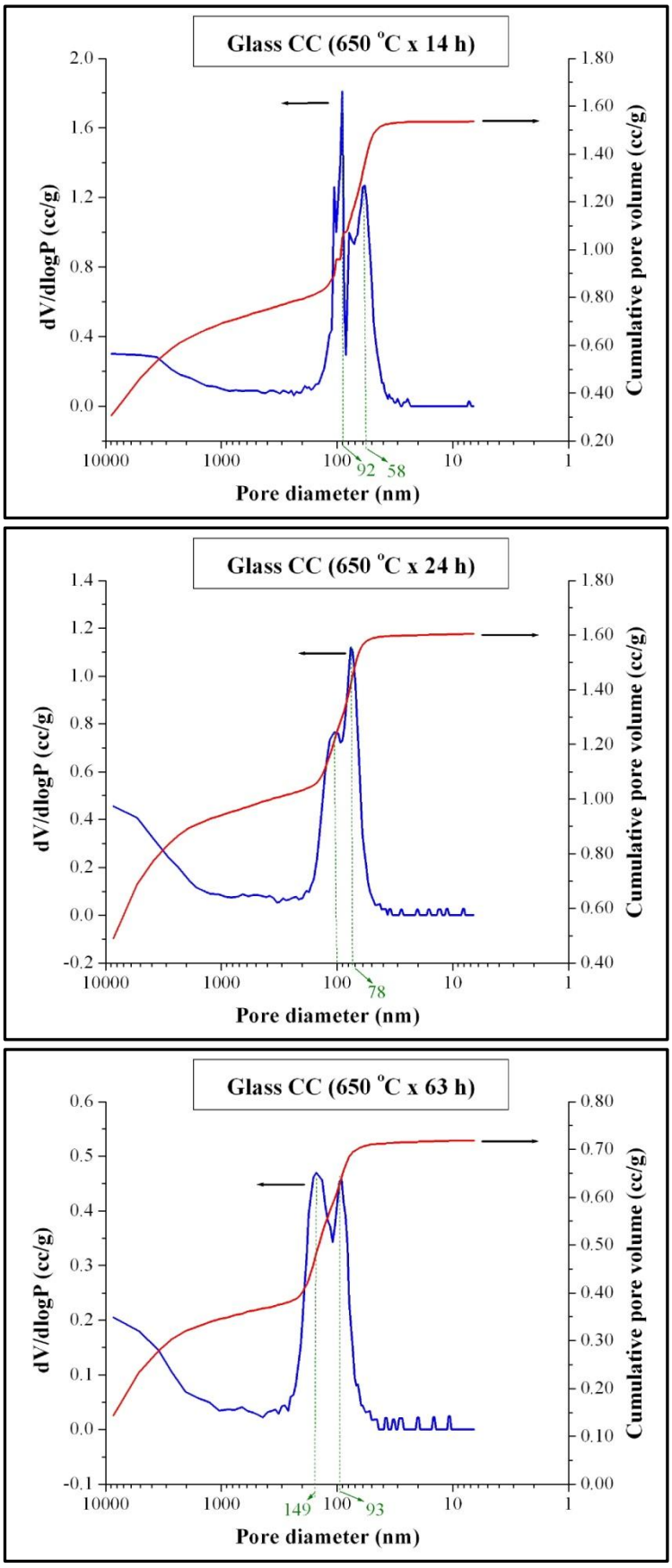

Figure 4.48: Pore-size distribution curves of porous Glass CC determined by mercury intrusion.

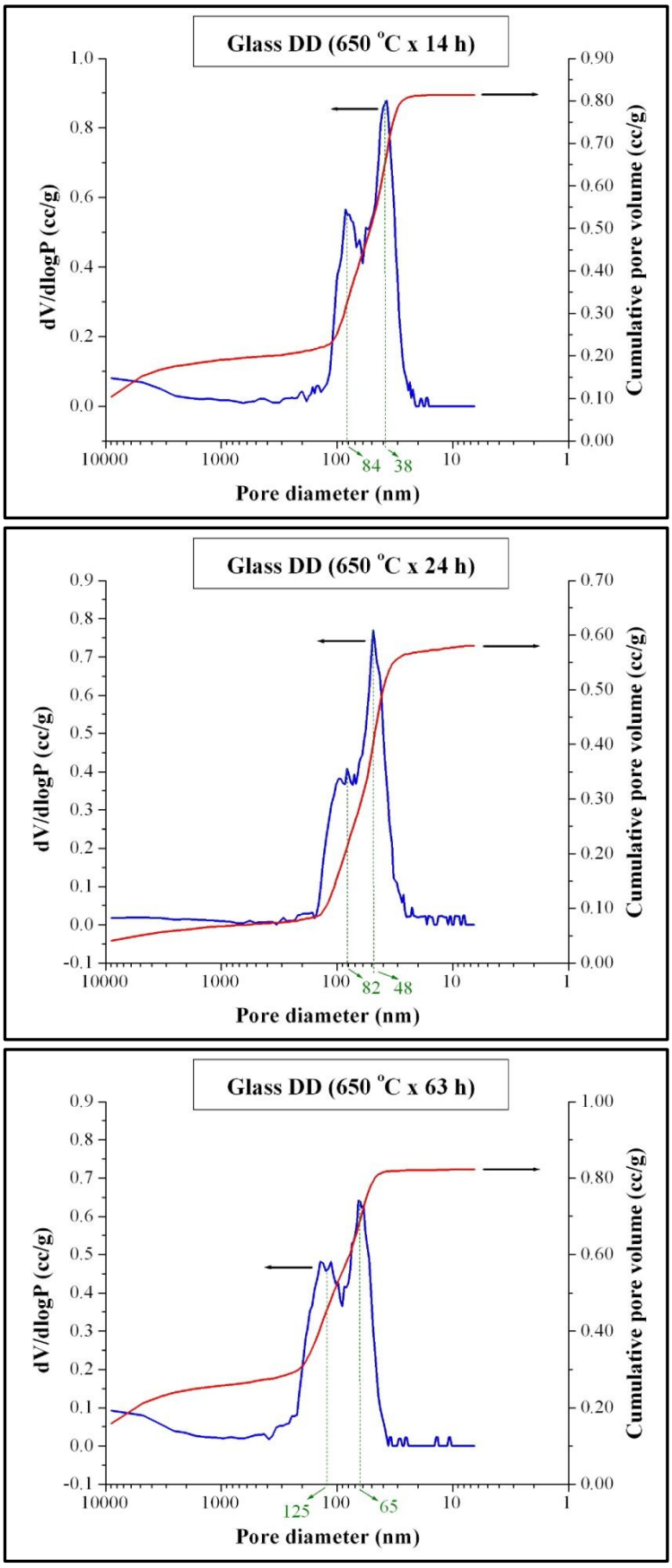

Figure 4.49: Pore-size distribution curves of porous Glass DD determined by mercury intrusion.

Dual peaks remained in glass DD when heat-treated at 680 °C for 14 h and 24 h (see Figure 4.50). The pore-size distribution changed slightly with increasing heat-treatment dwell time. The mean pore size remained constant with increasing heat-treatment dwell time (14–24 h), whilst the surface area decreased.

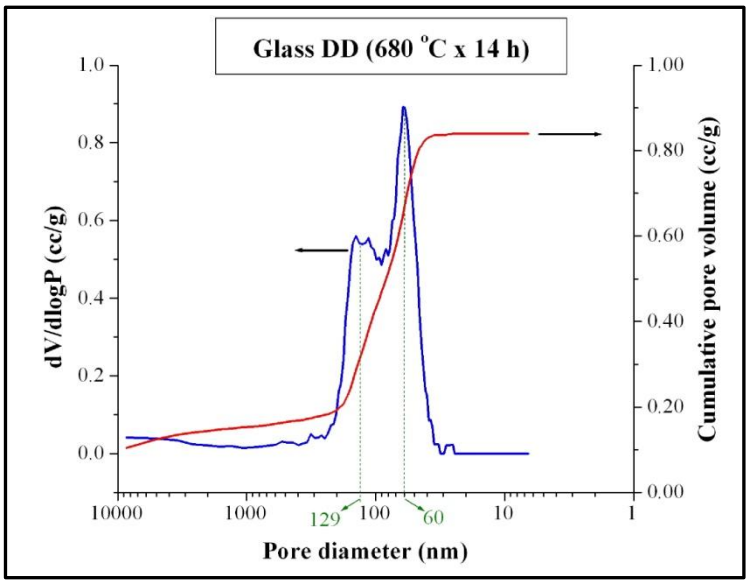

(a)

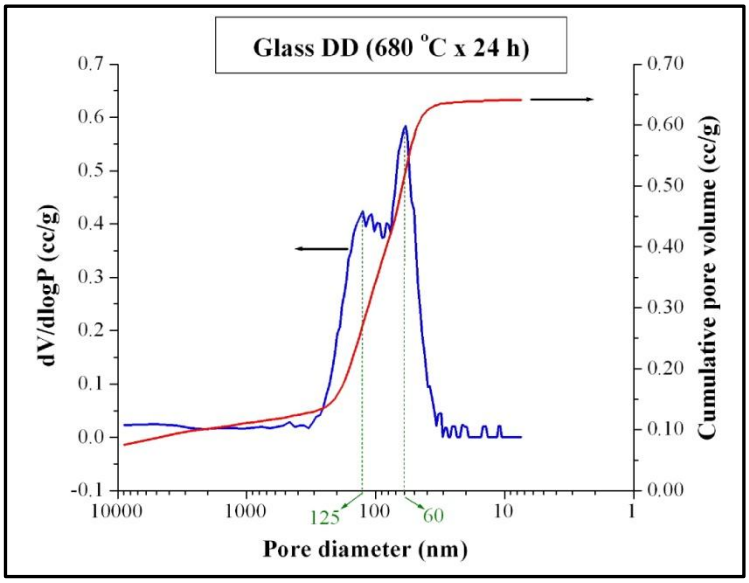

(b)

Figure 4.50: Pore-size distribution curves of porous Glass DD determined by mercury intrusion after heat-treatment at 680 °C for (a) 14 h and (b) 24 h.

(iv) Glass EE ($54SiO_2$-$25B_2O_3$-$6Na_2O$-$15ZrSiO_4$)

A single sharp peak was observed for glass EE when heat-treated at 650 °C for 14 h, with a narrow pore-size distribution encompassing pores of ~ 50 – 100 nm. The pore-size distribution became broader with increasing heat-treatment dwell time.

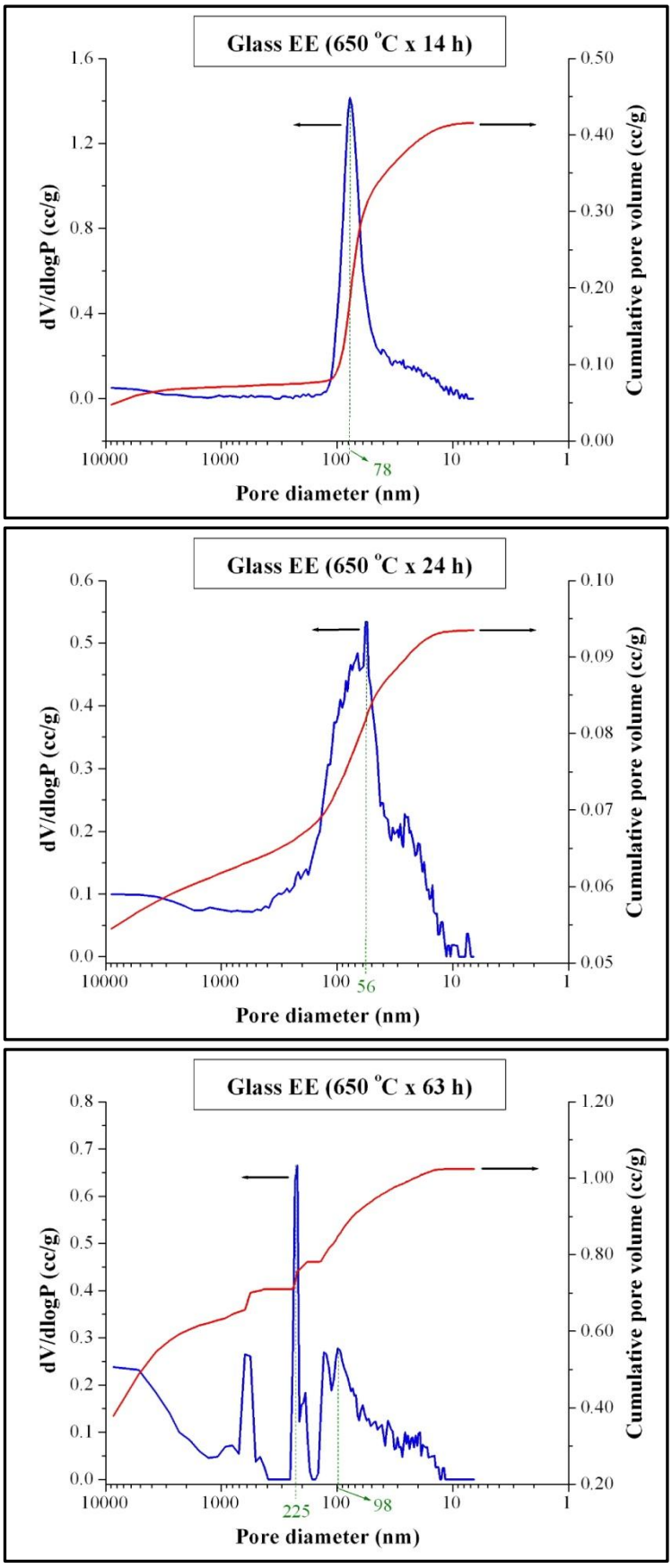

Figure 4.51: Pore-size distribution curves of porous Glass EE determined by mercury intrusion.

The total pore volume increased with increasing heat-treatment dwell time, whilst the surface area decreased as well as percent pore volume < 1000 nm.

The mean pore size decreased when $ZrSiO_4$ added ≥ 11 wt% in sodium borosilicate glass system. Kukizaki [48] found in his study with a similar glass system that addition of ZrO_2 increases the activation energy for diffusion in phase separation at a given heat-treatment time. Thus addition of ZrO_2 reduced the mean pore diameter of the resultant glass. Figure 4.52 shows the relationship between the mean pore diameter and the square root of heat-treatment dwell time at 650 °C for glass series AA–EE. It is evident that for each glass in glass series AA–EE, the mean pore diameter is linearly related to square root of heat-treatment dwell time.

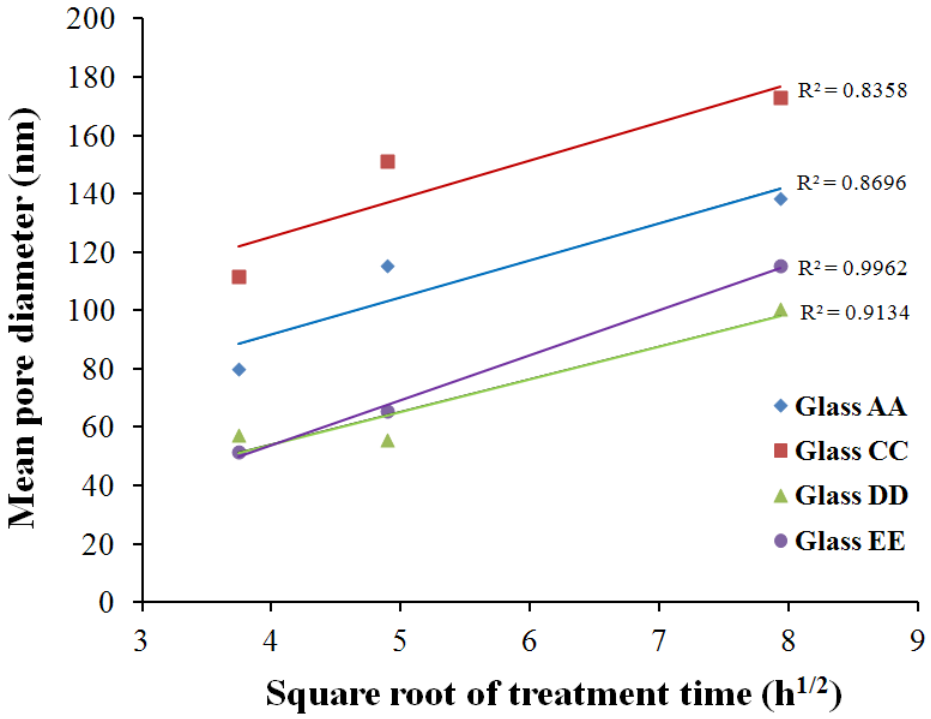

Figure 4.52: Relationship between heat-treatment dwell time and pore diameter for glass series AA–EE after heat-treatment at 650 °C.

4.7.1.5 Commercially available porous glass and hydroxyapatitie

Figure 4.53 shows the pore-size distribution of commercially available Controlled Pore Glass (CPG) of grade CPG 1000CL from Merck Millipore, Ireland, and CHT ceramic hydroxyapatite type II from Bio-Rad Laboratories Ltd., UK. The pore characteristics data of CPG 1000CL and Bio-Rad CHT type II are presented in Table

4.10. The pore-size distribution of CPG 1000 CL was found to be narrow, encompassing pore sizes of ~ 110 – 160 nm. The total pore volume and surface area were measured as 1.58 cm^3/g and ~ 24 m^2/g respectively. The Bio-Rad CHT type II also shows a narrow distribution of pores ranged from 70 to 130 nm. Both the mean pore size and surface area were found to be smaller for Bio-Rad CHT type II compared to CPG 1000 CL. The results obtained by mercury porosimetry were consistent with specifications listed in the data sheet for both materials.

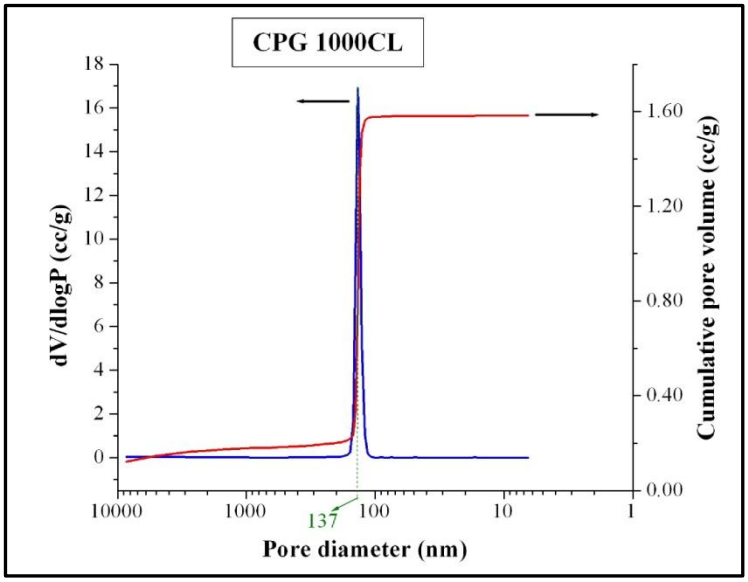

(a)

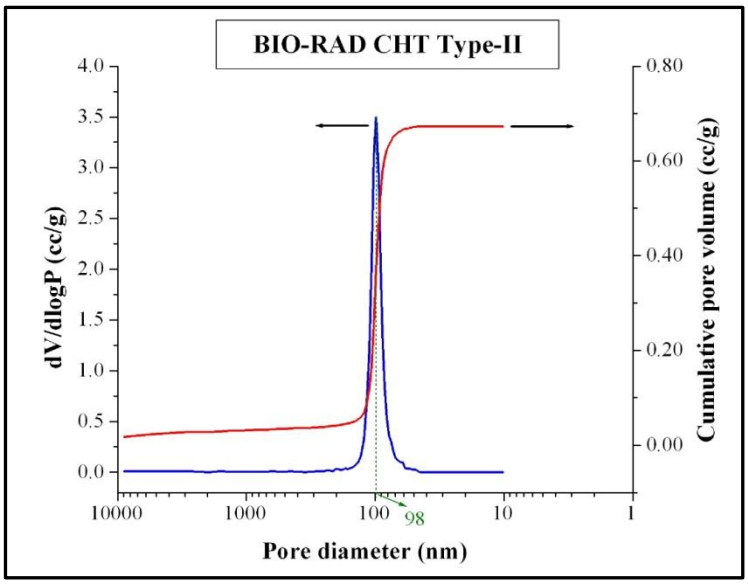

(b)

Figure 4.53: Pore-size distribution curves of (a) CPG 1000CL and (b) BIO-RAD CHT Type-II, determined by mercury intrusion.

Table 4.10: Pore characteristics data of as received porous glasses by mercury porosimetry.

Glass	Mean pore diameter (nm)	Specific surface area (m^2/g)	Pore volume (cm^3/g)	pore volume <1000 nm %	Porosity %	Porosity <1000 nm %
CPG 1000CL	141	23.65	1.582	89	27.16	24.11
BIO-RAD CHT Type-II	100	15.01	0.673	95	17.23	16.41

4.7.2 Pore analysis by Nitrogen gas adsorption

With the nitrogen adsorption analysis, pores with a diameter range of 3–200 nm can be measured [120]. For textural analysis of macroporous material (pore width > 50 nm), mercury porosimetry is considered as most useful and reliable [133]. However, nitrogen adsorption porosimetry was conducted on selective glasses, e.g. base glasses (glass A and glass AA) and glasses containing 6 wt% of Na_2O and 15 wt% $ZrO_2/ZrSiO_4$ (Glass E-II and Glass EE), to compare it to the results that were obtained using the mercury porosimetry method. Table 4.11 shows the textural data of different porous glass compositions as determined by nitrogen adsorption.

Table 4.11: Effect of thermal treatment on pore characteristics of different glass compositions measured by nitrogen adsorption.

Glass	Thermal treatment		Mean pore diameter	Specific surface area	Pore volume < 140 nm pore diameter
	Temperature (°C)	Period (h)	(nm)	(m^2/g)	(cm^3/g)
A	650	14	5	47.25	0.058
A	650	24	16	3.57	0.014
AA	650	14	8	27.87	0.058
AA	650	24	9	21.81	0.048
AA	650	63	10	18.39	0.045
E-II	650	14	10	97.74	0.253
E-II	650	24	10	81.52	0.205
E-II	650	63	17	13.96	0.060
EE	650	14	22	29.66	0.165
EE	680	24	7	168.06	0.310
EE	680	63	22	22.03	0.122

The total pore volumes measured by mercury porosimetry are significantly higher compare to those measured by nitrogen adsorption. Since mercury porosimetry covers a wide range of pores, including the larger ones that have a relatively greater contribution towards the total pore volume. However, pores > 150 nm are not within the detection range of nitrogen adsorption. On the other hand nitrogen adsorption porosimetry can detect the smallest pores that contribute more to the total surface area. Table 4.12 compares the data obtained from nitrogen gas adsorption and mercury porosimetry in the overlapping pore region. The specific surface area

measured by nitrogen adsorption is far higher in those glass compositions with a pore number fraction < 10 nm. The pore-size distribution curve demonstrates the presence of this small pore number fraction, which is illustrated by a number of small peaks of < 10 nm in pore size. The proportion of pore volume below 140 nm of pores are similar according to both porosimetry measurement. It is difficult to make a direct comparison of both methods of porosimetry as they follow different principles and techniques. Nevertheless, an attempt was made to compare the results in the overlapping pore size region.

Table 4.12: Specific surface area and pore volume < 140 nm pore diameter obtained by nitrogen adsorption and mercury porosimetry.

			Nitrogen adsorption		**Mercury porosimetry**	
	Thermal treatment		**Specific surface area**	**Pore volume < 140 nm pore diameter**	**Specific surface area**	**Pore volume < 140 nm pore diameter**
Glass	**Temperature (°C)**	**Period (h)**	**(m^2/g)**	**(cm^3/g)**	**(m^2/g)**	**(cm^3/g)**
A	650	14	47.25	0.058	2.35	0.031
A	650	24	3.57	0.014	2.90	0.030
AA	650	14	27.87	0.058	12.37	0.337
AA	650	24	21.81	0.048	8.35	0.269
AA	650	63	18.39	0.045	5.17	0.050
E-II	650	14	97.74	0.252	34.88	0.361
E-II	650	24	81.52	0.205	18.23	0.243
E-II	650	63	13.96	0.060	7.96	0.127
EE	650	14	29.66	0.165	31.44	0.372
EE	680	24	168.06	0.310	28.65	0.517
EE	680	63	22.03	0.122	12.79	0.241

4.7.3 Scanning Electron Microscopy (SEM)

SEM was conducted on porous glasses after heat-treatment and leaching. A clear distinction in morphology between glass series A–E (10 wt% Na_2O) and other glasses (6 wt% Na_2O) was revealed. Spherical droplets with low connectivity were observed in glass series A–E (see Figure 4.54, Figure 4.55 and Figure 4.56) which are believed to be due to nucleation and growth process [32]. The percentage of porosity below 1000 nm was found much lower in glass series A–E compare to glass series AA–EE. The porosity is likely to decrease with an increasing ZrO_2 content up

to 11 wt%. When ZrO_2 > 11 wt% in the glass, the porosity begins to increase in the droplets. Figure 4.54 and Figure 4.55 present the SEM micrograph of leached glasses of composition C (7wt% ZrO_2), heat-treated at various temperatures and times. The formation of columnar cristobalite crystals was observed (see Figure 4.55) when the heat-treatment temperature is increased from 650 °C to 700 °C. A more pronounced columnar cristobalite crystals was observed in glass D (11 wt% ZrO_2) when the heat-treatment temperature increased from 650 °C to 700 °C. Small pores are found in abundance within large droplets in glass E (15 wt% ZrO_2). This finding is in good agreement with the pore-size distribution curve as shown in Figure 4.41, where small peaks are observed in the lower pore-size range.

A dramatic change is observed in pore structure when the Na_2O content in sodium borosilicate glass system was reduced in glass E-II (6 wt% Na_2O, 15 wt% ZrO_2) as compare to glass E (10 wt% Na_2O, 15 wt% ZrO_2) (see Figure 4.55, Figure 4.56, and Figure 4.57). An interconnected structure consisting of two mutually penetrating interconnected phases was observed in glass E-II (see Figure 4.57). The extent of phase separation is more pronounced in porous glass F. It is well-established that CaO accelerates phase separation [8, 9, 76].

Classical skeleton-like microstructures with highly connected pores are observed for porous glass compositions of glass series AA–EE (see Figure 4.58 and Figure 4.59). These spherical droplet-like pores with a high degree of connectivity are usually formed by spinodal decomposition [6, 32]. It is evident that a high degree of phase separation occurred in this glass series. Pore size was also found to increase with increasing heat-treatment dwell time, which is consistent with the mercury porosimetry findings (see Table 4.9).

SEM photographs of commercially available Controlled Pore Glass (CPG) of grade CPG 1000CL and porous CHT ceramic hydroxyapatite type II are shown in Figure 4.60. The morphology of CPG 1000CL is more or less identical to glass series AA–EE as it is based on the sodium borosilicate glass system. However, the morphology of CHT ceramic hydroxyapatite type II is different, with a smaller degree of interconnection.

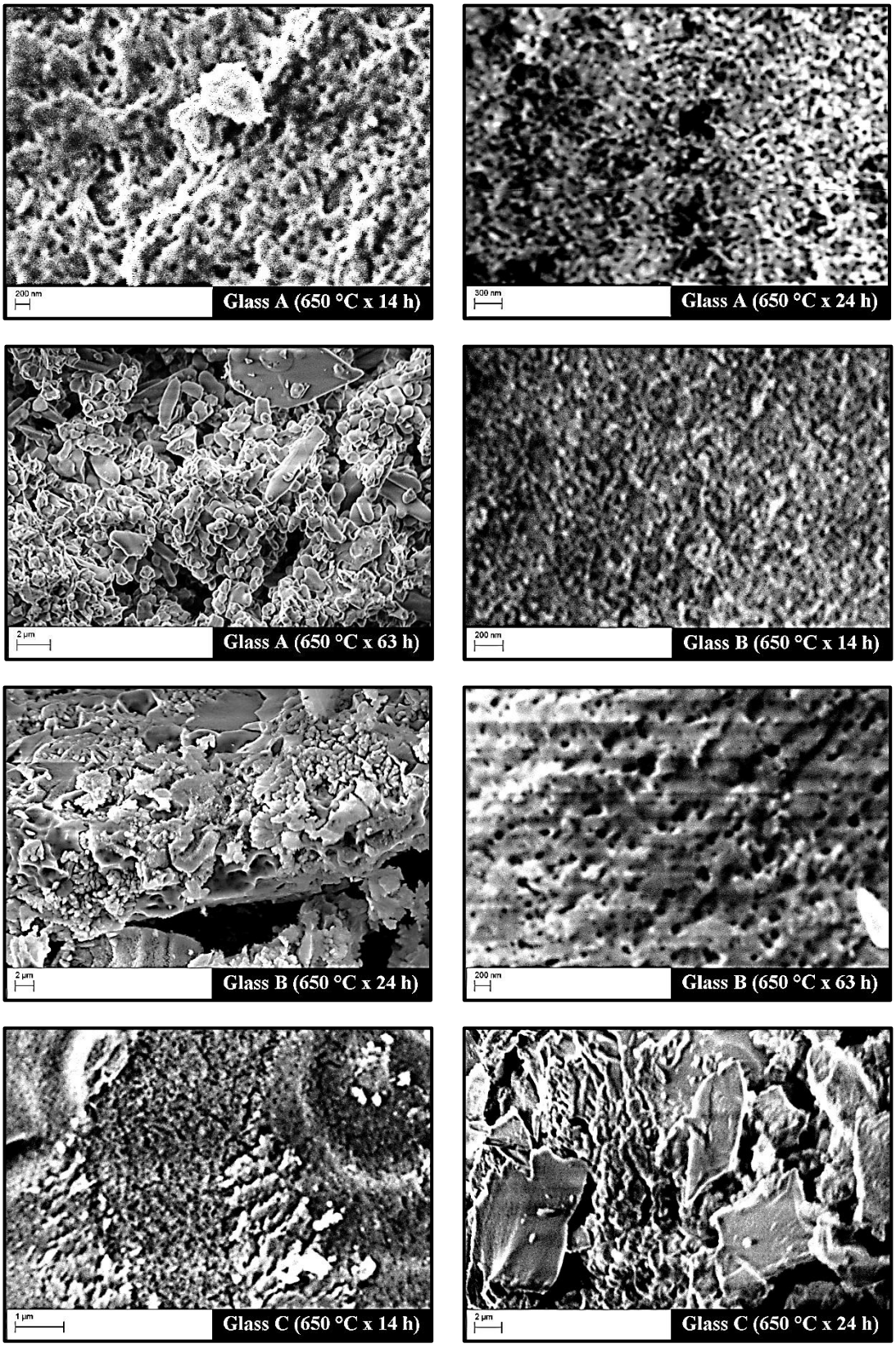

Figure 4.54: SEM photographs of glass series A–E after leaching (continued).

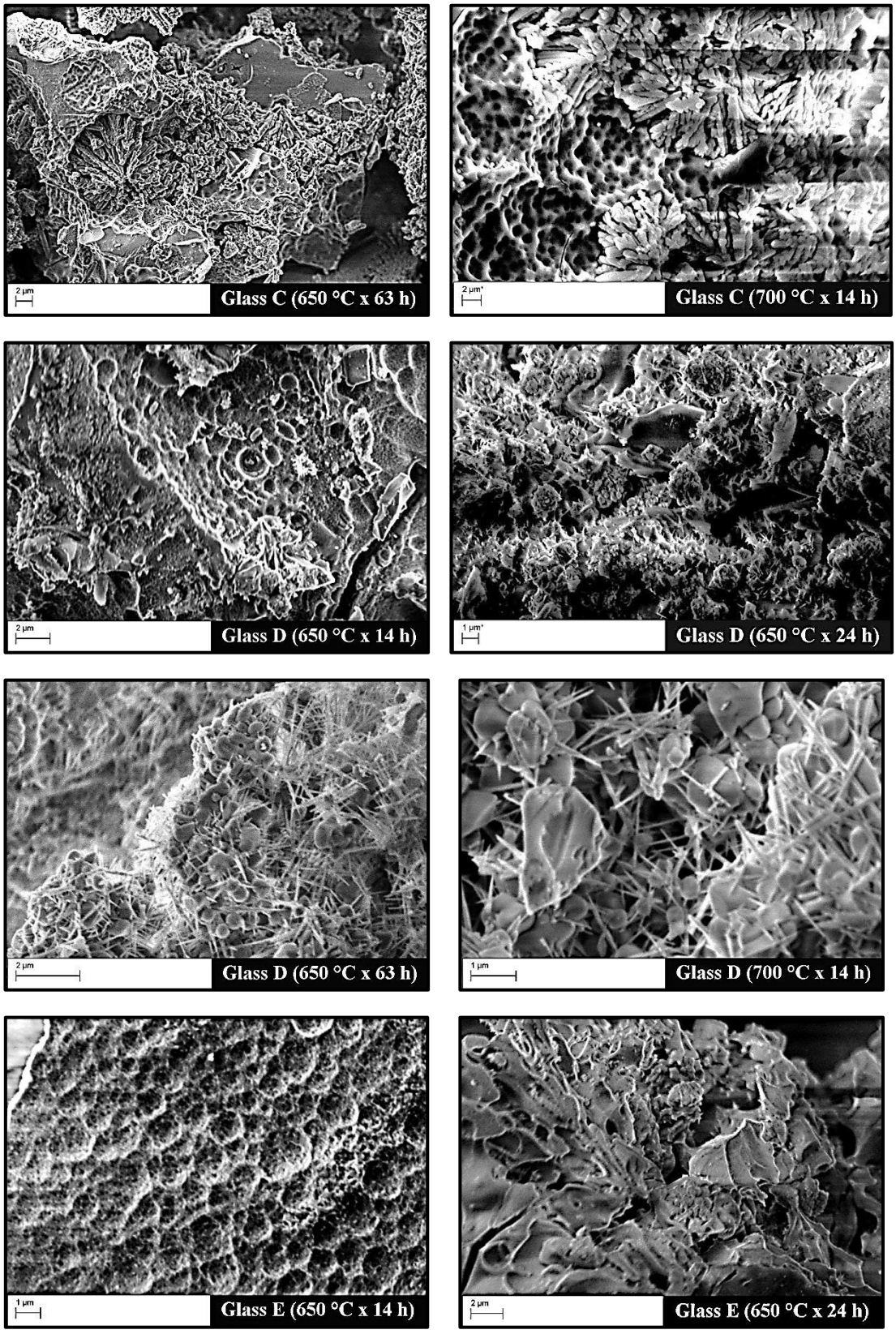

Figure 4.55: SEM photographs of glass series A–E after leaching (continued).

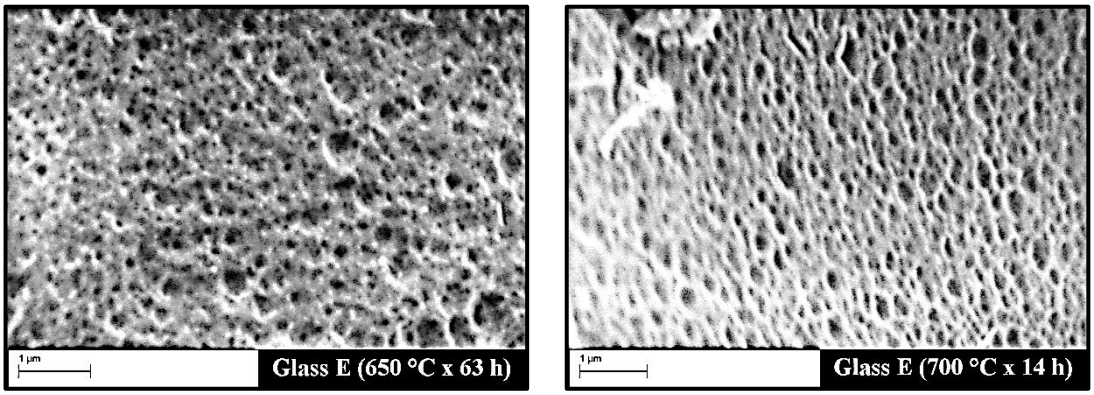

Figure 4.56: SEM photographs of glass series A–E after leaching.

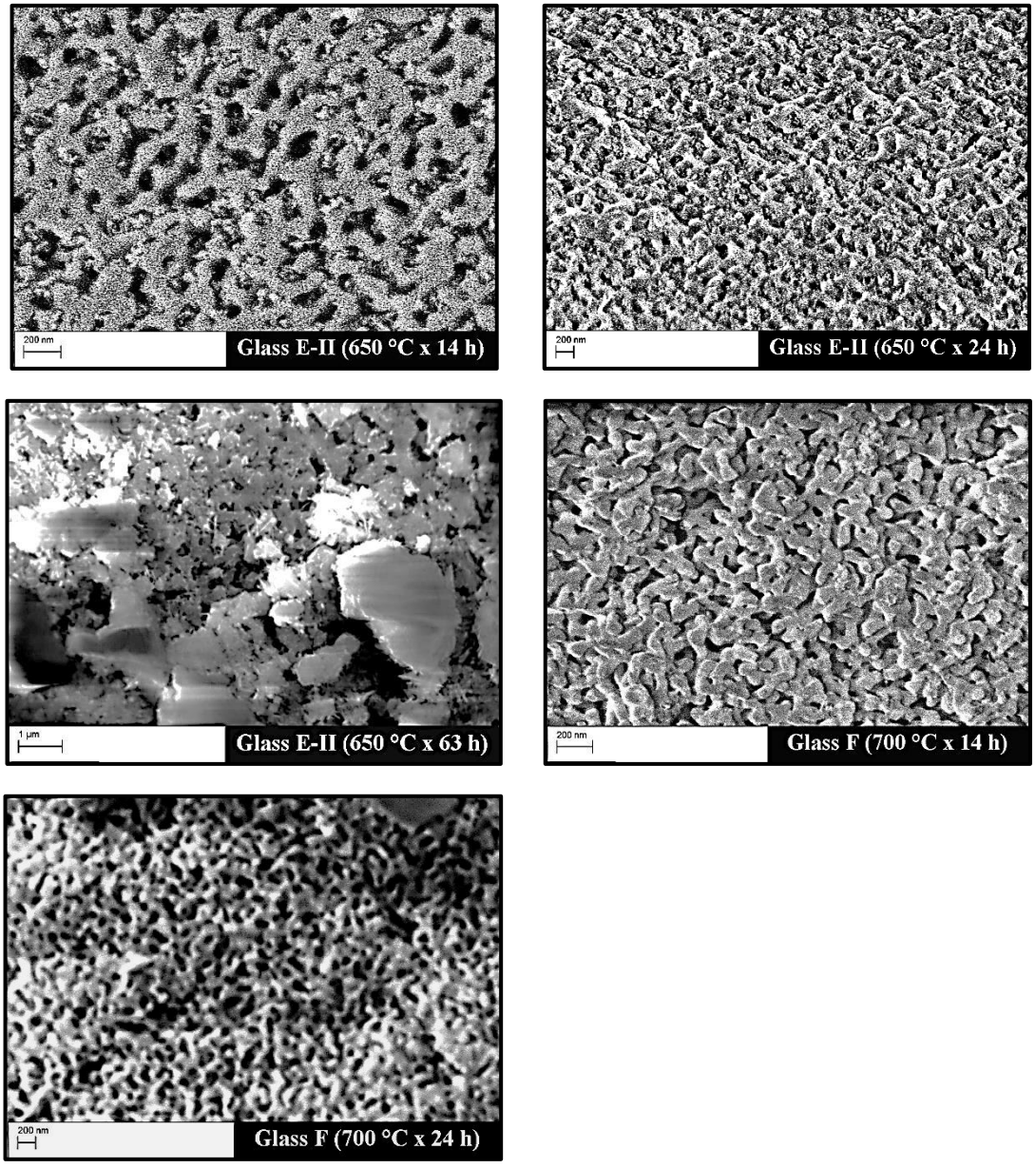

Figure 4.57: SEM photographs of glass E-II and glass F after leaching.

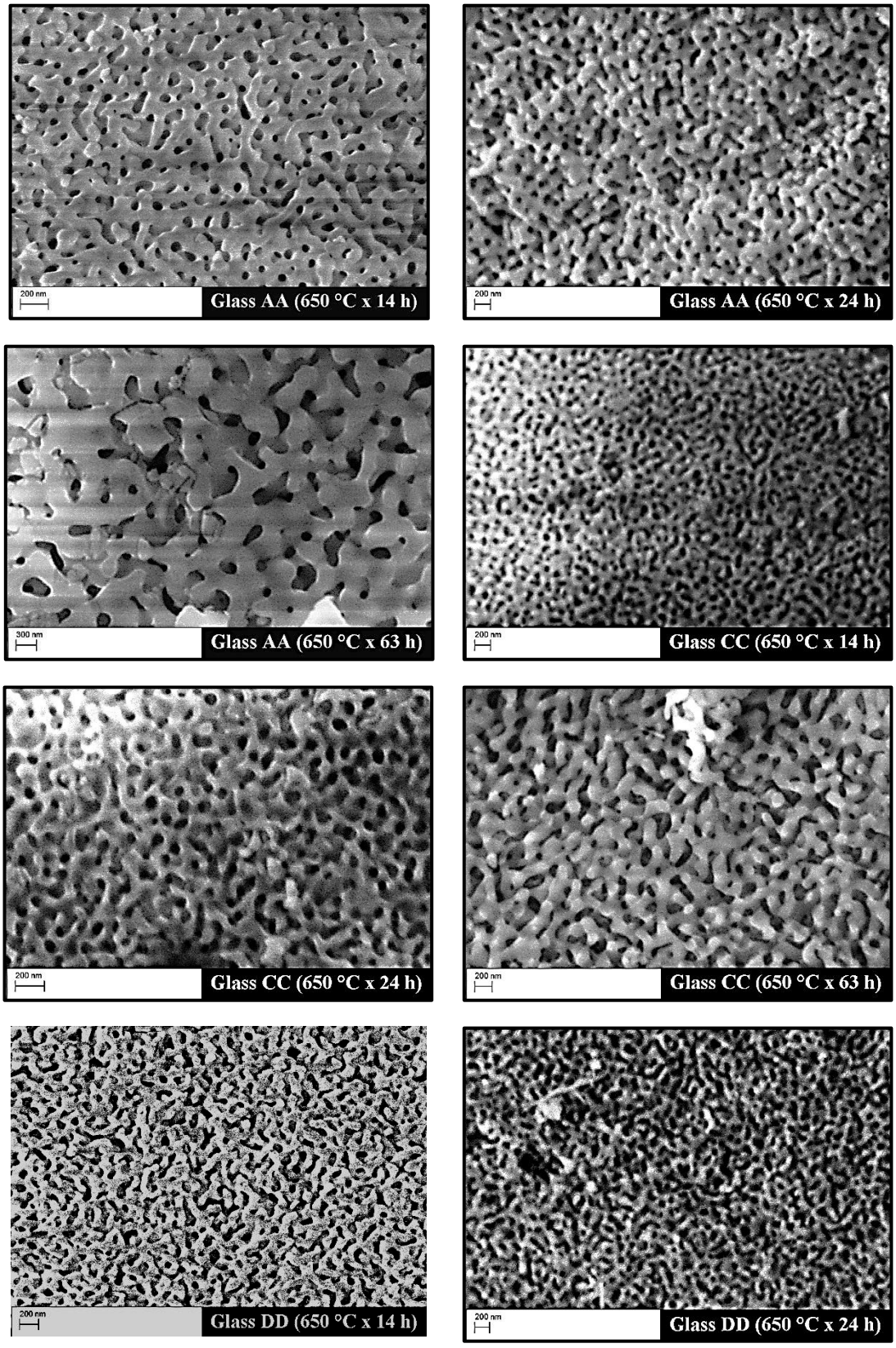

Figure 4.58: SEM photographs of glass series AA–EE after leaching (continued).

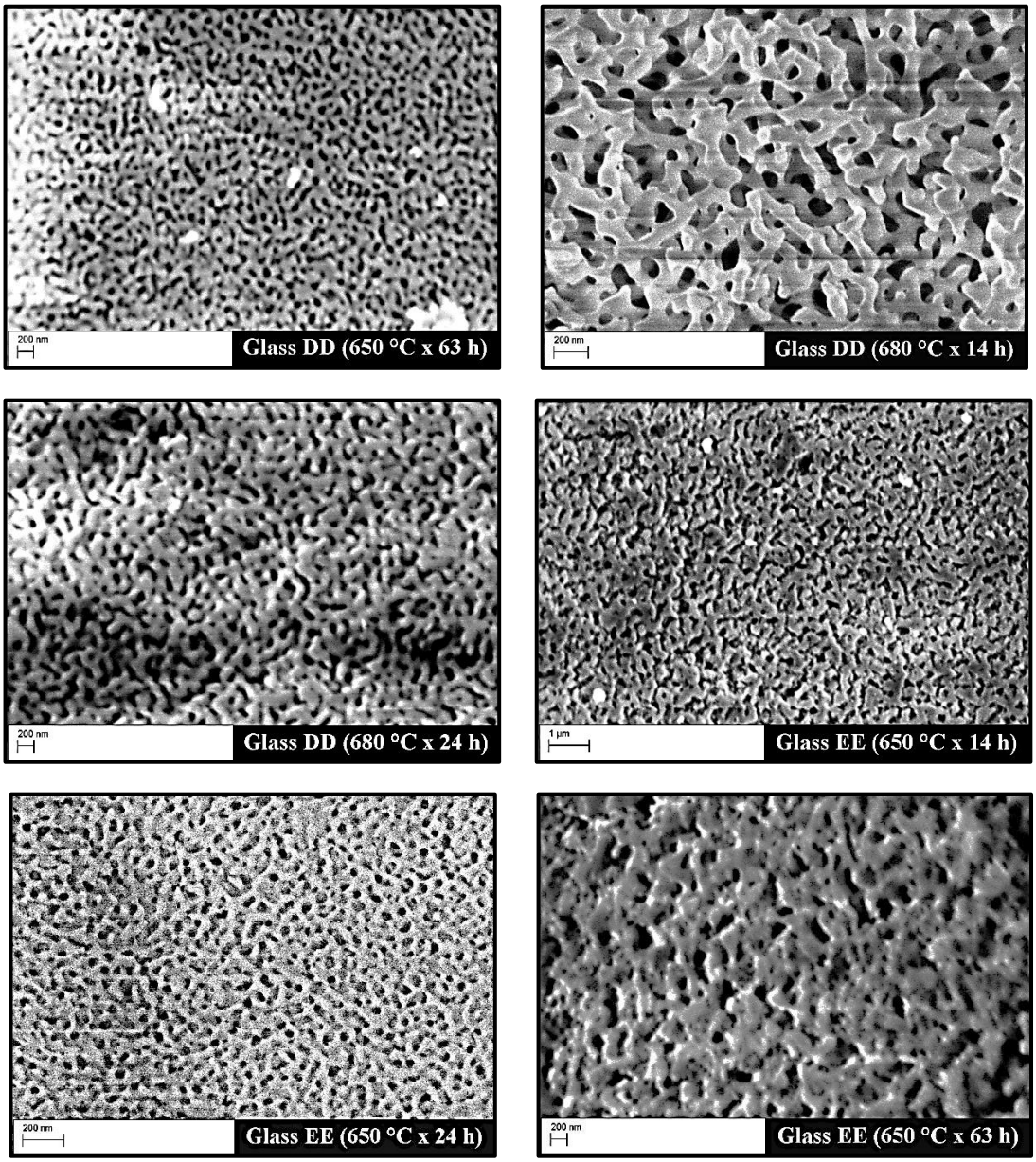

Figure 4.59: SEM photographs of glass series AA–EE after leaching.

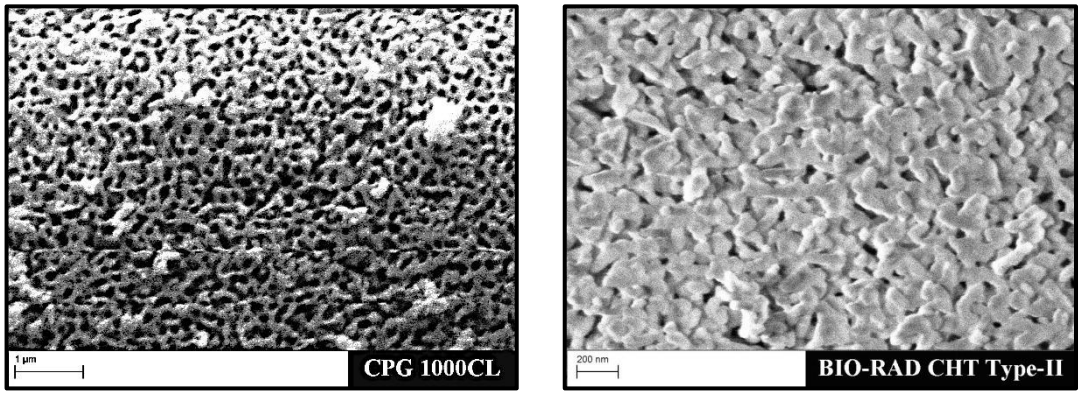

(a) (b)

Figure 4.60: SEM photographs of commercially available (a) CPG 1000CL and (b) BIO-RAD CHT Type-II.

4.7.4 Energy Dispersive X-ray Spectroscopy (EDXS)

Table 4.13 summarises the EDXS elemental analysis of the porous glass compositions after heat-treatment and leaching. Unfortunately the EDXS system can not detect boron. However, it was expected that all boron content would be eluted during leaching. Increasing alkali content in sodium borate glass compositions converts BO_3 triangles to four-coordinated BO_4 tetrahedra. The bond valence model studied by Connelly et al. [148] showed that BO_3 bonds are more likely to form Zr–O–B than that of four-coordinated BO_4. With a high Na_2O to B_2O_3 ratio in glass series A–E (Na_2O/B_2O_3=0.4), the fraction of BO_3 available for forming Zr–O–^{III}B is significantly smaller than in glass series AA–EE (Na_2O/B_2O_3=0.24). Therefore, in glass series A–E, Zr formed the bond Si–O–Zr, going to the non-leachable silicon-rich phase and finally remaining in the porous glass. EDXS analysis also identified the presence of Zr in glasses B–E. While in glass series AA–DD, Zr formed Zr–O–^{III}B with BO_3, which then completely eluted during leaching. No trace of Zr was detected by EDXS for the glass compositions CC and DD. An exception was observed for glass EE and E-II, where the presence of Zr was found to be optimum by EDXS. A possible explanation for this might be the content of ZrO_2 or $ZrSiO_4$ (15 wt%) used in the sodium borosilicate glass system. Beyond a certain content of ZrO_2/$ZrSiO_4$ in sodium borosilicate glass systems, which in this study was >11 wt%, possibly no more BO_3 is available to form bonds with Zr. As a result, Zr moves to the silica-rich phase by forming the Si–O–Zr bond and remains in the porous glass after leaching. The fraction of BO_4 showed a sharp increase when CaO was added up to 3.3 wt% [160]. In glass F the EDXS results showed a dramatic reduction in Zr compared to glass EE and E-II. This dramatic fall in Zr is possibly due the content of CaO (6 wt%) used in glass F. Miyoshi et al. [160] in their study with similar sodium borosilicate glass compositions found that the addition of > 5.3 wt% of CaO resulted in a saturated concentration of BO_4. Therefore, a possible explanation for this observation is that with a saturated BO_4 concentration in glass F, a major fraction of ZrO_2 preferentially moves to the boron rich phase and is ultimately eluted during leaching.

Table 4.13: Elemental analysis of porous glass compositions by means of EDXS.

Glass	Thermal treatment		Si	Na	Zr	O
	Temperature (°C)	Period (h)	(wt%)	(wt%)	(wt%)	(wt%)
A	650	14	43	5	-	52
A	650	24	44	2	-	54
A	650	63	49	1	-	50
B	650	14	43	5	2	50
B	650	24	48	2	1	49
B	650	63	44	3	-	54
C	650	14	35	7	8	51
C	650	24	35	5	7	54
C	650	63	39	5	5	50
C	700	14	49	1	-	50
D	650	14	34	6	9	51
D	650	24	44	2	-	53
D	650	63	39	1	19	42
D	700	14	31	1	28	40
E	650	14	33	7	11	49
E	650	24	44	3	5	48
E	650	63	34	6	14	47
E	700	14	32	7	13	48
E-II	650	14	29	1	23	48
E-II	650	24	34	-	18	49
E-II	650	63	38	-	20	42
F	700	14	39	3	3	55
F	700	24	42	4	3	52
AA	650	14	47	1	-	53
AA	650	24	45	1	-	54
AA	650	63	47	1	-	52
CC	650	14	43	2	-	55
CC	650	24	55	1	-	44
CC	650	63	43	1	-	56
DD	650	14	44	1	-	55
DD	650	24	43	-	-	57
DD	650	63	41	1	-	58
DD	680	14	42	1	-	57
DD	680	24	39	1	-	60
EE	650	14	32	-	22	46
EE	650	24	26	2	24	48
EE	650	63	24	1	28	47

4.8 DENSITY MEASUREMENT BY PYCNOMETRY

The density measured by helium gas pycnometry is often considered as "true density", provided that the gas is not absorbed and the sample does not contain closed pores [37]. Table 4.14 presents density values of selected porous glass compositions obtained by helium gas pycnometry.

Table 4.14: Density measured by helium pycnometry.

Glass	Thermal treatment		Density (ρ_H) (g/cc)
	Temperature (°C)	Period (h)	
AA	650	14	2.2282±0.0014
AA	650	24	2.2640±0.0059
AA	650	63	2.2722±0.0048
CC	700	14	2.3038±0.0068
CC	650	24	2.3247±0.0045
D	650	63	2.6474±0.0046
D	700	14	2.6911±0.0066
DD	650	14	2.2392±0.0015
DD	650	24	2.2132±0.0033
DD	650	63	2.2646±0.0019
DD	680	14	2.2537±0.0031
DD	680	24	2.2297±0.0030
E-II	650	14	2.7028±0.0078
E-II	650	24	2.5838±0.0040
EE	650	14	2.7543±0.0119
EE	650	24	2.6665±0.0034
EE	650	63	3.3779±0.0637
F	700	14	2.2587±0.0034
F	700	24	3.0843±0.0369
CPG 1000CL	-	-	2.3228±0.0093
BIO-RAD CHT Type-II	-	-	3.4502±0.0315

The percentage porosity of the leached glass compositions in present study was determined by using the following equation [115]:

$$\text{Percent porosity, } \varepsilon = \left(1 - \frac{\rho_b}{\rho_s}\right) \times 100 \qquad \text{Equation 4.3}$$

Where, ρ_b is bulk density and ρ_s is skeletal density. These values were obtained from mercury porosimetry results. In some studies true density, measured by helium pycnometer, is used instead of skeletal density [120, 123]. Kukizaki [48], in his study, measured membrane porosity by using the following equation:

$$\text{Porosity, } \varepsilon = \frac{V_p}{V_p + (1/\rho_H)} \qquad \text{Equation 4.4}$$

Where, V_P is the pore volume per unit sample mass as determined by mercury porosimetry. And, ρ_H is the true density of the sample measured by helium pycnometry. A comparison of the percentage porosity using both equations for selected porous glass compositions is presented in Table 4.15.

Table 4.15: Comparison of % porosity using different equations.

Glass	Thermal treatment		Porosity using Equation 4.1	Porosity using Equation 4.2
	Temperature (°C)	Period (h)	%	%
AA	650	14	12.35	55.22
AA	650	24	15.63	60.56
AA	650	63	13.44	56.25
CC	700	14	23.99	77.97
CC	650	24	26.59	78.86
D	650	63	23.59	75.25
D	700	14	21.65	77.03
DD	650	14	15.00	64.57
DD	650	24	13.60	56.22
DD	650	63	17.73	65.08
DD	680	14	18.14	65.41
DD	680	24	14.77	58.85
E-II	650	14	21.10	74.77
E-II	650	24	16.02	63.66
EE	650	14	23.02	52.66
EE	650	24	21.49	71.98
EE	650	63	18.26	77.57
F	700	14	10.32	50.62
F	700	24	25.67	79.29

4.9 ALKALI RESISTANCE TEST

The alkali resistance of different porous glass series are shown in Table 4.16, Table 4.17 and Table 4.18. There are many factors that influence the alkali resistance, especially the surface area. The surface area is used in calculating the weight loss in accordance with standard procedure ISO 695 [109]. High surface area and interconnected structures can be achieved where glass composition is properly selected and optimum heat-treatments are applied. In the present study, glass compositions with higher surface area and interconnected pore structures were achieved in the glass series AA–EE and E-II, which had lower amounts of alkali oxide (6 wt% Na_2O). Alkali resistance of the porous glasses was improved by the addition of ZrO_2 or $ZrSiO_4$.

The alkali resistance remains almost constant for the glass series A–E, which contained a higher amount of alkali oxide (10 wt% Na_2O) (see Table 4.16). For these glasses the phase separation process is believed to be dominated by nucleation and growth, as opposed to spinodal decomposition. An exception was identified in the case of glass D when heat-treated at 700 °C for 14h. In this treatment condition crystallisation was predominant, as confirmed by SEM (Figure 4.55). As can be seen from data presented in Table 4.16, the glasses that had crystallised with longer duration of heat-treatment, lost less weight in alkali resistance compared to those without crystallisation. But, when surface area was taken into account in the alkali resistance calculation, the results showed a low resistance to alkali solution because the surface area decreased with increasing heat-treatment dwell time. However, the percentage of weight loss decreased with increasing ZrO_2 content in glass series A–E. On the other hand, the phase separation process in glass E-II, glass F, and glass series AA–EE, is believed to have been dominated by spinodal decomposition. These glasses have a higher surface area and interconnected silica skeleton compare to glass series A–E. Even though percent weight loss is higher in glass E-II and glass F (see Table 4.17), the weight loss per unit surface area shows more resistance when compared to glasses of glass series A–E.

Table 4.16: ZrO_2 content and alkali resistance of glass series A-E.

Glass	Thermal treatment		ZrO_2 content	Weight loss	Weight loss per total surface area
	Temperature (°C)	Period (h)	(wt%)	%	(mg/dm^2)
A	650	14	0	9	0.36
A	650	24	0	9	0.30
A	650	63	0	7	0.59
B	650	14	3	18	0.29
B	650	24	3	25	0.30
B	650	63	3	10	0.67
C	650	14	7	11	0.46
C	650	24	7	10	0.65
C	650	63	7	9	0.41
C	700	14	7	11	0.31
D	650	14	11	10	0.67
D	650	24	11	25	0.31
D	650	63	11	4	0.13
D	700	14	11	6	0.06
E	650	14	15	9	0.39
E	650	24	15	19	0.31
E	650	63	15	8	0.42
E	700	14	15	6	0.41

Table 4.17: ZrO_2 content and alkali resistance of glass E-II and F.

Glass	Thermal treatment		ZrO_2 content	Weight loss	Weight loss per total surface area
	Temperature (°C)	Period (h)	(wt%)	%	(mg/dm^2)
E-II	650	14	15	65	0.19
E-II	650	24	15	60	0.33
E-II	650	63	15	18	0.23
F	700	14	15	51	0.15
F	700	24	15	32	0.50

The alkali resistance remains almost constant for glass AA–DD. From the EDXS results (see Table 4.13), no Zr was detected in these glasses. It is therefore presumed that Zr moved to the boron rich phase and eluted in the leaching stages. Therefore, the glass samples AA–DD showed similar result with respect to alkali resistance. The small difference which was identified was due to their textural properties, i.e. surface area. Presence of Zr was detected in glass EE by EDXS and it showed significant improvement in terms of alkali resistance, as shown in Table 4.18. The

alkali resistance of the porous glass of composition EE is 3–4 times superior to that of porous glass obtained from composition AA without ZrO_2 or $ZrSiO_4$. At the same time, porous glass (EE) containing $ZrSiO_4$ was found to be more alkali resistant than that of glass (E-II) containing ZrO_2 with the same composition.

Table 4.18: $ZrSiO_4$ content and alkali resistance of glass series AA-EE.

Glass	Thermal treatment		$ZrSiO_4$ content	Weight loss	Weight loss per total surface area
	Temperature (°C)	Period (h)	(wt%)	%	(mg/dm^2)
AA	650	14	0	43	0.35
AA	650	24	0	24	0.28
AA	650	63	0	12	0.24
CC	650	14	7	73	0.29
CC	650	24	7	40	0.24
CC	650	63	7	37	0.49
DD	650	14	11	84	0.30
DD	650	24	11	59	0.27
DD	650	63	11	71	0.47
DD	680	14	11	70	0.36
DD	680	24	11	59	0.39
EE	650	14	15	27	0.09
EE	650	24	15	52	0.18
EE	650	63	15	27	0.21

Table 4.19 shows the alkali resistance of commercially available Controlled Pore Glass (CPG) of grade CPG 1000CL and of CHT ceramic hydroxyapatite type II. It was found that CPG 1000 CL, which is produced from a sodium borosilicate glass system, shows identical results as regards alkali resistance as glass AA. Whereas CHT type-II shows a much superior alkali resistance compare to glass AA. However, the CHT type-II is stable only in pH range 6.5–14.

Table 4.19: Alkali resistance of commercial porous glass types.

Glass	Weight loss	Weight loss per total surface area
	%	(mg/dm^2)
CPG 1000CL	75	0.32
BIO-RAD CHT Type-II	14	0.09

CHAPTER FIVE

CONCLUSIONS AND FUTURE WORK

5.1 CONCLUSIONS

The findings of this thesis are presented in the following main points:

(a) Thermal behaviour analysis of the glass compositions

DTA and dilatometry can be used to determine basic thermal properties such as glass transition temperature, dilatometric softening temperature, and the linear thermal expansion coefficient of sodium borosilicate glass. Since the Na_2O/B_2O_3 ratio was <0.5 for all the glass compositions used, the boric oxide anomaly played a major role in the T_g shift. Increasing alkali content in sodium borosilicate glass compositions converted BO_3 triangles to BO_4 tetrahedra, thereby increasing the network connectivity. Therefore, the glass transition temperature value was higher in glass series A–E (10 wt% Na_2O) compared to glass series AA–EE (6 wt% Na_2O). Additions of $ZrO_2/ZrSiO_4$ also increased the glass transition temperature. A sharp exothermic peak was observed in the DTA curve for the glass compositions containing 15 wt% of $ZrSiO_4$. This sharp peak suggests bulk crystallisation. A similar glass composition (glass E-II) with ZrO_2 replacing $ZrSiO_4$ showed a broad exothermic effect that is likely associated with surface crystallisation. A TTT diagram indicated the ranges of onset crystallisation temperature and time, and the heat-treatment temperature and time needed to achieve phase separation without crystallisation.

(b) Heat-treatment and phase separation

Based on the findings of the thermal behaviour of glasses, controlled heat-treatments were implemented to separate the glass into two-phases; a silica-rich phase, and an

alkali-rich borate phase. X-ray diffraction (XRD) was used to identify any crystal phases present in the as-quenched and heat-treated glasses. FTIR analysis is found to be effective in investigating phase separation. A combination of FTIR and XRD analysis was used to compare the extent of phase separation and crystallisation behaviour.

(c) Leaching of phase separated glasses

The effect of the concentration of acid and the duration of leaching, as well as the duration of alkali washing, on the morphology of the pores was studied. It was found that leaching does not work properly without using washing step with NaOH. A non-linear effect of HNO_3 concentration was observed on total pore volume and surface area. This behaviour can be attributed to the formation of silica and zirconia gel within the pores. Removing the gel by means of washing increased the total pore volume and surface area. A combination of leaching and washing steps using 1 N HNO_3 (24 h) followed by 3 N H_2SO_4 (24 h) and 0.5 N NaOH (5 h) led to a higher surface area with larger pore volume. However, with CaO containing glass (glass F), implementing the zirconia gel removing step was difficult, as the heat-treated glass wholly moved into solution during second stage of leaching (3 N H_2SO_4). Therefore, this second step in leaching was completely avoided and therefore the resultant porous glass (leached glass) still had the zirconia gel remaining inside the pores, which affected the pore volume and surface area.

(d) Leached glass characterisation

Using optimised leaching steps separated the boron rich phase from silica and left a skeletal structure consisting mostly of silica and zirconia. This final silica structure had finely distributed nano-sized pores. Porosimetry was used to study the structure of pores resulting from leached glass. Additions of $ZrO_2/ZrSiO_4$ to the sodium borosilicate glass system reduced the growth rate of phase separation. As a result, mean pore size of the porous glass decreased with addition of $ZrO_2/ZrSiO_4$. A linear relationship implied between mean pore size and the square root of heat-treatment dwell time. For longer heat-treatment times, mean pore size increased. Morphological examination using SEM also indicated that the glass containing 6wt%

Na_2O resulted in a narrowly distributed pores. Alkali oxide content in the glass composition was found to play an important role in the phase separation mechanism. Where 6 wt% of alkali oxide (Na_2O) was used, interconnected pore structures with higher pore volumes were achieved, whereas glasses with 10 wt% of Na_2O yielded spherical droplets with low pore connectivity. Glass compositions containing higher alkali oxide (10 wt% Na_2O) were found to retain more Zr in the porous glass when ZrO_2 is $\leq$ 11 wt%. Whereas, no traces of Zr was detected by EDXS in the case of glasses containing lower alkali oxide (6 wt% Na_2O) and with a $ZrSiO_4$ content of < 15 wt%. However, a dramatic reduction in Zr content in porous glass was detected in CaO containing glass as compared to other glasses containing 15 wt% ZrO_2/$ZrSiO_4$. This decrease in Zr retention in glass containing CaO is believed to be due to the saturation of BO_4 concentration, which led the major fraction of ZrO_2 preferentially moved to boron rich phase and ultimately being eluted during leaching.

(e) Alkali resistance test

The alkali resistance remained almost constant for the porous glasses in glass series A–E, which contained a greater amount of alkali oxide (10 wt% Na_2O). For these glass compositions the phase separation process is believed to be dominated by nucleation and growth, as opposed to spinodal decomposition. A significant improvement was observed when the amount of alkali oxide (Na_2O) was reduced to 6 wt% in glass E-II, and in glass series AA–EE, in which the phase separation process is believed to have been dominated by spinodal decomposition. Zr was found to be present in porous glass skeletons when 15 wt% of ZrO_2/$ZrSiO_4$ was added in glass series AA–EE and glass E-II. These porous glasses containing Zr were 3-4 times more alkali resistant than the basic sodium borosilicate glass.

5.2 FUTURE WORK

Leaching was found to be one of the important determining factors in preparing porous glass with specific characteristics. In this study, optimising leaching condition was found to be effective. A further investigation could be carried out considering the leaching duration as well as outcome efficiency based on individual glass compositions.

It was observed that particle size significantly influenced the optimal heat-treatment conditions. The smaller the particles, the greater are the chances that crystallisation will occur. Therefore, a detailed study on the effect of particle size on heat-treatment and phase separation will be useful to fine tune heat-treatment temperatures and times to insure optimal results.

CaO, added as $CaCO_3$ in glass compositions, has been widely used in last two decades to retain zirconia in silica skeleton after leaching, while at the same time enhancing phase separation during heat-treatment. It was found difficult to leach glasses containing CaO. Thus, TiO_2 might be a good alternative choice to enhance phase separation in zirconia/zircon containing glass and experimentally testing this alternative could prove beneficial.

REFERENCES

[1] H. P. Hood, M. E. Nordberg. 1938. *Treated borosilicate glass.* US Patent, No. 2106744.

[2] W. Haller. 1983. *Application of controlled pore glass in solid phase biochemistry, in:* W. H. Scouten (Ed.), Solid Phase Biochemistry. John Wiley & Sons, New York. pp 535-597.

[3] W. Haller. 1970. *Material and method for performing steric separations.* US Patent, No. 3549524.

[4] N. Ford, R. Todhunter. 1989. *Applications of microporous glasses, in:* M. H. Lewis (Ed.), Glasses and Glass-Ceramics. Chapman and Hall, London. pp 203-225.

[5] A. Jungbauer. 2005. Chromatographic media for bioseparation. *Journal of Chromatography A,* 1065, 1, pp 3-12.

[6] K. Nakashima, K. Noda, K. Mori. 1997. Time-temperature-transformation diagrams for borosilicate glasses and preparation of chemically durable porous glasses. *J. Am. Ceram. Soc.,* 80, 5, pp 1101-1110.

[7] W. Haller. 1973. *Porous material and method of making the same.* US Patent, No. 3,758,284.

[8] K. Eguchi, H. Tanaka, T. Yamaguro, T. Yazawa. 1988. *Chemically durable porous glass and process for the manufacture thereof.* US Patent, No. 4,778,777.

[9] T. Yazawa, H. Tanaka, K. Eguchi, S. Yokoyama. 1994. Novel alkali-resistant porous glass prepared from a mother glass based on the SiO_2-B_2O_3-RO-ZrO_2 (R = Mg, Ca, Sr, Ba and Zn) system. *J. Mater. Sci.,* 29, 13, pp 3433-3440.

[10] W. Du, K. Kuraoka, T. Akai, T. Yazawa. 2001. Effect of Additive ZrO_2 on Spinodal Phase Separation and Pore Distribution of Borosilicate Glasses. *J. Phys. Chem. B,* 105, 48, pp 11949-11954.

[11] R. W. Stout. 1986. *Metal oxide stabilized chromatography packings.* US Patent, No. 4,600,646.

[12] Y. Murakami. 1987. *Method of strengthening the alkali resistance of a porous glass.* US Patent, No. 4,661,138.

[13] K. Wada, Y. Tsurita. 1990. *Porous glass and process for its production.* US Patent, No. 4,978,641.

[14] T. Kokubu. 1986. *Porous titanate glass and a method of producing it.* European Paten, No. EP0174851A1.

[15] H. Hosono, Y. Sakai, M. Fasano, Y. Abe. 1990. Preparation of Monolithic Porous Titania-Silica Ceramics. *J. Am. Ceram. Soc.*, 73, 8, pp 2536-2538.

[16] C. V. McNeff, P. W. Carr, S. J. Rupp, D. R. Stoll, D. R. Hawker, L. D. Zigan, K. G. Johnson. 2005. *High stability porous metal oxide spherules used for one-step antibody purifications.* US Patent, No. 6,846,410.

[17] S. T. Kawamoto, K. S. Yamamoto. 1991. *Alkali-resistant glass for forming glass fibers.* US Patent, No. 5,064,785.

[18] A. J. Connelly, R. J. Hand, P. A. Bingham, N. C. Hyatt. 2011. Mechanical properties of nuclear waste glasses. *J. Nucl. Mater.*, 408, 2, pp 188-193.

[19] P. W. McMillan. 1979. *Glass-Ceramics.* Academic Press, London.

[20] A. Paul. 1990. *Chemistry of Glasses.* 2nd ed., Chapman and Hall, London.

[21] ASTM C162. C162-Compilation of ASTM Standard Definitions. The American Society for Testing Materials, Philadelphia PA 1945.

[22] A. K. Varshneya, J. C. Mauro. 2010. Comment on Misconceived ASTM Definition of "Glass" by A. C. Wright. *Eur. J. Glass Sci. Technol. A*, 51, 1, pp 28-30.

[23] R. H. Doremus. 1994. *Glass Science.* 2nd ed., John Wiley & Sons, New York.

[24] J. E. Shelby, M. Lopes. 2005. *Introduction to glass science and technology*, 2nd ed., The Royal Society of Chemistry, Cambridge.

[25] J. Zarzycki. 1991. *Glasses and the Vitreous State.* Cambridge University Press, Cambridge.

[26] MIT lecture note 3.091, 3.091 – Introduction to Solid State Chemistry, Lecture Notes No. 7, GLASSES, http://web.mit.edu/3.091/www/WittNotes/Notes_7.pdf, [accessed: October 14, 2012].

[27] W. D. Kingery, D. R. Uhlmann, H. K. Bowen. 1976. *Introduction to Ceramics.* 2nd ed., Wiley, New York.

[28] M. Lancry, E. Régnier, B. Poumellec. 2012. Fictive temperature in silica-based glasses and its application to optical fiber manufacturing. *Progress in Materials Science,* 57, 1, pp 63-94.

[29] D. R. Uhlmann, N. J. Kreidl. 1983. *Glass-Forming Systems.* Academic Press, New York.

[30] W. H. Zachariasen. 1932. The atomic arrangement in glass. *J. Am. Chem. Soc.*, 54, 10, pp 3841-3851.

[31] W. Vogel, N. J. Kreidl, E. Lense. 1985. *Chemistry of Glass.* American Ceramic Society, Columbus, Ohio.

[32] B. R. Wheaton, A. G. Clare. 2007. Evaluation of phase separation in glasses with the use of atomic force microscopy. *J. Non Cryst. Solids,* 353, 52-54, pp 4767-4778.

[33] W. Haller. 1965. Rearrangement Kinetics of the Liquid-Liquid Immiscible Microphases in Alkali Borosilicate Melts. *J. Chem. Phys.,* 42, 2, pp 686-8.

[34] M. L. Bauccio. 1994. *Engineered materials reference book*, 2nd ed., ASM International, USA.

[35] L. Bloomfield. 2001. *How Things Work: The Physics of Everyday Life.* 2nd ed., Wiley, New York.

[36] T. H. Elmer. 1992. Porous and Reconstructed Glasses. *Engineered Materials Handbook,* 4, pp 427-432.

[37] IUPAC. 1994. International Union of Pure and Applied Chemistry Physical Chemistry Division Commission on Colloid and Surface Chemistry, Subcommittee on Characterization of Porous Solids: "Recommendations for the characterization of porous solids (Technical Report)". *Pure Appl. Chem.,* 66, 8, pp 1739-1758.

[38] B. Zdravkov, J. Čermák, M. Šefara, J. Janků. 2007. Pore classification in the characterization of porous materials: A perspective. *Central European Journal of Chemistry,* 5, *2,* pp 385-395.

[39] M. Kord, V. K. Marghussian, B. Eftekhari-yekta, A. Bahrami. 2009. Phase separation, crystallization and leaching of microporous glass ceramics in the CaO–TiO_2–P_2O_5 system. *J. Non Cryst. Solids,* 355, 2, pp 141-147.

[40] S. Scholes, F. C. F. Wilkinson. 1970. Glassy phase separation in sodium borosilicate glasses. *Discuss. Faraday Soc.,* 50, pp 175-181.

[41] J. J. Hammel, T. Allersma. 1976. *Phase separatable borosilicate glass compositions.* US Patent, No. 3,972,720.

[42] W. Kiefer. 1989. *Borosilicate glass.* US Patent, No. 4,870,034.

[43] P. Shorrock, B. Yale. 1993. *Borosilicate glass composition.* US Patent, No. 5,219,801.

[44] T. Yazawa, K. Kuraoka, W. Du. 1999. Effect of Cooling Rate on Pore Distribution in Quenched Sodium Borosilicate Glasses. *The Journal of Physical Chemistry B,* 103, *45,* pp 9841-9845.

[45] M. M. Lima, R. Monteiro. 2001. Characterisation and thermal behaviour of a borosilicate glass. *Thermochim. Acta,* 373, 1, pp 69-74.

[46] A. Ledieu, F. Devreux, P. Barboux, L. Sicard, O. Spalla. 2004. Leaching of borosilicate glasses. I. Experiments. *J. Non Cryst. Solids,* 343, 1-3, pp 3-12.

[47] P. Marques. 2008. *Borosilicate glass compositions and uses thereof.* US Patent, No. 7,341,966.

[48] M. Kukizaki. 2010. Large-scale production of alkali-resistant Shirasu porous glass (SPG) membranes: Influence of ZrO_2 addition on crystallization and phase separation in $Na_2O–CaO–Al_2O_3–B_2O_3–SiO_2$ glasses; and alkali durability and pore morphology of the membranes. *J. Membr. Sci.,* 360, 1–2, pp 426-435.

[49] O. Koroleva, L. Shabunina, V. Bykov. 2011. Structure of borosilicate glass according to raman spectroscopy data. *Glass and Ceramics,* 67, 11, pp 340-342.

[50] Z. Zhou. 2011. Effect of heat treatment on $7Na_2O–23B_2O_3–70SiO_2$ glass. *Ceram. Int.,* 37, 6, pp 1769-1773.

[51] M. E. Davis, C. Saldarriaga, C. Montes, J. Garces, C. Crowder. 1988. VPI-5: The first molecular sieve with pores larger than 10 Ångstroms. *Zeolites,* 8, 5, pp 362-366.

[52] C. C. Freyhardt, M. Tsapatsis, R. F. Lobo, K. J. Balkus, M. E. Davis. 1996. A high-silica zeolite with a 14-tetrahedral-atom pore opening. *Nature,* 381, 6580, pp 295-298.

[53] J. S. Beck, et al. 1992. A new family of mesoporous molecular sieves prepared with liquid crystal templates. *J. Am. Chem. Soc.,* 114, 27, pp 10834-10843.

[54] D. Zhao, J. Feng, Q. Huo, N. Melosh, G. H. Fredrickson, B. F. Chmelka, G. D. Stucky. 1998. Triblock Copolymer Syntheses of Mesoporous Silica with Periodic 50 to 300 Angstrom Pores. *Science,* 279, 5350, pp 548-552.

[55] R. Ryoo, C. H. Ko, M. Kruk, V. Antochshuk, M. Jaroniec. 2000. Block-Copolymer-Templated Ordered Mesoporous Silica: Array of Uniform Mesopores or Mesopore–Micropore Network? *J. Phys. Chem. B,* 104, 48, pp 11465-11471.

[56] Q. Lu, F. Gao, S. Komarneni, T. E. Mallouk. 2004. Ordered SBA-15 nanowire arrays inside porous alumina membrane. *J. Am. Chem. Soc.,* 126, 28, pp 8650-8651.

[57] J. Yao, W. Tjandra, Y. Z. Chen, K. C. Tam, J. Ma, B. Soh. 2003. Hydroxyapatite nanostructure material derived using cationic surfactant as a template. *J. Mater. Chem.,* 13, pp 3053-3057.

[58] Inc Bio-Rad Laboratories, Specifications for CHT Ceramic Hydroxyapatite, http://www3.bio-rad.com/B2B/BioRad/product/, [accessed: 03 October 2012].

[59] W. -. Du, K. Kuraoka, T. Akai, T. Yazawa. 2000. Study of kinetics of the phase separation in sodium borate glasses. *J. Mater. Sci.,* 35, 15, pp 3913-3921.

[60] Y. Tsurita, M. Nogami. 2001. Preparation of porous supports in the SiO_2-ZrO_2-Na_2O system from microspherical silica gels. *J. Mater. Sci.*, 36, 18, pp 4365-4375.

[61] J. J. Hammel, T. Allersma. 1974. *Method of Making thermally stable and crush resistant microporous glass catalyst support.* US Patent, No. 3,843,341.

[62] J. J. Hammel, T. Allersma. 1975. *Thermally stable and crush resistant microporous glass catalyst supports and methods of making.* US Patent, No, 3,923,688.

[63] A. Paul. 1977. Chemical durability of glasses; a thermodynamic approach. *Journal of Materials Science,* 12, 11, pp 2246-2268.

[64] Y. Tsurita, K. Wada. 1998. Preparation of Porous Supports in the SiO_2–ZrO_2–Na_2O System. *Bull. Chem. Soc. Jpn.*, 71, 2, pp 503-511.

[65] M. H. Bartl, K. Gatterer, H. P. Fritzer, S. Arafa. 2001. Investigation of phase separation in Nd^{3+} doped ternary sodium borosilicate glasses by optical spectroscopy. *Spectrochimica Acta Part A: Molecular and Biomolecular Spectroscopy*, 57, 10, pp 1991-1999.

[66] K. Saiki, S. Sakida, Y. Benino, T. Nanba. 2010. Phase separation of borosilicate glass containing sulfur. *J. Ceram. Soc. Japan,* 118, 7, pp 603-607.

[67] M. M. R. A. Lima, F. M. B. Fernandes, R. C. C. Monteiro. 2002. Study of the crystallization of a borosilicate glass, *Key Engineering Materials*, 230-232, pp 157-160.

[68] D. Chen, H. Miyoshi, H. Masui, T. Akai, T. Yazawa. 2004. NMR study of structural changes of alkali borosilicate glasses with heat treatment. *J. Non Cryst. Solids,* 345-346, pp 104-107.

[69] M. Reben, H. Li. 2011. Thermal Stability and Crystallization Kinetics of MgO-Al_2O_3-B_2O_3-SiO_2 Glasses. *International Journal of Applied Glass Science,* 2, 2, pp 96-107.

[70] P. B. Rose, D. I. Woodward, M. I. Ojovan, N. C. Hyatt, W. E. Lee. 2011. Crystallisation of a simulated borosilicate high-level waste glass produced on a full-scale vitrification line. *J. Non Cryst. Solids,* 357, 15, pp 2989-3001.

[71] H. P. Hood, M. E. Nordberg. 1940. *Borosilicate glass.* US Patent, No. 2,221,709.

[72] C. E. Curtis, H. G. Sowman. 1953. Investigation of the Thermal Dissociation, Reassociation, and Synthesis of Zircon. *J. Am. Ceram. Soc.*, 36, 6, pp 190-198.

[73] N. Zhirnowa. 1934. Melting diagram of system ZrO_2-SiO_2. *Z. Anorg. Allgem. Chem.*, 218, pp 193-200.

[74] N. A. Toropov, F. Y. Galakhov. 1956. Liquidation in the system ZrO_2–SiO_2. *Izv. Akad. Nauk. USSR, Ser. Khim.,* 2, pp 153-156.

[75] U. Peuchert, C. Kunert, R. Bartsch. 2004. *Borosilicate glass with high chemical resistance and use thereof.* US Patent, No. 6,794,323.

[76] Y. Kokubu, J. Chiba, K. Saita. 1987. *Porous glass, process for its production and glass material used for the production.* US Patent, No. 4,665,039.

[77] E. Watzke, A. Kampfer, P. Brix, F. Ott. 1998. *Borosilicate glass of high chemical resistance and low viscosity which contains zirconium oxide and lithium oxide.* US Patent, No. 5,736,476.

[78] M. Kord, V. K. Marghussian, B. Eftekhari-yekta, A. Bahrami. 2009. Effect of ZrO_2 addition on crystallization behaviour, porosity and chemical–mechanical properties of a CaO–TiO_2–P_2O_5 microporous glass ceramic. *Mater. Res. Bull.,* 44, 8, pp 1670-1675.

[79] S. C. Mojumdar. 2004. The Microstructure and optical transmittance thermal analysis of sodium borosilicate bio-glasses. *Journal of Thermal Analysis and Calorimetry*, 78, 1, pp 145-152.

[80] D. Enke, F. Janowski, W. Gille, W. Schwieger. 2001. Structure and texture analysis of colloidal silica in porous glasses. *Colloids Surf. Physicochem. Eng. Aspects,* 187–188, pp 131-139.

[81] H. Tanaka, T. Yazawa, K. Eguchi, H. Nagasawa, N. Matsuda, T. Einishi. 1984. Precipitation of colloidal silica and pore size distribution in high silica porous glass. *J. Non-Cryt. Solids,* 65, 2-3, pp 301-309.

[82] T. Kasuga, H. Hosono, Y. Abe. 2003. *Biocomposite materials for biotechnology, in:* D. Shi (Ed.), Biomaterials and Tissue Engineering. Springer.

[83] O. V. Mazurin, E. A. Porai-Koshits. 1984. *Phase separation in glass,* Elsevier Science Ltd., Amsterdam.

[84] R. Hill, A. Calver, A. Stamboulis, N. Bubb. 2007. Real-time nucleation and crystallization studies of a fluorapatite glass-ceramics using small-angle neutron scattering and neutron diffraction. *J. Am. Ceram. Soc.,* 90, 3, pp 763-768.

[85] H. Jianjun, X. Feng, L. Jiandang, Z. Xiujian. 2007. Inflect of thermal treatment and acid leaching process on pore characteristics of nanometer porous glass. *J. Wuhan Univ. Technol. -Mat. Sci. Edit.,* 22, 1, pp 129-131.

[86] H. P. Hood, M. E. Nordberg. 1942. *Method of treating borosilicate glasses.* US Patent, No. 2,286,275.

[87] G. Toquer, C. Delchet, M. Nemec, A. Grandjean. 2011. Effect of leaching concentration and time on the morphology of pores in porous glasses. *J. Non Cryst. Solids,* 357, 6, pp 1552-1557.

[88] R. K. Iler. 1979. *The Chemistry of Silica: Solubility, Polymerization, Colloid and Surface Properties, and Biochemistry.* Wiley, New York.

[89] R. D. Smith, P. E. Corbin. 1949. Attack of Glasses by Alkaline Solution. *J. Am. Ceram. Soc.,* 32, 6, pp 195-198.

[90] M. P. Xavier, B. Vallejo, M. D. Marazuela, M. C. Moreno-Bondi, F. Baldini, A. Falai. 2000. Fiber optic monitoring of carbamate pesticides using porous glass with covalently bound chlorophenol red. *Biosensors and Bioelectronics,* 14, 12, pp 895-905.

[91] P. T. Sotomayor, I. M. Raimundo Jr., A. J. G. Zarbin, J. J. R. Rohwedder, G. O. Neto, O. L. Alves. 2001. Construction and evaluation of an optical pH sensor based on polyaniline–porous Vycor glass nanocomposite. *Sensors Actuators B: Chem.,* 74, 1–3, pp 157-162.

[92] M. J. Plodinec. 2000. Borosilicate glasses for nuclear waste immobilisation. *Glass Technology,* 41, 6, pp 186-192.

[93] J. D. Vienna. 2010. Nuclear Waste Vitrification in the United States: Recent Developments and Future Options. *International Journal of Applied Glass Science,* 1, 3, pp 309-321.

[94] A. Marković, D. Stoltenberg, D. Enke, E. -. Schlünder, A. Seidel-Morgenstern. 2009. Gas permeation through porous glass membranes: Part II: Transition regime between Knudsen and configurational diffusion. *J. Membr. Sci.,* 336, 1–2, pp 32-41.

[95] K. Kuraoka, R. Amakawa, K. Matsumoto, T. Yazawa. 2000. Preparation of molecular-sieving glass hollow fiber membranes based on phase separation. *J. Membr. Sci.,* 175, 2, pp 215-223.

[96] T. Takahashi, Y. Yanagimoto, T. Matsuoka, T. Kai. 1996. Hydrogenation activity of benzenes on nickel catalysts supported on porous glass prepared from borosilicate glass with small amounts of metal oxides. *Microporous Materials,* 6, 4, pp 189-194.

[97] J. Park, S. Lee. 1995. Mechanism of Preventing Crystallization in Low-Firing Glass/Ceramic Composite Substrates. *J. Am. Ceram. Soc.,* 78, 4, pp 1128-1130.

[98] R. R. Tummala. 1991. Ceramic and Glass-Ceramic Packaging in the 1990s. *J. Am. Ceram. Soc.,* 74, 5, pp 895-908.

[99] R. A. Messing. 1974. *Adsorbing and crosslinking enzymes within the pores of porous glass.* US Patent, No. 3,804,719.

[100] R. A. Messing. 1975. *Method of making porous inorganic bodies.* US Patent, No. 3,892,580.

[101] D. L. Eaton . 1975. *Porous glass support material.* US Patent, No. 3,904,422.

[102] Size exclusion chromatography, C. M. Gibson. http://wikidoc.org/index.php/Size_exclusion_chromatography, [accessed: 10 October 2012].

[103] G. Sigel, M. Shahriari, Q. Zhou. 1993. *Method for making porous glass optical fiber sensor.* US Patent, No. 5,250,095.

[104] G. B. Alexander, W. M. Heston, R. K. Iler. 1954. The Solubility of Amorphous Silica in Water. *J. Phys. Chem.,* 58, 6, pp 453-455.

[105] R. G. Simhan. 1983. Chemical Durability of ZrO_2 Containing Glasses. *J. Non Cryst. Solids,* 54, 3, pp 335-343.

[106] D. A. McKeown, I. S. Muller, A. C. Buechele, I. L. Pegg, C. A. Kendziora. 2000. Structural characterization of high-zirconia borosilicate glasses using Raman spectroscopy. *J. Non Cryst. Solids,* 262, 1-3, pp 126-134.

[107] T. Kokubu, M. Yamane. 1987. Thermal and Chemical-Properties of TiO_2-SiO_2 Porous-Glass Ceramics. *J. Mater. Sci.,* 22, 7, pp 2583-2588.

[108] D. R. Devilliers, M. A. Res, R. O. Heckroodt. 1986. Alkali-Resistant Porous-Glass Produced from a Na_2O-B_2O_3-Y_2O_3-ZrO_2 Glass. *J. Mater. Sci. Lett.,* 5, 3, pp 277-278.

[109] ISO 695. 1991. Glass - resistance to attack by boiling aqueous solution of mixed alkali - method of test and classification, in: Anonymous International Organization for Standardization.

[110] J. Brooks, I. M. Reaney, P. F. James, K. Beyzavi. 1997. Porous ceramics for affinity chromatography applications. *Electron Microscopy and Analysis,* 153, pp 527-530.

[111] M. Arbab, V. K. Marghussian, H. Sarpoolaky, M. Kord. 2007. The effect of RO oxides on microstructure and chemical durability of borosilicate glasses opacified by P_2O_5. *Ceram. Int.,* 33, 6, pp 943-950.

[112] B. A. Proctor, B. Yale. 1980. Glass-Fibers for Cement Reinforcement. *Philos. Trans. R. Soc. Lond. Ser. A-Math. Phys. Eng. Sci.,* 294, 1411, pp 427-436.

[113] L. Y. Mohri, M. T. Hiroishi, M. K. Sano, M. K. Huruya, M. T. Muramoto, M. M. Tao. 1978. *Alkali-resistant glass composition.* US Patent, No. 4,066,465.

[114] B. Bergeron, L. Galoisy, P. Jollivet, F. Angeli, T. Charpentier, G. Calas, S. Gin. 2010. First investigations of the influence of IVB elements (Ti, Zr, and Hf) on the chemical durability of soda-lime borosilicate glasses. *J. Non Cryst. Solids,* 356, 44-49, pp 2315-2322.

[115] P. A. Webb, C. Orr. 1997. *Analytical Methods in Fine Particle Technology.* Micromeritics Instrument Corporation, Norcross, USA.

[116] J. I. Calvo, A. Hernández, P. Prádanos, L. Martınez, W. R. Bowen. 1995. Pore Size Distributions in Microporous Membranes II. Bulk Characterization of Track-Etched Filters by Air Porometry and Mercury Porosimetry. *J. Colloid Interface Sci.,* 176, 2, pp 467-478.

[117] J. V. Brakel, S. Modry, M. Svata. 1981. Mercury porosimetry: state of the art *Powder Technology,* 29, 1, pp 1-12.

[118] H. Giesche. 2006. Mercury Porosimetry: A General (Practical) Overview. *Particle & Particle Systems Characterization,* 23, 1, pp 9-19.

[119] K. L. Stefanopoulos, T. A. Steriotis, A. C. Mitropoulos, N. K. Kanellopoulos, W. Treimer. 2004. Characterisation of porous materials by combining mercury porosimetry and scattering techniques. *Physica B: Condensed Matter,* 350, 1–3, Supplement, pp E525-E527.

[120] S. Westermarck, A. M. Juppo, L. Kervinen, J. Yliruusi. 1998. Pore structure and surface area of mannitol powder, granules and tablets determined with mercury porosimetry and nitrogen adsorption. *European Journal of Pharmaceutics and Biopharmaceutics,* 46, 1, pp 61-68.

[121] S. P. Rigby, R. S. Fletcher, S. N. Riley. 2004. Characterisation of porous solids using integrated nitrogen sorption and mercury porosimetry. *Chemical Engineering Science,* 59, 1, pp 41-51.

[122] F. Porcheron, M. Thommes, R. Ahmad, P. A. Monson. 2007. Mercury Porosimetry in Mesoporous Glasses: A Comparison of Experiments with Results from a Molecular Model. *Langmuir,* 23, 6, pp 3372-3380.

[123] C. A. León y León. 1998. New perspectives in mercury porosimetry. *Adv. Colloid Interface Sci.,* 76–77, pp 341-372.

[124] J. Van Brakel, S. Modrý, M. Svatá. 1981. Mercury porosimetry: state of the art. *Powder Technol.,* 29, 1, pp 1-12.

[125] A. W. Adamson, A. P. Gast. 1997. *Physical Chemistry of Surfaces.* 6th ed., Wiley-Interscience.

[126] L. C. Drake, H. L. Ritter. 1945. Macropore-Size Distributions in Some Typical Porous Substances. *Ind. Eng. Chem. Anal. Ed.,* 17, 12, pp 787-791.

[127] P. A. Webb. 2001. *An Introduction to the Physical Characterization of Materials by Mercury Intrusion Porosimetry with Emphasis on Reduction and Presentation of Experimental Data.* Micromeritics Instrument Corp., Georgia, USA.

[128] S. Diamond. 2000. Mercury porosimetry: An inappropriate method for the measurement of pore size distributions in cement-based materials. *Cem. Concr. Res.,* 30, 10, pp 1517-1525.

[129] S. P. Rigby, K. J. Edler. 2002. The Influence of Mercury Contact Angle, Surface Tension, and Retraction Mechanism on the Interpretation of Mercury Porosimetry Data. *J. Colloid Interface Sci.*, 250, 1, pp 175-190.

[130] C. Salmas, G. Androutsopoulos. 2001. Mercury Porosimetry: Contact Angle Hysteresis of Materials with Controlled Pore Structure. *J. Colloid Interface Sci.*, 239, 1, pp 178-189.

[131] J. Rouquerol, et al. 2012. Liquid intrusion and alternative methods for the characterization of macroporous materials (IUPAC Technical Report). 84, 1, pp 107-136.

[132] M. Thommes. 2010. Physical Adsorption Characterization of Nanoporous Materials. *Chemie Ingenieur Technik*, 82, 7, pp 1059-1073.

[133] J. Rouquerol, et al. 2012. The characterization of macroporous solids: An overview of the methodology. *Microporous and Mesoporous Materials*, 154, pp 2-6.

[134] Quantacrome Instruments. 2009. PoreMaster/PoreMaster GT Operating Manual.

[135] P. W. Atkins. 1982. *Physical Chemistry.* 2d ed., Oxford University Press, Oxford.

[136] S. Lowell, J. E. Shields, M. A. Thomas, M. Thommes, S. Lowell, J. E. Shields, M. A. Thomas, M. Thommes. 2004. *Characterization of Porous Solids and Powders: Surface Area, Pore Size and Density.* Springer Netherlands.

[137] S. Lowell, J. E. Shields. 1984. *Powder Surface Area and Porosity.* 2nd ed., Chapman and Hall, New York.

[138] S. J. Gregg, K. S. W. Sing. 1967. *Adsorption, Surface Area, and Porosity.* U.S. ed. ed., Academic Press, London.

[139] L. Girard, M. Arab, O. Spalla. 2008. Time resolved alteration process of oxide glasses. *Journal of Colloid and Interface Science*, 319, 1, pp 214-225.

[140] M. Kukizaki, M. Goto. 2007. Preparation and characterization of a new asymmetric type of Shirasu porous glass (SPG) membrane used for membrane emulsification. *J. Membr. Sci.*, 299, 1–2, pp 190-199.

[141] N. M. Jalil. 2011. The Preparation and Characterisation of Mesoporous Films for Electrochemical Applications.

[142] Y. Kato, H. Yamazaki, M. Tomozawa. 2001. Detection of phase separation by FTIR in a liquid-crystal-display substrate aluminoborosilicate glass. *J. Am. Ceram. Soc.*, 84, 9, pp 2111-2116.

[143] S. Fujita, Y. Kato, M. Tomozawa. 2003. IR peak shift due to phase separation of Na_2O–SiO_2 system glasses. *Journal of Non-Crystalline Solids*, 328, 1-3, pp 64-70.

[144] P. Pisciella, M. Pelino. 2005. FTIR spectroscopy investigation of the crystallisation process in an iron rich glass. *Journal of the European Ceramic Society,* 25, 11, pp 1855-1861.

[145] E. P. Barrett, L. G. Joyner, P. P. Halenda. 1951. The Determination of Pore Volume and Area Distributions in Porous Substances. I. Computations from Nitrogen Isotherms. *J. Am. Chem. Soc.,* 73, 1, pp 373-380.

[146] Micromeritics Instrument Corporation, Gas Adsorption Theory Presented by Micromeritics Instrument Corporation, http://www.micromeritics.com/repository/files/gas_adsorption_theory_poster.pdf, [accessed: September 26, 2012].

[147] José R. Almirall, Tatiana Trejos, "Introduction to the Examination and Comparison of Glass Evidence"- Web-based course, Florida International University, Department of Chemistry and Biochemistry and InternationalForensic Research Institute, http://teaf.fiu.edu/Training_Downloads/Glass_Online_Course.pdf, [accessed: September 27, 2012].

[148] A. J. Connelly, N. C. Hyatt, K. P. Travis, R. J. Hand, E. R. Maddrell, R. J. Short. 2011. The structural role of Zr within alkali borosilicate glasses for nuclear waste immobilisation. *J. Non Cryst. Solids,* 357, 7, pp 1647-1656.

[149] Z. Wang, B. S. Hsiao, S. Srinivas, G. M. Brown, A. H. Tsou, S. Z. D. Cheng, R. S. Stein. 2001. Phase transformation in quenched mesomorphic isotactic polypropylene. *Polymer,* 42, 18, pp 7561-7566.

[150] M. S. Hernández-Crespo, M. Romero, J. M. Rincón. 2006. Nucleation and crystal growth of glasses produced by a generic plasma arc-process. *Journal of the European Ceramic Society,* 26, 9, pp 1679-1685.

[151] J. W. Dodd, K. H. Tonge. 1987. *Thermal Methods (Analytical Chemistry by Open Learning).* John Wiley & Sons, London.

[152] A. P. Novaes de Oliveira, A. Bonamartini Corradi, L. Barbieri, C. Leonelli, T. Manfredini. 1996. The effect of the addition of $ZrSiO_4$ on the crystallization of $30Li_2O/70SiO_2$ powdered glass. *Thermochimica Acta,* 286, 2, pp 375-386.

[153] J. A. Augis, J. E. Bennett. 1978. Calculation of the Avrami parameters for heterogeneous solid state reactions using a modification of the Kissinger method. *J. Thermal Anal.,* 13, 2, pp 283-292.

[154] M. Avrami. 1939. Kinetics of phase change. I. General theory. *J. Chem. Phys.,* 7, pp 1103-1112.

[155] M. Avrami. 1940. Kinetics of phase change. II. Transformation-time relations for random distribution of nuclei. *J. Chem. Phys.,* 8, pp 212-224.

[156] I. Ban'kovskaya, D. Kolovertnov, L. Efimenko. 2011. Preparation of composites in the ZrB_2-Si system and investigation of their properties. *Glass Physics and Chemistry,* 37, 2, pp 188-195.

[157] A. Hu, K. Liang, M. Li, D. Mao. 2006. Effect of nucleation temperatures and time on crystallization behavior and properties of $Li_2O–Al_2O_3–SiO_2$ glasses. *Materials Chemistry and Physics,* 98, 2-3, pp 430-433.

[158] T. Wakasugi, L. L. Burgner, M. C. Weinberg. 1999. A DTA study of crystal nucleation in $Na_2O–SiO_2$ glasses. *J. Non Cryst. Solids,* 244, 1, pp 63-73.

[159] M. J. Cattell, T. C. Chadwick, J. C. Knowles, R. L. Clarke, D. Y. D. Samarawickrama. 2006. The nucleation and crystallization of fine grained leucite glass-ceramics for dental applications. *Dental Materials,* 22, 10, pp 925-933.

[160] H. Miyoshi, D. Chen, H. Masui, T. Yazawa, T. Akai. 2004. Effect of calcium additive on structural changes under heat treatment in sodium borosilicate glasses. *J. Non Cryst. Solids,* 345-346, pp 99-103.

[161] J. Kerc, S. Srcic. 1995. Thermal analysis of glassy pharmaceuticals. *Thermochimica Acta,* 248, pp 81-95.

[162] H. E. Kissinger. 1956. Variation of peak temperature with heating rater in differential thermal analysis. *J. Res. Natl. Bureau Std.,* 57, 4, pp 217-221.

[163] N. P. Bansal, R. H. Doremus. 1986. *Handbook of Glass Properties.* Academic Press, Orlando.

[164] H. Hijiya, T. Kishi, A. Yasumori. 2009. Effect of phase separation on crystallization of glasses in the $BaO–TiO_2–SiO_2$ system. *J. Ceram. Soc. Jpn.,* 117, 1, pp 120-126.

[165] R. Takahashi, S. Sato, T. Sodesawa, Y. Tomita. 2005. Thermal properties of monolithic silica and silica-zirconia with bimodal pore structures. *Nippon Seramikkusu Kyokai Gakujutsu Ronbunshi Y.,* 113, 1, pp 92-96.

[166] A. Agarwal, K. M. Davis, M. Tomozawa. 1995. A simple IR spectroscopic method for determining fictive temperature of silica glasses. *J. Non Cryst. Solids,* 185, 1–2, pp 191-198.

[167] M. Lubas, M. Sitarz, Z. Fojud, S. Jurga. 2005. Structure of multicomponent $SiO_2–Al_2O_3–Fe_2O_3–CaO–MgO$ glasses for the preparation of fibrous insulating materials. *J. Mol. Struct.,* 744–747, pp 615-619.

[168] E. F. Medvedev. 2007. Determination of sodium borosilicate bands in the IR spectrum of a multicomponent batch. *Glass Ceram.,* 64, 9-10, pp 300-304.

APPENDICES

Appendix 1: DTA curves of the glasses in heating rates of 10 °C/min, 15 °C/min and 20 °C/min.

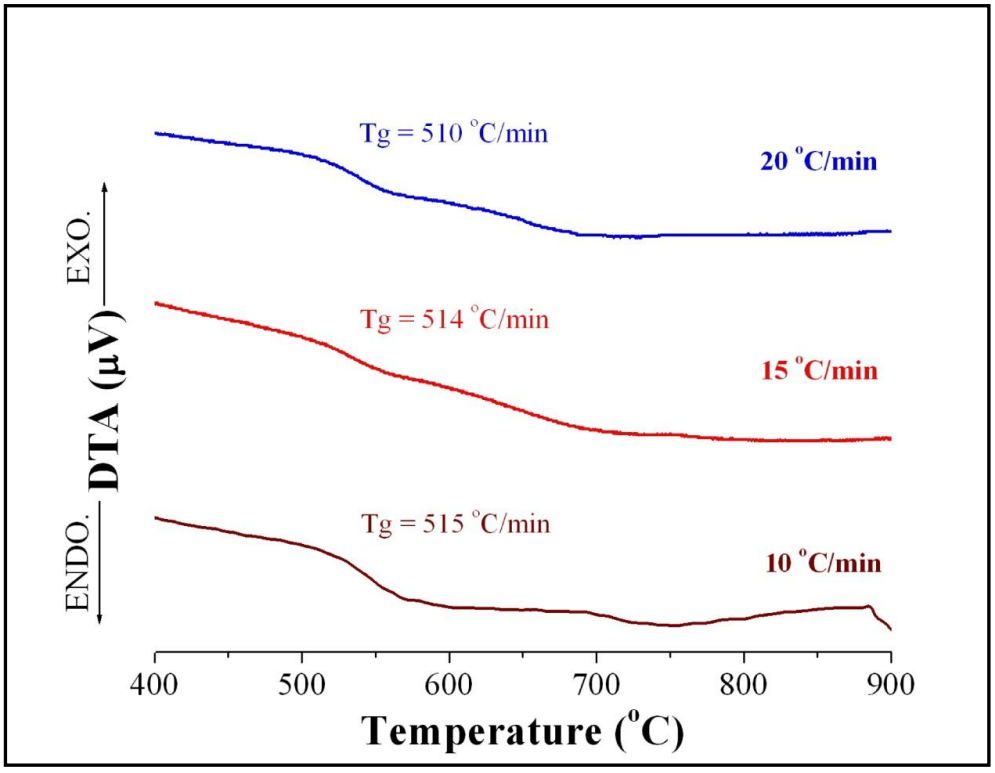

(a) Composition A

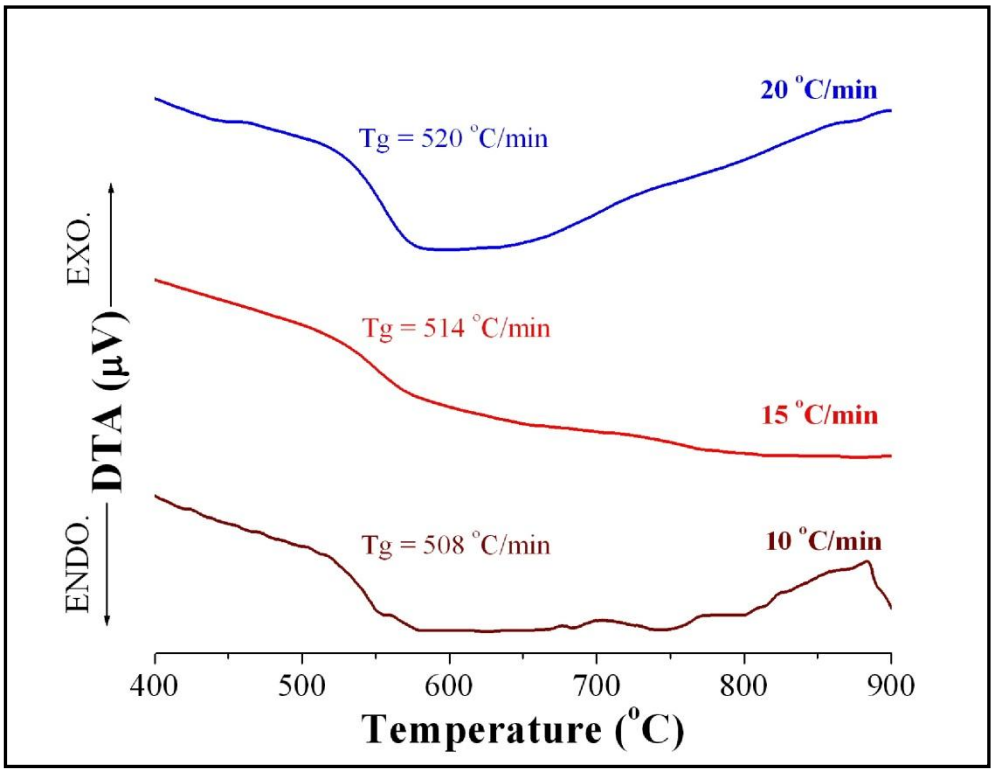

(b) Composition B

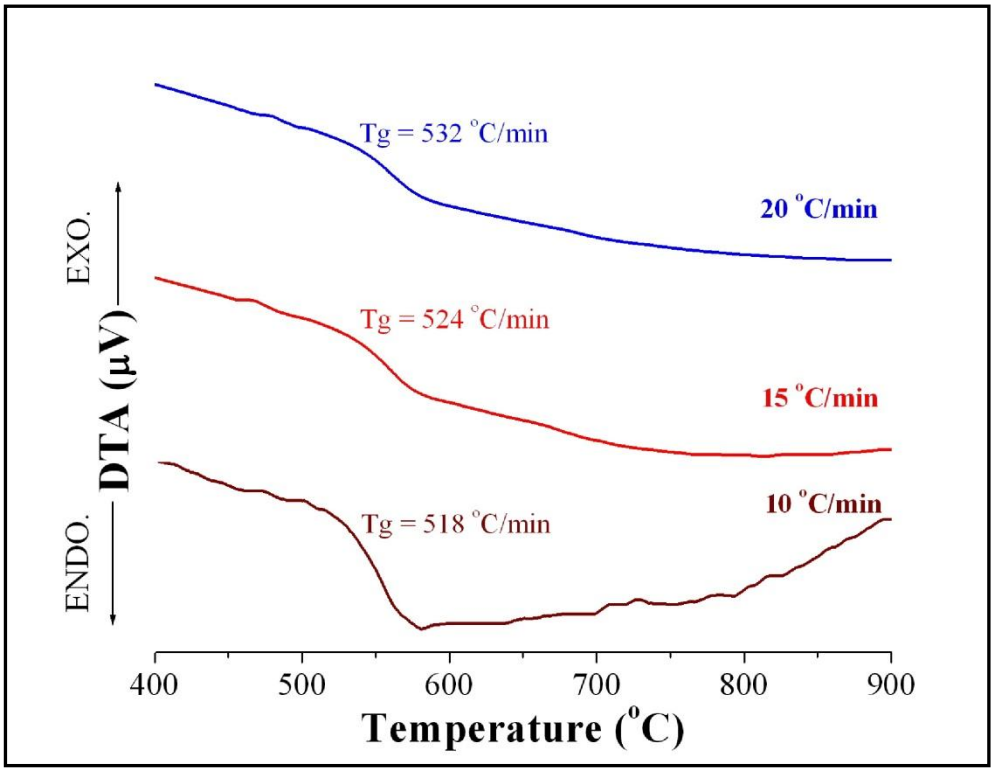

(c) Composition C

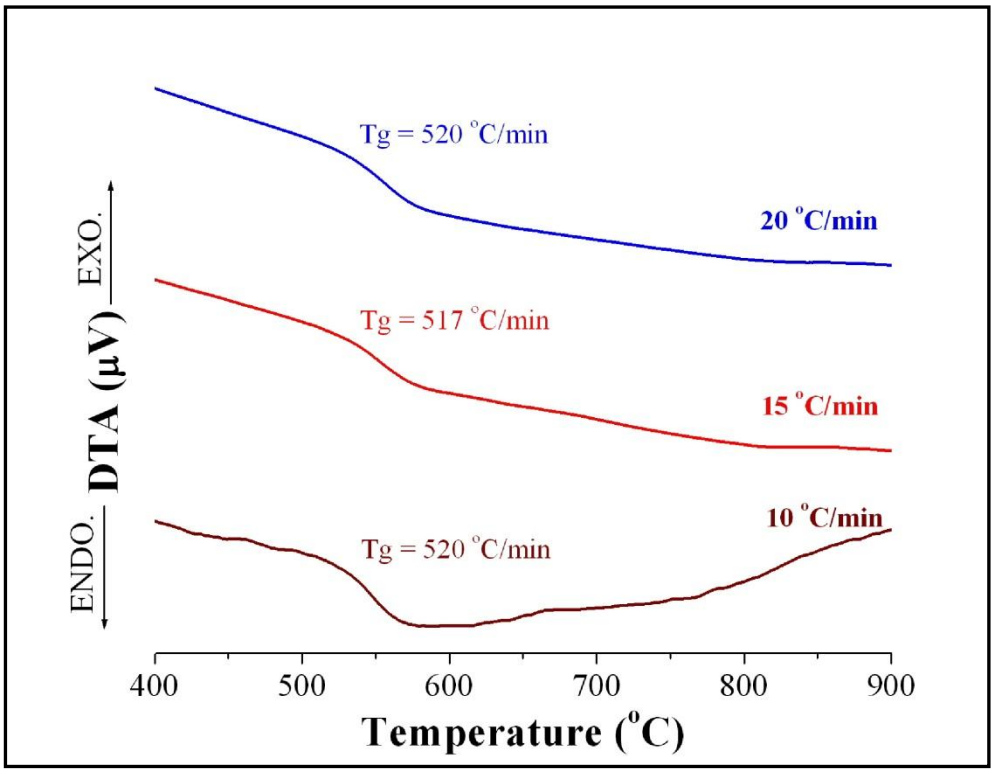

(d) Composition D

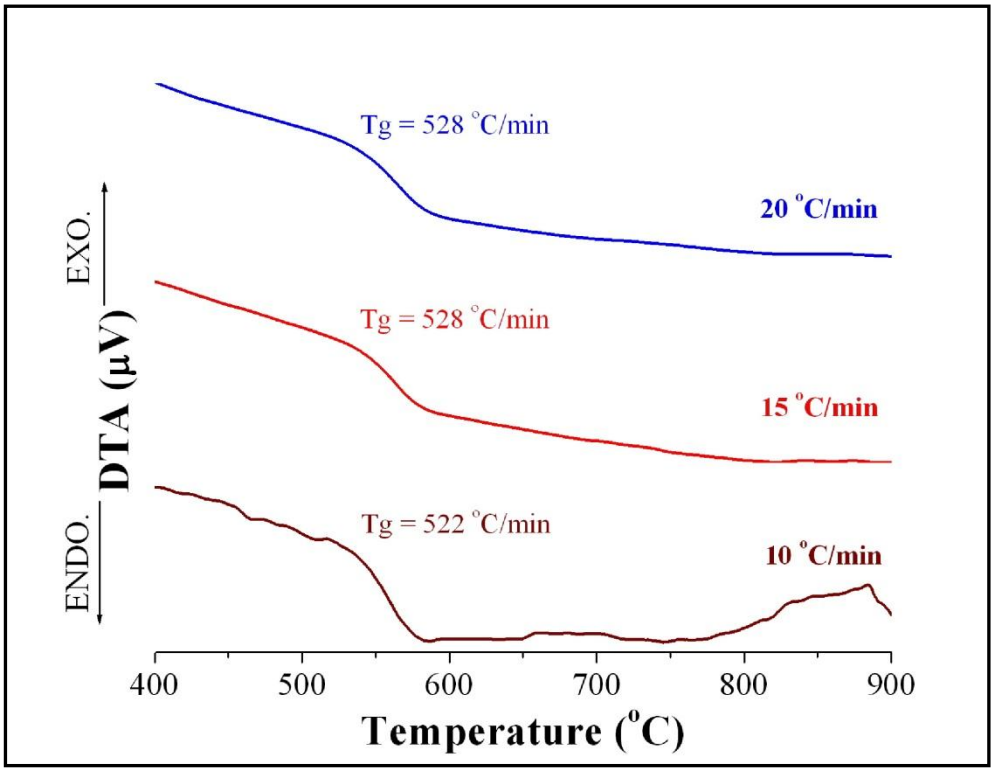

(e) Composition E

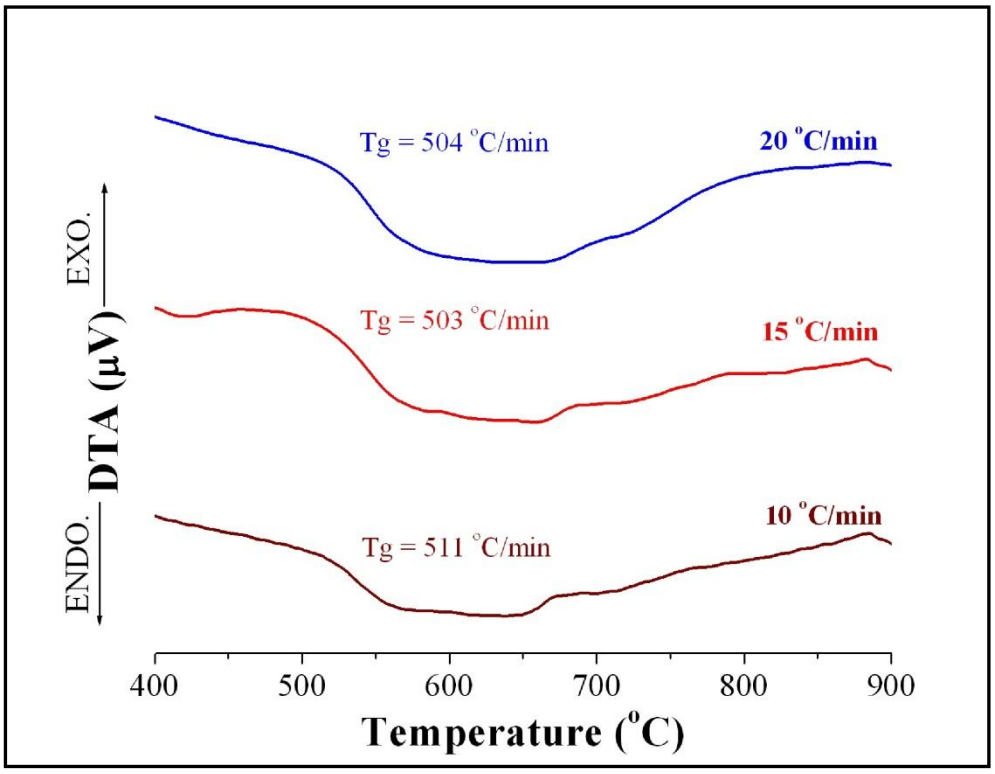

(f) Composition E-II

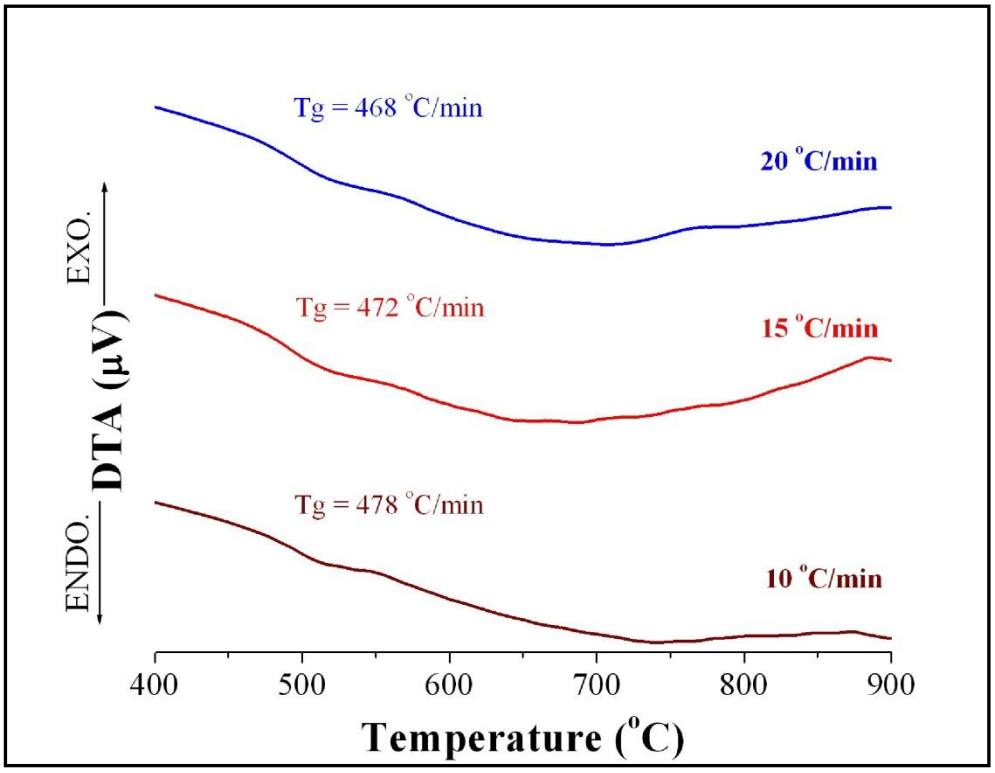

(g) Composition AA

Appendix 2: List of Publications

A) Peer reviewed journal

M. Hasanuzzman, M. Sajjia, A. Rafferty, A. G. Olabi, "Thermal behaviour of zircon/zirconia-added chemically durable borosilicate porous glass", Thermochimica Acta, 2013, 555, 81– 88.

M. Hasanuzzman, A. Rafferty, A. G. Olabi, "Effects of zircon addition on porous structure and alkali durability of borosilicate glasses", under review, Ceramics International, 2013.

B) Peer reviewed conference paper

M. Hasanuzzman, A. G. Olabi, "Development of alkali-resistant porous glass based on $(69–x)SiO_2$-$25B_2O_3$-$6Na_2O$-$xZrSiO_4$ system", 37th Int'l Conf & Expo on Advanced Ceramics & Composites (ICACC 2013) proceedings, accepted for publication, 2013.

C) Others

M. Hasanuzzman, A. G. Olabi, "Effect of nucleation temperature and time on crystallization behaviour of zirconia/ zircon added borosilicate glass", 15th European Conference on Composite Materials (ECCM15), Venice, Italy, 24th-28th June 2012, ECCM15 Conference Proceedings, file 2155.